

Universidade de São Paulo
Instituto de Física

Teletransporte quântico incondicional de
estados de variáveis contínuas de cores distintas:
do infravermelho próximo às bandas de
telecomunicações

Felipe Lucas Gewers

Paulo Nussenzveig

Orientador: Prof. Dr. Paulo Alberto Nussenzveig

Tese de doutorado apresentada ao Instituto de Física
da Universidade de São Paulo, como requisito parcial
para a obtenção do título de Doutor em Ciências.

Banca Examinadora:

Prof. Dr. Marcelo Martinelli (IFUSP)
Prof. Dr. Diogo de Oliveira Soares Pinto (IFSC USP)
Prof. Dr. Antonio Zelaquett Khoury (UFF)
Prof. Dr. Pablo Lima Saldanha (UFMG)
Profa. Dra. Valeria Loureiro da Silva (SENAI CIMATEC)

São Paulo
2025

FICHA CATALOGRÁFICA
Preparada pelo Serviço de Biblioteca e Informação
do Instituto de Física da Universidade de São Paulo

Gewers, Felipe Lucas

Teletransporte quântico incondicional de estados de variáveis contínuas de cores distintas: do infravermelho próximo às bandas de telecomunicações / Unconditional quantum teleportation of multi-color continuous-variable states: from near-infrared to telecommunications bands. São Paulo, 2025.

Tese (Doutorado) – Universidade de São Paulo. Instituto de Física. Departamento de Física Experimental.

Orientador: Prof. Dr. Paulo Alberto Nussenzveig

Área de Concentração: Óptica

Unitermos: 1. Óptica quântica; 2. Óptica não linear; 3. Oscilador paramétrico óptico; 4. Emaranhamento; 5. Teletransporte;

USP/IF/SBI-025/2025

University of São Paulo
Physics Institute

Unconditional quantum teleportation of multi-color continuous-variable states: from near-infrared to telecommunications bands

Felipe Lucas Gewers

Paulo Nussenzveig

Supervisor: Prof. Paulo Alberto Nussenzveig

Thesis submitted to the Physics Institute of the
University of São Paulo in partial fulfillment of the
requirements for the degree of Doctor of Science.

Examining Committee:

Prof. Marcelo Martinelli (IFUSP)
Prof. Diogo de Oliveira Soares Pinto (IFSC USP)
Prof. Antonio Zelaquett Khoury (UFF)
Prof. Pablo Lima Saldanha (UFMG)
Prof. Valeria Loureiro da Silva (SENAI CIMATEC)

São Paulo
2025

*To my mother,
whose relentless determination ensured
I received a quality education*

ACKNOWLEDGEMENTS

Physics thrives on collaboration, and this principle is no different in the project described in this thesis. This work is the result of the collective efforts of many extraordinary people who contributed in various ways. Some dedicated themselves with daily effort, while others provided crucial advice or occasional but impactful contributions that shaped the direction of the project, and many more contributed through their support and engaging discussions about physics. In the following lines, I will express my gratitude to these indispensable individuals, without whom the achievements of this work would not have been possible.

The guidance and vision of great scientists were essential to the work presented here. I am deeply grateful to my advisors, Prof. Marcelo Martinelli and Prof. Paulo Nussenzveig, for their mentorship, which has helped me grow tremendously as a scientist. I am sincerely thankful for their rigorous yet inspiring scientific discussions, their contagious enthusiasm for science, their patience and understanding during challenging times, and, above all, the trust they placed in me to lead this ambitious experimental project. Being part of the outstanding LMCAL laboratory under their guidance has been a privilege, and I am profoundly grateful for everything.

During these years, I had the privilege of working alongside excellent and experienced scientists who closely collaborated with me in developing this project. Their daily support was invaluable in advancing the experiment, guiding critical steps in decision-making, and engaging in insightful discussions about physics in general and the experimental challenges we faced. I am deeply thankful to Dr. Gabriel Borba, who worked with me on this project for two years. Not only did he play an essential role in several aspects of the experiment, but his companionship was a source of constant encouragement. His positivity and willingness to take on challenges made every step of the journey more enjoyable. I am especially thankful for his patience and determination during the final teleportation measurements. I would like to extend my sincere gratitude to Dr. Igor Konieczniak. Although we worked together for only six months, far shorter than I would have hoped, I learned an incredible amount from him. His insightful discussions, always conducted with patience, his innovative ideas, and his exceptionally clear and didactic way of explaining complex concepts was invaluable. Without the advances and strategies he developed, both during this project and in his earlier work as a Ph.D. student in the lab, achieving these results would not have been possible.

During my time at the institute, I greatly benefited from its excellent infrastructure, which included specialized workshops and expert technical support. I am particularly grateful to the team at the mechanical workshop, especially Marcos Santos de Souza,

whose meticulous attention to detail in all fabricated components was invaluable. I also greatly appreciated his willingness to discuss strategies and his patience in teaching me the principles of mechanical design. I also extend my gratitude to Alexandre Malafronte, a vacuum technician, for his invaluable assistance in designing the vacuum system and performing leak tests with his helium leak detector. A special thanks goes to Eduardo Monteiro from the electronics workshop for his care in implementing advanced circuit designs that often exceeded the original requirements. Lastly, I would like to thank Sergio Kunihiro Korogui from the IT department for his help in connecting devices to the institute's network and upgrading our computers.

I would also like to express my gratitude to the current and former members of the LMCAL, with whom I had the pleasure of working and interacting. From countless lunches filled with lively discussions about physics and every imaginable topic, to unforgettable shared experiences, these interactions made my journey so much more enjoyable. Thank you, Alvaro Montaña Guerrero, Beatriz Vilela de Moura, Gabriel Couto Rickli, Guilherme Jorge, Hans Marin Florez, Lucas Nunes Faria, Luiz Couto Corrêa Pinto, Marcelo Marcelino, Raúl Leonardo Rincón Celis, Roger Alfredo Kogler, Théo Louzada Meireles, and Yuri Sacha Lopes da Silva. A special thanks goes to Roger for his companionship during my time in Berlin, his patience in listening to my extensive discussions about this thesis, and his thoughtful advice.

With love and gratitude, I want to thank my family, who shaped me into the person I am today and provided the unwavering support I so greatly needed during the challenging moments of this work. To my mother, Carla Adriana Lucas, thank you for teaching me the value of education from the very beginning and for making endless sacrifices to give me access to quality education, even in the face of adversity. To my father, Luiz Adolfo Gewers, you have been a constant source of wisdom, always taking the time to understand the challenges I faced and providing guidance in moments of uncertainty. To my late grandmother, Luzia Costa de Sousa, lovingly known as Dona Zi, who, even without fully understanding my pursuits, continually encouraged me to follow my chosen path, and finally, to my aunt Geane Carla Lucas and my cousin Lucas Costa Simoes, thank you for being there for me and offering your support throughout this journey.

Lastly, I would like to express my gratitude to my friends outside of LMCAL for their companionship, which kept me motivated throughout this journey. Specifically related to the development of this work, I would like to thank Ivan Almeida for reviewing my qualification text, Diogo Batista dos Santos for his valuable insights on electronic filtering, and Rebeca Rabia for her assistance with some of the figures in this work. Additionally, I extend my heartfelt thanks to the 'Chaos Dpto.' RPG group for being a significant part of my social interaction during the isolating pandemic period.

This work was financed in part by the Conselho Nacional de Desenvolvimento

Científico e Tecnológico (CNPq), under process number 140442/2019-7, and by the São Paulo Research Foundation (FAPESP), Brazil, under process numbers 2022/08865-0, 2015/18834-0 and 2009/52157-5.

*“The first principle is that you must not fool yourself
and you are the easiest person to fool.”*

Richard P. Feynman

ABSTRACT

Quantum teleportation is the basis for numerous quantum applications, with the continuous-variable (CV) protocol having the significant advantage of being unconditional and deterministic, allowing every input state to be teleported. In the context of quantum networks, quantum channels connecting different wavelengths can be used in quantum hybrid technologies, linking different quantum platforms with distinct purposes that interact with light at specific wavelengths.

Our approach to building these continuous-variable quantum channels is through quantum teleportation between quadratures of fields at widely different frequencies. To achieve this, we employ a triply resonant optical parametric oscillator (TROPO) operating above threshold as a source of two-mode entangled states. Pumped by a 532 nm Nd:YAG second harmonic laser, the system generates intense beams at 794.4(4) nm (377 THz; near-infrared compatible with the rubidium D1 line) and 1611(3) nm (186 THz; telecommunication L-band), with a frequency separation of 191 THz, which is over one octave. Using the resonator-assisted auto-homodyne technique, we implement the teleportation protocol to transfer a displaced coherent state from the infrared to the telecommunication band.

In this work, we report the first demonstration of multi-color continuous-variable (CV) quantum teleportation bridging distinct frequency bands. This also marks the first implementation of teleportation between the sideband modes of intense beams that surpasses the classical fidelity limit. Additionally, we provide the first full characterization of the individual sideband modes in widely separated signal and idler fields generated by an above-threshold optical parametric oscillator. This demonstration paves the way for the development of hybrid quantum systems with enhanced connectivity.

Keywords: Quantum optics; Optical parametric oscillator; Squeezing; Entanglement; Teleportation.

RESUMO

O teletransporte quântico é a base para inúmeras aplicações quânticas, com o protocolo de variáveis contínuas (CV) possuindo a significativa vantagem de ser incondicional e determinístico, permitindo que qualquer estado de entrada seja teleportado. No contexto das redes quânticas, canais quânticos conectando diferentes comprimentos de onda podem ser utilizados em redes quânticas híbridas, vinculando várias plataformas quânticas com propósitos distintos que interagem com a luz em comprimentos de onda específicos.

Nossa abordagem para construir esses canais quânticos em variáveis contínuas é através do teletransporte quântico entre as quadraturas dos campos em frequências amplamente diferentes. Para isso, usamos um oscilador paramétrico óptico triplamente ressonante (TROPO), operando no regime acima do limiar, como fonte de estados emaranhados de dois modos. Ao bombear com um laser de segundo harmônico de Nd:YAG (532 nm), geramos feixes intensos em 794.4(6) nm (377 THz), no infravermelho próximo compatível com a linha D1 dos átomos de rubídio, e em 1611(3) nm (186 THz), na banda L de telecomunicações. Utilizando a técnica de detecção auto-homodina com cavidades ópticas, implementamos o protocolo de teletransporte para transferir um estado coerente deslocado do infravermelho para as bandas de telecomunicações.

Nesse trabalho, relatamos a primeira demonstração de teletransporte quântico multicolorido de variáveis contínuas (CV) entre bandas de frequência distintas. Isso também marca a primeira implementação de teletransporte entre os modos de bandas laterais de feixes intensos que ultrapassa o limite de fidelidade clássico. Adicionalmente, fornecemos a primeira caracterização completa dos modos individuais de bandas laterais dos campos de sinal e complementar amplamente separados em frequência, gerados por um oscilador paramétrico óptico operando acima do limiar. Esta demonstração abre caminho para o desenvolvimento de sistemas quânticos híbridos com conectividade aprimorada.

Palavras-chave: Óptica quântica; Óptica não linear; Oscilador paramétrico óptico; Emaranhamento; Teletransporte.

LIST OF FIGURES

Figure 1 – Schematic of coherent and single-mode squeezed states in the phase space	40
Figure 2 – Diagram of a non-degenerate triple-resonant optical parametric oscillator (TROPO)	47
Figure 3 – Representation of optical field spectrum with carrier and sideband modes	54
Figure 4 – Schematic of the balanced detection strategy for shot noise measurement	58
Figure 5 – Schematic representation of photocurrent quadrature demodulation . .	64
Figure 6 – Visualization of the c-coefficients in the single field spectral noise density	81
Figure 7 – Simulated spectral noise density of a state with asymmetrical excess noise	83
Figure 8 – Visualization of c-coefficients in two-fields spectral noise density . . .	85
Figure 9 – Schematic representation of the quantum teleportation protocol	101
Figure 10 – Simplified representation of the teleportation experimental setup	103
Figure 11 – Simplified representation of the EPR station experimental setup	104
Figure 12 – Simplified representation of Victor’s experimental setup for input state creation	106
Figure 13 – Simplified representation of Alice station	108
Figure 14 – Simplified representation of Bob station	110
Figure 15 – Simplified representation of Victor’s experimental setup for quantum tomography of the teleported state	113
Figure 16 – Diagram of the Loss Model in the Teleportation Protocol	116
Figure 17 – Schematic of the optical setup used in the teleportation experiment .	138
Figure 18 – Filter cavity schematic and spectral attenuation	141
Figure 19 – Schematic of PPKTP crystal	144
Figure 20 – Exploded diagram and photograph of the OPO assembly in use	147
Figure 21 – Interacting field intensities in OPO above threshold	150
Figure 22 – Signal and idler wavelengths in terms of crystal temperature	151
Figure 23 – Schematic and photographs of OPO vacuum setup	153
Figure 24 – Schematic and visibility of the Mach-Zehnder interferometer for input state creation	158
Figure 25 – Schematic of Alice’s setup and analysis cavity photos	160
Figure 26 – Schematic of Bob’s experimental setup	165
Figure 27 – Schematic of quantum tomography setup at Victor station	168
Figure 28 – Quantum efficiency of Alice and Victor’s detectors	172
Figure 29 – Electronic signal processing system for detected HF signals	173
Figure 30 – Power spectrum of Alice’s phase quadrature detector	174
Figure 31 – Standard deviation of balanced detection HF signals for digital gain correction	176

Figure 32 – Optical power dependence of teleportation detectors SNR	177
Figure 33 – Classical channel modulation artifacts and digital filtering	180
Figure 34 – Shot noise calibration: HF-demodulated voltage subtraction vs. incident optical power	190
Figure 35 – OPO’s pump threshold estimation by fitting the measured fraction of incident pump power	191
Figure 36 – Variances and covariances of the amplitude quadratures of the signal and idler	192
Figure 37 – Variances of the subtraction and sum of the amplitude quadratures of the signal and idler	193
Figure 38 – Validation of stationarity conditions for the measured spectral photocurrents	195
Figure 39 – Fisher kurtosis analysis of spectral photocurrents for Gaussianity and stationarity verification	196
Figure 40 – Transmission and reflection of both cavities in the tomography measurement	199
Figure 41 – Variance of subtracted and summed accessed quadratures in the tomography measurement	200
Figure 42 – Normalized variance of signal and idler quadratures in the tomography measurement	202
Figure 43 – Cross-correlations between signal and idler accessed quadratures in the tomography measurement	203
Figure 44 – Expected fidelity for the teleportation protocol from tomography measurement	209
Figure 45 – Transmission and reflection from analysis cavities during teleportation .	211
Figure 46 – SNR of the demodulated HF voltages during the teleportation measurement	212
Figure 47 – Alice’s variance of the measured quadratures during teleportation . . .	213
Figure 48 – Mean variances of Alice’s measured amplitude and phase quadratures for displaced coherent and vacuum input states	214
Figure 49 – Variances of the quadratures measured at Victor station for the teleported displaced coherent state	215
Figure 50 – Teleported state covariance matrix elements for displaced coherent and vacuum input states	216
Figure 51 – Displaced coherent input state mean quadrature values from teleportation measurement	218
Figure 52 – Displaced input state mean quadratures measured at Alice’s station during teleportation	219

Figure 53 – Mean value of the accessed quadratures during Victor’s quantum tomography of the teleported state	219
Figure 54 – Mean quadratures of teleported displaced coherent states across all tomography measurements	220
Figure 55 – Comparison of mean quadrature values and amplitude for input and teleported states	222
Figure 56 – Teleportation gain values in terms of the control voltage	223
Figure 57 – Teleportation fidelity for displaced coherent and vacuum input states by gain without accounting losses	225
Figure 58 – Teleportation fidelity for the Alice corrected losses scenario	228
Figure 59 – Fidelity of the teleported state corrected for Victor’s optical losses . . .	231
Figure 60 – Mean and variance values from Alice’s station for the measurement near unitary gain (second run)	233
Figure 61 – Displaced teleported state mean and variance for gain closest to unity (second run)	234
Figure 62 – Comparison of mean quadratures and determination of gain (second run)	234
Figure 63 – Fidelity results with uncorrected and Alice’s station corrected losses (second run)	237
Figure 64 – Fidelity results with Victor’s loss correction for the (second run)	240
Figure 65 – Transmission and reflection from analysis cavities during third teleportation run	241
Figure 66 – Alice mean and variance values closest to unitary gain (third run) . . .	242
Figure 67 – Victor mean and variance values closest to unitary gain (third run) . .	243
Figure 68 – Comparison of mean quadratures and determination of gain (third run)	243
Figure 69 – Fidelity results with uncorrected and Alice’s station corrected losses (third run)	245
Figure 70 – Fidelity results with Victor’s loss correction (third run)	247
Figure 71 – Signal-to-noise ratio from quantum tomography	278
Figure 72 – Single-field stationarity conditions for the signal and idler in quantum tomography	279
Figure 73 – Two-field stationarity conditions from quantum tomography measurement	280
Figure 74 – Kurtosis for the signal and idler from quantum tomography measurement	281

LIST OF TABLES

Table 1 – Relevant parameters of an OPO to describe the signal and idler noise spectrum	52
Table 2 – Diabolo Laser Specifications	139
Table 3 – Filter cavity parameters	143
Table 4 – Specifications of the PPKTP crystal as provided by the manufacturer, Raicol.	145
Table 5 – OPO cavity parameters	148
Table 6 – Alice cavity parameters	162
Table 7 – Bob cavity parameters	167
Table 8 – Victor cavity parameters	169
Table 9 – ADC Channel Variables and Notations	184
Table 10 – Covariance matrix elements of signal and idler local states from tomography measurement	204
Table 11 – Two-field covariance matrix elements of signal and idler states from tomography measurement	205
Table 12 – Variances in the subtraction and sum space and DGCZ criterion	207
Table 13 – PPT criterion for bipartitions of the four sideband modes	208
Table 14 – Victor’s analysis cavity parameters obtained from the fitting in the teleportation measurement	214
Table 15 – Quadrature values of displaced coherent input and teleported states without considering losses	224
Table 16 – Characterized optical losses in Alice’s and Victor’s measurements	227
Table 17 – Quadrature values of input and teleported states in Alice’s loss-corrected scenario	229
Table 18 – Quadrature values of the displaced input state and teleported state after correcting for losses at Victor’s station	230
Table 19 – Quadrature values of the displaced input and teleported states for corrected losses at both Alice’s and Victor’s stations.	231
Table 20 – Teleportation parameters for uncorrected and Alice’s corrected losses scenarios (second run)	236
Table 21 – Teleportation parameters for Victor’s corrected losses and fully corrected losses scenarios (second run)	239
Table 22 – Teleportation parameters for uncorrected and Alice’s corrected losses scenarios (third run)	244
Table 23 – Teleportation parameters for Victor’s corrected losses and fully corrected losses scenarios (third run)	246

Table 24 – Analysis cavities parameters from fitting in the tomography measurement.	282
Table 25 – DGCZ criterion applied to the upper and lower sideband modes	283
Table 26 – Purity, mean occupation number, and coherence quantifier for the sub-systems in the symmetric/antisymmetric basis	283
Table 27 – Von Neumann entropy, mutual information and quantum discord in the symmetric/antisymmetric basis	284

LIST OF ABBREVIATIONS AND ACRONYMS

AC	Alice's corrected losses scenario.
ADC	Analog-to-digital converter.
AM	Amplitude modulation.
AOM	Acousto-optic modulator.
AOI	Angle of incidence.
AR	Anti-reflective.
AU	Alice's uncorrected losses scenario.
BS	Beam splitter.
C-band	Conventional telecommunications band (1530-1565 nm).
CV	Continuous variables.
CV-QKD	Continuous-variable quantum key distribution.
DC	Direct current.
DGCZ	Duan-Giedke-Cirac-Zoller.
DPSS	Diode-pumped solid-state.
DV	Discrete variables.
EDFA	Erbium-doped fiber amplifier.
eLO	Electronic local oscillator.
EOM	Electro-optic modulator.
EPR	Einstein-Podolsky-Rosen.
FFT	Fast Fourier transform.
FPGA	Field-programmable gate array.
FSR	Free spectral range.
FWHM	Full width at half maximum.
FWM	Four-wave mixing.

GKP	Gottesman-Kitaev-Preskill.
GRIIRA	Green-induced infrared absorption.
HF	High-frequency.
HR	High-reflective.
L-band	Long wavelength band in telecommunications (1565-1625 nm).
LO	Local oscillator.
LPF	Low-pass filter.
MZI	Mach-Zehnder interferometer.
Nd:YAG	Neodymium-doped yttrium aluminum garnet.
NIR	Near-infrared.
OAM	Orbital angular momentum.
OPO	Optical parametric oscillator.
PBS	Polarizing beam splitter.
PDH	Pound-Drever-Hall.
PID	Proportional-integral-derivative.
PIN	P-type, intrinsic, N-type semiconductor.
PM	Phase modulation.
PPKTP	Periodically poled potassium titanyl phosphate.
PPT	Positive partial transpose.
PR	Partially-reflective.
PZT	Piezoelectric transducer.
PyRPL	Python Red Pitaya Lockbox.
QKD	Quantum key distribution.
Qubit	Quantum bit.
RBW	Resolution bandwidth.
RF	Radiofrequency.

SHG	Second harmonic generation.
SMF	Single-mode fiber.
SMSV	Single-mode squeezed vacuum.
SN	Shot noise.
SNR	Signal-to-noise ratio.
SPDC	Spontaneous parametric down-conversion.
SQL	Standard quantum limit.
TEC	Thermoelectric cooling.
TEM ₀₀	Transverse electromagnetic mode of order 00.
TIA	Transimpedance amplifier.
TMSV	Two-mode squeezed vacuum.
TROPO	Triply resonant optical parametric oscillator.
VC	Victor's corrected losses scenario.
VBW	Video bandwidth.
WDM	Wavelength division multiplexing.

CONTENTS

1 Introduction	27
I Theoretical Concepts	33
2 Theoretical Frameworks in Quantum Optics	35
2.1 Fundamental Concepts of Gaussian States	35
2.1.1 Quadratures of Quantum Fields	35
2.1.2 Gaussian States	37
2.1.3 Quantum States of Light	39
2.1.3.1 Coherent States	39
2.1.3.2 Thermal States	40
2.1.3.3 Single-Mode Squeezed States	41
2.1.3.4 Two-Mode Squeezed State	42
2.1.4 Separability Criteria and Quantum Entanglement	44
2.1.4.1 DGCZ Entanglement Criterion	45
2.1.4.2 PPT Entanglement Criterion	46
2.2 Optical Parametric Oscillator	47
2.2.1 Quantized Hamiltonian of the Optical Parametric Oscillator	48
2.2.2 Noise Spectrum of the Generated Fields	50
3 Detection of Quadrature Quantum Noise and Quantum State Reconstruction	53
3.1 Photocurrent Operator	55
3.1.1 Balanced Detection Scheme	58
3.1.2 Spectral Photocurrent Observables	61
3.1.3 Spectral Noise Density and Stationary Conditions	64
3.1.3.1 Two-Fields Correlation and Stationary Condition	65
3.1.3.2 Stationarity Analysis in the Phase-Mixing Regime	66
3.2 Covariance Matrix of Stationary Fields	68
3.2.1 Covariance Matrix of a Single Field	68
3.2.2 Covariance Matrix of Two Fields	70
3.2.3 Semiclassical Quadratures and Spectral Matrix	72
3.3 Auto-Homodyne Resonator Detection Scheme	75
3.3.1 Quadrature Mean Values in Auto-Homodyne Detection	79
3.3.2 Quantum Tomography of a Single Field	80

3.3.3	Quantum Tomography of Two Fields	83
3.3.4	Cavity Mismatch Effects on Auto-Homodyne Detection	85
3.3.5	Electronic Phase Discrepancy in the Two-Field Measurement	92
3.4	Optical Modulation	94
3.4.1	Amplitude Modulation	94
3.4.2	Phase Modulation	97
3.4.3	Phase-Controlled Rotation Technique	98
4	Quantum Teleportation Protocol	101
4.1	Theoretical Principles of the CV Teleportation Protocol	103
4.1.1	EPR Station: Entangled State Generation	104
4.1.2	Victor: Input State Preparation	106
4.1.3	Alice: Joint Measurement	108
4.1.4	Bob: State Reconstruction	110
4.1.5	Victor: Quantum Tomography	113
4.2	Realistic Scenario: Exploring Losses and Finite Squeezing	114
4.2.1	Considering Finite Squeezing	114
4.2.2	Impact of Optical Losses on the Protocol	116
4.2.2.1	State Measured by Alice: Uncorrected Losses Scenario	119
4.2.2.2	Victor's Prepared State: Corrected Losses Scenario	121
4.2.2.3	Loss Compensation in Victor Measurements	123
4.2.3	Experimental Adjustment of Gain	123
4.3	Evaluating the Protocol Success: Fidelity	125
4.3.1	Fidelity for Specific Quantum States	127
4.3.1.1	Coherent Input State	128
4.3.1.2	Thermal Input State	129
4.3.2	Teleportation Protocol Benchmarks	130
4.3.2.1	Classical Limit	130
4.3.2.2	No-Cloning Limit	133
II	Experimental Development and Results	135
5	Experimental Setup	137
5.1	Laser Source	137
5.1.1	Auxiliary Lasers	140
5.1.2	Filter Cavity	141
5.2	Optical Parametric Oscillator	143
5.2.1	Cavity Characterization	146
5.2.2	Temperature Dynamics	150

5.2.3	Vacuum System	153
5.2.4	Locking System	155
5.3	Teleportation Stations	156
5.3.1	Victor: Input State Station	157
5.3.1.1	Phase Displacement Operation	157
5.3.1.2	Mach-Zehnder Interferometer	157
5.3.2	Alice Station	159
5.3.2.1	Alice's Analysis Cavity	159
5.3.2.2	Alice's Detection Schemes	163
5.3.2.3	Optical Losses	163
5.3.3	Bob Station	164
5.3.3.1	Conditioned Displacement Operation	164
5.3.3.2	Bob's Analysis Cavity	166
5.3.4	Victor: State Tomography Station	167
5.3.4.1	Victor's Analysis Cavity	168
5.4	Detection system and classical communication	170
5.4.1	Detectors	170
5.4.2	Demodulation and Data Acquisition	172
5.4.3	Classical channel	176
6	Experimental Results	183
6.1	Data Analysis and Shot Noise Calibration	183
6.1.1	Overview of the Data Analysis Approach	183
6.1.2	Shot Noise Calibration	188
6.2	Quantum Resource Characterization: EPR State Tomography	197
6.2.1	Reconstruction of the Two-Field Covariance Matrix	198
6.2.2	Entanglement and Predicted Teleportation Fidelity	205
6.3	Execution of the CV Quantum Teleportation Protocol	209
6.3.1	Teleported State Reconstruction	210
6.3.1.1	Teleportation Quadrature Variances	212
6.3.1.2	Teleportation Quadrature Mean Values	217
6.3.2	Evaluating Protocol Performance	220
6.3.2.1	Teleportation Gain Determination	221
6.3.2.2	Teleportation Fidelity	223
6.3.3	Considering Losses	225
6.3.4	Additional Teleportation Executions	232
6.3.4.1	Short-Term Reproducibility and Stability	232
6.3.4.2	Teleportation via Simultaneous Gain Scanning	241
7	Conclusion and Perspectives	249

Bibliography	251
Appendix	269
A Canonical Quantization of the Free Electromagnetic Field	271
A.1 Free Field Plane Wave Decomposition	271
A.2 Energy of the Electromagnetic Field	273
A.3 Canonical Quantization	275
B Supplementary Characterizations of Quantum Tomography Measurements	277
B.1 Signal-to-Noise Ratio and Stationary Conditions	277
B.2 Additional Characterizations of the Measured State	282
C Publications	285

1 INTRODUCTION

In recent years, the study of various quantum systems has gained significant momentum, driven by the advances in the second quantum revolution. The first quantum revolution, which started in the early 20th century, laid the theoretical foundation of quantum mechanics, leading to the discovery of fundamental principles such as wave-particle duality, quantum superposition, and entanglement [1]. These breakthroughs enabled the development of transformative technologies, including semiconductors (the basis of modern computing), optical lasers, solar cells, magnetic resonance imaging (MRI), and others, which are now integral to daily life. However, in these first-generation technologies, quantum mechanics mainly served as a theoretical framework to describe phenomena and optimize material properties [2].

The second quantum revolution marks a paradigm shift, moving beyond the passive application of quantum principles toward the direct manipulation of quantum states for technological advantage. This transition has given rise to a new class of quantum technologies based on quantum information theory that harness phenomena such as quantum coherence, entanglement, and superposition to achieve unprecedented capabilities [3]. These emerging technologies are broadly classified into three domains:

- **Quantum Computing:** Exploits quantum superposition, interference, and entanglement to perform calculations exponentially faster than classical computers for a specific group of tasks. Key applications include cryptography (e.g., Shor's algorithm for factoring large numbers [4]), quantum simulations for material and drug discovery, and solving optimization problems [5, 6].
- **Quantum Communication:** Utilizes quantum entanglement and measurement principles to enable fundamentally secure classical information transmission, as well as communication and synchronization of distant quantum systems. One key application is quantum key distribution (QKD), which ensures the secure exchange of encryption keys [7]. Quantum teleportation and quantum memories further enhance this by enabling the transfer and storage of quantum states across distant nodes, paving the way for the large-scale quantum internet [8, 9].
- **Quantum Sensing and Metrology:** Leverages quantum coherence, squeezing, and entanglement to achieve measurement sensitivities beyond classical limits. Applications include ultra-precise atomic clocks, gravitational wave detection (LIGO/Virgo), medical imaging, and high-precision spectroscopy [10, 11].

This work is situated within the second quantum revolution, particularly in the domain of quantum communication. In the field of quantum technologies, multiple physical platforms are being explored, each offering distinct advantages and limitations. This diversity drives research into identifying the optimal platform for specific applications. A promising approach is to envision quantum technologies as hybrid systems, where different physical platforms perform specialized tasks while being interconnected through quantum communication. A useful analogy is classical computing, where a CPU (processor), RAM (temporary memory), and hard drive (long-term memory) collaborate, each fulfilling a specific role. Another useful comparison is communication networks, where distributed hubs manage processing tasks, exchanging information via interconnected links. Similarly, quantum networks consist of quantum nodes, responsible for processing tasks, and quantum channels, which transmit quantum information between them [8].

Photonic architectures are highly promising for implementing quantum channels. Their compatibility with classical optical tools allows for efficient manipulation, high-speed transmission, signal multiplexing, and high-efficiency detection [12]. Furthermore, their robustness against environmental disturbances and low transmission losses make them well-suited for practical quantum communication [9]. However, a significant challenge arises from the fact that various quantum platforms (such as trapped ions, neutral atoms, color centers, and quantum dots) interact with light at different, often incompatible, wavelengths. This issue is compounded by the reality that optimal low-loss transmission in standard silica-based optical fibers is restricted to specific telecommunications windows, like the C-band (1530 – 1565 nm) and L-band (1565 – 1625 nm) [13]. Consequently, there is a critical need to develop quantum channels that can operate across a broad range of wavelengths to bridge different quantum technologies and facilitate efficient quantum information transfer.

In a quantum internet, channels connecting processing nodes will incorporate components like switches and quantum repeaters [8, 14]. While switches route information between nodes, repeaters are designed to counteract the signal loss and decoherence inherent in long-distance transmission [9]. A repeater divides the total distance into smaller segments [15, 16]. Within each segment, a bipartite entangled state is generated, one part of this state is stored locally in a quantum memory, while the other is transmitted to the segment's end. Because this transmission is probabilistic, quantum memories are essential for holding successfully established entangled links while waiting for adjacent segments to succeed [17, 18]. Once all links are ready, a series of entanglement swapping operations connects them, creating a single end-to-end entangled resource. This shared resource is then used to teleport the desired quantum state, ideally, effectively mitigating the exponential decay of success probability with distance and reducing it to a more manageable polynomial scaling [19, 20]. However, many promising platforms for quantum memories do not operate at telecommunication wavelengths, necessitating the development

of interfaces to bridge this spectral mismatch [21, 22].

To address this challenge, we employ quantum teleportation across different optical wavelengths, focusing on the interface between the near-infrared and the telecommunication L-band. Specifically, we aim to establish a quantum communication channel between the 795 nm D1 transition of rubidium atoms and the 1608 nm telecommunication wavelength. Rubidium atoms serve as excellent candidates for quantum memory, enabling the storage and processing of quantum information [23, 24]. Moreover, they can be used to generate non-classical states, such as squeezed and entangled states [25–27]. On the other hand, the telecommunication band allows for the efficient transmission of quantum states over long distances via optical fibers. Additionally, it is compatible with silicon-nitride (Si_3N_4) microphotonic devices, which promise scalable quantum photonic architectures capable of acting as a processing platform for the quantum nodes [28–30]. Our research group actively investigates both platforms, with a focus on hot rubidium vapors and silicon-nitride microring resonators.

Quantum teleportation is a well-established protocol in quantum information science that enables the transfer of an unknown quantum state from one physical system, located at station A (Alice), to another physical system at a potentially distant station B (Bob) [31]. This process relies on two key resources: quantum entanglement and classical communication. Importantly, the physical systems at Alice's and Bob's stations do not need to be identical, as long as an entangled state exists between them. This flexibility makes quantum teleportation a promising mechanism for establishing quantum channels between different systems. Specifically, in our case, it enables quantum state transfer between widely separated optical wavelengths. As a cornerstone of quantum information science [32], teleportation is not only essential for quantum communication but is also a foundational tool for advanced quantum technologies like measurement-based quantum computing [33] and quantum error correction [34], and it also finds key applications in quantum metrology [35].

Quantum information can be encoded in various degrees of freedom of light. This encoding can use discrete variables (DV), such as polarization, orbital angular momentum, optical path, and time-bin, or continuous variables (CV), such as the quadratures of the field. In this work, we focus on the continuous-variable quantum teleportation protocol, where the quadratures of the field are teleported. A major advantage of CV quantum teleportation is that it is unconditional, meaning every input state is successfully teleported. In contrast, discrete-variable (DV) teleportation often relies on post-selection due to the difficulty of performing a complete Bell measurement, which requires inefficient nonlinear optical components [36]. However, inherent physical constraints render the entanglement resource in the CV teleportation protocol imperfect, fundamentally limiting the achievable performance, quantified by its fidelity. Despite this, there is no fundamental upper bound

on the quality of entanglement that can be achieved in CV systems. Furthermore, it is possible to improve teleportation fidelity by sacrificing the unconditional property and incorporating probabilistic tools from DV protocols [17, 37, 38]. For coherent input states, a fidelity exceeding the classical limit of 50% signifies a definitive quantum advantage over any classical strategy [32]. On the path toward fault-tolerant quantum computation, CV teleportation is an indispensable tool for implementing measurement-based models that employ Gottesman-Kitaev-Preskill (GKP) states [39] for error correction [40–42].

The quantum teleportation protocol was first introduced by Bennett et al. in 1993 in the context of discrete variables [43]. The first experimental demonstration followed four years later, utilizing polarization degrees of freedom and post-selection [44]. In the continuous-variable domain, the teleportation protocol was theoretically proposed by Braunstein and Kimble in 1998 [45], with the first experimental realization occurring just a year later through the teleportation of a displaced coherent state [46]. Since then, various unconditional continuous-variable teleportation protocols have been executed with increasing precision [47, 48], with the highest reported fidelity reaching 83(1)% [49]. Notable advancements include the development of a tripartite teleportation network, enabling the teleportation of a coherent state between any two parties under the control of a third [50]. Furthermore, entanglement swapping has been successfully demonstrated with a high-fidelity teleportation protocol [51]. In a notable hybrid experiment, entanglement was swapped between discrete and continuous variable systems [52]. Further breakthroughs include the teleportation of a squeezed state [53, 54] and even a cat state [55]. An interesting step toward high-dimensional teleportation was achieved with the simultaneous teleportation of coherent states across nine parallel orbital angular momentum (OAM) channels [56]. The CV quantum teleportation protocol over long optical fiber channels has also been realized, demonstrating a clear quantum advantage over distances up to 10 km [57, 58]. Of particular relevance, our group previously conducted a teleportation experiment that, although not surpassing the classical limit, demonstrated a significant advantage in quantum teleportation between 1055 nm and 1072 nm, compared to an equivalent scheme using a classical Nd:YAG laser [59, 60].

Despite these complex and groundbreaking implementations, unconditional CV teleportation between distant frequency modes in the spectrum remains unexplored. In contrast, teleportation protocols for discrete-variable (DV) quantum states have seen substantial progress, with numerous experiments successfully demonstrating frequency-mode teleportation [36, 61]. A notable achievement in our operating wavelength regions was the teleportation of a time-bin qubit, encoded in an attenuated laser pulse, from 1532 nm to a 795 nm photon over a distance of 6.2 km [62]. The entangled photon pairs connecting these wavelengths were generated using a PPLN crystal. A related experiment used a frequency conversion step to teleport the polarization state encoded in an attenuated laser pulse from 795 nm to 1560 nm [63]. Another remarkable demonstration involved

teleporting time-bin photons from 1436 nm to 606 nm, where they were successfully stored in a solid-state quantum memory [64]. More recently, researchers achieved the teleportation of a time-bin photon state at 795 nm to a diamond NV center qubit, employing a frequency conversion step from 795 nm to 637 nm [65].

Here, we report the first experimental realization of continuous-variable quantum teleportation between the infrared and telecommunication bands. Specifically, we teleported a displaced coherent state from 794.4(6) nm to 1611(3) nm, achieving a fidelity of 57.1(8)% without accounting for optical losses and 53.8(5)% when considering losses at Alice's station, with both values significantly exceeding the classical limit of 50%. Notably, this is the first teleportation protocol to employ an optical parametric oscillator (OPO) operating in the above-threshold regime while successfully violating the classical limit. The information capacity of our protocol is effectively doubled by using an auto-homodyne measurement technique that resolves individual sideband modes [66]. Using this scheme, we also present the first full characterization of the individual sideband states of both the signal and idler fields produced by an above-threshold OPO at widely separated wavelengths, differing by more than one octave. This work demonstrates a quantum link between distinct spectral domains, providing an important building block that paves the way for advanced hybrid quantum systems and scalable heterogeneous networks.

Part I

Theoretical Concepts

2 THEORETICAL FRAMEWORKS IN QUANTUM OPTICS

In this chapter, we establish the fundamental concepts and a portion of the notation used throughout this text. We begin by introducing the formalism of Gaussian states, which are central to our study and are the states produced and manipulated in our laboratory. We will review their mathematical description, key properties, and their experimental relevance in quantum optics and continuous-variable quantum information.

Next, we present the quantum theory of the optical parametric oscillator (OPO), which serves as our source of entangled states. The OPO is an important source in continuous-variable quantum optics, enabling the robust generation of squeezed and entangled light states. We provide an overview of its operational principles, introduce the core quantum Hamiltonian framework, and present the expected quantum correlations between its output fields.

2.1 Fundamental Concepts of Gaussian States

In this section, we introduce the set of Gaussian states, which are central to the framework of continuous-variable (CV) quantum information, as any process governed by Hamiltonians up to the second order in field operators, such as linear optics and quadrature squeezing, maintains the Gaussian nature of the initial state [67, 68]. Most quantum states of light generated and manipulated in standard laboratory settings are Gaussian, such as coherent states, squeezed states, and thermal states, all of which will be discussed in this chapter. These states form the foundation for numerous CV quantum information protocols, with notable applications in quantum communication like quantum key distribution (CV-QKD) and quantum teleportation [69]. In this work, we demonstrate the CV teleportation protocol using exclusively Gaussian states.

2.1.1 Quadratures of Quantum Fields

The quantized electromagnetic field serves as the basis for all discussions presented in this work. A concise review of the canonical quantization procedure is provided in Appendix A. In this formalism, the quantized free electric field operator at a spatial position \mathbf{r} and time t is expressed as [70]:

$$\hat{\mathbf{E}}(\mathbf{r}, t) = \sum_{\mathbf{k}, s} i\mathcal{E}_{ks}^{(1)} \boldsymbol{\epsilon}_{\mathbf{k}s} \left(\hat{a}_{\mathbf{k}s} e^{i(\mathbf{k} \cdot \mathbf{r} - \omega_{\mathbf{k}s} t)} - \hat{a}_{\mathbf{k}s}^\dagger e^{-i(\mathbf{k} \cdot \mathbf{r} - \omega_{\mathbf{k}s} t)} \right). \quad (2.1)$$

Here, \mathbf{k} denotes the wave vector, which determines the direction and wavelength of the field mode, while $s \in 1, 2$ is the polarization index, labeling the two independent transverse polarization states. The polarization vector $\epsilon_{\mathbf{ks}}$ is orthogonal to \mathbf{k} , ensuring transversality of the field. The field mode frequency $\omega_{\mathbf{ks}}$ is related to the magnitude of \mathbf{k} by the relation $|\mathbf{k}| = \omega_{\mathbf{ks}}/c$, where c is the speed of light in vacuum. The coefficient $\mathcal{E}_{\mathbf{ks}}^{(1)}$ represents a normalization factor that ensures the correct energy scaling per photon mode (Equation A.6). The non-Hermitian annihilation and creation operators, $\hat{a}_{\mathbf{ks}}$ and $\hat{a}_{\mathbf{ks}}^\dagger$, respectively, satisfy the following bosonic commutation relations, where the field modes are indexed by $\ell \equiv (\mathbf{k}, s)$:

$$[\hat{a}_\ell, \hat{a}_{\ell'}^\dagger] = \delta_{\ell, \ell'}, \quad [\hat{a}_\ell, \hat{a}_{\ell'}] = [\hat{a}_\ell^\dagger, \hat{a}_{\ell'}^\dagger] = 0, \quad \text{where } \ell, \ell' \in \{(\mathbf{k}, s)\}. \quad (2.2)$$

An alternative formulation of the electric field operator uses Hermitian quadrature operators, allowing the field to be expressed as:

$$\hat{\mathbf{E}}(\mathbf{r}, t) = - \sum_{\mathbf{k}, s} \mathcal{E}_{\mathbf{ks}}^{(1)} \epsilon_{\mathbf{ks}} [\hat{p}_{\mathbf{ks}} \sin(\mathbf{k} \cdot \mathbf{r} - \omega_{\mathbf{ks}} t) + \hat{q}_{\mathbf{ks}} \cos(\mathbf{k} \cdot \mathbf{r} - \omega_{\mathbf{ks}} t)]. \quad (2.3)$$

The quadrature operators \hat{p}_ℓ and \hat{q}_ℓ are related to the annihilation and creation operators through the definitions:

$$\hat{p}_\ell = \hat{a}_\ell + \hat{a}_\ell^\dagger, \quad \hat{q}_\ell = -i(\hat{a}_\ell - \hat{a}_\ell^\dagger), \quad (2.4)$$

which satisfy the commutation relations:

$$[\hat{p}_\ell, \hat{q}_{\ell'}] = 2i\delta_{\ell\ell'}, \quad [\hat{p}_\ell, \hat{p}_{\ell'}] = [\hat{q}_\ell, \hat{q}_{\ell'}] = 0. \quad (2.5a)$$

Since \hat{p}_ℓ and \hat{q}_ℓ correspond to non-commuting observables, the Heisenberg uncertainty principle constrains their measurement variances as [71]:

$$\Delta^2 \hat{p}_\ell \Delta^2 \hat{q}_\ell \geq 1. \quad (2.6)$$

This expresses a fundamental quantum limitation on the simultaneous measurement of these two observable quadratures.

The Hamiltonian describing the dynamics of the quantized free electromagnetic field is given by:

$$\hat{H} = \sum_\ell \frac{\hbar\omega_\ell}{4} (\hat{p}_\ell^2 + \hat{q}_\ell^2) = \sum_\ell \hbar\omega_\ell \left(\hat{a}_\ell^\dagger \hat{a}_\ell + \frac{1}{2} \right). \quad (2.7)$$

This Hamiltonian describes an ensemble of independent quantum harmonic oscillators, where each mode ℓ represents an oscillator with frequency ω_ℓ , evolving separately due to the absence of intermode coupling.

The quantization of the electromagnetic field, also known as second quantization, differs from the first quantization, which applies to individual particles whose position and momentum are described by operators [70]. In this formalism, each mode of the electromagnetic field corresponds to a quantum state residing in an infinite-dimensional Hilbert space, where the canonical quadrature operators serve as the fundamental observables.

2.1.2 Gaussian States

We begin our description of Gaussian quantum states by considering a system of n optical modes, labeled by $\ell \in \{1, 2, 3, \dots, n\}$. Each mode is characterized by a pair of normalized canonical quadrature operators \hat{p}_ℓ and \hat{q}_ℓ , which act on the infinite-dimensional Hilbert space \mathcal{H}_ℓ . Organizing these observables into a vector, we define the quadrature operator vector as:

$$\hat{\mathbf{x}} = [\hat{p}_1, \hat{q}_1, \hat{p}_2, \hat{q}_2, \dots, \hat{p}_n, \hat{q}_n]^T, \quad (2.8)$$

in the total Hilbert space: $\mathcal{H} = \mathcal{H}_1 \otimes \mathcal{H}_2 \otimes \dots \otimes \mathcal{H}_n$.

The elements of $\hat{\mathbf{x}}$ must satisfy the standard commutation relations presented in Equation 2.5. In symplectic form, these relations can be written as:

$$[\hat{\mathbf{x}}, \hat{\mathbf{x}}^T] = 2i\Omega, \quad (2.9)$$

where the symplectic matrix Ω is given by:

$$\Omega = \bigoplus_{\ell=1}^n i\sigma_y^{(\ell)}, \quad \text{with} \quad i\sigma_y^{(\ell)} = \begin{bmatrix} 0 & 1 \\ -1 & 0 \end{bmatrix}. \quad (2.10)$$

Here, $\sigma_y^{(\ell)}$ is the Pauli-Y matrix, and the symbol \bigoplus represents the direct sum, placing the $i\sigma_y^{(\ell)}$ matrices in the diagonal blocks of Ω . Any physical operation applied to a system described by a quadrature vector must preserve the canonical commutation relations. In this context, a linear transformation S is a valid transformation if it satisfies:

$$S\Omega S^T = \Omega. \quad (2.11)$$

The set of all $2n \times 2n$ real matrices that satisfy the above condition is called the real symplectic group $S_p(2n, \mathbb{R})$, whose elements are called symplectic transformations [72].

Gaussian states are fully characterized by the first and second-order moments of the quadrature operators $\hat{\mathbf{x}}$, with higher-order moments being fully determined by these values. This mathematical structure provides a powerful approach for describing quantum systems in an analytically and computationally efficient manner. Furthermore, key quantum properties, including entanglement and purity, which remain unchanged under unitary local transformations, are fully determined by the second-order moments. The first-order moments are described by a $2n$ -length column vector $\langle \hat{\mathbf{x}} \rangle$, while the second-order moments are represented by a $2n \times 2n$ covariance matrix \mathbf{V} defined by:

$$\mathbf{V} = \frac{1}{2}(\langle \hat{\mathbf{x}} \cdot \hat{\mathbf{x}}^T \rangle + \langle \hat{\mathbf{x}} \cdot \hat{\mathbf{x}}^T \rangle^T) - \langle \hat{\mathbf{x}} \rangle \cdot \langle \hat{\mathbf{x}} \rangle^T. \quad (2.12)$$

The covariance matrix is a real, symmetric, and positive semi-definite matrix. Explicitly, for a two-mode state, denoted here as modes 1 and 2, the matrix has the form:

$$\mathbf{V} = \begin{pmatrix} \Delta^2 \hat{p}_1 & C(\hat{p}_1 \hat{q}_1) & C(\hat{p}_1 \hat{p}_2) & C(\hat{p}_1 \hat{q}_2) \\ & \Delta^2 \hat{q}_1 & C(\hat{q}_1 \hat{p}_2) & C(\hat{q}_1 \hat{q}_2) \\ & & \Delta^2 \hat{p}_2 & C(\hat{p}_2 \hat{q}_2) \\ & & & \Delta^2 \hat{q}_2 \end{pmatrix}, \quad (2.13)$$

where the main diagonal contains the quadrature variances, while the off-diagonal elements correspond to the covariances between different quadratures. As the matrix is symmetric, only the upper triangle is shown. The Wigner quasi-probability distribution, or Wigner function, of a Gaussian state, $\hat{\rho}_{\text{Gauss}}$, is given by [73]:

$$W[\hat{\rho}_{\text{Gauss}}](\mathbf{x}) = \left(\frac{2}{\pi}\right)^n \frac{1}{\sqrt{\det \mathbf{V}}} \exp\left[-\frac{1}{2}(\mathbf{x} - \langle \hat{\mathbf{x}} \rangle)^T \mathbf{V}^{-1} (\mathbf{x} - \langle \hat{\mathbf{x}} \rangle)\right]. \quad (2.14)$$

As expected for Gaussian states, this function follows a multivariate normal distribution and remains strictly non-negative.

For an arbitrary covariance matrix \mathbf{V} to describe a physically valid quantum state, it must satisfy the Robertson-Schrödinger uncertainty relation [72, 74]. This physicality criterion, which applies universally to all quantum states (both Gaussian and non-Gaussian), can be expressed in the compact matrix form:

$$\mathbf{V} + i\Omega \geq 0, \quad (2.15)$$

which is equivalent to the uncertainty principle given in Equation 2.9. An analogous and often more practical test is based on the matrix's symplectic eigenvalues. This condition states that all symplectic eigenvalues must be greater than or equal to one, which can be written as [75]:

$$\text{Eigs}[-(\mathbf{V}\Omega)^2] \geq 1, \quad (2.16)$$

where $\text{Eigs}[\mathbf{A}]$ denotes the set of eigenvalues of the matrix \mathbf{A} . Satisfying this criterion ensures that the covariance matrix \mathbf{V} represents a physically realizable quantum state.

2.1.3 Quantum States of Light

As discussed earlier, Gaussian states play a crucial role in quantum optics, forming the foundation for many experimentally and theoretically significant optical states. Notably, all the states considered in this work fall within this category. In this section, we provide an overview of the Gaussian states most relevant to our approach: the coherent state, the single-mode squeezed state, the two-mode squeezed state, and the thermal state. Each of these states possesses distinct quantum properties that are essential to our discussion.

2.1.3.1 Coherent States

Coherent states are quantum states that exhibit the minimum uncertainty allowed by the Heisenberg principle, with this uncertainty being equally distributed between all quadratures. This means the variance of any quadrature measurement is independent of the measurement angle. Specifically, they satisfy the condition $\Delta^2\hat{p} = \Delta^2\hat{q} = 1$, which implies that their covariance matrix is diagonal, with elements given by $V_{ij} = \delta_{ij}$. These states are formally defined as the right eigenstates of the annihilation operator [71]:

$$\hat{a}|\alpha\rangle = \alpha|\alpha\rangle, \quad (2.17)$$

where $\alpha \in \mathbb{C}$ determines both the amplitude and phase of the state. Figure 1a illustrates a coherent state $|\alpha\rangle$ in phase space. The red arrow represents the mean displacement of the state, while the blue-shaded region indicates quantum fluctuations. Since a coherent state is defined by a symmetric covariance matrix, its uncertainty is isotropic, forming a circular distribution, as shown by the blue dotted circle.

A notable example is the vacuum state $|0\rangle$, which has zero quadrature mean values and shares the same covariance matrix structure. More generally, any coherent state $|\alpha\rangle$ can be obtained by applying the displacement operator:

$$\hat{D}(\alpha) = \exp(\alpha\hat{a}^\dagger - \alpha^*\hat{a}), \quad (2.18)$$

to the vacuum state, leading to:

$$|\alpha\rangle = \hat{D}(\alpha)|0\rangle. \quad (2.19)$$

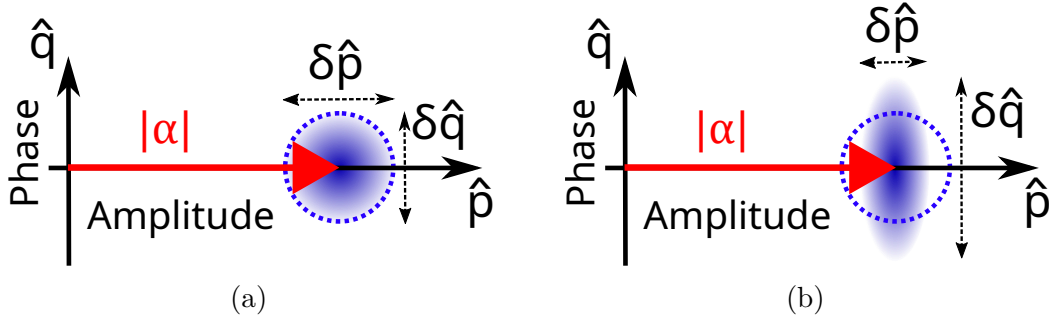


Figure 1 – Schematic representation of the phase space containing: (a) a coherent state, (b) a single-mode squeezed state. The red arrow represents the mean displacement of the state, corresponding to its quadrature expectation values. The blue-shaded region illustrates quantum fluctuations. The dotted blue circle indicates the fundamental limit imposed by the Heisenberg uncertainty principle for symmetric quadrature fluctuations.

This reveals that coherent states are simply displaced versions of the vacuum state in phase space, retaining the vacuum's minimum uncertainty properties while having non-zero mean quadrature values. When expanded in the Fock (or number) basis, the coherent state is a superposition of number states $|n\rangle$ with a Poissonian distribution:

$$|\alpha\rangle = e^{-|\alpha|^2/2} \sum_{n=0}^{\infty} \frac{\alpha^n}{\sqrt{n!}} |n\rangle. \quad (2.20)$$

2.1.3.2 Thermal States

A thermal state is the quantum state that describes a system, such as a mode of light, in thermal equilibrium with a large heat bath at a specific temperature. It is a mixed state representing a statistical ensemble of energy eigenstates. Formally, a thermal state is defined as the state that maximizes the von Neumann entropy [72]:

$$S_{vn} = -Tr(\hat{\rho} \ln \hat{\rho}), \quad (2.21)$$

for a fixed average energy $Tr(\hat{p}\hat{a}^\dagger\hat{a}) = \langle \hat{n} \rangle$, where $\langle \hat{n} \rangle \geq 0$ is the mean number of photons in the mode. This principle means the thermal state is the most disordered quantum state for any given mean energy.

In phase space, a thermal state is characterized by having zero mean quadrature values ($\langle \hat{p} \rangle = \langle \hat{q} \rangle = 0$). For any non-zero mean photon number ($\langle \hat{n} \rangle > 0$), it exhibits an equal amount of excess noise in all quadratures. This means the variance is identical for any measurement angle and always greater than the vacuum noise level. In the limit of zero energy ($\langle \hat{n} \rangle \rightarrow 0$), the thermal state reduces to the pure vacuum state. These properties

are fully captured by the state's single-mode covariance matrix, which is diagonal and symmetric:

$$\mathbf{V}_{th} = \begin{pmatrix} 2\langle\hat{n}\rangle + 1 & 0 \\ 0 & 2\langle\hat{n}\rangle + 1 \end{pmatrix}. \quad (2.22)$$

In the Fock basis, the density matrix of a thermal state is diagonal, signifying it is a statistical mixture of number states $|n\rangle$ with no quantum coherence between them:

$$\hat{\rho}_{th}(\langle\hat{n}\rangle) = \sum_{n=0}^{\infty} \frac{\langle\hat{n}\rangle^n}{(\langle\hat{n}\rangle + 1)^{n+1}} |n\rangle\langle n|, \quad (2.23)$$

The diagonal elements represent the probability of detecting n photons, which follow a specific Bose-Einstein distribution determined by the mean photon number $\langle\hat{n}\rangle$ [71]. While a formal thermal state is uniquely defined by this specific distribution, the term is sometimes used more colloquially. In this less precise sense, it can refer to any quantum state that has become significantly mixed or exhibits very low purity, even if its photon statistics do not perfectly match the Bose-Einstein distribution.

2.1.3.3 Single-Mode Squeezed States

A single-mode squeezed state is a quantum state where the uncertainty in one quadrature is reduced below the standard quantum limit (squeezed), while the uncertainty in the conjugate quadrature is increased (anti-squeezed). For ideal, pure squeezed states, this trade-off preserves the minimum uncertainty condition ($\Delta^2\hat{p}\Delta^2\hat{q} = 1$), allowing for noise reduction in a specific direction. This effect has many applications in quantum metrology and quantum optics in general. A squeezed state is generated by applying the squeezing operator, $\hat{S}(\zeta)$, to a coherent state [76]:

$$\hat{S}(\zeta) = \exp\left(\frac{1}{2}\zeta^*\hat{a}^2 - \frac{1}{2}\zeta\hat{a}^{\dagger 2}\right), \quad (2.24)$$

where the complex parameter $\zeta = re^{i\theta}$ encodes both the squeezing parameter r and the squeezing angle θ , which determines the orientation of the squeezing ellipse in phase space. Figure 1b provides a visual representation of a displaced single-mode squeezed state in phase space, with its squeezing axis aligned with a quadrature axis.

A deeper understanding of the photon-number statistics in a squeezed state can be obtained by examining the effect of the squeezing operator acting on the vacuum state, expressed in the Fock basis as follows [70]:

$$S(\zeta)|0\rangle = |SMSV\rangle = \frac{1}{\sqrt{\cosh(r)}} \sum_{n=0}^{\infty} \frac{\sqrt{(2n)!}}{n!} \left[-\frac{1}{2} e^{i\theta} \tanh(r) \right]^n |2n\rangle. \quad (2.25)$$

This expression reveals that the squeezed vacuum state is a coherent superposition of even-numbered Fock states. The absence of odd-photon components indicates that the generation process responsible for such states must inherently produce photon pairs rather than single photons. One of the most common techniques for generating quantum states with properties similar to squeezed states is degenerate spontaneous parametric down-conversion (SPDC). In this nonlinear optical process, a high-energy pump photon is converted into two lower-energy photons within a nonlinear medium, where the degenerate case indicates that both photons are generated in the same mode. This process directly aligns with the photon-number statistics observed in squeezed states.

2.1.3.4 Two-Mode Squeezed State

The two-mode squeezed state is an entangled quantum state that describes the joint state of two distinct physical modes. It is often called an Einstein-Podolsky-Rosen (EPR) state because its entanglement manifests in quadrature combinations analogous to the position and momentum variables discussed in the original EPR paper [77]. Due to their intrinsic entanglement properties and the ability to generate close analogs in laboratory settings without requiring complex quantum engineering, two-mode squeezed states are a foundational resource for many continuous-variable quantum protocols. The state is generated by applying the two-mode squeezing operator to a pair of initially independent coherent states, introducing quantum correlations between the modes. The two-mode squeezing operator is defined as:

$$\hat{S}_{12}(\zeta) = \exp \left(\frac{1}{2} \zeta^* \hat{a}_1 \hat{a}_2 - \frac{1}{2} \zeta \hat{a}_1^\dagger \hat{a}_2^\dagger \right), \quad (2.26)$$

where \hat{a}_1 and \hat{a}_2 are the annihilation operators associated with modes 1 and 2, respectively. This equation closely resembles the single-mode squeezing operator defined in Equation 2.24, with the complex squeezing parameter $\zeta = re^{i\theta}$ playing the same role in determining both the magnitude and direction of the two-mode squeezing. In this thesis, we use non-pure analogs of these states as the fundamental quantum resource for our teleportation experiment. They establish the quantum channel between the sender and receiver and are responsible for the protocol's quantum advantage.

Consider a bipartite quantum system where each subsystem, labeled by $\ell \in \{1, 2\}$, is characterized by the quadrature operators \hat{p}_ℓ and \hat{q}_ℓ . To analyze the quantum correlations inherent in this system, we introduce the following quadrature combination operators:

$$\hat{p}_\pm = \frac{\hat{p}_1 \pm \hat{p}_2}{\sqrt{2}}, \quad (2.27a)$$

$$\hat{q}_\pm = \frac{\hat{q}_1 \pm \hat{q}_2}{\sqrt{2}}. \quad (2.27b)$$

The commutator between these operators satisfies $[\hat{p}_\pm, \hat{q}_\mp] = 0$, which implies that the pairs (\hat{p}_-, \hat{q}_+) and (\hat{p}_+, \hat{q}_-) can be determined simultaneously with arbitrary precision. The two-mode squeezed state exhibits EPR-like correlations, where the sum of the phase quadratures (\hat{q}_+) and the difference of the amplitude quadratures (\hat{p}_-) demonstrate squeezing with noise reduced below the standard quantum limit. In contrast, the difference of phase quadratures (\hat{q}_-) and the sum of amplitude quadratures (\hat{p}_+) are anti-squeezed, leading to increased noise. This noise suppression and amplification can be expressed in terms of the squeezing parameter r for a squeezing angle $\theta = 0$, as follows:

$$\Delta^2 \hat{p}_\pm = e^{\pm 2r}, \quad (2.28a)$$

$$\Delta^2 \hat{q}_\pm = e^{\mp 2r}. \quad (2.28b)$$

This squeezing in the quadrature combinations, as will become clear later, serves as evidence that the two modes are entangled. For a pure two-mode squeezed state aligned with the quadrature axes ($\theta = 0$), the corresponding covariance matrix is given by [78]:

$$\mathbf{V}_{TMSV} = \begin{pmatrix} \cosh(2r) \mathbb{1}_2 & \sinh(2r) \sigma_z \\ \sinh(2r) \sigma_z & \cosh(2r) \mathbb{1}_2 \end{pmatrix}, \quad (2.29)$$

It is insightful to examine the photon statistics associated with the two-mode squeezing operator. To this end, we investigate its action on two independent modes described by vacuum states, which results in the two-mode squeezed vacuum (TMSV) state, expressed in the Fock basis as:

$$\begin{aligned} \hat{S}_{12}(\zeta) |0; 0\rangle &= |TMSV\rangle \\ &= \frac{1}{\cosh(r)} \sum_{n=0}^{\infty} \left[-e^{i\theta} \tanh(r) \right]^n |n; n\rangle. \end{aligned} \quad (2.30)$$

This expression explicitly shows that the two-mode squeezed vacuum state has perfect photon-number correlations, meaning that whenever mode 1 contains n photons, the mode 2 contains exactly n photons as well. A state with similar properties naturally arises in non-degenerate spontaneous parametric down-conversion (SPDC), where a pump photon probabilistically splits into two correlated photons, each occupying a distinct mode. To

further analyze the properties of the individual modes, we take the partial trace over mode 2 to obtain the reduced density matrix for mode 1:

$$\hat{\rho}_1 = \text{Tr}_2[|TMSV\rangle\langle TMSV|] = \frac{1}{\cosh^2(r)} \sum_{n=0}^{\infty} [\tanh(r)]^{2n} |n\rangle\langle n|. \quad (2.31)$$

The resulting state for the individual mode is a statistical mixture, as indicated by the absence of off-diagonal terms. More specifically, this density matrix has the exact mathematical form of a thermal state with the mean photon number $\langle \hat{n} \rangle = \sinh^2(r)$ related to the two-mode squeezing [72]. This property is a direct consequence of entanglement: while the global two-mode state is pure, its local subsystems are not, meaning complete information is only available by observing the composite system. We will explore this and other aspects of entanglement in greater detail in the next section.

2.1.4 Separability Criteria and Quantum Entanglement

Quantum entanglement is one of the most intriguing and counterintuitive phenomena in quantum mechanics, playing a fundamental role in quantum information science. As mentioned, it describes a composite system where the individual subsystems, even when spatially separated, cannot be fully characterized independently of one another. Mathematically, a quantum state is said to be entangled when its global density matrix cannot be written as a tensor product of individual subsystem states [79]. This means the information associated with the state of each subsystem is inherently dependent on the information associated with the state of the others, no matter how far apart they are. Consequently, any attempt to describe the global system using only local operations and measurements results in a loss of information about the full quantum state. To fully describe an entangled system, one must account for the quantum correlations between subsystems. This is done by considering the joint density matrix of the entire system rather than treating each subsystem separately. These powerful correlations are the foundational resource for many quantum technologies, including quantum communication, sensing, and computing [6].

Using the formalism of density operators, the global state $\hat{\rho}$ of a multipartite quantum system composed of n subsystems is said to be separable if its density operator can be expressed as a convex sum of product density operators corresponding to its subsystems [79]:

$$\hat{\rho} = \sum_i p_i (\hat{\rho}_i^{(1)} \otimes \hat{\rho}_i^{(2)} \otimes \dots \otimes \hat{\rho}_i^{(n)}). \quad (2.32)$$

in the Hilbert space $\mathcal{H} = \mathcal{H}_1 \otimes \mathcal{H}_2 \otimes \dots \otimes \mathcal{H}_n$,

where $\sum_i p_i = 1$. A quantum state $\hat{\rho}$ is entangled if it cannot be written in the separable form given by Equation (2.32). In other words, entanglement arises when a state cannot be expressed as a probabilistic mixture of product states. For bipartite Gaussian states, the question of separability can be answered entirely in terms of their covariance matrices. Consider a state described by a covariance matrix \mathbf{V} shared between two parties (subsystems), each holding any number of modes. This state is separable if and only if there exist valid local covariance matrices, \mathbf{V}_1 and \mathbf{V}_2 , for each subsystem that satisfy the condition [80]:

$$\mathbf{V} \geq \mathbf{V}_1 \oplus \mathbf{V}_2 \quad (2.33)$$

in the Hilbert space $\mathcal{H} = \mathcal{H}_1 \otimes \mathcal{H}_2$,

where the direct sum \oplus creates a block-diagonal matrix, and the inequality means that the matrix $\mathbf{V} - \mathbf{V}_1 \oplus \mathbf{V}_2$ is positive semi-definite. If no such local matrices \mathbf{V}_1 and \mathbf{V}_2 can be found to satisfy this inequality, the state is entangled.

While the criterion in Equation 2.33 is general for bipartite Gaussian states, its direct application is often impractical. Alternative entanglement witnesses can be formulated to simplify computations, reduce parameter complexity, or detect specific forms of entanglement. In the following sections, we introduce two additional entanglement criteria: the DGCZ criterion and the PPT criterion.

2.1.4.1 DGCZ Entanglement Criterion

In this section, we present the Duan-Giedke-Cirac-Zoller (DGCZ) criterion, commonly known as the Duan criterion, which serves as an entanglement witness for bipartite continuous-variable quantum states, where each subsystem comprises a single mode [81]. This criterion is specifically formulated to detect entanglement in EPR-type states by analyzing specific correlations between their quadratures. The criterion is based on the fact that these states exhibit quantum squeezing in the sum and difference of the canonical quadrature operators associated with each subsystem.

The DGCZ criterion, expressed in terms of the variances of the quadrature operators defined in Equation 2.27, is given by [81]:

$$\frac{\Delta^2 \hat{p}_- + \Delta^2 \hat{q}_+}{2} \geq 1. \quad (2.34)$$

A violation of this inequality serves as evidence of entanglement between the two single-mode subsystems. The DGCZ criterion assumes specific correlation symmetries between the two subsystems, making it a sufficient but not necessary condition for entanglement. In

particular, it assumes that quantum correlations manifest as the combination quadratures \hat{p}_- and \hat{q}_+ acquiring some degree of squeezing. This assumption imposes a limitation, as it does not account for other forms of entanglement. However, these are the exact quadrature combinations used in our teleportation protocol. This direct correspondence means the DGCZ criterion is an effective tool for verifying the necessary entanglement for successful quantum teleportation, with its value directly related to the protocol's performance. Therefore, it is the most relevant entanglement witness for our work.

2.1.4.2 PPT Entanglement Criterion

An alternative approach to detecting entanglement is the positive partial transpose (PPT) criterion, also known as the Peres–Horodecki criterion. Originally formulated for discrete-variable systems, this criterion identifies bipartite entanglement by applying a partial transposition to a given multipartite density matrix [82]. This approach was later generalized to continuous-variable systems by Rajiah Simon, who reformulated it in terms of the covariance matrix [83].

Considering a single continuous-variable (CV) mode characterized by the quadrature operators \hat{p} and \hat{q} , the transposition of its density matrix $\hat{\rho}$ corresponds to a reflection in phase space, expressed as:

$$\hat{\rho} \rightarrow \hat{\rho}^T \iff W(\hat{p}, \hat{q}) \rightarrow W(\hat{p}, -\hat{q}). \quad (2.35)$$

where $W(\hat{p}, \hat{q})$ represents the Wigner function. The transposition transformation results in a sign reversal of the \hat{q} quadrature while leaving \hat{p} unchanged. Extending this concept to a multipartite quantum state with covariance matrix \mathbf{V} consisting of $m + n$ modes, the partial transposition with respect to the n modes is given by:

$$\mathbf{V}_{PPT} = T \mathbf{V} T, \quad (2.36)$$

where the transformation matrix T is defined as:

$$T = \mathbb{1}_{2m} \oplus \Sigma_n, \quad (2.37a)$$

$$\Sigma_n = \bigoplus_{\ell=1}^n \sigma_z. \quad (2.37b)$$

Here, σ_z is the Pauli-Z matrix, which applies a reflection of the phase-space coordinates for the corresponding modes. As a result, the effect of T on \mathbf{V} is to reverse the sign of the \hat{q} quadrature for the last n modes.

Under this framework, the entanglement between the m and n modes can be verified by examining the partial transposed covariance matrix \mathbf{V}_{PPT} . Specifically, the bipartition is entangled if \mathbf{V}_{PPT} does not satisfy the physicality condition, meaning it does not fulfill the inequalities described in Equations 2.15 and 2.16. This condition is particularly significant for Gaussian states, where it provides a necessary and sufficient condition for separability when one of the subsystems consists of a single mode, i.e., either $m = 1$ or $n = 1$ [80].

2.2 Optical Parametric Oscillator

The optical parametric oscillator (OPO) has attracted substantial interest in the field of nonlinear optics, given its remarkable ability to generate coherent and tunable light across a wide range of wavelengths. This device consists of an optical cavity containing a nonlinear medium and operates on the principles of optical parametric amplification, where a high-frequency pump field is converted into two lower-frequency signal and idler fields, conserving energy and momentum [84]. While the specific resonance conditions of an optical parametric oscillator (OPO) can vary, at least one of the generated fields must resonate within the cavity. Additionally, the cavity may also be resonant to the other generated field, the pump field, or both. If the generated signal and idler fields have identical frequencies, the OPO is classified as degenerate; otherwise, it is non-degenerate. This study utilizes a non-degenerate triple-resonant optical parametric oscillator (TROPO), a schematic of which is presented in Figure 2.

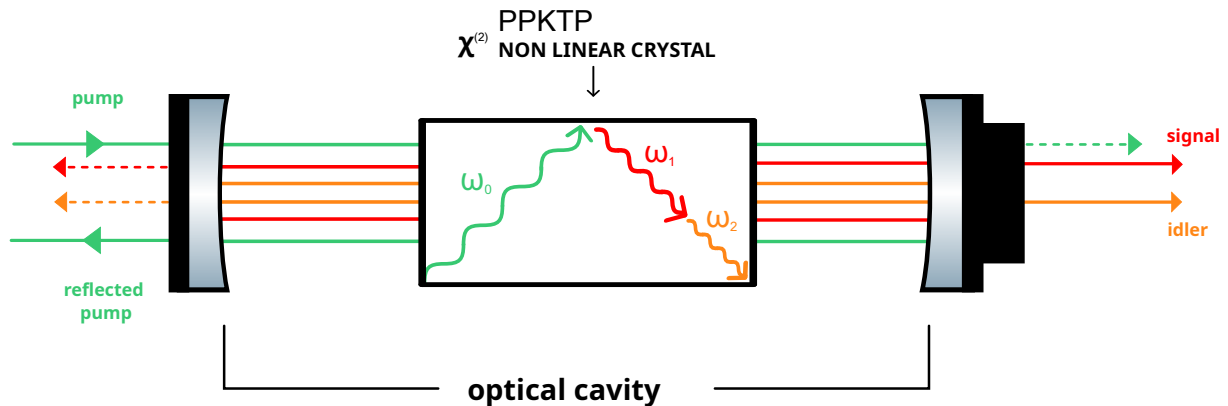


Figure 2 – Diagram of a non-degenerate triple-resonant optical parametric oscillator (TROPO). The system consists of an optical cavity containing a nonlinear medium, where a high-frequency pump field is converted into two lower-frequency fields, signal and idler, while conserving energy and momentum.

The interaction of the three overlapping beams in the nonlinear medium follows the principles of nonlinear optics [70]. In our case, the initial generation of signal and idler photons occurs via spontaneous parametric down-conversion (SPDC). Under proper phase-matching conditions and energy conservation, the interaction among the three fields

leads to a parametric amplification of the signal and idler amplitudes, with the gain parametrized by the pump power. The presence of an optical cavity introduces a feedback mechanism, which, in conjunction with the intracavity gain, enables the generated fields to oscillate. This oscillation occurs when the round-trip gain surpasses the round-trip losses. Since the losses are usually independent of the pump power, increasing the pump power enhances the gain, eventually allowing oscillation of the generated fields. The value of pump power at which this oscillation begins is known as the oscillation threshold. In this work, we operate in the regime where the pump power exceeds the threshold, resulting in the generation of bright signal and idler fields.

The quantum state of the signal and idler modes generated by a non-degenerate OPO is not a pure two-mode squeezed state but rather a mixed state that retains many of its defining characteristics. Nevertheless, its behavior closely resembles that of a two-mode squeezed state, justifying it being referred as such. The quantum treatment of the involved field interactions in an optical parametric oscillator (OPO) operating in the above-threshold regime has been extensively explored in the literature, with significant contributions from our group. The first works demonstrating quantum correlations in this regime can be found in [85, 86]. Additionally, our group has conducted several studies, both theoretical and experimental, investigating these quantum correlations under various conditions and examining the interplay between the different modes of the three interacting fields [87–95]. Given the extent of existing research, we will limit our discussion here to a brief overview of the quantum description of the OPO in the above-threshold regime.

2.2.1 Quantized Hamiltonian of the Optical Parametric Oscillator

The dynamics of an optical parametric oscillator (OPO) are governed by the interplay of nonlinear interaction, external driving, and cavity losses. The core nonlinear process is spontaneous parametric down-conversion (SPDC), whose governing interaction Hamiltonian in a nonlinear optical cavity is given by [96, 97]:

$$\hat{H}_{int} = 2i\hbar \frac{\chi^{(2)}}{\tau} (\hat{a}_1^\dagger \hat{a}_2^\dagger \hat{a}_0 - \hat{a}_1 \hat{a}_2 \hat{a}_0^\dagger), \quad (2.38)$$

where $\chi^{(2)}$ is the second-order nonlinear susceptibility, $\tau = L/c$ represents the round-trip time of the field inside the cavity, and \hbar is the reduced Planck constant. The annihilation operators \hat{a}_0 , \hat{a}_1 , and \hat{a}_2 correspond to the pump, signal, and idler fields, respectively. This Hamiltonian describes the parametric interaction, wherein a pump photon is annihilated, leading to the simultaneous creation of a signal and an idler photon, as well as the reverse process of photon recombination.

To capture the complete time evolution of the system, we must account for the coupling between the intracavity modes (\hat{a}_i) and a reservoir of external modes. This

coupling occurs via partially reflective cavity mirrors and internal scattering. The external reservoir is modeled as a very large set of decoupled harmonic oscillators, described by the annihilation operators \hat{b}_i^k , where the index $i \in \{0, 1, 2\}$ corresponds to the intracavity mode it interacts with, and $k \in \{0, 1, \dots, N\}$ with $N \rightarrow \infty$ indexes the reservoir modes. This interaction, which describes the exchange of photons between the cavity and the reservoir, is governed by a beam-splitter-like Hamiltonian. The total interaction Hamiltonian is the sum of the individual contributions for each mode [79, 98]:

$$\hat{H}_I = \sum_{i=0}^2 \hat{H}_I^i, \quad \hat{H}_I^i = \hbar \sum_k \left[g_i^k \hat{a}_i (\hat{b}_i^k)^\dagger + (g_i^k)^* \hat{a}_i^\dagger \hat{b}_i^k \right], \quad (2.39)$$

where g_i^k are the coupling coefficients dependent on the mirror transmission properties. Under the Born-Markov approximation, we assume the reservoir is large enough that it remains in its vacuum state, and its state is not significantly altered by the interaction. In this limit, the effect of the reservoir interaction Hamiltonian on the system's reduced density matrix, $\hat{\rho}$, can be described by a Lindblad master equation. The dissipative part of this evolution, which models photon loss from the cavity, is given by the Lindblad dissipator:

$$\mathcal{L}_{\text{diss}}(\hat{\rho}) = \sum_{i=0}^2 \frac{\gamma'_i}{\tau} \left(2\hat{a}_i \hat{\rho} \hat{a}_i^\dagger - \hat{\rho} \hat{a}_i^\dagger \hat{a}_i - \hat{a}_i^\dagger \hat{a}_i \hat{\rho} \right). \quad (2.40)$$

The parameter γ'_i represents the total round-trip losses in the cavity for the field mode i . It can be written as the sum of two components: $\gamma'_i = \gamma_i + \mu_i$. Here, γ_i represents the useful (or external) losses, which occur through a coupling mirror. These losses are essential by design, as they allow the pump field to enter the cavity and the generated signal and idler fields to be extracted. In contrast, μ_i represents the spurious (or internal) losses, which account for all unintentional or parasitic effects, such as photon absorption and scattering within the crystal or at other optical surfaces. The useful losses are directly related to the coupling mirror's intensity transmission, T_i , by:

$$T_i = 1 - R_i = 1 - e^{-2\gamma_i} \approx 2\gamma_i, \quad (2.41)$$

where the final approximation is valid for high-finesse cavities where the coupler transmission is very small ($T_i \ll 1$).

To sustain the parametric process, energy must be supplied to the system. This is achieved by driving the pump mode with an external laser field. The Hamiltonian for this interaction is:

$$\hat{H}_{in} = i\hbar \frac{\sqrt{2\gamma_0}}{\tau} \alpha_0^{in} (\hat{a}_0^\dagger - \hat{a}_0). \quad (2.42)$$

This term represents the injection of a classical pump field into the cavity, where the incident pump amplitude α_0^{in} is assumed to be real, setting its phase as the reference for the other fields involved in the system. The dimensionless parameter γ_0 quantifies the coupling strength through the input cavity mirror for the pump mode.

In the interaction picture (rotating frame), the free-field Hamiltonians of the intracavity modes are given by:

$$\hat{H}_{free} = -\hbar \sum_{i=0}^2 \frac{2\gamma'_i}{\tau} \Delta_i \hat{a}_i^\dagger \hat{a}_i, \quad (2.43)$$

where $\Delta_i = (\omega^{(i)} - \omega_{cav}^{(i)})/\Delta\omega_{cav}^{(i)}$ is the normalized cavity detuning for mode i , with the cavity bandwidth given by $\Delta\omega_{cav}^{(i)} = 2\gamma'_i/\tau$. The total Hamiltonian governing the OPO dynamics is then given by:

$$\hat{H} = \hat{H}_{int} + \hat{H}_{in} + \hat{H}_{free}. \quad (2.44)$$

The time evolution of an initial intracavity state described by the density operator $\hat{\rho}(t)$ follows the Lindblad master equation:

$$\frac{d}{dt} \hat{\rho} = \frac{1}{i\hbar} [\hat{H}, \hat{\rho}] + \mathcal{L}_{\text{diss}}(\hat{\rho}). \quad (2.45)$$

2.2.2 Noise Spectrum of the Generated Fields

The explicit derivation of the quantum noise characteristics of a non-degenerate OPO operating above threshold is a standard treatment in quantum optics, with the foundational expressions for the noise spectra having been rigorously established in [99]. The solution method, while not presented in full here, follows a well-defined theoretical path. The starting point is the Lindblad master equation, presented in the previous section, which describes the evolution of the system's density operator under the influence of both the internal Hamiltonian dynamics and the dissipative coupling to the environment. To make the problem tractable, the density operator is represented in phase space by the Wigner function, transforming the master equation into a Fokker-Planck equation. This, in turn, is mathematically equivalent to a system of Langevin equations, which are stochastic differential equations that govern the system's complex field amplitudes.

To solve the Langevin equations in a regime well above the oscillation threshold, where the generated fields are intense, the field amplitudes are decomposed into a classical mean value and a quantum fluctuation term [87]:

$$\alpha_i(t) = \langle \alpha_i(t) \rangle + \delta\alpha_i(t). \quad (2.46)$$

This linearization allows the dynamics of the quantum fluctuations to be isolated. These fluctuations are then described in terms of their quadrature components, which represent fluctuations in amplitude and phase relative to the mean field. Subsequently, transformations are used to describe the quadrature fluctuations of the generated fields in terms of their sum and difference components (Equation 2.27). The final step involves applying a Fourier transform to obtain the spectral components of the fluctuations, which are the quantities of experimental interest. The noise power spectrum of a quadrature \hat{p}_- at an analysis frequency Ω is given by the Fourier transform of its autocorrelation function [79]:

$$S_{\hat{p}_-}(\Omega) \propto \langle \delta\hat{p}_-(\Omega)\delta\hat{p}_-(-\Omega) \rangle. \quad (2.47)$$

Upon proper normalization to the shot noise level, where a spectrum value of 1 corresponds to the standard quantum limit (SQL), the noise spectrum becomes numerically equivalent to the variance of the quadrature fluctuations, $S_{\hat{p}_-}(\Omega) = \Delta^2\hat{p}_-(\Omega)$. Using this formalism, the noise spectra for the sum and difference of the signal and idler quadratures, at resonance (zero detuning), are obtained as [99]:

$$S_{\hat{p}_-} = 1 - \frac{\gamma}{\gamma'} \frac{1}{1 + \Omega'^2}, \quad (2.48a)$$

$$S_{\hat{q}_-} = 1 + \frac{\gamma}{\gamma'} \frac{1}{\Omega'^2}, \quad (2.48b)$$

$$S_{\hat{p}_+} = |\kappa_p|^2 S_{p_0}^{in} + |2\gamma\xi - 1|^2 + \frac{\mu_0}{\gamma_0} |\kappa_p|^2 + 4\gamma\mu |\xi|^2, \quad (2.48c)$$

$$S_{\hat{q}_+} = |\kappa_q|^2 S_{q_0}^{in} + |2\gamma\zeta - 1|^2 + \frac{\mu_0}{\gamma_0} |\kappa_q|^2 + 4\gamma\mu |\zeta|^2, \quad (2.48d)$$

The parameters used in these expressions are listed in Table 1, and the relevant transfer functions are defined as follows:

$$\kappa_p = \frac{2\sqrt{2}\gamma'\beta\sqrt{\gamma_0\gamma}}{\gamma'_0 + 2i\gamma'\Omega'} \xi, \quad (2.49a)$$

$$\kappa_q = \frac{2\sqrt{2}\gamma'\beta\sqrt{\gamma_0\gamma}}{\gamma'_0 + 2i\gamma'\Omega'} \frac{1}{\zeta}, \quad (2.49b)$$

$$\xi = 2i\gamma'\Omega' + \frac{2\gamma'^2\beta^2}{\gamma'_0 + 2i\gamma'\Omega'}, \quad (2.49c)$$

$$\zeta = \left(2\gamma' + 2i\gamma'\Omega' + \frac{2\gamma'^2\beta^2}{\gamma'_0 + 2i\gamma'\Omega'} \right)^{-1}. \quad (2.49d)$$

We are particularly interested in the noise spectrum $S_{\hat{p}_-}$, which represents the subtraction of amplitude fluctuations, and $S_{\hat{q}_+}$, which corresponds to the sum of phase fluctuations. Under appropriate conditions, both $S_{\hat{p}_-}$ and $S_{\hat{q}_+}$ can exhibit noise levels below

Table 1 – List of parameters used in the analytical expressions for the noise spectra of the field interactions in the OPO. These parameters describe the intracavity and external coupling losses, normalized frequency detunings, and other relevant system properties.

Symbol	Description
$S_{p_0}^{in}$	Amplitude noise of the pump
$S_{q_0}^{in}$	Phase noise of the pump
γ'_0	Total intracavity losses for pump
γ_0	Transmission useful losses for pump
μ_0	Spurious losses for pump
γ'	Total intracavity losses for signal and idler
γ	Transmission useful losses for signal and idler
μ	Spurious losses for signal and idler
σ	Pump optical power normalized by the OPO oscillation threshold
β	Ratio between the amplitude of the generated beams and that of the pump
Ω'	Analysis frequency normalized by the OPO cavity bandwidth

the standard quantum limit ($S < 1$), indicating the presence of two-mode quadrature squeezing. Since these noise spectra are equivalent to the variances of the respective quadratures, the simultaneous squeezing of both combinations leads to the condition:

$$\frac{\Delta^2 \hat{p}_- + \Delta^2 \hat{q}_+}{2} < 1. \quad (2.50)$$

This result signifies a violation of the Duan criterion, presented in Equation 2.34, confirming that the beams generated by the OPO can be entangled. Such EPR-like entanglement is of central interest, as it enables quantum teleportation with an advantage over any classical attempt, a topic that will be demonstrated in the following chapters.

3 DETECTION OF QUADRATURE QUANTUM NOISE AND QUANTUM STATE RECONSTRUCTION

To characterize the quantum correlations of the fields generated by our source (OPO) and validate the performance of the teleportation protocol, we perform a complete quantum tomography. This method reconstructs the density matrix of the joint quantum system describing all relevant quantum modes in the measured fields. In the continuous-variable regime, the states we manipulate are described using the quadrature operators \hat{p} and \hat{q} of the field. Instead of the density matrix, we use a quasi-probability distribution like the Wigner function to represent these states [71].

Quantum fluctuations in the fields of interest are analyzed through the statistical properties of the quadrature operators and their correlations. For bright fields with a well-established frequency (narrow bandwidth), such as those generated by an OPO operating in the above-threshold regime, a common approach involves decomposing the electromagnetic field operators into an average value and a fluctuation term [87, 95]. The average value is associated with the carrier frequency, representing the densely populated central frequency mode. Meanwhile, the fluctuation term corresponds to the energy distribution across the sideband frequency modes where photon concentrations are significantly smaller. These fluctuations can be interpreted as small modulations of the carrier field, analogous to classical field modulations [100]. For instance, a bright field at 795 nm with a power of 1 mW, parameters compatible with the fields generated by the OPO used in this work, exhibits a photon flux of 4×10^{15} photons per second in the carrier mode. In contrast, the flux in the sidebands is only a few photons per second when integrated over a bandwidth of hundreds of kHz [101]. Figure 3 illustrates the spectral regions of a field.

In this work, we focus on the quantum states encoded within the sideband modes, where the low photon density accentuates their quantum features, facilitating their measurement and analysis [102]. The specific regions within the sideband spectrum where nonclassical correlations can be observed with high precision are determined by our experimental apparatus. In our setup, an optical parametric oscillator (OPO) is used to generate quantum-correlated fields, and the quantum state tomography is performed via the resonator-assisted self-homodyne detection technique [103]. The bandwidth of the OPO ($\Delta\omega_{OPO}$) determines the frequency range over which entanglement, a critical resource for quantum teleportation, is produced. Consequently, the upper frequency limit of the sideband region of interest is given by $\Omega_{sup} = \Delta\omega_{OPO}/2$. On the other hand, the self-homodyne detection relies on an analysis cavity for the measurement procedure. This cavity bandwidth ($\Delta\omega_{acav}$) sets the minimum sideband frequency that can be resolved with high accuracy, without being affected by the cavity interior losses, defining the lower

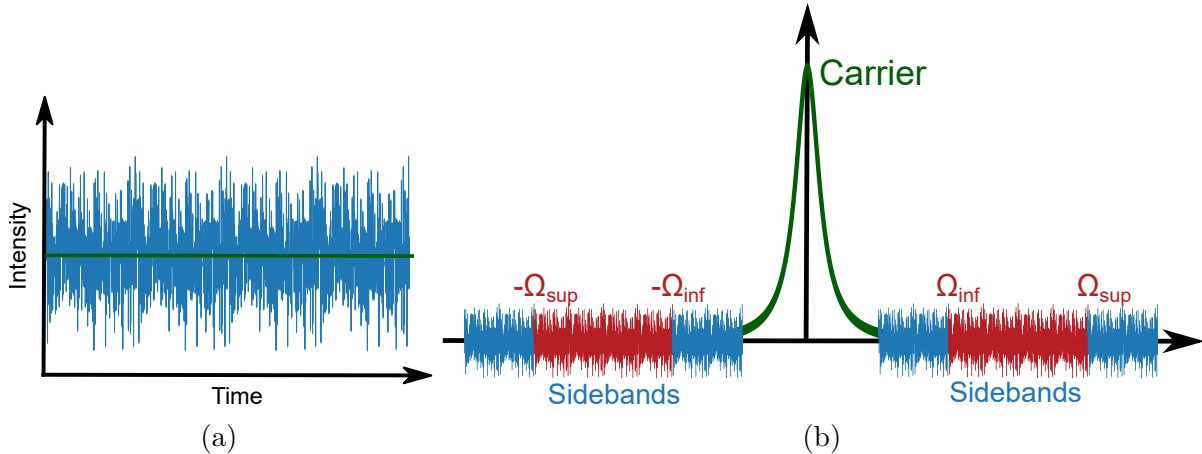


Figure 3 – (a) The intensity of an optical field, measured in the time domain, can be represented as the sum of an average value and a fluctuation term. (b) Representation of the intensity spectrum of an optical field. The central region corresponds to the densely populated carrier mode, while the blue and red areas denote sideband modes with lower photon concentrations. The red region represents the region of interest, where we expect to be able to measure its modes with good accuracy and expect a substantial amount of quantum resources.

limit of the interest region as $\Omega_{\text{inf}} = \sqrt{2}\Delta\omega_{\text{acav}}$.

The information about a field's quantum state is obtained via photodetection, which produces a time-varying photocurrent. To measure the orthogonal quadrature information of weak sideband modes, an interferometric technique is employed that uses an intense reference field, known as a local oscillator (LO). When the LO and the signal field share the same central frequency, the method is called homodyne detection [104]. Conversely, if their central frequencies differ, it is known as heterodyne detection [105]. The beating interaction between the sideband and the LO translates the quadrature information into a frequency range measurable by modern photodetectors. This process can be understood as an amplification of the quantum noise amplitude of the sideband modes mediated by the LO. The specific quadrature axis measured is determined by the phase relationship between the local oscillator and the sideband mode being analyzed.

In the case of a bright field, the carrier can act as its own local oscillator (LO) for measuring the sidebands. Because the carrier maintains a well-defined phase relationship with the sidebands, a direct intensity measurement of the field provides information about the quadrature aligned with the carrier's complex amplitude. We define this quadrature, accessed without applying any phase shift to the carrier or sidebands, as the amplitude quadrature, \hat{p} , and will use this term throughout the text. To obtain information about the orthogonal quadrature, the phase quadrature \hat{q} , we use the previously mentioned resonator-assisted self-homodyne technique. This method employs a resonator cavity to adjust the phase relationship between the carrier and the sidebands, thereby enabling access to the information encoded in the phase quadrature.

3.1 Photocurrent Operator

No detector is currently fast enough to directly measure electric field oscillations in the optical domain, which occur at frequencies of hundreds of terahertz (THz). In this spectral region, conventional measurement devices are typically photodetectors, which are sensitive only to temporal averages of light intensity rather than real-time field fluctuations. In our experiment, we quantify optical intensity using photodiodes, which are PIN semiconductor devices. These devices operate based on the photoelectric effect, generating a photocurrent that is directly proportional to the incident photon flux [106].

The treatment presented in this section follows the approach used in the references [95, 107]. The intensity of light measured by the photodiode is an observable operator proportional to the autocorrelation Glauber function [108]:

$$\hat{I}(\mathbf{r}, t) = \kappa \hat{E}^{(-)}(\mathbf{r}, t) \hat{E}^{(+)}(\mathbf{r}, t), \quad (3.1)$$

where \hat{I} is the photocurrent observable operator, the non-hermitian operators $\hat{E}^{(+)}(\mathbf{r}, t) = [\hat{E}^{(-)}(\mathbf{r}, t)]^\dagger$ are the positive and negative frequency parts of the electric field for a given polarization ϵ , t is the measurement time, \mathbf{r} is the position of the detector, and κ is a factor accounting for the photodetector's gain and quantum efficiency. We will now drop the spatial dependence of the electric field, which represents the integration of the field over the photodetector area.

The classical photocurrent obtained by the measurement procedure is the temporal average, defined by the integration time of the photodetector, of the photocurrent operator:

$$\langle \hat{I}(t) \rangle = \kappa \langle \hat{E}^{(-)}(t) \hat{E}^{(+)}(t) \rangle, \quad (3.2)$$

where $\langle \hat{O} \rangle$ is the expectation value of the operator \hat{O} with respect to state of the field $\hat{\rho}$.

In the laboratory, we generate bright fields characterized by a well-defined carrier frequency, ω_0 , accompanied by a continuum of sideband modes in the frequency range surrounding the carrier. The generated carrier is narrowband but will be considered monochromatic to facilitate the following theoretical treatment, this can be done without loss of generality when measuring far sideband modes. The quantum state $\hat{\rho}_\psi$ of these sideband modes, residing in the Hilbert space \mathcal{H}_{sb} , exhibits a precise phase relationship with the carrier. The carrier itself can be effectively described as a coherent state $|\alpha_{\omega_0}\rangle$ within its Hilbert space \mathcal{H}_c , with an amplitude given by $\alpha_{\omega_0} = |\alpha_{\omega_0}| \exp(i\varphi)$ [107]. Consequently, the global state of the bright field can be expressed as the tensor product:

$$\hat{\rho}_\Psi = |\alpha_{\omega_0}\rangle\langle\alpha_{\omega_0}| \otimes \hat{\rho}_\psi, \quad \text{in the Hilbert space } \mathcal{H} = \mathcal{H}_c \otimes \mathcal{H}_{sb}. \quad (3.3)$$

The positive- and negative-frequency components of the electric field in free space, where the boundary conditions permit a continuum of frequency modes, are expressed as:

$$\hat{E}^{(+)}(t) = i \int_{-\infty}^{\infty} e^{-i\omega t} \hat{a}_{\omega} d\omega, \quad \hat{E}^{(-)}(t) = [\hat{E}^{(+)}(t)]^\dagger. \quad (3.4)$$

The field operator can be separated into a component associated with the carrier and another with the sidebands:

$$\hat{E}^{(+)}(t) = \hat{E}_c^{(+)}(t) + \hat{E}_{sb}^{(+)}(t). \quad (3.5)$$

Using Equations (3.3) and (3.5), which describe the carrier and sideband states, in conjunction with Equation (3.2) for the mean photocurrent, we obtain the following expression for the intensity measurement:

$$\begin{aligned} \langle \hat{I}(t) \rangle &= \kappa \text{Tr} \left(\hat{\rho}_{\psi} \langle \alpha_{\omega_0} | [\hat{E}_c^{(-)}(t) + \hat{E}_{sb}^{(-)}(t)][\hat{E}_c^{(+)}(t) + \hat{E}_{sb}^{(+)}(t)] | \alpha_{\omega_0} \rangle \right) \\ &= [\langle \hat{E}_c^{(-)}(t) \hat{E}_c^{(+)}(t) \rangle + \langle \hat{E}_c^{(-)}(t) \hat{E}_{sb}^{(+)}(t) \rangle + \langle \hat{E}_{sb}^{(-)}(t) \hat{E}_c^{(+)}(t) \rangle + \langle \hat{E}_{sb}^{(-)}(t) \hat{E}_{sb}^{(+)}(t) \rangle]. \end{aligned} \quad (3.6)$$

The first three terms in Equation (3.6) can be evaluated using Equation (3.4) alongside the relation $\hat{a}_{\omega} |\alpha_{\omega_0}\rangle = \delta(\omega - \omega_0) \alpha_{\omega_0} |\alpha_{\omega_0}\rangle$, which reflects the monochromatic nature of the carrier. This results in:

$$\langle \hat{E}_c^{(-)}(t) \hat{E}_c^{(+)}(t) \rangle = |\alpha_{\omega_0}|^2, \quad (3.7a)$$

$$\langle \hat{E}_c^{(-)}(t) \hat{E}_{sb}^{(+)}(t) \rangle = |\alpha_{\omega_0}| e^{-i\varphi} \text{Tr} \left(\hat{\rho}_{\psi} \int^{\omega \neq \omega_0} d\omega e^{-i(\omega - \omega_0)t} \hat{a}_{\omega} \right), \quad (3.7b)$$

$$\langle \hat{E}_{sb}^{(-)}(t) \hat{E}_c^{(+)}(t) \rangle = |\alpha_{\omega_0}| e^{i\varphi} \text{Tr} \left(\hat{\rho}_{\psi} \int^{\omega \neq \omega_0} d\omega e^{i(\omega - \omega_0)t} \hat{a}_{\omega}^\dagger \right). \quad (3.7c)$$

The last term in Equation 3.6, corresponding exclusively to the sideband modes ($\langle \hat{E}_{sb}^{(-)}(t) \hat{E}_{sb}^{(+)}(t) \rangle$), contributes minimally to the photocurrent. This is because the sideband contribution is not amplified by the carrier field, which significantly enhances other terms involving the carrier-sideband interaction. Specifically, the inequality:

$$\langle \alpha_{\omega_0} | \hat{a}_{\omega_0}^\dagger \hat{a}_{\omega_0} | \alpha_{\omega_0} \rangle \gg \text{Tr} \left(\hat{\rho}_{\psi} \int d\omega \hat{a}_{\omega}^\dagger \hat{a}_{\omega} \right) \quad (3.8)$$

is satisfied, where the left-hand side represents the photon number in the carrier mode, and the right-hand side represents the total photon number in the sideband modes. Thus, the sideband-only term is excluded from further consideration due to its negligible contribution.

Based on Equations 3.6 and 3.7, the mean photocurrent is given by:

$$\langle \hat{I}(t) \rangle = \kappa \left\{ |\alpha_{\omega_0}|^2 + |\alpha_{\omega_0}| \text{Tr} \left[\hat{\rho}_\psi \left(e^{-i\varphi} \hat{a}(t) + e^{i\varphi} \hat{a}^\dagger(t) \right) \right] \right\}, \quad (3.9)$$

where the temporal bosonic operators of annihilation $\hat{a}(t)$ and creation $\hat{a}^\dagger(t)$ are defined as:

$$\hat{a}(t) = \int^{\omega \neq \omega_0} d\omega e^{-i(\omega - \omega_0)t} \hat{a}_\omega, \quad \hat{a}^\dagger(t) = \int^{\omega \neq \omega_0} d\omega e^{i(\omega - \omega_0)t} \hat{a}_\omega^\dagger. \quad (3.10)$$

The first term in Equation 3.9 is independent of time and represents the mean intensity of the field measured by the photodiode, it represents the low-frequency component of the photocurrent, known as the DC signal. The second term is associated with the sidebands that are amplified by the carrier amplitude, it can be related to the high-frequency fluctuations of the photocurrent (HF signal). These fluctuations carry information about the sideband modes, which we are interested in measuring. Defining the photocurrent fluctuation operator as $\delta \hat{I}_\varphi(t)$, it can be expressed in terms of the temporal quadrature fluctuations $\delta \hat{X}^\varphi(t)$ as [68]:

$$\langle \hat{I}(t) \rangle = \kappa |\alpha_{\omega_0}|^2 + \langle \delta \hat{I}_\varphi(t) \rangle, \quad (3.11a)$$

$$\text{where } \delta \hat{I}_\varphi(t) = \kappa |\alpha_{\omega_0}| [e^{-i\varphi} \hat{a}(t) + e^{i\varphi} \hat{a}^\dagger(t)] = \kappa |\alpha_{\omega_0}| \delta \hat{X}^\varphi(t). \quad (3.11b)$$

Equation (3.10) can be rewritten to centralize the carrier frequency by introducing the substitution $\Omega = \omega - \omega_0$, where Ω represents the frequency detuning relative to the carrier. Furthermore, simplifying the notation $\hat{a}_{\Omega+\omega_0} \rightarrow \hat{a}_\Omega$ leads to the following expression for the photocurrent fluctuation operator:

$$\delta \hat{I}_\varphi(t) = \kappa |\alpha_{\omega_0}| e^{-i\varphi} \int'_{-\infty}^{\infty} d\Omega e^{-i\Omega t} \hat{a}_\Omega + e^{i\varphi} \int'_{-\infty}^{\infty} d\Omega e^{i\Omega t} \hat{a}_\Omega^\dagger \quad (3.12a)$$

$$= \kappa |\alpha_{\omega_0}| \int'_{-\infty}^{\infty} d\Omega \left[e^{-i\Omega t} \left(e^{-i\varphi} \hat{a}_\Omega + e^{i\varphi} \hat{a}_{-\Omega}^\dagger \right) \right] \quad (3.12b)$$

$$= \kappa |\alpha_{\omega_0}| \int'_0^{\infty} d\Omega \left[e^{-i\Omega t} \left(e^{-i\varphi} \hat{a}_\Omega + e^{i\varphi} \hat{a}_{-\Omega}^\dagger \right) + e^{i\Omega t} \left(e^{-i\varphi} \hat{a}_{-\Omega} + e^{i\varphi} \hat{a}_\Omega^\dagger \right) \right]. \quad (3.12c)$$

Here, the prime symbol ('') in the integral indicates that the contribution at $\Omega = 0$ (the carrier frequency) is excluded. The progression from Equation (3.12a) to Equation (3.12b) involves a change of variables in the second integral, substituting $\Omega \rightarrow -\Omega$. Subsequently, the transition from Equation (3.12b) to Equation (3.12c) involves splitting the integration range into positive frequencies, simplifying the expression for further analysis. This final form of the temporal photocurrent fluctuation operator facilitates its treatment in the spectral domain.

3.1.1 Balanced Detection Scheme

Directing a beam onto a photodetector produces a photocurrent whose temporal fluctuations are described by Equation 3.11. These fluctuations are directly proportional to the temporal quadrature fluctuations of the optical field. The proportionality constant depends on the carrier amplitude, $|\alpha_{\omega_0}|$, and constants related to the photodetector, κ . To extract the statistics of the field quadratures in units consistent with our definition (Equation 2.4), the photocurrent fluctuations must be normalized. This normalization factor is known as the shot noise (SN).

To obtain the shot noise value, we use the balanced detection scheme [100] shown in Figure 4. This method involves splitting the beam under measurement using a 50 : 50 beam splitter (BS) and simultaneously detecting both outputs with two identical photodetectors, labeled 1 and 2. By summing the photocurrents, we extract the intensity fluctuations of the measured field. Conversely, subtracting the photocurrents cancels these fluctuations, providing the corresponding shot noise fluctuations. This process enables the simultaneous acquisition of the field's noise and its fundamental shot noise level.

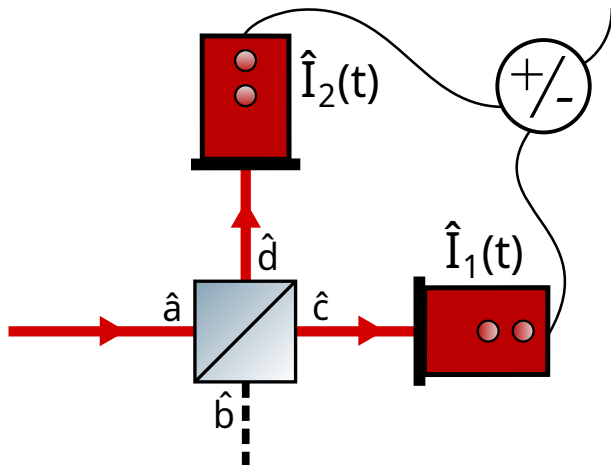


Figure 4 – Schematic of the balanced detection scheme used to measure the shot noise value.

The beam under investigation is split using a 50 : 50 beam splitter, with the two outputs detected simultaneously by identical photodetectors (1 and 2). The sum of the photocurrents provides information about the field fluctuations, while their difference yields the shot noise value, enabling simultaneous acquisition of both.

Considering the beam splitter illustrated in Figure 4, the beam to be measured is described by the input mode \hat{a} . Meanwhile, the other input mode, \hat{b} , describes a vacuum state being coupled by the open port. Consequently, the state entering the beam splitter is given as:

$$\hat{\rho}_{AB} = \hat{\rho}_A \otimes |0\rangle\langle 0|. \quad (3.13)$$

Upon interaction with the 50 : 50 beam splitter, the output modes \hat{c} and \hat{d} are related to the input modes via the transformation [109]:

$$\hat{c} = \frac{1}{\sqrt{2}}(\hat{a} + \hat{b}), \quad (3.14a)$$

$$\hat{d} = \frac{1}{\sqrt{2}}(\hat{a} - \hat{b}), \quad (3.14b)$$

where the coefficients reflect the beam splitter's equal splitting ratio. Assuming the input beam \hat{a} has a large classical amplitude α_{ω_0} and referencing Equation 3.11, the photocurrent measured at each detector can be expressed in a linearized form as:

$$\langle \hat{I}_1(t) \rangle = \frac{|\alpha_{\omega_0}|^2}{2} + \langle \delta \hat{I}_1^\varphi(t) \rangle, \quad \text{where } \delta \hat{I}_1^\varphi(t) = \kappa \frac{|\alpha_{\omega_0}|}{\sqrt{2}} [e^{-i\varphi} \hat{c}(t) + e^{i\varphi} \hat{c}^\dagger(t)], \quad (3.15a)$$

$$\langle \hat{I}_2(t) \rangle = \frac{|\alpha_{\omega_0}|^2}{2} + \langle \delta \hat{I}_2^\varphi(t) \rangle, \quad \text{where } \delta \hat{I}_2^\varphi(t) = \kappa \frac{|\alpha_{\omega_0}|}{\sqrt{2}} [e^{-i\varphi} \hat{d}(t) + e^{i\varphi} \hat{d}^\dagger(t)]. \quad (3.15b)$$

In an experiment, the temporal fluctuations are accessed by separating the AC component (fluctuations) from the DC component (average value) of the measured photocurrent. Using the beam splitter transformation (Equation 3.14) and the input state (Equation 3.13), the sum of the measured photocurrent fluctuations is expressed as:

$$\begin{aligned} \langle \delta \hat{I}_+(t) \rangle &= \langle \delta \hat{I}_1^\varphi(t) \rangle + \langle \delta \hat{I}_2^\varphi(t) \rangle \\ &= \kappa \frac{|\alpha_{\omega_0}|}{\sqrt{2}} \text{Tr} \left\{ \hat{\rho}_{CD} [e^{-i\varphi} (\hat{c}(t) + \hat{d}(t)) + e^{i\varphi} (\hat{c}^\dagger(t) + \hat{d}^\dagger(t))] \right\} \\ &= \kappa |\alpha_{\omega_0}| \text{Tr} \left\{ \hat{\rho}_{AB} [e^{-i\varphi} \hat{a}(t) + e^{i\varphi} \hat{a}^\dagger(t)] \right\} \\ &= \kappa |\alpha_{\omega_0}| \delta \hat{X}_a^\varphi(t). \end{aligned} \quad (3.16)$$

The sum directly yields the temporal quadrature fluctuations, $\delta \hat{X}_a^\varphi(t)$, of the input mode \hat{a} . This result shows that the summed signal contains the same information as would be obtained by directing the entire beam into a single detector, with parameters identical to those of the pair of detectors used in the balanced scheme, as a comparison with Equation 3.11b demonstrates. For the subtraction of the temporal photocurrent fluctuations, we have:

$$\begin{aligned}
\langle \delta \hat{I}_-(t) \rangle &= \langle \delta \hat{I}_1^\varphi(t) \rangle - \langle \delta \hat{I}_2^\varphi(t) \rangle \\
&= \kappa \frac{|\alpha_{\omega_0}|}{\sqrt{2}} \text{Tr} \left\{ \hat{\rho}_{CD} [e^{-i\varphi}(\hat{c}(t) - \hat{d}(t)) + e^{i\varphi}(\hat{c}^\dagger(t) - \hat{d}^\dagger(t))] \right\} \\
&= \kappa |\alpha_{\omega_0}| \text{Tr} \left\{ \hat{\rho}_{AB} [e^{-i\varphi}\hat{b}(t) + e^{i\varphi}\hat{b}^\dagger(t)] \right\} \\
&= \kappa |\alpha_{\omega_0}| \delta \hat{X}_v^\varphi(t).
\end{aligned} \tag{3.17}$$

The subtracted signal reflects the fluctuations of the vacuum state coupled through the beam splitter's open port (mode \hat{b}). The vacuum state, being a coherent state, is defined by its minimum uncertainty and its variance is equal for any quadrature direction. Based on the adopted quadrature definition (Equation 2.4), this coherent state variance is unity, $\Delta^2 \hat{X}_v^\varphi(t) = 1$, regardless of the phase φ . Therefore, the variance of the subtracted signal is given by:

$$\Delta^2 \langle \delta \hat{I}_-(t) \rangle = \Delta^2 \hat{I}_{Shot} = \kappa^2 |\alpha_{\omega_0}|^2. \tag{3.18}$$

This result represents the shot noise variance and serves as the normalization factor. The normalized quadrature fluctuations of the signal are then extracted as:

$$\frac{\langle \delta \hat{I}_+(t) \rangle}{\sqrt{\Delta^2 \hat{I}_{Shot}}} = \delta \hat{X}_a^\varphi(t). \tag{3.19}$$

This approach allows us to extract the quadrature fluctuations directly from our measurements. When normalized in this way, the variance of the signal quadrature is expressed in shot noise units (s.n.u.).

An alternative method for obtaining the shot noise involves using a beam with a coherent state in the sidebands and measuring this beam at different power levels to create a shot noise calibration curve. However, this approach poses several challenges: it requires a coherent state at the same wavelength as the measured beam, with an intensity matching the range of the measured beams, and under similar alignment conditions. Additionally, this method necessitates performing two separate measurements, whereas balanced detection allows for simultaneous normalization. In our case, this approach was not feasible due to the lack of access to coherent lasers at the wavelength of our generated fields.

It is important to note that the presentation in this section does not account for the electronic noise of the detectors, which must be considered to accurately extract the quadrature information. This aspect will be addressed in detail in the data analysis discussions presented in the upcoming chapters. For the remainder of this chapter, all

presented photocurrents are assumed to be shot noise normalized according to the procedure described here.

3.1.2 Spectral Photocurrent Observables

To extract details about the quantum states of light in specific sideband modes, we perform a spectral analysis of the photocurrent. This frequency-domain analysis, centered on a single Fourier frequency, Ω_{af} , known as the analysis frequency, allows us to examine the quantum state at the optical sidebands symmetrically located at $\omega_0 \pm \Omega_{af}$ relative to the carrier frequency. The analysis frequency is chosen to be high enough to avoid significant low-frequency technical noise, while remaining within the bandwidth of the photodetectors and processing electronics. For these reasons, the analysis frequency is generally chosen within the MHz range.

The spectral component of the photocurrent is defined as the Fourier transform of the temporal photocurrent fluctuations operator (Equation 3.12):

$$\hat{I}_\Omega = \int_{-\infty}^{\infty} \frac{dt}{2\pi} \delta\hat{I}(t) e^{i\Omega t}, \quad \delta\hat{I}(t) = \int_{-\infty}^{\infty} d\Omega \hat{I}_\Omega e^{-i\Omega t}. \quad (3.20)$$

By comparing Equation 3.20 with Equation 3.12b, we can identify the spectral component of the photocurrent as:

$$\hat{I}_\Omega = e^{-i\varphi} \hat{a}_\Omega + e^{i\varphi} \hat{a}_{-\Omega}^\dagger. \quad (3.21)$$

This expression reveals that the spectral photocurrent operator, \hat{I}_Ω , is non-Hermitian, satisfying the relation $\hat{I}_\Omega^\dagger = \hat{I}_{-\Omega}$. It contains contributions from both the lower and upper sideband modes at frequencies $\omega_0 - \Omega$ and $\omega_0 + \Omega$, respectively, and as a non-Hermitian operator, the spectral component of the photocurrent is not directly observable. However, its real and imaginary parts, which are Hermitian operators, can be accessed and correspond to measurable quantities.

To experimentally access the photocurrent information in the vicinity of a specific analysis frequency, Ω_{af} , we pass the output signal of the photodetector through a quadrature demodulation system. In this system, the photocurrent is mixed with an electronic local oscillator (eLO) at the analysis frequency, Ω_{af} , followed by a low-pass filter (LPF) with a defined bandwidth. The resulting signal evolves on a time scale determined by the inverse of the filter bandwidth. The electronic oscillator can be described by a current given as follows:

$$I_{eo}(t) = I_{af} e^{i\Omega_{af} t} + I_{af}^* e^{-i\Omega_{af} t} \quad (3.22)$$

The mixer performs the multiplication operation between the photocurrent and the electronic oscillator. Using Equations 3.12a and 3.22, the resulting mixed photocurrent can be expressed as:

$$\begin{aligned}\hat{I}_{mix} &= \delta\hat{I}_\varphi(t)I_{eo}(t) \\ &= e^{-i\varphi} \int_{-\infty}^{\infty} d\Omega e^{-i(\Omega-\Omega_{af})t} \hat{a}_\Omega I_{af} + e^{i\varphi} \int_{-\infty}^{\infty} d\Omega e^{i(\Omega-\Omega_{af})t} \hat{a}_\Omega^\dagger I_{af}^* \\ &\quad + e^{-i\varphi} \int_{-\infty}^{\infty} d\Omega e^{-i(\Omega+\Omega_{af})t} \hat{a}_\Omega I_{af}^* + e^{i\varphi} \int_{-\infty}^{\infty} d\Omega e^{i(\Omega+\Omega_{af})t} \hat{a}_\Omega^\dagger I_{af}.\end{aligned}\quad (3.23)$$

The output signal is then processed through a low-pass filter (LPF) with a narrow bandwidth. An ideal low-pass filtering operation where the cutoff frequency tends to zero can be represented mathematically as a time integration of the mixed photocurrent. Consequently, the photocurrent operator after demodulation is given by:

$$\begin{aligned}\hat{I}_{out} &= \int_{-\infty}^{\infty} dt \hat{I}_{mix} \\ &= e^{-i\varphi} \int_{-\infty}^{\infty} d\Omega \hat{a}_\Omega I_{af} \delta(\Omega - \Omega_{af}) + e^{i\varphi} \int_{-\infty}^{\infty} d\Omega \hat{a}_\Omega^\dagger I_{af}^* \delta(\Omega - \Omega_{af}) \\ &\quad + e^{-i\varphi} \int_{-\infty}^{\infty} d\Omega \hat{a}_\Omega I_{af}^* \delta(\Omega + \Omega_{af}) + e^{i\varphi} \int_{-\infty}^{\infty} d\Omega \hat{a}_\Omega^\dagger I_{af} \delta(\Omega + \Omega_{af}) \\ &= (e^{-i\varphi} \hat{a}_{\Omega_{af}} + e^{i\varphi} \hat{a}_{-\Omega_{af}}^\dagger) I_{af} + (e^{-i\varphi} \hat{a}_{-\Omega_{af}} + e^{i\varphi} \hat{a}_{\Omega_{af}}^\dagger) I_{af}^*\end{aligned}\quad (3.24a)$$

$$= \hat{I}_{\Omega_{af}} I_{af} + \hat{I}_{-\Omega_{af}} I_{af}^*. \quad (3.24b)$$

We verify in Equation (3.24b) the relationship between the spectral component of the photocurrent at the analysis frequency Ω_{af} and the demodulated photocurrent operator. To explicitly express the observable operators in the demodulated photocurrent, we decompose the complex amplitude of the electronic oscillator, $I_{af} = |\mathcal{A}|e^{i\theta}$ into its real and imaginary components as follows:

$$\hat{I}_{out} = \sqrt{2}|\mathcal{A}| \left[\cos \theta \left(\frac{\hat{I}_\Omega + \hat{I}_{-\Omega}}{\sqrt{2}} \right) + i \sin \theta \left(\frac{\hat{I}_\Omega - \hat{I}_{-\Omega}}{\sqrt{2}} \right) \right] \quad (3.25a)$$

$$= \sqrt{2}|\mathcal{A}| (\cos \theta \hat{I}_{cos} - \sin \theta \hat{I}_{sin}). \quad (3.25b)$$

Here, the operators $\hat{I}_{cos} = (\hat{I}_\Omega + \hat{I}_{-\Omega})/\sqrt{2}$ and $\hat{I}_{sin} = (\hat{I}_\Omega - \hat{I}_{-\Omega})/\sqrt{2}i$ are Hermitian and represent the electronic quadrature components. These operators commute, $[\hat{I}_{cos}, \hat{I}_{sin}] = 0$, and are related to the spectral photocurrent by:

$$\hat{I}_\Omega = \frac{\hat{I}_{cos} + i\hat{I}_{sin}}{\sqrt{2}} \quad (3.26)$$

The observables \hat{I}_{cos} and \hat{I}_{sin} can be expressed in terms of the creation and annihilation operators as follows:

$$\hat{I}_{cos} = \frac{1}{\sqrt{2}}(e^{-i\varphi}\hat{a}_\Omega + e^{i\varphi}\hat{a}_{-\Omega}^\dagger + e^{i\varphi}\hat{a}_\Omega^\dagger + e^{-i\varphi}\hat{a}_{-\Omega}) \quad (3.27a)$$

$$= \frac{1}{\sqrt{2}}[\cos\varphi(\hat{p}_\Omega + \hat{p}_{-\Omega}) + \sin\varphi(\hat{q}_\Omega + \hat{q}_{-\Omega})], \quad (3.27b)$$

$$\hat{I}_{sin} = \frac{1}{\sqrt{2}i}(e^{-i\varphi}\hat{a}_\Omega + e^{i\varphi}\hat{a}_{-\Omega}^\dagger - e^{i\varphi}\hat{a}_\Omega^\dagger - e^{-i\varphi}\hat{a}_{-\Omega}) \quad (3.27c)$$

$$= \frac{1}{\sqrt{2}}[\cos\varphi(\hat{q}_\Omega - \hat{q}_{-\Omega}) - \sin\varphi(\hat{p}_\Omega - \hat{p}_{-\Omega})], \quad (3.27d)$$

where the Hermitian canonical quadrature operators for the upper (Ω) and lower ($-\Omega$) sidebands are defined as:

$$\hat{p}_{\pm\Omega} = \hat{a}_{\pm\Omega} + \hat{a}_{\pm\Omega}^\dagger, \quad \hat{q}_{\pm\Omega} = -i(\hat{a}_{\pm\Omega} - \hat{a}_{\pm\Omega}^\dagger). \quad (3.28)$$

From Equation 3.27, we can see that the observables I_{cos} and I_{sin} depend on symmetric and antisymmetric combinations of the quadratures of the upper and lower sidebands. This motivates us to introduce the symmetric (s) and antisymmetric (a) basis for the canonical quadrature operators, defined as:

$$\hat{p}_{s,a} = \frac{\hat{p}_\Omega \pm \hat{p}_{-\Omega}}{\sqrt{2}}, \quad (3.29a)$$

$$\hat{q}_{s,a} = \frac{\hat{q}_\Omega \pm \hat{q}_{-\Omega}}{\sqrt{2}}. \quad (3.29b)$$

Rewriting Equation 3.27 in terms of the symmetric and antisymmetric basis yields:

$$\hat{I}_{cos} = \cos\varphi\hat{p}_s + \sin\varphi\hat{q}_s = \hat{x}_s^\varphi, \quad (3.30a)$$

$$\hat{I}_{sin} = \cos\varphi\hat{q}_a - \sin\varphi\hat{p}_a = \hat{x}_a^{\varphi+\frac{\pi}{2}}, \quad (3.30b)$$

we observe that the component \hat{I}_{cos} measures the symmetric mode quadratures, while \hat{I}_{sin} measures the anti-symmetric mode quadratures [107]. As noted earlier, the observables \hat{I}_{cos} and \hat{I}_{sin} commute, making it possible to measure them simultaneously. Experimentally, this measurement is performed by dividing the photocurrent into two separate components and demodulating each using electronic oscillators that are phase-shifted by $\pi/2$ (i.e., in quadrature). This process, known as quadrature demodulation [110], is illustrated in Figure 5.

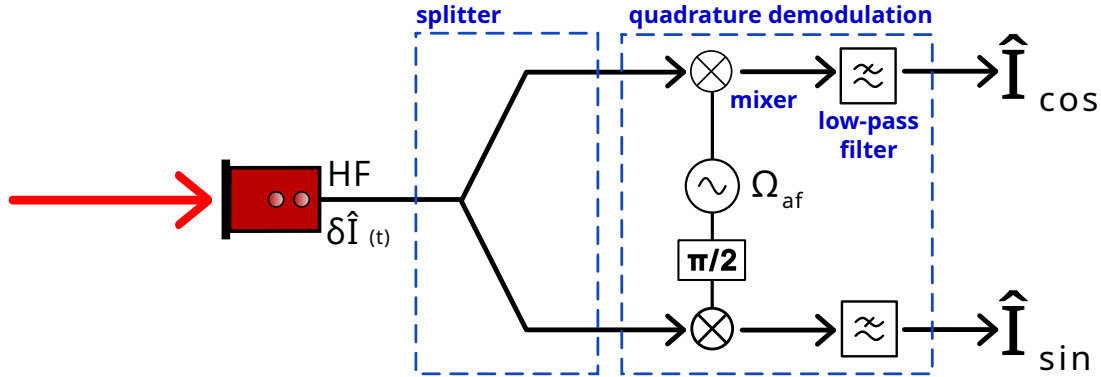


Figure 5 – Schematic of the quadrature demodulation used to simultaneously obtain the components \hat{I}_{\cos} and \hat{I}_{\sin} of the photocurrent signal. The input photocurrent is split into two paths. Each path is mixed with one of two electronic reference signals that are in quadrature, and the resulting signal then passes through a low-pass filter.

3.1.3 Spectral Noise Density and Stationary Conditions

The autocorrelation function of the temporal photocurrent fluctuation operator, defined in Equation 3.11, provides a quantitative measure of the correlations between photocurrent fluctuations at different times. It is given by [106]:

$$C_{\delta\hat{I}}(t, t') = \langle \delta\hat{I}(t)\delta\hat{I}(t') \rangle, \quad (3.31)$$

where t and t' are two points in time. This function provides insight into how the fluctuations evolve over time and their degree of temporal dependence. For a stationary process, where statistical properties remain invariant under time translation, the autocorrelation function depends only on the time difference $\tau = t - t'$. In such cases, the autocorrelation function can be written as:

$$C_{\delta\hat{I}}(\tau) = \langle \delta\hat{I}(\tau + t')\delta\hat{I}(t') \rangle, \quad \text{for any time } t'. \quad (3.32)$$

This simplification reflects the fact that the correlation does not depend on the choice of the reference time t' . In our laboratory experiment, considering the optical systems and the active stabilization controls in use, the fields are expected to exhibit stationarity during the time intervals relevant for individual measurements. This assumption can be experimentally verified and is essential for reconstructing the covariance matrix of our quantum states, as detailed later in this chapter.

According to the Wiener–Khinchin theorem, the spectral noise density $S(\Omega)$ of a stationary photocurrent, which characterizes the fluctuations in the frequency domain, is defined as the Fourier transform of the autocorrelation function [76]:

$$S(\Omega) = \int_{-\infty}^{\infty} C_{\delta\hat{I}}(\tau) e^{i\Omega\tau} d\tau. \quad (3.33)$$

The spectral noise density represents the distribution of fluctuation power across different frequencies. Using Equation 3.20, the correlation between the positive and negative frequency components of the photocurrent can be expressed in terms of the noise spectrum as follows:

$$2\pi \langle \hat{I}_{\Omega} \hat{I}_{-\Omega'} \rangle = \frac{1}{2\pi} \left\langle \int_{-\infty}^{\infty} dt e^{i\Omega t} \delta\hat{I}(t) \int_{-\infty}^{\infty} dt' e^{-i\Omega' t'} \delta\hat{I}(t') \right\rangle \quad (3.34a)$$

$$= \frac{1}{2\pi} \int_{-\infty}^{\infty} d\tau C(\tau) e^{i\Omega'\tau} \int_{-\infty}^{\infty} dt e^{it(\Omega-\Omega')} \quad (3.34b)$$

$$= S(\Omega) \delta(\Omega - \Omega'). \quad (3.34c)$$

Based on Equation 3.34, apart from a constant factor, the following conditions are satisfied for a stationary process:

$$S(\Omega) = \langle \hat{I}_{\Omega} \hat{I}_{-\Omega} \rangle \quad \text{and}, \quad (3.35a)$$

$$\langle \hat{I}_{\Omega} \hat{I}_{\Omega'} \rangle = 0 \quad \forall \quad \Omega' \neq -\Omega. \quad (3.35b)$$

In particular, it follows that stationarity imposes the condition $\langle \hat{I}_{\Omega} \hat{I}_{\Omega} \rangle = 0$. In this context, the spectral density is proportional to the total energy contained in the sideband modes. Using the relation described in Equation 3.26 together with the stationary conditions presented in Equation 3.35, we have:

$$\langle \hat{I}_{\Omega} \hat{I}_{-\Omega} \rangle = \frac{1}{2} \langle \hat{I}_{\cos}^2 \rangle + \frac{1}{2} \langle \hat{I}_{\sin}^2 \rangle \quad \text{and}, \quad (3.36a)$$

$$\langle \hat{I}_{\Omega} \hat{I}_{\Omega} \rangle = 0 \rightarrow \begin{cases} \langle \hat{I}_{\cos}^2 \rangle - \langle \hat{I}_{\sin}^2 \rangle = 0, \\ \langle \hat{I}_{\cos} \hat{I}_{\sin} \rangle = 0. \end{cases} \quad (3.36b)$$

From Equation 3.36b, it is clear that stationarity requires the absence of correlation between the spectral photocurrent quadrature components, as well as symmetry in their statistical properties.

3.1.3.1 Two-Fields Correlation and Stationary Condition

To fully characterize the quantum state formed by the two optical fields generated by the OPO, specifically the signal (s) and idler (i) fields, it is essential to analyze the correlations between the photocurrents obtained from detecting each field. These

correlations capture essential information about the quantum properties of the fields, including entanglement and coherence, and are necessary for fully reconstructing the density matrix of the composite quantum state. The cross-correlation of the spectral photocurrents corresponding to the signal and idler fields can be expressed as:

$$\langle \hat{I}_{\Omega}^{(s)} \hat{I}_{-\Omega}^{(i)} \rangle = \frac{1}{2} \langle (\hat{I}_{cos}^{(s)} + i\hat{I}_{sin}^{(s)})(\hat{I}_{cos}^{(i)} - i\hat{I}_{sin}^{(i)}) \rangle \quad (3.37a)$$

$$= \frac{1}{2} [\langle \hat{I}_{cos}^{(s)} \hat{I}_{cos}^{(i)} \rangle + \langle \hat{I}_{sin}^{(s)} \hat{I}_{sin}^{(i)} \rangle + i(\langle \hat{I}_{sin}^{(s)} \hat{I}_{cos}^{(i)} \rangle - \langle \hat{I}_{cos}^{(s)} \hat{I}_{sin}^{(i)} \rangle)]. \quad (3.37b)$$

From this, the real and imaginary parts of the cross-correlation are identified as follows:

$$Re\{\langle \hat{I}_{\Omega}^{(s)} \hat{I}_{-\Omega}^{(i)} \rangle\} = \frac{1}{2} [\langle \hat{I}_{cos}^{(s)} \hat{I}_{cos}^{(i)} \rangle + \langle \hat{I}_{sin}^{(s)} \hat{I}_{sin}^{(i)} \rangle], \quad (3.38a)$$

$$Im\{\langle \hat{I}_{\Omega}^{(s)} \hat{I}_{-\Omega}^{(i)} \rangle\} = \frac{1}{2} [\langle \hat{I}_{sin}^{(s)} \hat{I}_{cos}^{(i)} \rangle - \langle \hat{I}_{cos}^{(s)} \hat{I}_{sin}^{(i)} \rangle]. \quad (3.38b)$$

These quantities describe the coupling between the spectral components of the signal and idler fields. Notably, the real part reflects symmetric correlations, while the imaginary part captures asymmetric (phase-sensitive) correlations.

Given that the signal and idler fields are stationary, their statistical properties do not change over time. This stationarity implies that the temporal correlation between their detected photocurrents is also time-invariant:

$$C_{\delta \hat{I}}^{(s,i)}(\tau) = \langle \delta \hat{I}^{(s)}(\tau + t') \delta \hat{I}^{(i)}(t') \rangle, \quad \text{for any time } t'. \quad (3.39)$$

By extending the logic used in Equation 3.34 for the stationarity condition of a single field to the temporal correlation between the signal and idler fields, $C_{\delta \hat{I}}^{(s,i)}(\tau)$, we can derive the implications of stationarity on the correlation between their spectral photocurrent components. Thus, stationarity in both fields leads to the following conditions:

$$\langle \hat{I}_{\Omega}^{(s)} \hat{I}_{\Omega}^{(i)} \rangle = 0 \rightarrow \begin{cases} \langle \hat{I}_{cos}^{(s)} \hat{I}_{cos}^{(i)} \rangle = \langle \hat{I}_{sin}^{(s)} \hat{I}_{sin}^{(i)} \rangle, \\ \langle \hat{I}_{sin}^{(s)} \hat{I}_{cos}^{(i)} \rangle = -\langle \hat{I}_{cos}^{(s)} \hat{I}_{sin}^{(i)} \rangle. \end{cases} \quad (3.40)$$

3.1.3.2 Stationarity Analysis in the Phase-Mixing Regime

The exact measurement of the spectral photocurrent components \hat{I}_{cos} and \hat{I}_{sin} requires a well-defined phase relationship between the electronic local oscillator (eLO), used in the demodulation process, and the optical local oscillator (LO). In our experiment, this condition is not met, resulting in phase diffusion between the LO and eLO. However,

the phase diffusion is sufficiently slow to ensure that individual measurements, each taking $1.7 \mu\text{s}$, remain unaffected. As a result, each measurement still corresponds to a phase-locked pure quadrature observable, represented by a mixture of the sine and cosine electronic quadrature components as:

$$\hat{I}_\theta = \cos \theta \hat{I}_{cos} + \sin \theta \hat{I}_{sin}, \quad (3.41a)$$

$$\hat{I}_{\theta+\frac{\pi}{2}} = -\sin \theta \hat{I}_{cos} + \cos \theta \hat{I}_{sin}. \quad (3.41b)$$

However, reconstructing the quantum state requires multiple measurements to achieve reliable statistics [111]. Over this longer period, phase dispersion becomes a dominant factor, exceeding the coherence time between the LO and eLO. To account for this, the phase shift θ , in Equation 3.41, caused by dispersion is averaged during the collection of statistical data. Defining the fluctuation operator $\delta \hat{I}_\theta = \hat{I}_\theta - \langle \hat{I}_\theta \rangle$, the variance and covariance of the spectral photocurrent measured component can be written as:

$$\begin{aligned} \Delta^2 \hat{I}_\theta &= \frac{1}{2\pi} \int d\theta' \left\langle (\delta \hat{I}_{\theta+\theta'})^2 \right\rangle \\ &= \frac{1}{2} \Delta^2 \hat{I}_{cos} + \frac{1}{2} \Delta^2 \hat{I}_{sin} \quad \forall \theta, \end{aligned} \quad (3.42a)$$

$$\begin{aligned} \left\langle \delta \hat{I}_\theta \delta \hat{I}_{\theta+\frac{\pi}{2}} \right\rangle &= \frac{1}{2\pi} \int d\theta' \left\langle \delta \hat{I}_{\theta+\theta'} \delta \hat{I}_{\theta+\frac{\pi}{2}+\theta'} \right\rangle \\ &= \left\langle \delta \hat{I}_{cos} \delta \hat{I}_{sin} - \delta \hat{I}_{sin} \delta \hat{I}_{cos} \right\rangle = 0 \quad \forall \theta. \end{aligned} \quad (3.42b)$$

Here, the commutation relation $[\delta \hat{I}_\theta, \delta \hat{I}_{\theta+\pi/2}] = 0$ was applied to derive these equations. Equation 3.42 shows that in the phase-mixing regime, the stationary conditions defined in Equation 3.36 are always fulfilled. However, since this stationarity is entirely a consequence of the phase-mixing process and does not reflect any properties of the measured field itself, it cannot be used to infer that the field is stationary.

To determine the stationarity condition of the measured field, it is necessary to verify the higher-order moments of the measured spectral photocurrent components. Specifically, we analyze the Fisher's kurtosis, defined as the standardized fourth moment minus 3:

$$Kur_F[\hat{I}_\theta] = \frac{\mu_4}{\sigma^4} - 3 = \frac{\langle (\delta \hat{I}_\theta)^4 \rangle}{(\Delta^2 \hat{I}_\theta)^2} - 3, \quad (3.43)$$

where μ_4 denotes the fourth-order moment, and σ is the standard deviation of the measured photocurrent quadrature component. The Fisher's kurtosis is a diagnostic tool used to evaluate the deviation of a probability distribution from Gaussianity. If the Fisher's kurtosis is zero, it strongly indicates that the measured quantum state is Gaussian (Section 2.1.2),

except in rare cases of specific non-Gaussian states that are highly unlikely to be generated unintentionally. For a Gaussian quantum state, a null Fisher's kurtosis confirms that the phase-locked photocurrent components, \hat{I}_{cos} and \hat{I}_{sin} , satisfy the stationarity condition as described in Equation 3.36 [111]. By using this approach, we verify that the fields generated in our experimental setup under the phase-mixing regime satisfy the stationarity condition.

3.2 Covariance Matrix of Stationary Fields

Since we focus exclusively on Gaussian states in this work, the quadrature mean values and the covariance matrix together provide a complete description of our states. In the case of the fields generated by the OPO under the conditions described in Section 2.2, the sideband quadratures have zero mean values. As a result, these fields are fully characterized by their covariance matrix alone. This section explicitly presents the covariance matrix for one and two fields, using the symmetric (\mathcal{S}) and antisymmetric (\mathcal{A}) sideband basis, and relates its elements to the stationary condition. Additionally, we describe the method for transforming the covariance matrix from this basis to the lower ($-\Omega$) and upper (Ω) sideband basis.

3.2.1 Covariance Matrix of a Single Field

From our measurements, we obtain direct information about the field in both the symmetric (\mathcal{S}) and antisymmetric (\mathcal{A}) bases, as expressed in Equation 3.30. In these bases, the vector representing the quadratures for a single field can be written as:

$$\hat{\mathbf{X}}_{s/a} = [\hat{\mathbf{X}}_s; \hat{\mathbf{X}}_a] = (\hat{p}_s, \hat{q}_s, \hat{p}_a, \hat{q}_a)^T. \quad (3.44)$$

The covariance matrix in the symmetric/antisymmetric basis then takes the form:

$$\mathbf{V}_{s/a} = \frac{1}{2} \left\langle \hat{\mathbf{X}}_{s/a} \hat{\mathbf{X}}_{s/a}^T + (\hat{\mathbf{X}}_{s/a}^T \hat{\mathbf{X}}_{s/a})^T \right\rangle = \begin{pmatrix} \Delta^2 \hat{p}_s & C(\hat{p}_s \hat{q}_s) & C(\hat{p}_s \hat{p}_a) & C(\hat{p}_s \hat{q}_a) \\ C(\hat{q}_s \hat{p}_s) & \Delta^2 \hat{q}_s & C(\hat{q}_s \hat{p}_a) & C(\hat{q}_s \hat{q}_a) \\ C(\hat{p}_a \hat{p}_s) & C(\hat{p}_a \hat{q}_s) & \Delta^2 \hat{p}_a & C(\hat{p}_a \hat{q}_a) \\ C(\hat{q}_a \hat{p}_s) & C(\hat{q}_a \hat{q}_s) & C(\hat{q}_a \hat{p}_a) & \Delta^2 \hat{q}_a \end{pmatrix}, \quad (3.45)$$

where $C(\hat{a}, \hat{b}) = \langle \hat{a}\hat{b} + \hat{b}\hat{a} \rangle / 2$ is the covariance between the operators \hat{a} and \hat{b} , which reduces to $C(\hat{a}, \hat{b}) = \langle \hat{a}\hat{b} \rangle$ when the operators commute. By applying the stationarity conditions derived from Equation 3.36b into Equation 3.30, and defining specific variables for the variances and covariances of the quadratures, the covariance matrix in Equation 3.45 simplifies to:

$$\mathbf{V}_{s/a} = \begin{pmatrix} \alpha & \gamma & \delta & 0 \\ \gamma & \beta & 0 & \delta \\ \delta & 0 & \beta & -\gamma \\ 0 & \delta & -\gamma & \alpha \end{pmatrix} \equiv \begin{pmatrix} \mathbf{V}_s & \mathbf{C}_{(s/a)} \\ (\mathbf{C}_{(s/a)})^T & \mathbf{V}_a \end{pmatrix}. \quad (3.46)$$

Here, the single mode symmetric (\mathbf{V}_s) and antisymmetric (\mathbf{V}_a) covariance matrices are defined as:

$$\mathbf{V}_{s(a)} = \frac{\langle \hat{\mathbf{X}}_{s(a)} \hat{\mathbf{X}}_{s(a)}^T + (\hat{\mathbf{X}}_{s(a)}^T \hat{\mathbf{X}}_{s(a)})^T \rangle}{2}, \quad (3.47)$$

while the two-mode correlation matrix between the symmetric and antisymmetric modes $\mathbf{C}_{s/a}$, is given by:

$$\mathbf{C}_{s/a} = \langle \hat{\mathbf{X}}_s \hat{\mathbf{X}}_a^T \rangle. \quad (3.48)$$

We can see that stationarity imposes significant constraints on the structure of the symmetric/antisymmetric covariance matrix $\mathbf{V}_{s/a}$. Specifically, certain off-diagonal elements of the covariance matrix are forced to be zero. Additionally, stationarity ensures that the symmetric and antisymmetric modes (\mathbf{V}_s and \mathbf{V}_a) exhibit equivalent local quantum states, differing only by a $\pi/2$ phase rotation in the quadratures. As a result, stationarity significantly reduces the number of free parameters needed to fully characterize the covariance matrix. This reduction is not merely a simplification but an essential condition for us to achieve a complete quantum tomography of the states we manipulate in the experiment.

Based on Equation 3.29, the covariance matrix in the lower ($-\Omega$) and upper (Ω) sideband basis can be obtained by applying a unitary rotation operation. The transformation matrix Λ , which performs this rotation from the symmetric/antisymmetric (\mathcal{S}/\mathcal{A}) basis to the $\pm\Omega$ basis, is defined as:

$$\Lambda = \frac{1}{\sqrt{2}} \begin{pmatrix} 1 & 0 & -1 & 0 \\ 0 & 1 & 0 & -1 \\ 1 & 0 & 1 & 0 \\ 0 & 1 & 0 & 1 \end{pmatrix}. \quad (3.49)$$

Using this transformation, the quadrature vector in the $\pm\Omega$ basis is expressed as:

$$\hat{\mathbf{X}}_{\pm\Omega} = [\hat{\mathbf{X}}_{-\Omega}; \hat{\mathbf{X}}_{\Omega}] = (\hat{p}_{-\Omega}, \hat{q}_{-\Omega}, \hat{p}_{\Omega}, \hat{q}_{\Omega})^T = \Lambda \hat{\mathbf{X}}_{s/a}. \quad (3.50)$$

The corresponding covariance matrix in the $\pm\Omega$ basis, $\mathbf{V}_{\pm\Omega}$, is obtained via the unitary transformation applied to the covariance matrix in the symmetric/antisymmetric basis, $\mathbf{V}_{s/a}$:

$$\mathbf{V}_{\pm\Omega} = \Lambda \mathbf{V}_{s/a} \Lambda^T. \quad (3.51)$$

3.2.2 Covariance Matrix of Two Fields

For two quantum fields, the signal (s) and idler (i), we define the vector containing all the quadrature operators in the symmetric/antisymmetric \mathcal{S}/\mathcal{A} basis as:

$$\hat{\mathbf{X}}_{s/a}^{(s,i)} = [\hat{\mathbf{X}}_s^{(s)}; \hat{\mathbf{X}}_s^{(i)}; \hat{\mathbf{X}}_a^{(s)}; \hat{\mathbf{X}}_a^{(i)}] = (\hat{p}_s^{(s)}, \hat{q}_s^{(s)}, \hat{p}_s^{(i)}, \hat{q}_s^{(i)}, \hat{p}_a^{(s)}, \hat{q}_a^{(s)}, \hat{p}_a^{(i)}, \hat{q}_a^{(i)})^T. \quad (3.52)$$

The covariance matrix of this composite quantum state can be expressed as a block matrix [112]:

$$\mathbf{V}_{s/a}^{(s,i)} = \begin{pmatrix} \mathbf{V}_s^{(s,i)} & \mathbf{C}_{s/a}^{(s,i)} \\ \mathbf{C}_{s/a}^{(s,i)T} & \mathbf{V}_a^{(s,i)} \end{pmatrix}. \quad (3.53)$$

In this expression, $\mathbf{V}_s^{(s,i)}$ represents the symmetric covariance block, which contains correlations within the symmetric quadratures, while $\mathbf{V}_a^{(s,i)}$ describes the antisymmetric covariance block. The off-diagonal block $\mathbf{C}_{s/a}^{(s,i)}$ captures the cross-correlations between symmetric and antisymmetric quadratures.

Using the stationary conditions for single fields (Equation 3.36) and two fields correlations (Equation 3.40), together with the covariance element symbols defined in Equation 3.46 and defining additional symbols to represent the covariances between the two fields, the symmetric covariance matrix is expressed as:

$$\mathbf{V}_s^{(s,i)} = \frac{1}{2} \left\langle \hat{\mathbf{X}}_s^{(s,i)} (\hat{\mathbf{X}}_s^{(s,i)})^T + [(\hat{\mathbf{X}}_s^{(s,i)})^T \hat{\mathbf{X}}_s^{(s,i)}]^T \right\rangle \quad (3.54a)$$

$$= \begin{pmatrix} \Delta^2 \hat{p}_s^{(s)} & C(\hat{p}_s^{(s)} \hat{q}_s^{(s)}) & C(\hat{p}_s^{(s)} \hat{p}_s^{(i)}) & C(\hat{p}_s^{(s)} \hat{q}_s^{(i)}) \\ C(\hat{q}_s^{(s)} \hat{p}_s^{(s)}) & \Delta^2 \hat{q}_s^{(s)} & C(\hat{q}_s^{(s)} \hat{p}_s^{(i)}) & C(\hat{q}_s^{(s)} \hat{q}_s^{(i)}) \\ C(\hat{p}_s^{(i)} \hat{p}_s^{(s)}) & C(\hat{p}_s^{(i)} \hat{q}_s^{(s)}) & \Delta^2 \hat{p}_s^{(i)} & C(\hat{p}_s^{(i)} \hat{q}_s^{(i)}) \\ C(\hat{q}_s^{(i)} \hat{p}_s^{(s)}) & C(\hat{q}_s^{(i)} \hat{q}_s^{(s)}) & C(\hat{q}_s^{(i)} \hat{p}_s^{(i)}) & \Delta^2 \hat{q}_s^{(i)} \end{pmatrix} \quad (3.54b)$$

$$= \begin{pmatrix} \alpha^{(s)} & \gamma^{(s)} & \mu & \xi \\ \gamma^{(s)} & \beta^{(s)} & \zeta & \nu \\ \mu & \zeta & \alpha^{(i)} & \gamma^{(i)} \\ \xi & \nu & \gamma^{(i)} & \beta^{(i)} \end{pmatrix} = \begin{pmatrix} \mathbf{V}_s^{(s)} & \mathbf{C}_s^{(s,i)} \\ (\mathbf{C}_s^{(s,i)})^T & \mathbf{V}_s^{(i)} \end{pmatrix}. \quad (3.54c)$$

Following a structure analogous to the symmetric covariance matrix, the antisymmetric covariance matrix, $\mathbf{V}_a^{(s,i)}$, is given by:

$$\mathbf{V}_a^{(s,i)} = \frac{1}{2} \left\langle \hat{\mathbf{X}}_a^{(s,i)} (\hat{\mathbf{X}}_a^{(s,i)})^T + [(\hat{\mathbf{X}}_a^{(s,i)})^T \hat{\mathbf{X}}_a^{(s,i)}]^T \right\rangle \quad (3.55a)$$

$$= \begin{pmatrix} \Delta^2 \hat{p}_a^{(s)} & C(\hat{p}_a^{(s)} \hat{q}_a^{(s)}) & C(\hat{p}_a^{(s)} \hat{p}_a^{(i)}) & C(\hat{p}_a^{(s)} \hat{q}_a^{(i)}) \\ C(\hat{q}_a^{(s)} \hat{p}_a^{(s)}) & \Delta^2 \hat{q}_a^{(s)} & C(\hat{q}_a^{(s)} \hat{p}_a^{(i)}) & C(\hat{q}_a^{(s)} \hat{q}_a^{(i)}) \\ C(\hat{p}_a^{(i)} \hat{p}_a^{(s)}) & C(\hat{p}_a^{(i)} \hat{q}_a^{(s)}) & \Delta^2 \hat{p}_a^{(i)} & C(\hat{p}_a^{(i)} \hat{q}_a^{(i)}) \\ C(\hat{q}_a^{(i)} \hat{p}_a^{(s)}) & C(\hat{q}_a^{(i)} \hat{q}_a^{(s)}) & C(\hat{q}_a^{(i)} \hat{p}_a^{(i)}) & \Delta^2 \hat{q}_a^{(i)} \end{pmatrix} \quad (3.55b)$$

$$= \begin{pmatrix} \beta^{(s)} & -\gamma^{(s)} & \nu & -\zeta \\ -\gamma^{(s)} & \alpha^{(s)} & -\xi & \mu \\ \nu & -\xi & \beta^{(i)} & -\gamma^{(i)} \\ -\zeta & \mu & -\gamma^{(i)} & \alpha^{(i)} \end{pmatrix} = \begin{pmatrix} \mathbf{V}_a^{(s)} & \mathbf{C}_a^{(s,i)} \\ (\mathbf{C}_a^{(s,i)})^T & \mathbf{V}_a^{(i)} \end{pmatrix}. \quad (3.55c)$$

The cross-correlation matrix $\mathbf{C}_{s/a}^{(s,i)}$ contains the covariances between the symmetric and antisymmetric quadratures. It is expressed as:

$$\mathbf{C}_{s/a}^{(s,i)} = \left\langle \hat{\mathbf{X}}_s^{(s,i)} (\hat{\mathbf{X}}_a^{(s,i)})^T \right\rangle \quad (3.56a)$$

$$= \begin{pmatrix} C(\hat{p}_s^{(s)} \hat{p}_a^{(s)}) & C(\hat{p}_s^{(s)} \hat{q}_a^{(s)}) & C(\hat{p}_s^{(s)} \hat{p}_a^{(i)}) & C(\hat{p}_s^{(s)} \hat{q}_a^{(i)}) \\ C(\hat{q}_s^{(s)} \hat{p}_a^{(s)}) & C(\hat{q}_s^{(s)} \hat{q}_a^{(s)}) & C(\hat{q}_s^{(s)} \hat{p}_a^{(i)}) & C(\hat{q}_s^{(s)} \hat{q}_a^{(i)}) \\ C(\hat{p}_s^{(i)} \hat{p}_a^{(s)}) & C(\hat{p}_s^{(i)} \hat{q}_a^{(s)}) & C(\hat{p}_s^{(i)} \hat{p}_a^{(i)}) & C(\hat{p}_s^{(i)} \hat{q}_a^{(i)}) \\ C(\hat{q}_s^{(i)} \hat{p}_a^{(s)}) & C(\hat{q}_s^{(i)} \hat{q}_a^{(s)}) & C(\hat{q}_s^{(i)} \hat{p}_a^{(i)}) & C(\hat{q}_s^{(i)} \hat{q}_a^{(i)}) \end{pmatrix} \quad (3.56b)$$

$$= \begin{pmatrix} \delta^{(s)} & 0 & \kappa & -\eta \\ 0 & \delta^{(s)} & \tau & -\lambda \\ -\lambda & \eta & \delta^{(i)} & 0 \\ -\tau & \kappa & 0 & \delta^{(i)} \end{pmatrix}. \quad (3.56c)$$

Once again, the stationary condition proves essential in simplifying the structure of the covariance matrix. It forces certain elements to vanish and imposes well-defined relationships among the remaining terms. This leads to a drastic simplification of the parameter space, reducing the number of independent parameters required to describe the two-field quantum state covariance matrix from 36 to 16.

To obtain the covariance matrix in the lower ($-\Omega$) and upper (Ω) sideband basis, we use again the definition provided in Equation 3.29 to construct the unitary rotation transformation:

$$\Lambda^{(s,i)} = \frac{1}{\sqrt{2}} \begin{pmatrix} I_4 & -I_4 \\ I_4 & I_4 \end{pmatrix}, \quad (3.57)$$

where I_4 represents the 4×4 identity matrix. This transformation maps the quadrature vector from the symmetric/antisymmetric (\mathcal{S}/\mathcal{A}) basis to the lower/upper sideband ($(\pm\Omega)$) basis, expressed as:

$$\hat{\mathbf{X}}_{\pm\Omega}^{(s,i)} = [\hat{\mathbf{X}}_{-\Omega}^{(s)}; \hat{\mathbf{X}}_{-\Omega}^{(i)}; \hat{\mathbf{X}}_{\Omega}^{(s)}; \hat{\mathbf{X}}_{\Omega}^{(i)}] = (\hat{p}_{-\Omega}^{(s)}, \hat{q}_{-\Omega}^{(s)}, \hat{p}_{-\Omega}^{(i)}, \hat{q}_{-\Omega}^{(i)}, \hat{p}_{\Omega}^{(s)}, \hat{q}_{\Omega}^{(s)}, \hat{p}_{\Omega}^{(i)}, \hat{q}_{\Omega}^{(i)})^T = \boldsymbol{\Lambda} \hat{\mathbf{X}}_{s/a}^{(s,i)}. \quad (3.58)$$

Using this transformation, the covariance matrix in the $\pm\Omega$ basis is given by:

$$\mathbf{V}_{\pm\Omega}^{(s,i)} = \boldsymbol{\Lambda}^{(s,i)} \mathbf{V}_{s/a}^{(s,i)} (\boldsymbol{\Lambda}^{(s,i)})^T. \quad (3.59)$$

3.2.3 Semiclassical Quadratures and Spectral Matrix

In this section, we present the semiclassical quadratures, derived by treating the photocurrent as a semiclassical quantity. The quadratures are defined by directly imposing a single-mode interpretation onto the spectral photocurrent [107, 113]. This approach is justified by the observation that, apart from a local phase rotation, the \mathcal{S} and \mathcal{A} modes exhibit identical quantum statistical properties in a stationary state, as shown in Equation 3.46. By enforcing the single-mode structure in the spectral photocurrent in Equation 3.21, we arrive at the following relation:

$$\hat{I}_{\pm\Omega} = \cos \varphi \hat{P}_{\pm\Omega} + \sin \varphi \hat{Q}_{\pm\Omega}, \quad (3.60)$$

where $\hat{P}_{\pm\Omega}$ and $\hat{Q}_{\pm\Omega}$ are the semiclassical quadrature operators. By comparing this definition with Equations 3.21 and 3.30, we can derive the relationship between these new quadratures and the canonical quadratures of the sidebands in the \mathcal{S}/\mathcal{A} modes:

$$\hat{P}_{\pm\Omega} = \frac{\hat{p}_s \pm i\hat{q}_a}{\sqrt{2}}, \quad \hat{Q}_{\pm\Omega} = \frac{\hat{q}_s \mp i\hat{p}_a}{\sqrt{2}}, \quad \hat{X}_{\pm\Omega}^{\varphi} = \frac{\hat{x}_s^{\varphi} \pm i\hat{x}_a^{\varphi+\frac{\pi}{2}}}{\sqrt{2}}. \quad (3.61)$$

From these expressions, we observe that $\hat{P}_{\pm\Omega}$ and $\hat{Q}_{\pm\Omega}$ are non-Hermitian operators, representing mixtures of individual sideband quadratures.

Despite being non-Hermitian, the defined operators behave as effective single-mode quadrature operators when describing the spectral noise density and second-order moments in general. The amplitude and phase quadrature noise spectra, expressed in terms of the proper quadratures of the sidebands, are given by:

$$S_P(\Omega) \equiv \langle \hat{P}_\Omega \hat{P}_{-\Omega} \rangle = \frac{1}{2} \Delta^2 \hat{p}_s + \frac{1}{2} \Delta^2 \hat{q}_a, \quad (3.62a)$$

$$S_Q(\Omega) \equiv \langle \hat{Q}_\Omega \hat{Q}_{-\Omega} \rangle = \frac{1}{2} \Delta^2 \hat{p}_a + \frac{1}{2} \Delta^2 \hat{q}_s, \quad (3.62b)$$

where it is assumed that the quadratures have zero mean value. From these expressions, we observe that, despite $[\hat{P}_{\pm\Omega}, \hat{Q}_{\pm\Omega}] = 0$, the noise spectra $S_P(\Omega)$ and $S_Q(\Omega)$ satisfy the effective uncertainty relation $S_P(\Omega)S_Q(\Omega) \geq 1$. Therefore, considering only second-order moments, these operators exhibit behavior analogous to quadrature operators and can be treated as such. Similarly, the spectral density of the covariance between $\hat{P}_{\pm\Omega}$ and $\hat{Q}_{\pm\Omega}$ is defined as:

$$\begin{aligned} C_{PQ}(\Omega) &\equiv \frac{1}{2} \langle \hat{P}_\Omega \hat{Q}_{-\Omega} + \hat{Q}_{-\Omega} \hat{P}_\Omega \rangle \\ &= \frac{1}{2} \{C(\hat{p}_s \hat{q}_s) - C(\hat{p}_a \hat{q}_a) + i[C(\hat{p}_s \hat{p}_a) + C(\hat{q}_s \hat{q}_a)]\}. \end{aligned} \quad (3.63)$$

Here, we note that the spectral density of the covariance is generally a complex quantity, satisfying the relation $C_{PQ}(\Omega) = C_{PQ}^*(-\Omega)$. The real part of this covariance is associated with single-mode correlations, while its imaginary part reflects the correlations between the \mathcal{S} and \mathcal{A} modes. Notably, these cross-mode covariances ($C(\hat{p}_s \hat{p}_a)$ and $C(\hat{q}_s \hat{q}_a)$) cannot be accessed through standard homodyne detection when characterizing the quantum state in a single beam.

For a single field, we define the vectors of the semi-classical quadratures as follows:

$$\hat{Z}_{\pm\Omega} = (\hat{P}_{\pm\Omega}, \hat{Q}_{\pm\Omega})^T. \quad (3.64)$$

Using this representation, we define the Hermitian complex **spectral matrix**, which contains these second-order moments, similar to a covariance matrix. The spectral matrix is given by:

$$\mathbf{S} \equiv \langle \hat{Z}_\Omega \hat{Z}_{-\Omega}^T \rangle = \begin{pmatrix} S_P(\Omega) & C_{PQ}(\Omega) \\ C_{PQ}^*(\Omega) & S_Q(\Omega) \end{pmatrix}. \quad (3.65)$$

Unlike the usual covariance matrix, the spectral matrix is constructed from the semiclassical quantities of the photocurrent noise rather than the quantum observables of the field. Its real part can be expressed in terms of the covariance matrices of the \mathcal{S} and \mathcal{A} modes:

$$\text{Re}[\mathbf{S}] = \frac{1}{2} \mathbf{V}_s + \frac{1}{2} \mathbf{V}'_a, \quad (3.66)$$

where \mathbf{V}'_a is the single-field covariance matrix of mode \mathcal{A} , incorporating a local $\pi/2$ rotation (i.e., $\hat{p}'_a = \hat{q}_a$ and $\hat{q}'_a = -\hat{p}_a$). For stationary states, we have $\mathbf{V}_s = \mathbf{V}'_a$, and using Equation 3.46, the spectral matrix can be written as:

$$\mathbf{S} = \begin{pmatrix} \alpha & \gamma \\ \gamma & \beta \end{pmatrix} + i \begin{pmatrix} 0 & \delta \\ -\delta & 0 \end{pmatrix}. \quad (3.67)$$

Due to its complex nature, the spectral matrix \mathbf{S} does not generally correspond to a valid covariance matrix. This implies that, in most cases, the single-mode approximation of the sideband modes is not valid, necessitating a two-mode treatment. However, in the special case where $\delta = 0$, the spectral matrix can be formally interpreted as a valid covariance matrix, and the sidebands can be treated as a single mode without any loss of generality.

The states generated by an optical parametric oscillator (OPO) under standard operating conditions (Section 2.2) exhibit $\delta = 0$. This characteristic is also shared by the states we utilize in the teleportation protocol execution. Experimentally, this property can be verified using the resonator-assisted detection scheme implemented in our setup. As a result, the single-mode approximation can be applied to describe the sideband modes of these states. This approach not only simplifies the theoretical analysis but also reduces the number of parameters necessary to describe the teleportation protocol, making the treatment more efficient and manageable. However, it is important to emphasize that our experimental system teleports the individual sidebands and is capable of sideband-resolving measurements; the single-mode treatment is a mathematical convenience enabled by the symmetric nature of the states we generate.

Expanding the discussion to two fields, we define the semi-classical quadrature vector as:

$$\hat{Z}_{\pm\Omega}^{(s,i)} = (\hat{P}_{\pm\Omega}^{(s)}, \hat{Q}_{\pm\Omega}^{(s)}, \hat{P}_{\pm\Omega}^{(i)}, \hat{Q}_{\pm\Omega}^{(i)})^T. \quad (3.68)$$

Following the same strategy used for the single field case, the spectral matrix for two fields is defined as:

$$\mathbf{S}^{(s,i)} \equiv \left\langle \hat{Z}_{\Omega}^{(s,i)} \left(\hat{Z}_{-\Omega}^{(s,i)} \right)^T \right\rangle = \begin{pmatrix} \mathbf{S}^{(s)} & \mathbf{C}_{\mathbf{S}}^{(s,i)} \\ \mathbf{C}_{\mathbf{S}}^{(i,s)} & \mathbf{S}^{(i)} \end{pmatrix}. \quad (3.69)$$

Explicitly incorporating the covariance matrix elements introduced in previous sections, the spectral matrix takes the form:

$$\mathbf{S}^{(s,i)} = \begin{pmatrix} \alpha^{(s)} & \gamma^{(s)} & \mu & \xi \\ \gamma^{(s)} & \beta^{(s)} & \zeta & \nu \\ \beta & \zeta & \alpha^{(i)} & \gamma^{(i)} \\ \xi & \nu & \gamma^{(i)} & \beta^{(i)} \end{pmatrix} + i \begin{pmatrix} 0 & \delta^{(s)} & \eta & \kappa \\ -\delta^{(s)} & 0 & \lambda & \tau \\ -\eta & -\lambda & 0 & \delta^{(i)} \\ -\kappa & -\tau & -\delta^{(i)} & 0 \end{pmatrix}. \quad (3.70)$$

As before, correlations between the \mathcal{S} and \mathcal{A} modes appear exclusively in the imaginary part of the spectral matrix. The two-field covariance matrix for sideband modes in the \mathcal{S}/\mathcal{A} basis, denoted by $\mathbf{V}_{s/a'}$ (Equation 3.53, including the $\pi/2$ local rotation in the \mathcal{A} mode), can be expressed in terms of the spectral matrix blocks as:

$$\mathbf{V}_{s/a'} = \begin{pmatrix} \text{Re}[\mathbf{S}^{(s,i)}] & -\text{Im}[\mathbf{S}^{(s,i)}] \\ \text{Im}[\mathbf{S}^{(s,i)}] & \text{Re}[\mathbf{S}^{(s,i)}] \end{pmatrix}. \quad (3.71)$$

If correlations confined to symmetric and antisymmetric modes only, the imaginary part of \mathcal{S} becomes zero. In this scenario, the spectral matrix satisfies the conditions of a valid covariance matrix and contains all the information of the four-mode covariance matrix $\mathbf{V}_{s/a'}$. As a result, the spectral matrix can be used to describe the quantum state of both fields in a significantly simplified way, effectively halving the dimensionality of the associated Hilbert space. For such states, the spectral matrix is equivalent to the partial trace over either the \mathcal{S} or \mathcal{A} modes

Throughout this work, the quadrature operators introduced in this section will be denoted by uppercase symbols, and the corresponding mode will be referred to as the **single sideband mode** or **composed sideband mode**. By contrast, the lowercase symbols represent quadratures of the **two sideband modes**, also referred to as the **individual sideband modes**.

3.3 Auto-Homodyne Resonator Detection Scheme

In the continuous-variable regime, measuring the quadratures of a quantum state with a low photon population density requires transforming and amplifying the weak quadrature fluctuations into detectable intensity signals. A widely employed technique achieves this by utilizing an intense optical local oscillator (LO). The interference, or "beat," between the LO and the quantum field being measured effectively amplifies and converts the quadrature signals from the nearby frequency modes, particularly in the sidebands, into intensity signals suitable for detection. The local oscillator must maintain a well-defined phase relationship with the modes being measured. This phase coherence is crucial to distinguish and access the orthogonal quadratures of the quantum state individually, avoiding undesired mixing between them. Additionally, the phase difference φ between

the local oscillator and the quantum state must be precisely controlled to allow selective measurement of the orthogonal canonical quadratures. As illustrated in Equation 3.30, the spectral photocurrent components are expressed in terms of the sideband quadratures, with the phase φ determining which quadrature is accessed during the measurement.

Homodyne detection is the most widely used method to measure quantum quadrature fluctuations [100]. This method uses an external optical local oscillator that shares the same frequency as the field containing the quantum state. The two beams are mixed on a beam splitter, and the two outputs are directed to photodetectors. The difference between the photocurrents is then taken to obtain a signal proportional to the measured field's quadrature. To access both orthogonal quadratures, the phase difference φ between the LO and the quantum field is scanned, typically by adjusting the phase of the LO using a piezoelectric transducer (PZT) in the LO's optical path.

Despite its conceptual simplicity, the practical implementation of a homodyne detection scheme can become challenging in certain situations. One of the main difficulties lies in producing a local oscillator (LO) beam that maintains a stable and precise phase relationship with the quantum field being measured. Additionally, the LO must be carefully matched to the quantum field in all relevant degrees of freedom. For instance, the optical frequency of the LO must align precisely with that of the quantum field to ensure coherent interference. Similarly, the spatial mode structure of the LO beam, such as its transverse profile, must coincide with the quantum field's mode. Furthermore, the homodyne detection cannot measure the parameter δ of the covariance matrix (Equation 3.46), which is defined as $2\delta = (\Delta^2 \hat{p}_\Omega + \Delta^2 \hat{q}_\Omega) - (\Delta^2 \hat{p}_{-\Omega} + \Delta^2 \hat{q}_{-\Omega})$, representing the energy imbalance between the sideband modes. Since δ is inaccessible through homodyne detection, the technique is inherently limited in its ability to perform a complete tomography of a Gaussian state. Therefore, it is typically necessary to make the *a priori* assumption that the parameter δ is zero, implying symmetry in the energy distribution between the sideband modes [107]. This assumption simplifies the analysis but may restrict the generality of the conclusions drawn from the measurements.

In our system, the quantum states reside in the sidebands of bright optical fields generated by the OPO operating above the oscillation threshold. This configuration allows us to use the carrier field as a local oscillator to measure the quadratures of the sidebands. Since the carrier and the sidebands share a well-defined phase relationship, direct detection of the field provides information about a fixed quadrature of the sidebands, naturally aligned with the complex amplitude of the carrier. When there is no phase shift between the carrier and the sidebands, corresponding to a phase difference of $\varphi = 0$ in Equation 3.30, the measured quadrature is defined as the amplitude quadrature \hat{P} , which is composed of the symmetric \hat{p}_s and antisymmetric \hat{q}_a quadratures, as shown in Equation 3.61. To access information about the orthogonal quadrature, the phase quadrature \hat{Q} , it is necessary to

vary the phase difference φ between the carrier and the sidebands.

To achieve this, we implement the auto-homodyne resonator detection scheme. This method exploits the dispersive properties of the resonator, referred to as the analysis cavity, to manipulate the relative phase between the carrier and the sidebands. Additionally, the intrinsic losses of the resonator introduce asymmetry between the sideband modes, enabling the measurement of δ parameter. By accessing δ , the auto-homodyne scheme enables the reconstruction of the entire covariance matrix of the system without requiring any prior assumptions about the sidebands energy balance [103, 112]. In this section, we describe the procedure for extracting the elements of the covariance matrix using the auto-homodyne detection technique.

The transformation of the annihilation operator describing an incident optical field reflected by an optical resonator is expressed as [114]:

$$\hat{a}_\omega \rightarrow r(\Delta_\omega)\hat{a}_\omega + t(\Delta_\omega)\hat{v}_\omega, \quad (3.72)$$

where \hat{a}_ω is the annihilation operator of the incident field at frequency ω , and \hat{v}_ω is the annihilation operator of the mode, described by a vacuum state, coupled through the resonator's optical losses at the same frequency. The parameter Δ_ω describes the detuning of the field's mode frequency ω from the resonance frequency of the optical resonator ω_{acav} , normalized by the bandwidth of the resonator $\Delta\omega_{acav}$, expressed as $\Delta_\omega = (\omega - \omega_{acav})/\Delta\omega_{acav}$. The functions $r(\Delta_\omega)$ and $t(\Delta_\omega)$ represent the reflection and transmission coefficients of the cavity, respectively, as functions of the detuning. These coefficients are constrained by energy conservation, which requires that $|r(\Delta_\omega)|^2 + |t(\Delta_\omega)|^2 = 1$. For a high-finesse resonator, the reflection coefficient takes the form [100]:

$$r(\Delta_\omega) = -\frac{\sqrt{d} + 2i\Delta_\omega}{1 - 2i\Delta_\omega}, \quad (3.73)$$

where the parameter $d = |r(0)|^2$ is the impedance matching factor. This parameter quantifies the fraction of the field reflected when the system is precisely on resonance, i.e., when $\Delta_\omega = 0$.

The carrier mode of an optical field can be described by a coherent state, $\hat{a}_{\omega_0}|\alpha_{\omega_0}\rangle = |\alpha_{\omega_0}|e^{i\varphi}|\alpha_{\omega_0}\rangle$, as discussed in Section 3.1. When the carrier is reflected by the resonator, the effect on its state can be described by a transformation of its amplitude, $\alpha_{\omega_0} \rightarrow r(\Delta_{\omega_0})\alpha_{\omega_0}$. This transformation directly affects the phase φ of the carrier, as described by:

$$e^{i\varphi} \rightarrow \frac{r(\Delta_{\omega_0})}{|r(\Delta_{\omega_0})|}e^{i\varphi}. \quad (3.74)$$

The resonator interacts with both the carrier mode and the sideband modes of the incident optical field. To describe the resulting photocurrent generated by a measurement of the reflected field in terms of the incident field, we must account for how the resonator transforms these modes. This involves updating the spectral photocurrent described in Equation 3.21 by applying the resonator's reflection transformation for the sideband modes (Equation 3.72) and the phase shift experienced by the carrier (Equation 3.74). In this treatment, we do not consider the attenuation of the carrier, as only its phase shift is relevant for quadrature detection, provided its optical power far exceeds that of the sidebands. Using the simplified notation introduced earlier, $\hat{a}_\Omega = \hat{a}_{\Omega+\omega_0}$ (Equation 3.11), the spectral photocurrent operator for the reflected bright field is given by:

$$\hat{I}_\Omega = \frac{r^*(\Delta)}{|r(\Delta)|} e^{-i\varphi} (r(\Delta_\Omega) \hat{a}_\Omega + t(\Delta_\Omega) \hat{v}_\Omega) + \frac{r(\Delta)}{|r(\Delta)|} e^{i\varphi} (r^*(\Delta_{-\Omega}) \hat{a}_{-\Omega}^\dagger + t^*(\Delta_{-\Omega}) \hat{v}_{-\Omega}^\dagger), \quad (3.75)$$

where, to simplify the notation, $\Delta = \Delta_{\omega_0}$ represents the normalized detuning of the carrier, and $\Delta_{\pm\Omega} = \Delta \pm (\Omega/\Delta\omega_{acav})$ are the normalized detunings of the sidebands relative to the cavity resonance frequency.

To simplify the expressions appearing in Equation 3.75, we introduce the following functions:

$$R_{\pm\Omega}(\Delta) = \frac{r^*(\Delta)}{|r(\Delta)|} r \left(\Delta \pm \frac{\Omega}{\Delta\omega_{acav}} \right), \quad (3.76a)$$

$$T_{\pm\Omega}(\Delta) = \frac{r^*(\Delta)}{|r(\Delta)|} t \left(\Delta \pm \frac{\Omega}{\Delta\omega_{acav}} \right). \quad (3.76b)$$

The function $R_{\pm\Omega}(\Delta)$ captures the resonator's effect on the upper and lower sidebands, describing both their attenuation and the relative phase shift with respect to the carrier. On the other hand, $T_{\pm\Omega}(\Delta)$ accounts for the coupling between the vacuum fluctuations and the sidebands, induced by the resonator's losses and transmission. Using these definitions, we construct the auxiliary functions g_\pm to represent the symmetric and antisymmetric contributions to the photocurrent. These functions are given by:

$$g_+ = x_+ + iy_+ = \frac{R_\Omega(\Delta) + R_{-\Omega}^*(\Delta)}{2}, \quad (3.77a)$$

$$g_- = x_- + iy_- = \frac{i(R_\Omega(\Delta) - R_{-\Omega}^*(\Delta))}{2}, \quad (3.77b)$$

$$g_+^v = x_+^v + iy_+^v = \frac{T_\Omega(\Delta) + T_{-\Omega}^*(\Delta)}{2}, \quad (3.77c)$$

$$g_-^v = x_-^v + iy_-^v = \frac{i(T_\Omega(\Delta) - T_{-\Omega}^*(\Delta))}{2}. \quad (3.77d)$$

Here, x_{\pm} and y_{\pm} are the real and imaginary components of g_{\pm} . Substituting the definitions from Equations 3.76 and 3.77 into the spectral photocurrent (Equation 3.75) and applying the symmetric and antisymmetric quadrature definition (Equation 3.29), the spectral photocurrent operator can be written as:

$$\begin{aligned}\hat{I}_{\Omega} &= \frac{1}{\sqrt{2}} [(x_+ \hat{p}_s + x_- \hat{q}_s + y_- \hat{p}_a - y_+ \hat{q}_a) + i(y_+ \hat{p}_s + y_- \hat{q}_s - x_- \hat{p}_a + x_+ \hat{q}_a)] \\ &\quad + \frac{1}{\sqrt{2}} [(x_+^v \hat{p}_s^v + x_-^v \hat{q}_s^v + y_-^v \hat{p}_a^v - y_+^v \hat{q}_a^v) + i(y_+^v \hat{p}_s^v + y_-^v \hat{q}_s^v - x_-^v \hat{p}_a^v + x_+^v \hat{q}_a^v)].\end{aligned}\quad (3.78)$$

where the superscript v indicates operators and coefficients associated with the mode in vacuum \hat{v} , which couples to the field of interest through the resonator's transmission and losses. This formulation expresses the spectral photocurrent in terms of the symmetric and antisymmetric quadratures of the sidebands.

By comparing Equation 3.78 with the previously derived Equation 3.26, we can identify the electronic quadrature components associated with both the vacuum and the measured sideband modes, expressed in the form:

$$\hat{I}_{\Omega} = \frac{\hat{I}_{cos} + i\hat{I}_{sin}}{\sqrt{2}} + \hat{I}_v = \frac{\hat{I}_{cos} + i\hat{I}_{sin}}{\sqrt{2}} + \frac{\hat{I}_{cos}^v + i\hat{I}_{sin}^v}{\sqrt{2}}.\quad (3.79)$$

The quadratures of the measured field are explicitly given by:

$$\hat{I}_{cos} = x_+ \hat{p}_s + x_- \hat{q}_s + y_- \hat{p}_a - y_+ \hat{q}_a,\quad (3.80a)$$

$$\hat{I}_{sin} = y_+ \hat{p}_s + y_- \hat{q}_s - x_- \hat{p}_a + x_+ \hat{q}_a.\quad (3.80b)$$

The vacuum contributions, \hat{I}_{cos}^v and \hat{I}_{sin}^v , share the same structure, as can be seen in Equation 3.78. The observables \hat{I}_{cos} and \hat{I}_{sin} depend on all quadratures of the sideband field in the \mathcal{S}/\mathcal{A} basis, enabling a complete tomography of the measured Gaussian state.

3.3.1 Quadrature Mean Values in Auto-Homodyne Detection

The quadratures of the fields generated by the OPO exhibit a zero mean value under normal operating conditions. In the context of the teleportation protocol, however, the objective is to teleport a coherent state, with a nonzero quadrature mean values. This input state is generated during the protocol execution and directly affects the measurements at both the sender and receiver stations. Therefore, it becomes crucial to accurately extract the mean values of the quadratures from the experimentally measured observables. Since the quadratures of the vacuum field have a mean value of zero, $\langle \hat{I}_v \rangle = 0$, the mean values

of the quadratures for the states of interest can be directly inferred from the measured photocurrent observables through the relationships derived in Equation 3.80.

The mean values of the demodulated quadrature components relate to the mean quadratures of the two sideband modes in the \mathcal{S}/\mathcal{A} basis as follows:

$$\langle \hat{I}_{cos} \rangle = x_+ \langle \hat{p}_s \rangle + x_- \langle \hat{q}_s \rangle + y_- \langle \hat{p}_a \rangle - y_+ \langle \hat{q}_a \rangle, \quad (3.81a)$$

$$\langle \hat{I}_{sin} \rangle = y_+ \langle \hat{p}_s \rangle + y_- \langle \hat{q}_s \rangle - x_- \langle \hat{p}_a \rangle + x_+ \langle \hat{q}_a \rangle. \quad (3.81b)$$

By analyzing the average demodulated photocurrent signals, the sideband quadratures' mean values can be obtained, which are essential for characterizing the teleportation protocol. To convert these mean values from the symmetric/antisymmetric basis to the lower/upper sideband basis, we can use the rotation transformation presented in Equation 3.49.

3.3.2 Quantum Tomography of a Single Field

The spectral noise density of a single stationary field, as measured through the resonator-assisted detection scheme, can be derived using Equations 3.35 and 3.79. Specifically, the noise spectral density, $S(\Omega)$, can be expressed as:

$$S(\Omega) = \langle \hat{I}_\Omega \hat{I}_{-\Omega} \rangle \quad (3.82a)$$

$$= \frac{1}{2} \Delta^2 \hat{I}_{cos} + \frac{1}{2} \Delta^2 \hat{I}_{sin} + \Delta^2 \hat{I}_v, \quad (3.82b)$$

where it was assumed that the spectral photocurrent components have a mean value of zero. To describe the photocurrent components in terms of the two sideband mode quadratures in the \mathcal{S}/\mathcal{A} basis, we use the relation presented in Equation 3.80. By further incorporating the g_\pm functions defined in Equation 3.77 and applying the stationarity conditions (Equation 3.36b), the spectral noise density can be reformulated. This results in a simplified expression that depends directly on the covariance matrix elements, as defined in Equation 3.46:

$$S(\Omega) = c_\alpha \alpha + c_\beta \beta + c_\gamma \gamma + c_\delta \delta + c_v, \quad (3.83)$$

where the coefficients c_α , c_β , c_γ , c_δ and c_v describe the relation between the field-resonator interaction and the quantum state's covariance elements within the detected noise. These parameters are explicitly defined as:

$$\begin{aligned}
c_\alpha &= |g_+|^2, & c_\beta &= |g_-|^2, \\
c_\gamma &= 2\text{Re}[g_+^* g_-], & c_\delta &= 2\text{Im}[g_+^* g_-], \\
c_v &= 1 - c_\alpha - c_\beta.
\end{aligned} \tag{3.84}$$

These coefficients are functions of the cavity detuning Δ , the analysis frequency Ω , and specific properties of the resonator, such as its impedance matching and bandwidth. Figure 6 illustrates the behavior of these c -coefficients in terms of the normalized detuning Δ . For this simulation, the analysis frequency is set to $\Omega = 2\pi \times 15$ MHz, with a resonator bandwidth of $\Delta\omega_{acav} = 2\pi \times 6$ MHz, leading to a frequency ratio of $\Omega/\Delta\omega_{acav} = 2.5$. The resonator's impedance matching factor is chosen to be $d = 0.9$.

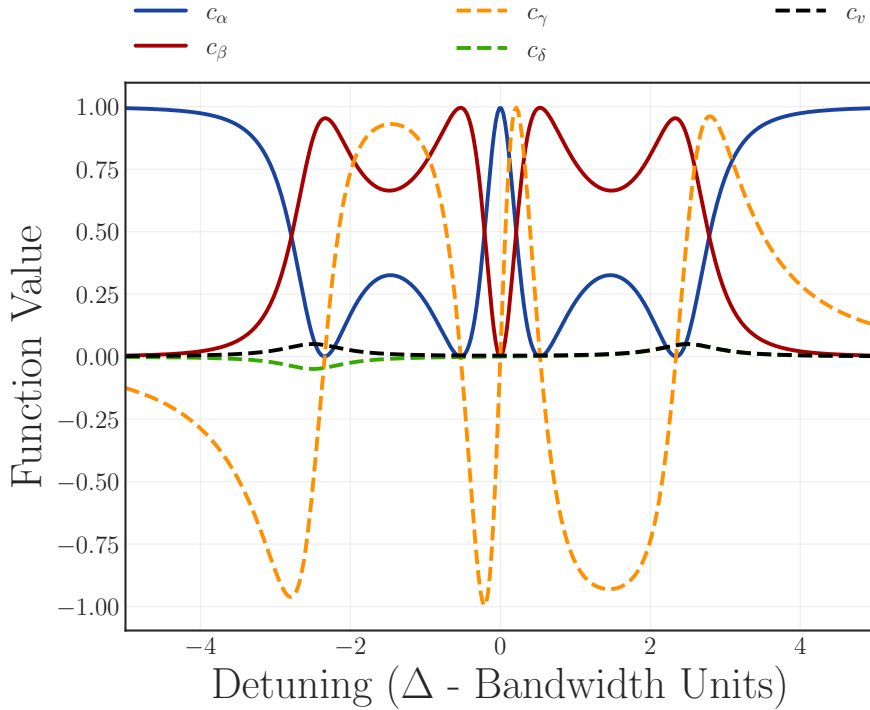


Figure 6 – The c -coefficients, which are the coefficients of the spectral noise density in Equation 3.83, are shown as functions of the normalized detuning of the carrier frequency. The simulation was performed using the following parameters: a resonator bandwidth of $\Delta\omega_{acav} = 2\pi \times 6$ MHz, an analysis frequency of $\Omega = 2\pi \times 15$ MHz, and a resonator impedance matching factor of $d = 0.9$.

In the context of the symmetric sideband mode, the coefficients c_α and c_β correspond to multiplicative functions of the variances of the amplitude and phase quadratures, respectively. The c_γ coefficient scales γ , which is associated with the covariance between the amplitude and phase quadratures. This covariance characterizes how well the noise ellipse aligns with the quadrature axes. Finally, the c_δ coefficient is linked to the δ parameter, which, as previously discussed, captures the correlation between the symmetric and antisymmetric modes. The δ parameter also quantifies the energy imbalance between the upper and lower sidebands.

In the simulation shown in Figure 6, the function c_β reaches a maximum for certain detunings, while c_α simultaneously reaches a minimum. This phenomenon is often described as noise ellipse rotation, describing how phase fluctuations are transformed into amplitude fluctuations, and vice versa, due to the resonator's effect on the field. The figure identifies four detuning points where this conversion occurs. For the two points closest to zero detuning, the carrier primarily interacts with the cavity while the sidebands are reflected, resulting in minimal losses for the sidebands and direct access to the phase quadrature. At the more distant detuning points ($\Delta = \pm 2.5$), the sidebands resonate with the cavity and couple with vacuum fluctuations through internal losses, evidenced by the increased value of the c_v function. At these detunings, the function c_δ also assumes a non-zero value, allowing δ to be measured. The measurement of δ relies on creating an imbalance between the sidebands by mixing one of them with the vacuum. For a system designed to measure δ , it is advantageous to have a cavity with a low resonator impedance matching factor (d), which increases the sensitivity of the detection.

Figure 7 illustrates a simulation of the spectral noise density, based on Equation 3.83, as a function of normalized detuning. The parameters used are consistent with previous simulations, and the measured state has asymmetrical noise in its quadratures. Specifically, the amplitude quadrature variance is $\alpha = \Delta^2 \hat{P} = \Delta^2 \hat{p}_s = 1.25$, while the phase quadrature variance is $\beta = \Delta^2 \hat{Q} = \Delta^2 \hat{q}_s = 3$. The remaining covariance elements, γ and δ , are zero. These values were chosen to clearly illustrate the effect of the resonator, with the plot highlighting four key detuning regions:

1. **Far from resonance:** The resonator does not introduce a phase shift to either the carrier or the sideband mode of interest. In this region, the amplitude quadrature is directly measured, identical to what would be observed from the incident beam detection without the resonator.
2. **Sideband resonance ($\Delta = \pm 2.5$):** At this detuning, one sideband becomes resonant with the cavity, undergoing a phase shift relative to the carrier and the other sideband. This enables measurement of the phase quadrature, although some losses are present. Furthermore, this region is where δ can be determined if it has a nonzero value, as it reflects an imbalance in the sidebands.
3. **Near resonance (phase-to-amplitude detuning):** The carrier experiences a $\pi/2$ phase shift relative to the sidebands, enabling accurate measurement of the phase quadrature without losses.
4. **Exact resonance:** At resonance, the carrier undergoes a π phase shift, providing access to the amplitude quadrature again.

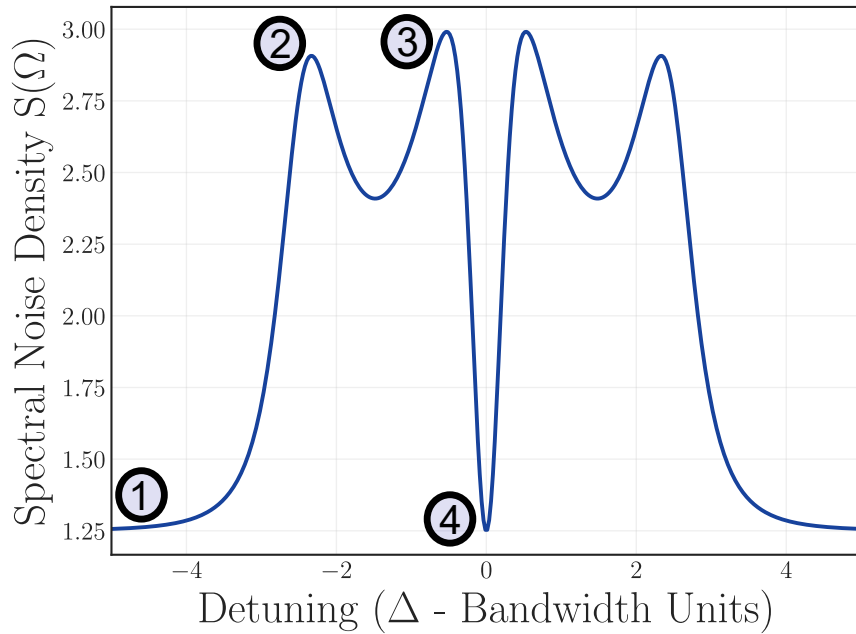


Figure 7 – Spectral noise density of a state with asymmetrical excess noise in the amplitude and phase quadratures. The simulation uses the same parameters as Figure 3.83, with the state defined by $\alpha = 1.25$, $\beta = 3$, and $\gamma = \delta = 0$. The regions correspond to: (1) Far from resonance, where the noise is determined solely by α ; (2) At detuning equal to the analysis frequency, where both β and δ are significant; (3) Near resonance, at the phase-to-amplitude detuning point, where only β contributes to the noise; and (4) At exact resonance, where the noise density equals α once more.

To measure the phase quadrature, the analysis cavity must apply a $\pi/2$ phase shift to the carrier while reflecting the measurement sidebands at $\pm\Omega$. However, this is not possible if the cavity's bandwidth $\Delta\omega_{acav}$ is too large relative to the analysis frequency Ω . Specifically, if $\Omega/\Delta\omega_{acav} \leq \sqrt{2}$, the detuning required to shift the carrier's phase also brings the sidebands into resonance, which corresponds to the merging of peaks (2) and (3) in Figure 7. Consequently, to be able to perform a clean measurement of the phase quadrature, free from cavity-induced losses on the sidebands, the system must satisfy the condition $\Omega/\Delta\omega_{acav} > \sqrt{2}$ [103].

3.3.3 Quantum Tomography of Two Fields

To achieve full tomography of two fields, signal (s) and idler (i), and determine all covariance matrix elements, it is necessary to obtain the correlations between their quadratures. Using the measured photocurrent components obtained via auto-homodyne detection, which are expressed in terms of the field quadratures as detailed in Equations 3.79 and 3.80, the cross-correlations between signal and idler spectral photocurrents

(Equation 3.38) are expressed as:

$$\begin{aligned} \text{Re}\{\langle\delta\hat{I}_{\Omega}^{(s)}(\Delta)\delta\hat{I}_{-\Omega}^{(i)}(\Delta)\rangle\} &= \frac{1}{2} [\langle\delta\hat{I}_{\cos}^{(s)}\delta\hat{I}_{\cos}^{(i)}\rangle + \langle\delta\hat{I}_{\sin}^{(s)}\delta\hat{I}_{\sin}^{(i)}\rangle] \\ &= c_{\mu}\mu + c_{\nu}\nu + c_{\kappa}\kappa + c_{\lambda}\lambda + c_{\xi}\xi + c_{\zeta}\zeta + c_{\eta}\eta + c_{\tau}\tau, \end{aligned} \quad (3.85a)$$

$$\begin{aligned} \text{Im}\{\langle\delta\hat{I}_{\Omega}^{(s)}(\Delta)\delta\hat{I}_{-\Omega}^{(i)}(\Delta)\rangle\} &= \frac{1}{2} [\langle\delta\hat{I}_{\sin}^{(s)}\delta\hat{I}_{\cos}^{(i)}\rangle - \langle\delta\hat{I}_{\cos}^{(s)}\delta\hat{I}_{\sin}^{(i)}\rangle] \\ &= -c_{\eta}\mu - c_{\tau}\nu + c_{\xi}\kappa + c_{\zeta}\lambda - c_{\kappa}\xi - c_{\lambda}\zeta + c_{\mu}\eta + c_{\nu}\tau. \end{aligned} \quad (3.85b)$$

where it was assumed that vacuum noise is uncorrelated with the field sidebands and with vacuum contributions from other sources. The parameters μ , ν , κ , λ , ξ , ζ , η and τ represent the elements of the covariance matrix for the two fields, as defined in Equations 3.54 and 3.56. The corresponding c -coefficients, derived from the g_{\pm} functions of each field (Equation 3.77), are given by:

$$c_{\mu} + ic_{\eta} = g_{+}^{*(s)}g_{+}^{(i)}, \quad (3.86a)$$

$$c_{\zeta} + ic_{\lambda} = g_{-}^{*(s)}g_{+}^{(i)}, \quad (3.86b)$$

$$c_{\nu} + ic_{\tau} = g_{-}^{*(s)}g_{-}^{(i)}, \quad (3.86c)$$

$$c_{\zeta} + ic_{\kappa} = g_{+}^{*(s)}g_{-}^{(i)}. \quad (3.86d)$$

The expression presented in Equation 3.85 establishes a fundamental relationship between the measured photocurrent components of the signal and idler fields and the covariance matrix elements that characterize their sideband quadrature correlations in the \mathcal{S}/\mathcal{A} basis. While Equation 3.85 determines the cross-correlations between the fields, the remaining elements of the covariance matrix depend solely on the local quantum states of each field. These local elements can be obtained using the formalism introduced in the preceding section, which analyzes each field's spectral quadratures independently.

The c -coefficients are determined by the detuning of both cavities, which means extracting the covariance elements from Equation 3.85 requires multiple resonator scans. Additionally, these elements are obtained by fitting the correlations between the measured photocurrent components of the signal and idler fields, but the large number of parameters makes it difficult to achieve accurate results. To address these challenges, we perform a complete quantum tomography using three separate measurements, each with a specific detuning configuration. This strategy ensures all correlations can be measured while providing additional data for consistency. In the first measurement, both analysis cavities are scanned synchronously to capture the correlations between the amplitude and phase quadratures of the fields. The second and third measurements independently scan the detuning of one resonator while keeping the other far from resonance. The behavior of

the c -coefficients across these three configurations is illustrated in Figure 8. The curves were obtained using an analysis frequency of $\Omega = 2\pi \times 15$ MHz, and resonators with a bandwidth of $\Delta\omega_{acav} = 2\pi \times 6$ MHz and an impedance matching factor of $d = 0.9$.

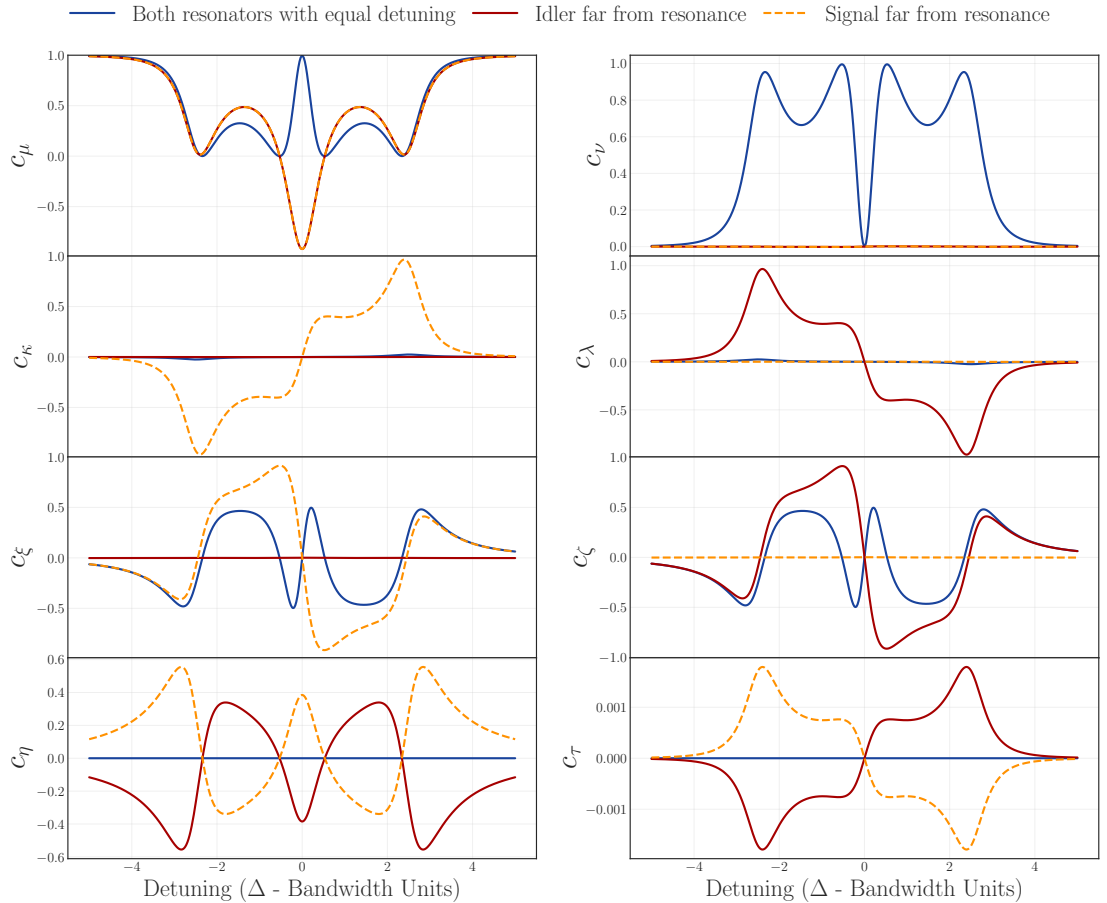


Figure 8 – Behavior of the c -coefficients, which define the two-field spectral noise density (Equation 3.83), across three detuning configurations used for complete quantum tomography of the signal and idler fields. Each plot displays three curves: the blue line represents synchronous scanning of both cavities, the red line corresponds to scanning only the signal cavity while the idler cavity remains far from resonance, and the dashed orange line represents the opposite scenario. The curves are calculated assuming an analysis frequency of $\Omega = 2\pi \times 15$ MHz, and both resonators with bandwidth of $\Delta\omega_{acav} = 2\pi \times 6$ MHz, and impedance matching factor of $d = 0.9$.

3.3.4 Cavity Mismatch Effects on Auto-Homodyne Detection

In the formalism derived up to this point, we have assumed that the coupling between the incident beam and the analysis cavity is unitary, meaning that the spatial

mode matching between the incident beam and the resonator's fundamental mode is perfect. However, in practical scenarios, achieving perfect mode matching is not feasible and can be challenging to optimize the visibility to values close to unity. Moreover, during system operation, variations in experimental degrees of freedom can lead to misalignments, thereby reducing the resonator coupling. This section explores the impact of spatial mode mismatch on auto-homodyne detection and develops a formalism to incorporate this effect into the quantum tomography analysis. The expressions derived here are based on the theoretical frameworks provided in [66] and [115]. However, to the best of our knowledge, this is the first time they have been fully presented in this form.

The spatial mode of the incident beam can be described using a spatial basis $\{\vec{F}_i(\mathbf{r})\}$, defined by the spatial eigenmodes of the resonator, such as Hermite-Gaussian or Laguerre-Gaussian modes. The electric field operator of the incident beam can be expressed in this basis as:

$$\hat{\mathbf{E}}^+(\mathbf{r}, t) = \vec{F}_1(\mathbf{r})\hat{A}(t) + \vec{F}_f(\mathbf{r})\hat{B}(t), \quad (3.87)$$

where $\vec{F}_f(\mathbf{r})$ accounts for the mismatch modes, which include all higher-order spatial modes that are not the cavity's target fundamental mode (TEM_{00}). The temporal field operators $\hat{A}(t)$ and $\hat{B}(t)$ correspond to the quantum fields associated with the fundamental mode and the mismatch modes, respectively.

We define the mismatch factor f as a parameter associated with the resonator coupling efficiency η_m , given by:

$$\eta_m = 1 - f^2. \quad (3.88)$$

The coupling efficiency η_m represents the fraction of the incident beam's intensity that is successfully coupled into the cavity. A mismatch factor $f = 0$ corresponds to perfect coupling, while $f = 1$ implies that the beam is entirely reflected by the cavity. The incident beam at frequency ω is described by the annihilation operator \hat{a} , associated with a specific spatial mode, while all other orthogonal spatial modes are in the vacuum state, represented by the operator \hat{c} . Using the linearity of spatial modes, the relationship between the analysis cavity modes and the incident beam modes, which define the detection modes, can be described by the following beamsplitter-like transformation:

$$\begin{pmatrix} \hat{A} \\ \hat{B} \end{pmatrix} = \begin{pmatrix} \sqrt{1-f^2} & -f \\ f & \sqrt{1-f^2} \end{pmatrix} \begin{pmatrix} \hat{a} \\ \hat{v} \end{pmatrix}. \quad (3.89)$$

When the incident beam is imperfectly coupled to the cavity, the cavity mode \hat{A} contains a mixture of the incident state in \hat{a} and the vacuum states from other spatial modes that

couple to the cavity. The mixture undergoes the effects of the cavity, whereas the mode \hat{B} is simply reflected without experiencing any modification.

By rewriting Equation 3.72 describing the unitary coupling scenario, the transformation of the spectral annihilation operator for an incident optical field reflected by an optical resonator, in the presence of mismatch, is expressed as:

$$\hat{a}_\omega \rightarrow \sqrt{1 - f^2} r(\Delta_\omega) \hat{A}_\omega + t(\Delta_\omega) \hat{v}_\omega + f \hat{B}_\omega, \quad (3.90)$$

where the expression is given in terms of the cavity spatial modes \hat{A}_ω and \hat{B}_ω , which explicitly describe the interaction of the incident field with the cavity. Specifically, \hat{A}_ω represents the component which experiences the cavity's effects, while \hat{B}_ω corresponds to the portion that is directly reflected without interacting with the resonator. Using Equation 3.90, and applying a similar approach to that used in deriving the auto-homodyne spectral photocurrent in Equation 3.75, we obtain the spectral photocurrent for the mismatch scenario expressed in terms of the cavity spatial modes. This derivation considers the attenuation of the carrier caused by resonator losses and transmission, given that the local oscillator (LO) attenuation is not uniform across all modes due to partial reflection of the carrier. The resulting spectral photocurrent, expressed in terms of the cavity spatial modes, is:

$$\begin{aligned} \hat{I}_\Omega = & \sqrt{1 - f^2} |r(\Delta)| \left[R_\Omega(\Delta) \delta \hat{A}_\Omega + T(\Delta_\Omega) \hat{v}_\Omega \right. \\ & \left. + R_{-\Omega}^*(\Delta) \delta \hat{A}_{-\Omega}^\dagger + T_{-\Omega}^*(\Delta) \hat{v}_{-\Omega}^\dagger \right] \\ & + f \left[\delta \hat{B}_\Omega + \delta \hat{B}_{-\Omega}^\dagger \right], \end{aligned} \quad (3.91)$$

where $r(\Delta)$ is defined in Equation 3.73, $R(\Delta_{\pm\Omega})$ and $T(\Delta_{\pm\Omega})$ are given in Equation 3.76, and \hat{v} represents the mode in a vacuum state coupled through cavity losses and transmission.

To transform the modes from the cavity basis $\{\hat{A}_\omega, \hat{B}_\omega\}$ to the detection basis $\{\hat{a}_\omega, \hat{c}_\omega\}$, we utilize the inverse rotation transformation from Equation 3.89. Applying this to the spectral photocurrent expression in Equation 3.91, we obtain:

$$\begin{aligned} \hat{I}_\Omega &= (1 - f^2) |r(\Delta)| \left[R_\Omega(\Delta) \hat{a}_\Omega + R_{-\Omega}^*(\Delta) \hat{a}_{-\Omega}^\dagger \right] + f^2 \left(\hat{a}_\Omega + \hat{a}_{-\Omega}^\dagger \right) + \hat{J}'_v \\ &= (1 - f^2) |r(\Delta)| \left[\frac{\hat{I}_{cos} + i \hat{I}_{sin}}{\sqrt{2}} \right] + f^2 \left[\frac{\hat{p}_s + i \hat{q}_a}{\sqrt{2}} \right] + \hat{I}'_v. \end{aligned} \quad (3.92)$$

Here, \hat{I}_{cos} and \hat{I}_{sin} represent the spectral photocurrent components in the perfect spatial mode-matching case, as described in Equation 3.80. The term \hat{I}'_v accounts for the vacuum contribution and is expressed as:

$$\begin{aligned}\hat{I}'_v &= f\sqrt{1-f^2} \left\{ \left[\hat{c}_\Omega + \hat{c}_{-\Omega}^\dagger \right] - |r(\Delta)| \left[R(\Delta_\Omega) \hat{c}_\Omega + R^*(\Delta_{-\Omega}) \hat{c}_{-\Omega}^\dagger \right] \right\} \\ &\quad + \sqrt{1-f^2} |r(\Delta)| \hat{I}_v,\end{aligned}\tag{3.93a}$$

$$\hat{I}_v = T(\Delta_\Omega) \hat{b}_\Omega + T^*(\Delta_{-\Omega}) \hat{b}_{-\Omega}^\dagger,\tag{3.93b}$$

where \hat{I}_v represents the vacuum contribution to the spectral photocurrent in the unitary spatial coupling case.

To derive the spectral noise density of a single stationary field under mismatch conditions, we begin by recognizing the following expression, which is derived from Equation 3.80:

$$\hat{I}_{cos} + i\hat{I}_{sin} = g_+ \hat{p}_s + g_- \hat{q}_s - ig_- \hat{p}_a + ig_+ \hat{q}_a,\tag{3.94}$$

where the auxiliary functions g_\pm are defined in Equation 3.77. By combining this relation with the covariance elements defined in Equation 3.46, we express the spectral noise density, derived from the spectral photocurrent in Equation 3.92, as:

$$\begin{aligned}S'_m(\Omega) &= \langle \hat{I}_\Omega \hat{I}_{-\Omega} \rangle \\ &= \alpha c'_\alpha + \beta c'_\beta + \gamma c'_\gamma + \delta c'_\delta + c'_v \\ &= \alpha [A' c_\alpha + B' Re\{g_+\} + f^4] \\ &\quad + \beta [A' c_\beta] \\ &\quad + \gamma [A' c_\gamma + B' Re\{g_-\}] \\ &\quad + \delta [A' c_\delta + B' Im\{g_-\}] \\ &\quad + \langle \hat{I}'_v \hat{I}'_{-v} \rangle,\end{aligned}\tag{3.95}$$

where it is assumed that the photocurrent components have zero mean and the single field c -coefficients are defined as in the perfect mode-matching case (Equation 3.84). The parameters A' and B' which depend on the mismatch factor and the carrier reflection coefficient, are expressed as:

$$A' = |r(\Delta)|^2 (1-f^2)^2,\tag{3.96a}$$

$$B' = 2r(\Delta)f^2(1-f^2).\tag{3.96b}$$

The vacuum contribution from the \hat{c} and \hat{v} modes is given by:

$$\begin{aligned}\langle \hat{I}'_v \hat{I}'_{-v} \rangle &= (1 - f^2) |r(\Delta)|^2 \langle \hat{I}_v \hat{I}_{-v} \rangle \\ &\quad + f^2(1 - f^2) [1 - 2|r(\Delta)|\text{Re}\{g_+\} + |r(\Delta)|^2 (c_\alpha + c_\beta)],\end{aligned}\quad (3.97a)$$

$$\langle \hat{I}_v \hat{I}_{-v} \rangle = 1 - c_\alpha - c_\beta. \quad (3.97b)$$

Analyzing Equation 3.95, we observe that for $f = 0$ the spectral noise density reduces to the unitary coupling efficiency case described in Equation 3.83. For $f = 1$, the noise density becomes $S'_m(\Omega) = \alpha$, indicating that only the amplitude quadrature is measured, as expected since the entire incident beam is reflected by the cavity. In the detuning limit $\Delta \rightarrow \infty$, corresponding to $r(\Delta) = R(\Delta_{\pm\Omega}) = 1$, the spectral noise density again simplifies to $S'_m(\Omega) = \alpha$ for all values of f . This behavior is consistent with the physical interpretation that, at this extreme detuning, the beam is fully reflected regardless of the mismatch factor.

An important case to consider is the spectral noise density obtained from an incident coherent state, characterized by $\alpha = \beta = 1$, and $\gamma = \delta = 0$. In this scenario, the spectral noise density simplifies to:

$$S'_m(\Omega) = S'_{shot}(\Omega) = |r(\Delta)|^2(1 - f^2) + f^2. \quad (3.98)$$

The spectral noise density of a coherent state is expected to be always equal to 1, as it corresponds to the quadrature variances of both the coherent state being measured and the involved vacuum states. This shows that Equation 3.95 is not normalized by the shot noise. The deviation arises because part of the carrier is attenuated when interacting with the cavity, while the remainder is simply reflected. To address this, the correct spectral noise density, providing second-moment values consistent with the quadrature definitions for any value of f , is given by normalizing Equation 3.95 by the shot noise:

$$S'(\Omega) = \frac{S'_m(\Omega)}{S'_{shot}(\Omega)} = \frac{S'_m(\Omega)}{|r(\Delta)|^2(1 - f^2) + f^2}. \quad (3.99)$$

This final expression is used to calculate the single field covariance matrix elements when mismatch is present.

To reconstruct the covariance matrix of the signal (s) and idler (i) fields under spatial mode mismatch, we calculate the cross-correlation following the method used for the ideal mode-matching case in Equation 3.37. Using the spectral photocurrent from Equation 3.92, we define the spectral noise density $S'^{(s,i)}(\Omega)$ for the two fields as:

$$\begin{aligned} S_m'^{(s,i)}(\Omega) &= \langle \hat{I}_\Omega^{(s)} \hat{I}_{-\Omega}^{(i)} \rangle \\ &= |r_{(s)}(\Delta)| |r_{(i)}(\Delta)| (1 - f_{(s)}^2)(1 - f_{(i)}^2) S_{pm}^{(s,i)}(\Omega) + S_{fm}'^{(s,i)}(\Omega), \end{aligned} \quad (3.100)$$

where $S_{pm}^{(s,i)}(\Omega)$ corresponds to the spectral noise under perfect spatial mode matching, as detailed in Equation 3.85. The mismatch related spectral noise component $S_{fm}'^{(s,i)}(\Omega)$ is given by:

$$\begin{aligned} S_{fm}'^{(s,i)}(\Omega) &= |r_{(s)}(\Delta)| f_{(i)}^2 (1 - f_{(s)}^2) \left[g_+^{(s)} \mu + g_-^{(s)} \zeta + i (g_-^{(s)} \lambda + g_+^{(s)} \eta) \right] \\ &\quad + |r_{(i)}(\Delta)| f_{(s)}^2 (1 - f_{(i)}^2) \left[g_+^{*(i)} \mu + g_-^{*(i)} \xi + i (g_+^{*(i)} \eta + g_-^{*(i)} \kappa) \right] \\ &\quad + f_{(s)}^2 f_{(i)}^2 (\mu + i \eta). \end{aligned} \quad (3.101)$$

The spectral noise density $S_m'^{(s,i)}(\Omega)$ (Equation 3.100) can be expressed in terms of its real and imaginary components, which directly correspond to the measured quadrature components of the spectral photocurrent. Using the covariance elements defined in Equations 3.54 and 3.56, we have:

$$\begin{aligned} \text{Re} \left\{ \langle \delta \hat{I}_\Omega^{(s)} \delta \hat{I}_{-\Omega}^{(i)} \rangle \right\} &= \frac{1}{2} \left[\langle \delta \hat{I}_{\cos}^{(s)} \delta \hat{I}_{\cos}^{(i)} \rangle + \langle \delta \hat{I}_{\sin}^{(s)} \delta \hat{I}_{\sin}^{(i)} \rangle \right] \\ &= \mu c'_\mu + \kappa c'_\kappa + \xi c'_\xi + \eta c'_\eta + \lambda c'_\lambda + \nu c'_\nu + \tau c'_\tau + \zeta c'_\zeta \\ &= \mu (A c_\mu + B \text{Re}\{g_+^{(s)}\} + C \text{Re}\{g_+^{*(i)}\} + D) \\ &\quad + \kappa (A c_\kappa - C \text{Im}\{g_-^{*(i)}\}) \\ &\quad + \xi (A c_\xi + C \text{Re}\{g_-^{*(i)}\}) \\ &\quad + \eta (A c_\eta - B \text{Im}\{g_+^{(s)}\} - C \text{Im}\{g_+^{*(i)}\}) \\ &\quad + \lambda (A c_\lambda - B \text{Im}\{g_-^{(s)}\}) \\ &\quad + \nu A c_\nu + \tau A c_\tau \\ &\quad + \zeta (A c_\zeta + B \text{Re}\{g_-^{(s)}\}), \end{aligned} \quad (3.102)$$

$$\begin{aligned}
Im \left\{ \langle \delta \hat{I}_{\Omega}^{(s)} \delta \hat{I}_{-\Omega}^{(i)} \rangle \right\} &= \frac{1}{2} \left[\langle \delta \hat{I}_{sin}^{(s)} \delta \hat{I}_{cos}^{(i)} \rangle - \langle \delta \hat{I}_{cos}^{(s)} \delta \hat{I}_{sin}^{(i)} \rangle \right] \\
&= -\mu c'_{\eta} + \kappa c'_{\xi} - \xi c'_{\kappa} + \eta c'_{\mu} + \lambda c'_{\zeta} - \nu c'_{\tau} + \tau c'_{\nu} - \zeta c'_{\lambda} \\
&= \mu \left(-A c_{\eta} + B Im\{g_+^{(s)}\} + C Im\{g_+^{*(i)}\} \right) \\
&\quad + \kappa \left(A c_{\xi} + C Re\{g_-^{*(i)}\} \right) \\
&\quad + \xi \left(-A c_{\kappa} + C Im\{g_-^{*(i)}\} \right) \\
&\quad + \eta \left(A c_{\mu} + B Re\{g_+^{(s)}\} + C Re\{g_+^{*(i)}\} + D \right) \\
&\quad + \lambda \left(A c_{\zeta} + B Re\{g_-^{(s)}\} \right) \\
&\quad - \nu A c_{\tau} + \tau A c_{\nu} \\
&\quad + \zeta \left(-A c_{\lambda} + B Im\{g_-^{(s)}\} \right), \tag{3.103}
\end{aligned}$$

where the two fields c -coefficients are defined in Equation 3.86. The parameters A , B , C , and D are functions of the spatial mode mismatch factor and the carrier reflection coefficients of both fields, and are expressed as follows:

$$A = |r_{(s)}(\Delta)| |r_{(i)}(\Delta)| (1 - f_{(s)}^2)(1 - f_{(i)}^2), \tag{3.104a}$$

$$B = |r_{(s)}(\Delta)| f_{(i)}^2 (1 - f_{(s)}^2), \tag{3.104b}$$

$$C = |r_{(i)}(\Delta)| f_{(s)}^2 (1 - f_{(i)}^2), \tag{3.104c}$$

$$D = f_{(s)}^2 f_{(i)}^2. \tag{3.104d}$$

Here again, it is essential to properly normalize the obtained spectral noise density to ensure that the covariance elements are consistent with our quadrature definitions. Using the shot noise normalization factor derived in Equation 3.98, the corrected spectral noise density for two fields in the presence of mismatch is expressed as:

$$\begin{aligned}
S'^{(s,i)}(\Omega) &= \frac{S_m'^{(s,i)}(\Omega)}{\sqrt{S_{shot}'^{(s)}(\Omega) S_{shot}'^{(i)}(\Omega)}} \\
&= \frac{S_m'^{(s,i)}(\Omega)}{\sqrt{[|r_{(s)}(\Delta)|^2 (1 - f_{(s)}^2) + f_{(s)}^2] [|r_{(i)}(\Delta)|^2 (1 - f_{(i)}^2) + f_{(i)}^2]}}. \tag{3.105}
\end{aligned}$$

From this expression, we observe that for a mismatch factor of $f = 0$, the usual equations for the unitary coupling scenario, as in Equation 3.85, are recovered. In the limiting case of $f = 1$, the measured spectral noise density simplifies to $S_m'^{(s,i)}(\Omega) = \mu + i\eta$, as expected, since these covariance elements correspond to the amplitude quadrature correlations.

3.3.5 Electronic Phase Discrepancy in the Two-Field Measurement

In our experiment, the use of different detectors for the signal and idler beams, which operate at distinct wavelengths, introduces a phase discrepancy in the acquired electrical signals. This phase difference influences the measured cross-correlations between the fields. Nevertheless, the quadrature demodulation strategy implemented in our measurement framework provides a mechanism to fully account for and correct this phase difference. This de-phasing process effectively rotates the two-field covariance matrix. In terms of the spectral matrix, it mixes the real and imaginary parts of the $\mathbf{C}_S^{(s,i)}$ matrix (Equation 3.69), represented as the 2×2 diagonal block matrix described in Equation 3.70.

In the presence of an electronic phase difference φ_e , the spectral photocurrent for the signal and idler fields can be expressed as follows:

$$\hat{I}_{\Omega}^{(s)} = \frac{1}{\sqrt{2}}(\hat{I}_{cos}^{(s)} + i\hat{I}_{sin}^{(s)})e^{i\varphi_e}, \quad (3.106a)$$

$$\hat{I}_{\Omega}^{(i)} = \frac{1}{\sqrt{2}}(\hat{I}_{cos}^{(i)} + i\hat{I}_{sin}^{(i)}). \quad (3.106b)$$

The cross-correlation of the spectral photocurrents is expressed as:

$$\begin{aligned} \langle \hat{I}_{\Omega}^{(s)} \hat{I}_{-\Omega}^{(i)} \rangle &= \frac{1}{2} \langle (\hat{I}_{cos}^{(s)} + i\hat{I}_{sin}^{(s)})(\hat{I}_{cos}^{(i)} - i\hat{I}_{sin}^{(i)})e^{i\varphi_e} \rangle \\ &= \frac{1}{2} [\cos \varphi_e (\langle \hat{I}_{cos}^{(s)} \hat{I}_{cos}^{(i)} \rangle + \langle \hat{I}_{sin}^{(s)} \hat{I}_{sin}^{(i)} \rangle) - \sin \varphi_e (\langle \hat{I}_{sin}^{(s)} \hat{I}_{cos}^{(i)} \rangle - \langle \hat{I}_{cos}^{(s)} \hat{I}_{sin}^{(i)} \rangle)] \\ &\quad + \frac{i}{2} [\cos \varphi_e (\langle \hat{I}_{sin}^{(s)} \hat{I}_{cos}^{(i)} \rangle - \langle \hat{I}_{cos}^{(s)} \hat{I}_{sin}^{(i)} \rangle) + \sin \varphi_e (\langle \hat{I}_{cos}^{(s)} \hat{I}_{cos}^{(i)} \rangle + \langle \hat{I}_{sin}^{(s)} \hat{I}_{sin}^{(i)} \rangle)]. \end{aligned} \quad (3.107)$$

To extract the real and imaginary parts of the cross-correlation, we reorganize the terms as:

$$Re[\langle \hat{I}_{\Omega}^{(s)} \hat{I}_{-\Omega}^{(i)} \rangle] = \frac{1}{2} [\cos \varphi_e (\langle \hat{I}_{cos}^{(s)} \hat{I}_{cos}^{(i)} \rangle + \langle \hat{I}_{sin}^{(s)} \hat{I}_{sin}^{(i)} \rangle) - \sin \varphi_e (\langle \hat{I}_{sin}^{(s)} \hat{I}_{cos}^{(i)} \rangle - \langle \hat{I}_{cos}^{(s)} \hat{I}_{sin}^{(i)} \rangle)], \quad (3.108a)$$

$$Im[\langle \hat{I}_{\Omega}^{(s)} \hat{I}_{-\Omega}^{(i)} \rangle] = \frac{1}{2} [\cos \varphi_e (\langle \hat{I}_{sin}^{(s)} \hat{I}_{cos}^{(i)} \rangle - \langle \hat{I}_{cos}^{(s)} \hat{I}_{sin}^{(i)} \rangle) + \sin \varphi_e (\langle \hat{I}_{cos}^{(s)} \hat{I}_{cos}^{(i)} \rangle + \langle \hat{I}_{sin}^{(s)} \hat{I}_{sin}^{(i)} \rangle)]. \quad (3.108b)$$

For the general case, the measured cross-correlation is related to the in-phase cross-correlation ($\varphi_e = 0$) through the relations:

$$Re[\langle \hat{I}_{\Omega}^{(s)} \hat{I}_{-\Omega}^{(i)} \rangle] = \cos \varphi_e Re[\langle \hat{I}_{\Omega}^{(s)} \hat{I}_{-\Omega}^{(i)} \rangle]_{\varphi_e=0} - \sin \varphi_e Im[\langle \hat{I}_{\Omega}^{(s)} \hat{I}_{-\Omega}^{(i)} \rangle]_{\varphi_e=0}, \quad (3.109a)$$

$$Im[\langle \hat{I}_{\Omega}^{(s)} \hat{I}_{-\Omega}^{(i)} \rangle] = \cos \varphi_e Im[\langle \hat{I}_{\Omega}^{(s)} \hat{I}_{-\Omega}^{(i)} \rangle]_{\varphi_e=0} + \sin \varphi_e Re[\langle \hat{I}_{\Omega}^{(s)} \hat{I}_{-\Omega}^{(i)} \rangle]_{\varphi_e=0}. \quad (3.109b)$$

Following the two-field quantum tomography analysis described in Section 3.3.3, using the out-of-phase cross-correlations, the obtained covariance elements, denoted by the superscript *op*, are given by:

$$\text{Re}[\langle \hat{I}_\Omega^{(s)} \hat{I}_{-\Omega}^{(i)} \rangle] = c_\mu \mu^{op} + c_\nu \nu^{op} + c_\kappa \kappa^{op} + c_\lambda \lambda^{op} + c_\xi \xi^{op} + c_\zeta \zeta^{op} + c_\eta \eta^{op} + c_\tau \tau^{op}, \quad (3.110a)$$

$$\text{Im}[\langle \hat{I}_\Omega^{(s)} \hat{I}_{-\Omega}^{(i)} \rangle] = -c_\eta \mu^{op} - c_\tau \nu^{op} + c_\xi \kappa^{op} + c_\zeta \lambda^{op} - c_\kappa \xi^{op} - c_\lambda \zeta^{op} + c_\mu \eta^{op} + c_\nu \tau^{op}. \quad (3.110b)$$

These should be compared to the in-phase cross-correlations, rewritten here for reference:

$$\text{Re}[\langle \hat{I}_\Omega^{(s)} \hat{I}_{-\Omega}^{(i)} \rangle]_{\varphi_e=0} = c_\mu \mu + c_\nu \nu + c_\kappa \kappa + c_\lambda \lambda + c_\xi \xi + c_\zeta \zeta + c_\eta \eta + c_\tau \tau, \quad (3.111a)$$

$$\text{Im}[\langle \hat{I}_\Omega^{(s)} \hat{I}_{-\Omega}^{(i)} \rangle]_{\varphi_e=0} = -c_\eta \mu - c_\tau \nu + c_\xi \kappa + c_\zeta \lambda - c_\kappa \xi - c_\lambda \zeta + c_\mu \eta + c_\nu \tau. \quad (3.111b)$$

In the case of significant mismatch in the analysis cavity, the *c*-coefficients in the equations above should be replaced with the *c'*-coefficients defined in Equations 3.102 and 3.103, with normalization applied as described in Equation 3.105. However, this substitution does not alter the relationships between the field correlations in the in-phase and out-of-phase electrical signal scenarios derived in this section.

By applying Equations 3.110 and 3.111 to the relation defined in Equation 3.109, and comparing the covariance elements multiplied by the same *c*-coefficients, we establish the relationship between the obtained covariance elements (*op*) and the in-phase elements in terms of the phase difference φ_e . These relationships are expressed as:

$$\begin{cases} \mu^{op} = \mu \cos \varphi_e - \eta \sin \varphi_e \\ \eta^{op} = \eta \cos \varphi_e + \mu \sin \varphi_e \end{cases}, \quad \begin{cases} \nu^{op} = \nu \cos \varphi_e - \tau \sin \varphi_e \\ \tau^{op} = \tau \cos \varphi_e + \nu \sin \varphi_e \end{cases}, \quad (3.112a)$$

$$\begin{cases} \xi^{op} = \xi \cos \varphi_e - \kappa \sin \varphi_e \\ \kappa^{op} = \kappa \cos \varphi_e + \xi \sin \varphi_e \end{cases}, \quad \begin{cases} \zeta^{op} = \zeta \cos \varphi_e - \lambda \sin \varphi_e \\ \lambda^{op} = \lambda \cos \varphi_e + \zeta \sin \varphi_e \end{cases}. \quad (3.112b)$$

These expressions clearly reveal the rotational transformation induced by the electronic phase difference φ_e between the electronic signals detecting the signal and idler modes. This phase difference couples the covariance elements within the symmetric and antisymmetric modes to the covariance elements between these modes. Consequently, the covariance elements between the two-field in the spectral matrix, $\mathbf{C}_S^{(s,i)}$ (as defined in Equation 3.69), exhibit a mixing of their real and imaginary parts.

To address this effect, one can either directly measure the electronic phase difference φ_e and compensate for it, or use prior knowledge of the quantum state under investigation

to determine φ_e via Equation 3.112. In our case, based on the expected state generated by the OPO, we assume that the covariance elements associated with correlations between the symmetric (\mathcal{S}) and antisymmetric (\mathcal{A}) modes are minimal. Therefore, φ_e is optimized to minimize these covariance elements by applying the rotational transformation in Equation 3.112.

3.4 Optical Modulation

The quadratures of an optical field can be precisely controlled using optical modulation. This can be achieved with an electro-optic modulator (EOM), where light propagates through a crystal subjected to an externally applied electric field. The crystal's refractive index is highly sensitive to and varies dynamically with the applied field. This enables precise modulation of the light's phase, polarization, and amplitude, depending on the experimental configuration. In this process, energy is redistributed from the carrier to the sidebands. For a sinusoidal modulation signal with a well-defined frequency Ω , a coherent signal is imprinted onto the sidebands at $\pm\Omega$. The resulting effect is equivalent to a displacement operator acting on these sideband modes, which increases the mean values of their centered quadratures [66].

In this section, we describe the effects of modulation on the quantum quadrature operators of the field. Additionally, we describe our experimental strategy for generating the teleportation input state, which utilizes an interferometric scheme to redistribute phase modulation across both amplitude and phase quadratures relative to the field in the interferometer's other path.

3.4.1 Amplitude Modulation

Considering the carrier electric field's analytic signal, $E^{(+)}(t) = \alpha e^{-i\omega_0 t}$, which describes a monochromatic classical field with a complex amplitude α . When subjected to amplitude modulation (AM) at a modulation frequency Ω , the field transforms as [116]:

$$\begin{aligned} E_{AM}^{(+)}(t) &= [1 + \epsilon_{AM} \cos(\Omega t + \phi_m)] E^{(+)}(t) \\ &= \alpha \left\{ e^{-i\omega_0 t} + \frac{\epsilon_{AM}}{2} \left[e^{-i\phi_m} e^{-i(\omega_0 + \Omega)t} + e^{i\phi_m} e^{-i(\omega_0 - \Omega)t} \right] \right\} \end{aligned} \quad (3.113)$$

Here, ϵ_{AM} represents the modulation depth, while ϕ_m denotes the relative phase of the modulation signal. From this expression, it becomes evident that the modulation process redistributes energy from the carrier frequency ω_0 into two sidebands located symmetrically at frequencies $\omega_0 - \Omega$ and $\omega_0 + \Omega$. In terms of the annihilation operator associated with

each sideband mode, the effect of amplitude modulation on the quantum state of the field can be described as [66]:

$$\hat{a}_\Omega \xrightarrow{\text{AM}} \alpha \frac{\epsilon_{AM}}{2} e^{-i\phi_m} + \hat{a}_\Omega, \quad \hat{a}_{-\Omega} \xrightarrow{\text{AM}} \alpha \frac{\epsilon_{AM}}{2} e^{i\phi_m} + \hat{a}_{-\Omega}. \quad (3.114)$$

This transformation corresponds to the action of a displacement operator $\hat{D}(\beta)$, which transforms the operator as $\hat{D}^\dagger(\beta)\hat{a}\hat{D}(\beta) = \hat{a} + \beta$, where β is the complex amplitude of the coherent signal added to the sideband.

It is important to emphasize that the transformation described in Equation 3.114 exclusively influences the mean values the field's quadratures. This is due to the assumption that the modulation bandwidth is sufficiently narrow, ensuring that it does not affect the frequency components around $\pm\Omega$. Consequently, after demodulating the photocurrents, only the mean values of the demodulated components are altered, while their variances remain unchanged. The variances are unaffected because they arise from fluctuations at other frequencies within the broader sideband frequency mode, which is defined by the low-pass filter used in the demodulation process.

We can express the single sideband mode quadratures, as defined in Equation 3.61, in terms of the annihilation and creation operators associated with the individual sidebands as follows:

$$\hat{P}_{\pm\Omega} = \frac{\hat{p}_s \pm i\hat{q}_a}{\sqrt{2}} = \hat{a}_{\pm\Omega} + \hat{a}_{\mp\Omega}^\dagger, \quad (3.115a)$$

$$\hat{Q}_{\pm\Omega} = \frac{\hat{q}_s \mp i\hat{p}_a}{\sqrt{2}} = -i(\hat{a}_{\pm\Omega} - \hat{a}_{\mp\Omega}^\dagger), \quad (3.115b)$$

where we have used the definitions from Equations 3.28 and 3.29. Based on these relations and the transformation of the annihilation operators at the exact frequencies $\pm\Omega$ described in Equation 3.114, we find that the effective mean values of the semiclassical quadratures for an initial vacuum state after amplitude modulation are given by:

$$\langle \hat{P} \rangle = \left\langle \sqrt{\hat{P}_\Omega \hat{P}_{-\Omega}} \right\rangle = \alpha \epsilon_{AM}, \quad (3.116a)$$

$$\langle \hat{Q} \rangle = \left\langle \sqrt{\hat{Q}_\Omega \hat{Q}_{-\Omega}} \right\rangle = 0. \quad (3.116b)$$

These expressions clearly show that amplitude modulation exclusively affects the amplitude quadrature, while the phase quadrature remains unchanged.

For the approach used in the following chapters, it is convenient to describe modulation in terms of the temporal annihilation operator of the field. This operator

can be expressed as a complex amplitude α representing the carrier, along with quantum fluctuations associated with the sidebands. Under this formalism, amplitude modulation is described as:

$$\begin{aligned}\hat{a} &= \alpha + \frac{1}{2}(\delta\hat{P} + i\delta\hat{Q}) \xrightarrow{\text{AM}} [1 + \epsilon_{AM} \cos(\Omega t + \phi_m)] \left[\alpha + \frac{1}{2}(\delta\hat{P} + i\delta\hat{Q}) \right] \\ &= \alpha + \frac{1}{2}\{[\delta\hat{P} + \alpha\epsilon_{AM}(t)] + i\delta\hat{Q}\},\end{aligned}\quad (3.117)$$

where $\epsilon_{AM}(t)$ captures the time-dependent component of the modulation. This expression shows that amplitude modulation introduces a coherent displacement in the amplitude quadrature, leaving the phase quadrature unperturbed. The transformation of the amplitude quadrature fluctuations follows:

$$\delta\hat{P} \xrightarrow{\text{AM}} \delta\hat{P} + \alpha\epsilon_{AM}(t) = \delta\hat{P} + P_M. \quad (3.118)$$

where $P_M = \alpha\epsilon_{AM}(t)$ represents the modulation-induced displacement in the amplitude quadrature.

Amplitude modulation can also be described in terms of individual sideband modes. Using the definitions from Equations 3.28 and 3.29, we express the symmetric and antisymmetric quadrature operators in terms of the annihilation and creation operators for the upper and lower sidebands as follows:

$$\hat{p}_{s,a} = \frac{\hat{p}_\Omega \pm \hat{p}_{-\Omega}}{\sqrt{2}} = \frac{\hat{a}_\Omega + \hat{a}_\Omega^\dagger \pm \hat{a}_{-\Omega} \pm \hat{a}_{-\Omega}^\dagger}{\sqrt{2}}, \quad (3.119a)$$

$$\hat{q}_{s,a} = \frac{\hat{q}_\Omega \pm \hat{q}_{-\Omega}}{\sqrt{2}} = \frac{-i(\hat{a}_\Omega - \hat{a}_\Omega^\dagger \pm \hat{a}_{-\Omega} \mp \hat{a}_{-\Omega}^\dagger)}{\sqrt{2}}. \quad (3.119b)$$

By applying the amplitude modulation transformation from Equation 3.114, we obtain the expected mean values for these quadrature operators:

$$\langle \hat{p}_s \rangle = \sqrt{2}\alpha\epsilon_{AM} \cos \phi_m, \quad \langle \hat{q}_a \rangle = -\sqrt{2}\alpha\epsilon_{AM} \sin \phi_m. \quad (3.120)$$

Meanwhile, the quadratures associated with phase fluctuations remain at zero mean value, $\langle \hat{q}_s \rangle = \langle \hat{p}_a \rangle = 0$. Comparing Equations 3.116a and 3.120, we obtain the following relation:

$$\langle \hat{P} \rangle^2 = \frac{\langle \hat{p}_s \rangle^2 + \langle \hat{q}_a \rangle^2}{2}. \quad (3.121)$$

This expression is used in practice to determine the mean value $\langle \hat{P} \rangle$, as our measurement is formulated in terms of the symmetric and antisymmetric quadrature operators.

3.4.2 Phase Modulation

The phase modulation (PM), which involves the modulation of the carrier field's phase, plays a central role in this work. For a sinusoidal driving signal, the transformation of the carrier's analytical signal under phase modulation is expressed as [116]:

$$\begin{aligned} E_{PM}^{(+)}(t) &= e^{i\delta_{PM}\cos(\Omega t + \phi_m)} E^{(+)}(t) \\ &= \alpha e^{-i\omega_0 t} \sum_{n=-\infty}^{\infty} i^n J_n(\delta_{PM}) e^{in(\Omega t + \phi_m)} \\ &\approx \alpha \left\{ e^{-i\omega_0 t} + \frac{i\delta_{PM}}{2} [e^{-i\phi_m} e^{-i(\omega_0 + \Omega)t} + e^{i\phi_m} e^{-i(\omega_0 - \Omega)t}] \right\} \end{aligned} \quad (3.122)$$

(3.123)

where the exponential was expanded using the Jacobi–Anger expansion in terms of the Bessel functions of the first kind, $J_n(x)$, with the approximation valid for small modulation depth ($\delta_{PM} \ll 1$) [117]. In terms of the annihilation operator associated with each individual sideband mode, the effect of phase modulation is described as [66]:

$$\hat{a}_\Omega \xrightarrow{\text{PM}} i\alpha \frac{\delta_{PM}}{2} e^{-i\phi_m} + \hat{a}_\Omega, \quad \hat{a}_{-\Omega} \xrightarrow{\text{PM}} i\alpha \frac{\delta_{PM}}{2} e^{i\phi_m} + \hat{a}_{-\Omega}. \quad (3.124)$$

Using Equation 3.115a, the effective mean values of the semiclassical quadratures for an initial vacuum state after the phase modulation are given by:

$$\langle \hat{P} \rangle = \left\langle \sqrt{\hat{P}_\Omega \hat{P}_{-\Omega}} \right\rangle = 0, \quad (3.125a)$$

$$\langle \hat{Q} \rangle = \left\langle \sqrt{\hat{Q}_\Omega \hat{Q}_{-\Omega}} \right\rangle = \alpha \delta_{PM}. \quad (3.125b)$$

In terms of the temporal quadrature operators, we have:

$$\begin{aligned} \hat{a} &= \alpha + \frac{1}{2}(\delta \hat{P} + i\delta \hat{Q}) \xrightarrow{\text{PM}} e^{i\delta_{PM}\cos(\Omega t + \phi_m)} \left[\alpha + \frac{1}{2}(\delta \hat{P} + i\delta \hat{Q}) \right] \\ &= \alpha + \frac{1}{2}\{\delta \hat{P} + i[\delta \hat{Q} + \alpha \delta_{PM}(t)]\}, \end{aligned} \quad (3.126)$$

here, $\delta_{PM}(t)$ again incorporates the time-dependent components. The resulting phase quadrature fluctuations modified by the phase modulation, is expressed as:

$$\delta \hat{Q} \xrightarrow{\text{PM}} \delta \hat{Q} + \alpha \delta_{PM}(t) = \delta \hat{Q} + Q_M. \quad (3.127)$$

Based on Equations 3.119 and 3.124, the mean values of the sideband quadrature operators in the symmetric/antisymmetric basis can be expressed as:

$$\langle \hat{q}_s \rangle = \sqrt{2}\alpha\epsilon_{AM} \cos \phi_m, \quad \langle \hat{p}_a \rangle = \sqrt{2}\alpha\epsilon_{AM} \sin \phi_m. \quad (3.128)$$

With the quadratures associated with amplitude fluctuations remaining at zero values $\langle \hat{p}_s \rangle = \langle \hat{q}_a \rangle = 0$. The effective mean value of the semiclassical phase quadrature is related to those in the \mathcal{S}/\mathcal{A} basis through the following expression:

$$\langle \hat{Q} \rangle^2 = \frac{\langle \hat{q}_s \rangle^2 + \langle \hat{p}_a \rangle^2}{2}. \quad (3.129)$$

Considering only the quantum state in the sideband mode being modulated, the modulation procedure effectively acts as a displacement unitary operation on that state [118]. This operation results in a non-zero mean value for the displaced quadrature, while the noise characteristics of the state remain unchanged. This analysis assumes that the modulation is driven by a pure sinusoidal wave, which is described by delta functions in the Fourier domain. However, if white noise is used as the modulation drive, additional noise is introduced into the quantum state, transforming an initial coherent state into a mixed state with excess noise in the modulated quadrature. A similar effect occurs if the sinusoidal wave driving the modulation has inherent noise, the resulting state will no longer be a pure coherent state but will instead be a displaced mixed state.

3.4.3 Phase-Controlled Rotation Technique

In this work, we only use phase electro-optical modulators to generate the input state and reconstruct the teleported state. The process of creating a generic coherent input state typically requires a displacement operation that acts on both the amplitude and phase quadratures. To address the absence of an amplitude electro-optical modulator, we use a Mach-Zehnder interferometer configuration. By controlling the field's propagation acquired phase in the modulated path, we can redistribute the phase modulation into both amplitude and phase components relative to the field in the interferometer's other path.

Consider a beam, where sideband states have zero mean value, incident on the interferometer. The first beam splitter divides the beam into two paths, labeled 1 and 2. The beam propagating through path 2 is subject to phase modulation. The fields entering the final beam splitter of the interferometer are expressed as:

$$\hat{a}_1 = \alpha_1 + \frac{1}{2}(\delta\hat{P}_1 + i\delta\hat{Q}_1), \quad (3.130a)$$

$$\hat{a}_2 = \alpha_2 + \frac{1}{2}[\delta\hat{P}_2 + i(\delta\hat{Q}_2 + \alpha_2\delta_{PM}(t))]. \quad (3.130b)$$

The outputs of the interferometer, labeled 3 and 4, are given by:

$$\hat{a}_3 = \frac{1}{\sqrt{2}} \{ \alpha_1 + \alpha_2 e^{i\theta} + \frac{1}{2} [\delta \hat{P}_1 + \delta \hat{P}_2 e^{i\theta} + i(\delta \hat{Q}_1 + \delta \hat{Q}_2 e^{i\theta} + \alpha_2 \delta_{PM}(t) e^{i\theta})] \}, \quad (3.131a)$$

$$\hat{a}_4 = \frac{1}{\sqrt{2}} \{ \alpha_1 - \alpha_2 e^{i\theta} + \frac{1}{2} [\delta \hat{P}_1 - \delta \hat{P}_2 e^{i\theta} + i(\delta \hat{Q}_1 - \delta \hat{Q}_2 e^{i\theta} - \alpha_2 \delta_{PM}(t) e^{i\theta})] \}, \quad (3.131b)$$

where θ is the controllable phase difference between the two paths, and the final beam splitter operates at a 50:50 ratio, splitting the beam equally. Using the field in path 1 as a reference, tuning θ allows us to redistribute the initial phase modulation into the amplitude quadrature. Expanding the exponential terms, we obtain:

$$\begin{aligned} \hat{a}_3 = & \frac{1}{\sqrt{2}} \{ \alpha_1 + \alpha_2 \cos \theta + i \alpha_2 \sin \theta + \frac{1}{2} [\delta \hat{P}_1 + \delta \hat{P}_2 \cos \theta - \delta \hat{Q}_2 \sin \theta - \alpha_2 \delta_{PM}(t) \sin \theta \\ & + i(\delta \hat{Q}_1 + \delta \hat{P}_2 \sin \theta + \delta \hat{Q}_2 \cos \theta + \alpha_2 \delta_{PM}(t) \cos \theta)] \} \end{aligned} \quad (3.132a)$$

$$\begin{aligned} \hat{a}_4 = & \frac{1}{\sqrt{2}} \{ \alpha_1 - \alpha_2 \cos \theta - i \alpha_2 \sin \theta + \frac{1}{2} [\delta \hat{P}_1 - \delta \hat{P}_2 \cos \theta + \delta \hat{Q}_2 \sin \theta + \alpha_2 \delta_{PM}(t) \sin \theta \\ & + i(\delta \hat{Q}_1 - \delta \hat{P}_2 \sin \theta - \delta \hat{Q}_2 \cos \theta - \alpha_2 \delta_{PM}(t) \cos \theta)] \}. \end{aligned} \quad (3.132b)$$

where we identify the mean values of the quadrature operators for the sideband modes as:

$$\langle \hat{P}_3 \rangle = -\frac{\alpha_2 \delta_{PM} \sin \theta}{\sqrt{2}}, \quad \langle \hat{Q}_3 \rangle = \frac{\alpha_2 \delta_{PM} \cos \theta}{\sqrt{2}}, \quad (3.133a)$$

$$\langle \hat{P}_4 \rangle = \frac{\alpha_2 \delta_{PM} \sin \theta}{\sqrt{2}}, \quad \langle \hat{Q}_4 \rangle = -\frac{\alpha_2 \delta_{PM} \cos \theta}{\sqrt{2}}. \quad (3.133b)$$

Here, the factor of $\sqrt{2}$ is a consequence of the 50:50 splitting ratio of the beam splitter. As a result, the amplitude quadrature is modulated. By adjusting the modulation depth δ_{PM} and the interferometer phase θ , we can displace the field state in any direction within the phase space. Defining the effective quadrature mean values as $P_M^{eff} = -\alpha_2 \delta_{PM} \sin \theta$ and $Q_M^{eff} = \alpha_2 \delta_{PM} \cos \theta$, the interferometer's output mean values can be expressed as:

$$\langle \hat{P}_3 \rangle = \frac{P_M^{eff}}{\sqrt{2}}, \quad \langle \hat{Q}_3 \rangle = \frac{Q_M^{eff}}{\sqrt{2}}, \quad (3.134a)$$

$$\langle \hat{P}_4 \rangle = -\frac{P_M^{eff}}{\sqrt{2}}, \quad \langle \hat{Q}_4 \rangle = -\frac{Q_M^{eff}}{\sqrt{2}}. \quad (3.134b)$$

These equations correspond to the expected behavior of the interferometer with zero phase difference ($\theta^{eff} = 0$), when amplitude and phase modulation are applied in path

2, generating the effective quadrature mean values P_M^{eff} and Q_M^{eff} , respectively. In our teleportation implementation, these effective modulations define the input state. This method allows us to create an arbitrary coherent state using only a phase modulator and precise control of the interferometer phase difference, reproducing the effect of applying both amplitude and phase modulation directly.

Additionally, the mean values of the individual sideband quadratures are given by:

$$\langle \hat{p}_s^3 \rangle = -\alpha_2 \delta_{PM} \sin \theta \cos \phi_m = P_M^{eff} \cos \phi_m, \quad \langle \hat{p}_a^3 \rangle = \alpha_2 \delta_{PM} \cos \theta \sin \phi_m = Q_M^{eff} \sin \phi_m, \quad (3.135a)$$

$$\langle \hat{q}_s^3 \rangle = \alpha_2 \delta_{PM} \cos \theta \cos \phi_m = Q_M^{eff} \cos \phi_m, \quad \langle \hat{q}_a^3 \rangle = \alpha_2 \delta_{PM} \sin \theta \sin \phi_m = -P_M^{eff} \sin \phi_m, \quad (3.135b)$$

$$\langle \hat{p}_s^4 \rangle = \alpha_2 \delta_{PM} \sin \theta \cos \phi_m = -P_M^{eff} \cos \phi_m, \quad \langle \hat{p}_a^4 \rangle = -\alpha_2 \delta_{PM} \cos \theta \sin \phi_m = -Q_M^{eff} \sin \phi_m, \quad (3.135c)$$

$$\langle \hat{q}_s^4 \rangle = -\alpha_2 \delta_{PM} \cos \theta \cos \phi_m = -Q_M^{eff} \cos \phi_m, \quad \langle \hat{q}_a^4 \rangle = -\alpha_2 \delta_{PM} \sin \theta \sin \phi_m = P_M^{eff} \sin \phi_m. \quad (3.135d)$$

4 QUANTUM TELEPORTATION PROTOCOL

Quantum teleportation is a quantum information protocol that consists of the transference of an unknown state between two distant parties, each one in a different location, as represented in Figure 9. This protocol should be performed using two channels: a classical channel and a quantum channel [119]. The classical channel is an information route that obeys the classical physics description. The quantum channel, in this case, is a bipartite entangled state shared between the sender, conventionally named Alice (station A), and the receiver, conventionally named Bob (station B). This entanglement is the fundamental resource for the quantum teleportation protocol, and the efficiency of the protocol is directly affected by the entanglement level of the quantum channel.

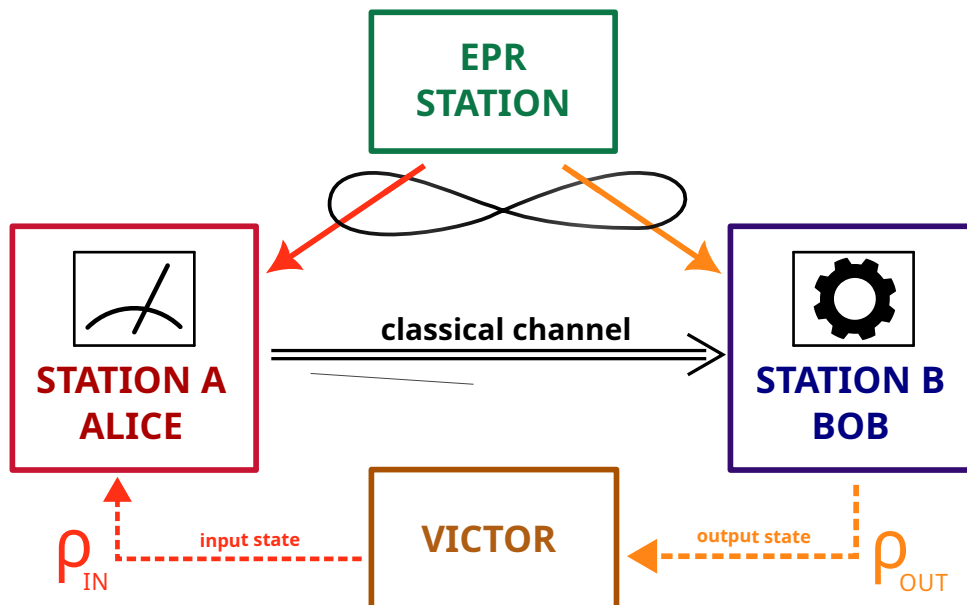


Figure 9 – Schematic representation of the quantum teleportation protocol.

The quantum teleportation protocol, as illustrated in Figure 9, is implemented through the following sequential steps [43]:

1. **Entanglement generation and distribution:** A bipartite entangled state is prepared at the EPR (Einstein-Podolsky-Rosen) station and distributed between the sender, Alice, and the receiver, Bob.
2. **Joint measurement and classical communication:** Alice receives an unknown quantum state $\hat{\rho}_{in}$ and performs a joint measurement involving her share of the entangled state and the input state. The resulting measurement outcomes are sent to Bob via a classical channel.

3. **Conditional unitary transformation and state reconstruction:** Bob performs a unitary operation on his share of the entangled state conditioned to the measurement results sent by Alice. This operation reconstructs the final state $\hat{\rho}_{out}$, completing the teleportation process.

In the ideal scenario, where Alice and Bob share a maximally entangled state and the systems involved have no loss or additional noise, the output state $\hat{\rho}_{out}$ retrieved by Bob is identical to the input state $\hat{\rho}_{in}$.

To evaluate the performance of the teleportation protocol, a third participant, the verifier Victor, is added to the scheme. Victor is responsible for generating and delivering the input state $\hat{\rho}_{in}$ to Alice. After the teleportation protocol is executed, Bob forwards the reconstructed state $\hat{\rho}_{out}$ to Victor. Victor then performs complete tomography of the output state through multiple iterations of the teleportation protocol, each utilizing the same input state. Given his precise knowledge of the prepared state, he analyzes the fidelity between $\hat{\rho}_{in}$ and $\hat{\rho}_{out}$ to quantify the protocol's efficiency and accuracy.

The quantum teleportation protocol has the following notable characteristics [120]:

- The protocol places no restrictions on the nature of the input state, provided that all parties agree on the mode in which the information is encoded (e.g., polarization, frequency, orbital angular momentum). Additionally, for successful teleportation, Alice and Bob must, respectively, be capable of performing accurate measurements and applying the necessary unitary transformations within the agreed mode.
- The integrity of the protocol relies on the input state remaining completely unknown to both Alice and Bob throughout the teleportation. If Alice obtains any information about the input state, for instance during the joint measurement, it affects the efficiency of the protocol, impairing the fidelity of the output state retrieved by Bob.
- During the quantum teleportation process, Alice's measurement induces an irreversible transformation of the input state, effectively erasing its original quantum information. This irreversible alteration is essential for upholding the no-cloning theorem, a fundamental principle of quantum mechanics that prohibits the replication of an unknown quantum state.
- The protocol respects the constraints of special relativity. The classical communication between Alice and Bob, inherently limited by the speed of light, is a critical step. Without this communication, Bob cannot reconstruct the information about the input state on his share of the entangled state.

This chapter begins by presenting our strategy for implementing the cross-band continuous-variable (CV) teleportation protocol in an idealized scenario. Following this,

the discussion is extended to a more realistic setting, incorporating practical constraints such as finite two-mode squeezing, optical losses, and the presence of electronic noise in the detection system. Finally, we provide a detailed explanation of the primary metric used to evaluate the performance of the teleportation protocol: the fidelity. Additionally, we derive the benchmarks used to identify quantum advantage, which serve as criteria for determining the success and practical significance of the implementation. The derivations in this chapter are based on foundational papers on continuous-variable (CV) teleportation [45, 46, 121, 122], several key reviews on the topic [32, 119, 120], as well as previous theses from the group, which further advanced the theoretical framework employed in this work [59, 60].

4.1 Theoretical Principles of the CV Teleportation Protocol

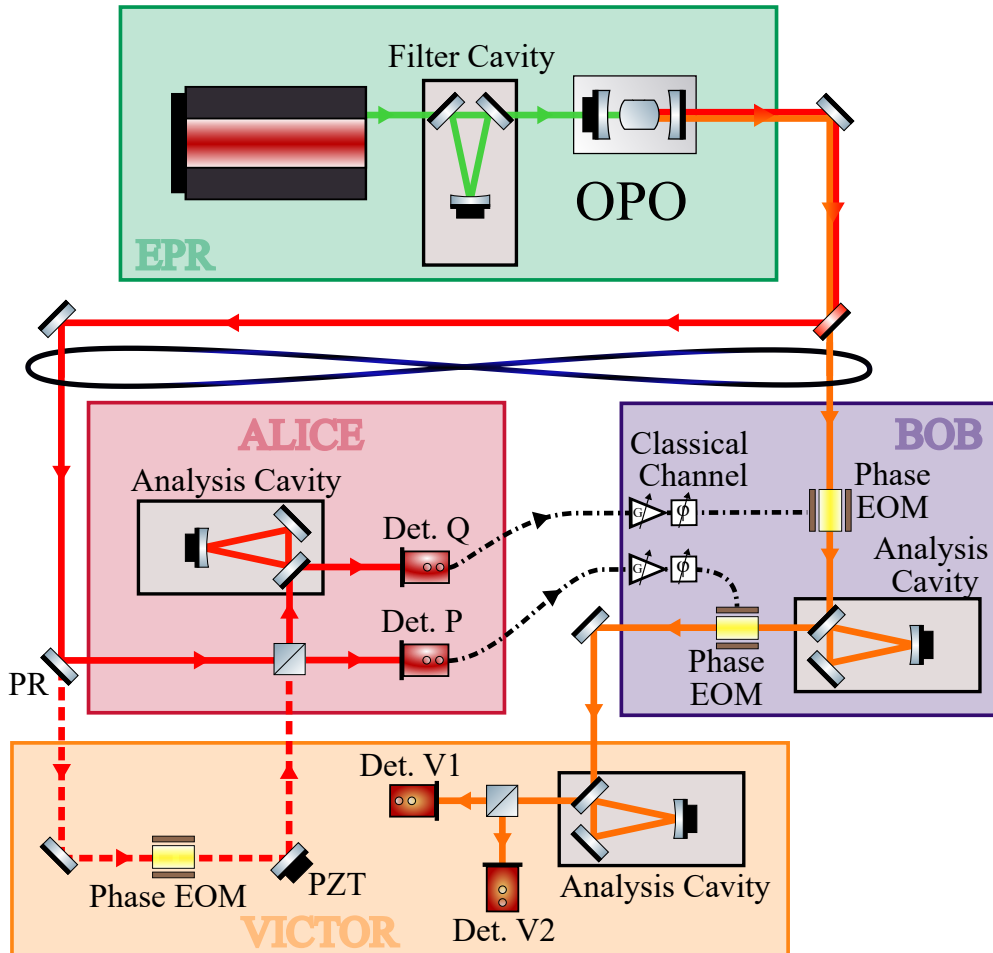


Figure 10 – Simplified representation of the experimental setup used to achieve continuous-variable teleportation between near-infrared (NIR) and the telecommunications L-band.

In this section, the theoretical foundation of the continuous-variable teleportation protocol implemented for sideband modes between the infrared and telecommunications

bands will be thoroughly examined. The discussion will focus on the core quantum mechanical concepts, the operational mechanisms, and the specific techniques used to enable the cross-band teleportation of quantum states. A simplified schematic of the experimental setup, shown in Figure 10, guides the discussion, with each station analyzed step by step. For clarity, the analysis presented here considers an idealized, lossless system, making it easier for the reader to grasp the core principles of quantum teleportation. A more realistic scenario will be addressed later in the text.

4.1.1 EPR Station: Entangled State Generation

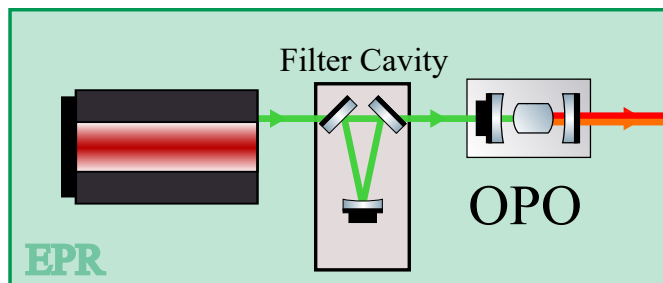


Figure 11 – The experimental setup for the EPR station is schematically represented in a simplified form. This setup comprises the 532 nm pump laser, the filter cavity, and the OPO chamber. The green line corresponds to the pump beam, while the signal beam (794.4(6) nm) sent to Alice and the idler beam (1611(3) nm) sent to Bob are shown in red and orange, respectively.

The first step of the protocol is the generation of the bipartite entangled state and its subsequent distribution to Alice and Bob. In the experiment, we generate the entangled state using a non-degenerate optical parametric oscillator (OPO) above the threshold. The schematic of the EPR station is shown in Figure 11. The resulting quantum state in the sideband modes of signal and idler beams is a mixed two-mode squeezed vacuum state (Section 2.1.3.4), which deviates from a pure state due to residual thermal noise and optical losses introduced during the generation process [87, 123]. The state is well-known for its EPR-type quantum correlations between the quadratures of the fields [91, 124]. Under proper conditions, the OPO generates intense signal and idler fields at 794.4(6) nm and 1611(3) nm, which are separated by a dichroic mirror and sent to Alice and Bob stations, respectively.

The state of interest, denoted as $\hat{\rho}_{AB}$, resides in the sidebands of the signal (A , Alice) and idler (B , Bob) fields, at an analysis frequency Ω relative to the carrier. The fields can be expressed using the following Heisenberg-picture operators, decomposed into their mean values and fluctuation components:

$$\hat{a}_A = \alpha_A + \delta\hat{a}_A, \quad (4.1a)$$

$$\hat{a}_B = \alpha_B + \delta\hat{a}_B, \quad (4.1b)$$

where α_A and α_B are the mean field amplitudes, and $\delta\hat{a}_A$, $\delta\hat{a}_B$ are the fluctuation operators. The amplitude and phase quadratures for these fields are defined as:

$$\hat{P}_{A,B} = \hat{a}_{A,B} + \hat{a}_{A,B}^\dagger, \quad (4.2a)$$

$$\hat{Q}_{A,B} = -i(\hat{a}_{A,B} - \hat{a}_{A,B}^\dagger). \quad (4.2b)$$

where $\hat{P}_{A,B}$ and $\hat{Q}_{A,B}$ represent the amplitude and phase quadratures, respectively.

The sidebands modes of the generated fields are Gaussian states with zero mean quadratures, and therefore, are fully described by their covariance matrix. For a pure two-mode squeezed vacuum state aligned with the quadrature axes, the covariance matrix takes the form [78, 125]:

$$\mathbf{V}_{AB} = \frac{1}{2} \left\langle \delta\hat{\mathbf{X}}_{AB} \delta\hat{\mathbf{X}}_{AB}^T + (\delta\hat{\mathbf{X}}_{AB}^T \delta\hat{\mathbf{X}}_{AB})^T \right\rangle = \begin{pmatrix} \cosh(2r)\mathbb{1}_2 & \sinh(2r)\sigma_z \\ \sinh(2r)\sigma_z & \cosh(2r)\mathbb{1}_2 \end{pmatrix}, \quad (4.3)$$

where $\delta\hat{\mathbf{X}}_{AB} = (\delta\hat{P}_A, \delta\hat{Q}_A, \delta\hat{P}_B, \delta\hat{Q}_B)^T$ is the vector of quadrature fluctuations, $\mathbb{1}_2$ is the 2-dimensional identity matrix, σ_z is the Pauli-Z matrix, and $r \geq 0$ is the two-mode squeezing parameter. By performing a rotation in the two-mode quadrature basis, we can define the following composite quadratures that involve both fields:

$$\delta\hat{P}_- = \frac{\delta\hat{P}_A - \delta\hat{P}_B}{\sqrt{2}}, \quad (4.4a)$$

$$\delta\hat{Q}_+ = \frac{\delta\hat{Q}_A + \delta\hat{Q}_B}{\sqrt{2}}. \quad (4.4b)$$

The variances of these composite quadratures exhibit noise suppression below the standard quantum limit, demonstrating two-mode squeezing:

$$\Delta^2 \hat{P}_- = e^{-2r}, \quad (4.5a)$$

$$\Delta^2 \hat{Q}_+ = e^{-2r}. \quad (4.5b)$$

This noise reduction below the vacuum level for both composite quadratures confirms the presence of entanglement in the two-mode squeezed vacuum state. This is verified by

the Duan-Giedke-Cirac-Zoller (DGCZ) criterion [81], which is discussed in more detail in Section 2.1.4.1.

The degree of two-mode squeezing directly corresponds to the level of entanglement in the state. In the non-physical limit $r \rightarrow \infty$, the state becomes maximally entangled, exhibiting perfect correlations in the amplitude quadratures and perfect anti-correlations in the phase quadratures:

$$\delta\hat{P}_A = \delta\hat{P}_B, \quad (4.6a)$$

$$\delta\hat{Q}_A = -\delta\hat{Q}_B. \quad (4.6b)$$

These conditions describe a perfect EPR state [77]. In practice, however, states generated by optical parametric oscillators (OPOs) are mixed, with covariance matrices deviating from the ideal case in Equation 4.3. Additionally, the achievable two-mode squeezing coefficient is limited, reducing the efficiency of quantum teleportation [99, 126]. Despite these considerations, the quantum teleportation achieved with the generated states outperforms any classical scheme relying on local states and classical communication.

4.1.2 Victor: Input State Preparation

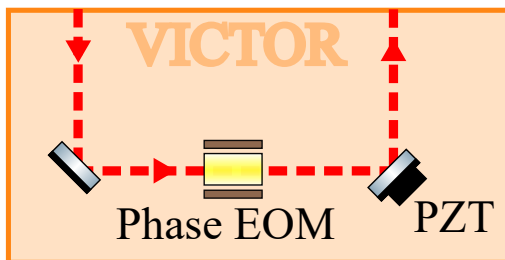


Figure 12 – Schematic diagram of the Victor station designed to generate the input state. The setup includes a phase electro-optic modulator (EOM) and a PZT-coupled mirror for precise stabilization of the interferometer’s phase. Victor determines the state to be created by adjusting the modulation signal’s amplitude and the interferometer’s locking position.

The input state is prepared at Victor station (Figure 12), keeping it unknown to Alice and Bob. To achieve this, a small fraction of the signal beam (less than 1%) is deflected, ensuring that the relevant sidebands in the deflected portion are well approximated by a vacuum state. Victor manipulates these sideband modes as desired to create an input state with specific characteristics. In this experiment, the focus is on teleporting coherent states with nonzero mean values.

An electro-optic modulator (EOM) is used by Victor to modulate the light field at the analysis frequency Ω , corresponding to the frequency of the sideband of interest.

The resulting effect is equivalent to a displacement operator acting on the sideband modes, which increases the mean values of their quadratures [127]. In this experiment, the input state is generated using only a phase electro-optical modulator. This choice is motivated by the inherent functionality of a Mach-Zehnder interferometer, which naturally forms when a small part of the signal beam is used to produce the input state and is subsequently interfered with Alice's beam. Although an amplitude modulator is not utilized in this experiment, the Mach-Zehnder interferometer configuration compensates for this by enabling precise control of the phase relationship between the input state's field and Alice's field. This phase adjustment effectively performs a rotation operation, redistributing the input state's phase modulation into both amplitude and phase components relative to Alice's carrier. Through this method, it is possible to construct any small coherent beam within the phase space. The theoretical description of this process is detailed in Section 3.4.

Following the phase modulation and quadrature rotation, the state of the field sent from Victor to Alice can be described as:

$$\hat{a}_{in} = \alpha_{in} + \frac{1}{2}[(\delta\hat{P}_{in} + P_{in}) + i(\delta\hat{Q}_{in} + Q_{in})], \quad (4.7)$$

where $\delta\hat{P}_{in}$ and $\delta\hat{Q}_{in}$ correspond to the input state fluctuations, while P_{in} and Q_{in} represent the mean values of the sideband quadratures resulting from modulation. Since the sidebands in the initial deflected field sent to Victor were assumed to be in a vacuum state, and the modulation process applies only a displacement operation without altering the sideband fluctuations, the fluctuations described by $\delta\hat{P}_{in}$ and $\delta\hat{Q}_{in}$ correspond to vacuum fluctuations. By selecting the appropriate amplitude of the electronic signal driving the modulation and the stabilized phase of the interferometer, the values of P_{in} and Q_{in} can be precisely controlled. The mean values of the single-mode quadratures can be expressed in terms of the individual sideband modes as:

$$|P_{in}| = \sqrt{\frac{p_s^2 + q_a^2}{2}}, \quad |Q_{in}| = \sqrt{\frac{p_a^2 + q_s^2}{2}}. \quad (4.8)$$

Here, we described the preparation of a coherent input state with small mean quadrature values, although this is not a strict requirement. The teleportation protocol can transfer any quantum state within the sideband modes, including non-classical states such as squeezed states, non-Gaussian states, or even states with a negative Wigner function. Our system is also capable of teleporting the individual sideband modes ($\pm\Omega$, Section 3.2), which can contain different quantum states, and characterizing these states using the auto-homodyne detection scheme (Section 3.3). In our current experimental setup, however, we are restricted to generating displaced coherent and thermal states. The generation of

thermal states, in particular, is achieved by introducing Gaussian noise into the electronic signal used to drive the EOM [128, 129].

4.1.3 Alice: Joint Measurement

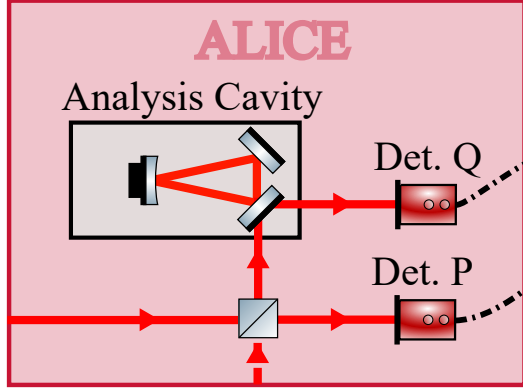


Figure 13 – Alice’s station experimental setup. The Mach-Zehnder interferometer is completed by interfering the fields containing the input state and Alice’s share of the EPR state, effectively mixing the states. The outputs from the final beam splitter are directed to separate detection systems for amplitude and phase quadratures. For the phase quadrature, the ellipse rotation technique is applied using an analysis cavity.

Alice receives the input state prepared by Victor and combines it with her portion of the EPR state using a 50:50 beam splitter, finalizing the setup of the Mach-Zehnder interferometer, as shown in Figure 13. She then performs a joint measurement of the conjugate amplitude and phase quadratures on the output paths of the beam splitter. The results of both measurements are sent through a classical channel to Bob, for the state reconstruction.

The states of the fields emerging from the outputs of the beam splitter, which mixes the input state, are expressed in terms of the fields entering the beam splitter as:

$$\hat{a}_{Ap} = \frac{\hat{a}_A - \hat{a}_{in}}{\sqrt{2}}, \quad \hat{a}_{Aq} = \frac{\hat{a}_A + \hat{a}_{in}}{\sqrt{2}}, \quad (4.9)$$

where \hat{a}_{Ap} and \hat{a}_{Aq} correspond to the fields directed towards the amplitude and phase quadrature measurements, respectively. By expanding the operators in terms of the quadrature fluctuations, we obtain:

$$\hat{a}_{Ap} = \frac{1}{\sqrt{2}} \left\{ \alpha_A - \alpha_{in} + \frac{1}{2} [\delta \hat{P}_A - \delta \hat{P}_{in} - P_{in} + i(\delta \hat{Q}_A - \hat{Q}_{in} - Q_{in})] \right\}, \quad (4.10a)$$

$$\hat{a}_{Aq} = \frac{1}{\sqrt{2}} \left\{ \alpha_A + \alpha_{in} + \frac{1}{2} [\delta \hat{P}_A + \delta \hat{P}_{in} + P_{in} + i(\delta \hat{Q}_A + \hat{Q}_{in} + Q_{in})] \right\}. \quad (4.10b)$$

As detailed in Section 3.3, amplitude quadrature measurements can be performed directly with a photodetector, while phase quadrature measurements require an interferometric approach. To achieve this, we utilize the dispersive properties of a cavity, referred to as the analysis cavity, to perform the noise ellipse rotation [103]. This process effectively converts the phase fluctuations into amplitude fluctuations. This method relies on stabilizing the cavity at a specific detuning during the measurement procedure. Since the complete conversion of amplitude to phase occurs at the lateral of the cavity's transmission peak, the transmission signal can be utilized as an error signal to perform a side-of-fringe lock at the required detuning [130].

The acquired photocurrent at each photodetector, defined up to a constant as $\hat{I}(t) = \hat{a}^\dagger \hat{a}$, is given by the following expressions [131]:

$$\hat{I}_{Ap} = \frac{|\alpha_A - \alpha_{in}|^2}{2} + |\alpha_A - \alpha_{in}| \frac{\delta \hat{P}_A - \delta \hat{P}_{in} - P_{in}}{\sqrt{2}}, \quad (4.11a)$$

$$\hat{I}_{Aq} = \frac{|\alpha_A + \alpha_{in}|^2}{2} + |\alpha_A + \alpha_{in}| \frac{\delta \hat{Q}_A + \delta \hat{Q}_{in} + Q_{in}}{\sqrt{2}}. \quad (4.11b)$$

At the detector, the low-frequency (DC) component is separated from the high-frequency (HF) component, which contains information about the field fluctuations, including the sideband mode we are manipulating. The HF component is then sent to Bob's station and is expressed as:

$$\delta \hat{I}_{Ap} = |\alpha_A - \alpha_{in}| \frac{\delta \hat{P}_A - \delta \hat{P}_{in} - P_{in}}{\sqrt{2}}, \quad (4.12a)$$

$$\delta \hat{I}_{Aq} = |\alpha_A + \alpha_{in}| \frac{\delta \hat{Q}_A + \delta \hat{Q}_{in} + Q_{in}}{\sqrt{2}}. \quad (4.12b)$$

4.1.4 Bob: State Reconstruction

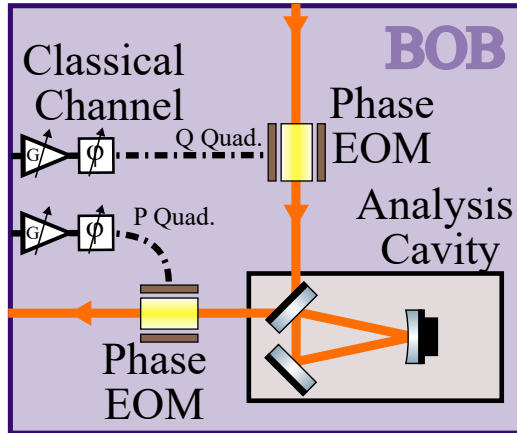


Figure 14 – Bob’s station scheme: Bob reconstructs the input state by manipulating his share of the EPR state based on Alice’s measurement results. This process involves two phase EOMs and an analysis cavity stabilized for phase-to-amplitude conversion.

The results of Alice’s joint measurements are transmitted to Bob’s station via two classical channels: one for the amplitude quadrature measurements and another for the phase quadrature measurements. Based on the received information, Bob applies two displacement operations, one on each quadrature, to his share of the EPR state, reconstructing the original input state. As illustrated in Figure 14, we use two phase EOMs to minimize crosstalk between orthogonal quadrature modulations. An analysis cavity, locked at the phase-to-amplitude conversion detuning, is used to switch amplitude and phase quadratures. This configuration ensures that the second phase EOM, placed after the cavity, acts on the previous amplitude fluctuations.

In the classical channels, the electronic signal passes through a variable amplifier and a phase shifter, which are crucial for fine-tuning Bob’s actions on his field. These adjustments ensure that the displacement amplitude is correctly calibrated to cancel the existing noise in his share using entanglement, while simultaneously incorporating the input state information [119]. Using Alice’s measurement results, as defined in Equation 4.12, the modulation applied to Bob’s field is given by:

$$\delta \hat{I}_{Ap}^{ch} = g_P \frac{\delta \hat{P}_A - \delta \hat{P}_{in} - P_{in}}{\sqrt{2}}, \quad \delta \hat{I}_{Aq}^{ch} = g_Q \frac{\delta \hat{Q}_A + \delta \hat{Q}_{in} + Q_{in}}{\sqrt{2}}, \quad (4.13)$$

where the complex parameters $g_{Q,P} = |g_{Q,P}|e^{i\phi_{Q,P}}$ are the electronic gains. These parameters account for all amplification and phase-shifting processes, from the detection stage to the EOM operation, while also incorporating the carrier field amplitude α from Alice’s signal beam.

The state reconstruction process begins with phase modulation, where the phase quadrature measurement from Alice is used to modulate Bob's field. After this step, the resulting field is given by:

$$\begin{aligned}\hat{a}_B^{pm} &= \alpha_B + \frac{1}{2} \left[\delta\hat{P}_B + i\delta\hat{Q}_B + ig_Q \frac{\delta\hat{Q}_A + \delta\hat{Q}_{in} + Q_{in}}{\sqrt{2}} \right] \\ &= \alpha_B + \frac{1}{2} \left[\delta\hat{P}_B + i \left(\frac{g_Q}{\sqrt{2}} \delta\hat{Q}_A + \delta\hat{Q}_B \right) + \frac{ig_Q}{\sqrt{2}} (\delta\hat{Q}_{in} + Q_{in}) \right].\end{aligned}\quad (4.14)$$

This modulation step introduces a term proportional to $\delta\hat{I}_{Aq}^{ch}$ into the phase quadrature fluctuations. The modulated field is then reflected from an analysis cavity designed to perform phase-to-amplitude quadrature conversion. This cavity operates at a stabilized detuning, where the carrier experiences a $\pi/2$ phase shift, while sidebands are assumed to reflect without any phase alteration:

$$\hat{a}_B^{pm} \xrightarrow{\text{Cav}} \hat{a}_B^{acav} = e^{i\frac{\pi}{2}} \alpha_B + \delta\hat{a}_B^{pm}. \quad (4.15)$$

In practice, sidebands undergo small phase shifts, but careful selection of the detuning preserves the effective phase-to-amplitude quadrature conversion [107]. The field reflected from the cavity is expressed as:

$$\hat{a}_B^{acav} = i \left\{ \alpha_B + \frac{1}{2} \left[\left(\frac{g_Q}{\sqrt{2}} \delta\hat{Q}_A + \delta\hat{Q}_B \right) + \frac{g_Q}{\sqrt{2}} (\delta\hat{Q}_{in} + Q_{in}) - i\delta\hat{P}_B \right] \right\}. \quad (4.16)$$

The global phase can be disregarded at this stage without any loss of generality in the description.

With the amplitude fluctuations now mapped to the phase of the field, the final step in the state reconstruction involves another phase modulation, this time using the amplitude quadrature measurements from Alice $\delta\hat{I}_{Ap}^{ch}$. The reconstructed field is then described as:

$$\begin{aligned}\hat{a}_B^{am} &= \alpha_B + \frac{1}{2} \left[\left(\frac{g_Q}{\sqrt{2}} \delta\hat{Q}_A + \delta\hat{Q}_B \right) + \frac{g_Q}{\sqrt{2}} (\delta\hat{Q}_{in} + Q_{in}) - i\delta\hat{P}_B + ig_P \frac{\delta\hat{P}_A - \delta\hat{P}_{in} - P_{in}}{\sqrt{2}} \right] \\ &= \alpha_B + \frac{1}{2} \left[(\Gamma_Q \delta\hat{Q}_A + \delta\hat{Q}_B) + i(\Gamma_P \delta\hat{P}_A - \delta\hat{P}_B) + \Gamma_Q (\delta\hat{Q}_{in} + Q_{in}) - i\Gamma_P (\delta\hat{P}_{in} + P_{in}) \right].\end{aligned}\quad (4.17)$$

Here, we define the teleportation gain as $\Gamma_{Q,P} = g_{Q,P}/\sqrt{2}$. This gain can also be expressed in terms of the mean values of the quadratures of the teleported state and the input state,

representing the ratio between them. The unitary gain condition, $\Gamma_{Q,P} = 1$, corresponds to the teleportation system achieving equal fidelity for any unknown coherent input state. Although the parameter $\Gamma_{Q,P}$ can be adjusted to improve the fidelity for a specific known state, only the system at unitary gain fairly teleports all possible coherent input states equally [120].

Under the unitary gain condition $\Gamma_{Q,P} = 1$, and in the idealized scenario of infinite two-mode squeezing, where perfect correlations exist between Alice's and Bob's fields (as described in Equation 4.6), the teleported field is expressed as:

$$\begin{aligned}\hat{a}_B^{out} &= \alpha_B + \frac{1}{2} [\delta\hat{Q}_{in} + Q_{in} - i(\delta\hat{P}_{in} + \hat{P}_{in})] \\ &= \alpha_B - \frac{i}{2} [\delta\hat{P}_{in} + \hat{P}_{in} + i(\delta\hat{Q}_{in} + Q_{in})] \\ &= \alpha_B - i\delta\hat{a}_{in}.\end{aligned}\tag{4.18}$$

We can observe that the input state is recovered, though with a $-\pi/2$ phase shift between the sideband mode and the carrier. This phase relationship causes the output state to be inverted, transferring the amplitude and phase of the input state into the phase and amplitude quadratures, respectively. However, this inversion is not significant, as it can be corrected through a local rotation operation. For instance, one could use the Victor analysis cavity, stabilized at the phase-to-amplitude conversion detuning, to perform this alignment.

An interesting case to consider is the variance of the teleported states when only classical fields are involved. Here, the EPR state is substituted with a pair of coherent states for Alice and Bob. These states have quadrature fluctuations with a variance of one and no correlations between them. In this case, the resulting teleported quadrature variances are:

$$\Delta^2\hat{P}_B^{out,cl} = \Gamma_P^2\Delta^2\hat{P}_{in}^2 + \Gamma_P^2 + 1,\tag{4.19a}$$

$$\Delta^2\hat{Q}_B^{out,cl} = \Gamma_Q^2\Delta^2\hat{Q}_{in}^2 + \Gamma_Q^2 + 1.\tag{4.19b}$$

For the unitary gain condition and a coherent input state, the expected variances without utilizing quantum resources are given by 3. This value is fundamental for defining the protocol's benchmarks and demonstrating the quantum advantage in reconstructing the input state.

This result reflects the unavoidable penalties , or quantum duties (quduties), in CV teleportation. These are inherent noise sources that arise from the protocol's interface between quantum and classical domains [45, 48]. The first penalty occurs at the Alice's

station and is a direct consequence of the Heisenberg uncertainty principle, her attempt to simultaneously measure conjugate variables of the input state inevitably adds one unit of vacuum noise to the classical information she obtains. The second penalty arises at the Bob's station when he uses this inherently noisy classical information to perform a displacement operation and reconstruct the quantum state, a process that adds a second unit of vacuum noise. Adding these two penalties to the inherent vacuum noise of the coherent input state results in a classical variance of 3 units. The crucial role of the shared entangled resource is to mitigate these penalties. The quantum correlations in the entangled state allow the noise from Alice's measurement to be partially canceled during Bob's reconstruction.

4.1.5 Victor: Quantum Tomography

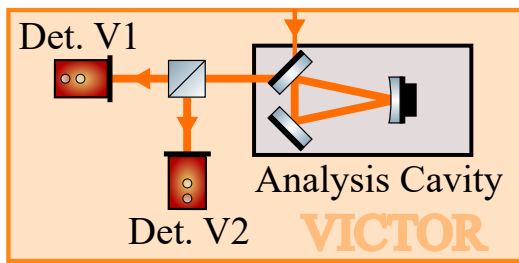


Figure 15 – Illustration of the Victor station setup designed for quantum tomography. The station receives the teleported quantum state and performs tomography using the auto-homodyne technique, which incorporates a scanning analysis cavity and a balanced detection system.

In a real-world teleportation system, the OPO produces fields with a finite amount of squeezing, and optical losses occur at each step of the protocol. As a result, the correlations between Alice's and Bob's fields are imperfect, and the teleported state is not an exact replica of the input state, as indicated by Equation 4.18. Therefore, the protocol's performance must be evaluated by comparing the teleported state to the input state. Since neither Alice nor Bob knows the input state, they cannot perform this comparison. Instead, it falls to Victor, who prepared the input state, to verify the success of the teleportation process.

To evaluate the teleportation protocol, Victor performs a comprehensive quantum state tomography of the teleported state received from Bob. This process requires maintaining a constant input state while using the auto-homodyne detection strategy to measure the output state [107], which is described in detail in Section 3.3. The implementation of this detection method involves a scanning analysis cavity along with a balanced detection system to simultaneously measure shot noise values, as shown in Figure 15. Using the tomography data, the performance of the system is evaluated by calculating the fidelity

between the input and teleported states. A detailed discussion about the fidelity and the protocol's benchmarks will be presented later in the text.

4.2 Realistic Scenario: Exploring Losses and Finite Squeezing

In this section, we expand the discussion presented in Section 4.1 by examining the single sideband mode quantum teleportation in a more realistic scenario. Here, the analysis incorporates two critical factors that impact the protocol's performance in practical implementations: the finite squeezing levels generated by the OPO and the optical losses that occur between the system's key components. These limitations introduce deviations from idealized behavior, necessitating a more comprehensive understanding of their influence on teleportation fidelity and overall system efficiency.

4.2.1 Considering Finite Squeezing

Accounting for the limited squeezing and mixed nature of the state generated by the OPO, the quadrature correlations between Alice and Bob can be expressed as:

$$\begin{cases} \delta\hat{P}_- = \frac{1}{\sqrt{2}}(\delta\hat{P}_A - \delta\hat{P}_B) = e^{-r_-}\delta\hat{P}_1^v, \\ \delta\hat{P}_+ = \frac{1}{\sqrt{2}}(\delta\hat{P}_A + \delta\hat{P}_B) = e^{r_+}\delta\hat{P}_2^v, \\ \delta\hat{Q}_- = \frac{1}{\sqrt{2}}(\delta\hat{Q}_A - \delta\hat{Q}_B) = e^{s_+}\delta\hat{Q}_1^v, \\ \delta\hat{Q}_+ = \frac{1}{\sqrt{2}}(\delta\hat{Q}_A + \delta\hat{Q}_B) = e^{-s_-}\delta\hat{Q}_2^v. \end{cases} \quad (4.20)$$

Here, r_- and r_+ correspond to the squeezing and anti-squeezing parameters for amplitude correlations, respectively, while s_- and s_+ describe the same for phase correlations, with $r_{\pm}, s_{\pm} \geq 0$. The fluctuation terms $\delta\hat{P}^v$ and $\delta\hat{Q}^v$ have the same statistics as a vacuum state, satisfying the condition $\Delta^2\hat{P}_{1,2}^v = \Delta^2\hat{Q}_{1,2}^v = 1$. Rewriting the correlations in terms of the quadrature fluctuations of Alice and Bob, we obtain:

$$\begin{cases} \delta\hat{P}_A = \frac{1}{\sqrt{2}}(e^{r_+}\delta\hat{P}_2^v + e^{-r_-}\delta\hat{P}_1^v), \\ \delta\hat{P}_B = \frac{1}{\sqrt{2}}(e^{r_+}\delta\hat{P}_2^v - e^{-r_-}\delta\hat{P}_1^v), \\ \delta\hat{Q}_A = \frac{1}{\sqrt{2}}(e^{-s_-}\delta\hat{Q}_2^v + e^{s_+}\delta\hat{Q}_1^v), \\ \delta\hat{Q}_B = \frac{1}{\sqrt{2}}(e^{-s_-}\delta\hat{Q}_2^v - e^{s_+}\delta\hat{Q}_1^v). \end{cases} \quad (4.21)$$

This corresponds to the expected output fields of a beam splitter when two single-mode squeezed vacuum states are incident upon it [46]. In this model, the squeezed vacuum states \hat{a}_1 and \hat{a}_2 are described by their quadratures:

$$\delta\hat{P}_1 = e^{-r_-}\delta\hat{P}_1^v, \quad \delta\hat{Q}_1 = e^{s_+}\delta\hat{Q}_1^v, \quad (4.22a)$$

$$\delta\hat{P}_2 = e^{r_+}\delta\hat{P}_2^v, \quad \delta\hat{Q}_2 = e^{-s_-}\delta\hat{Q}_2^v. \quad (4.22b)$$

By substituting Equation 4.21 into Bob's field expression after the second EOM, which completes the state reconstruction as described in Equation 4.17, we derive the following equation for the teleported state quadratures:

$$\delta\hat{P}_B^{out} = \frac{1}{\sqrt{2}} \left[(\Gamma_P + 1) e^{-r_-} \delta\hat{P}_1^v + (\Gamma_P - 1) e^{r_+} \delta\hat{P}_2^v \right] + \Gamma_P(\delta\hat{P}_{in} + P_{in}), \quad (4.23a)$$

$$\delta\hat{Q}_B^{out} = \frac{1}{\sqrt{2}} \left[(\Gamma_Q + 1) e^{-s_-} \delta\hat{Q}_2^v + (\Gamma_Q - 1) e^{s_+} \delta\hat{Q}_1^v \right] + \Gamma_Q(\delta\hat{Q}_{in} + Q_{in}). \quad (4.23b)$$

In this equation, we did not account for the $\pi/2$ phase shift introduced by Bob's analysis cavity during the state reconstruction procedure. As a result, the presented output state quadrature information is not inverted. This approach simplifies the discussion and will be maintained for the remainder of this section. The phase shift's effect can be easily incorporated into the final equations by performing the transformations $P_B^{out} \rightarrow Q_B^{out}$ and $Q_B^{out} \rightarrow -P_B^{out}$.

In the case of unitary gain ($\Gamma_Q = \Gamma_P = 1$), the teleported state, incorporating the effects of finite squeezing as given by Equation 4.23, is described by:

$$\delta\hat{P}_B^{out} = (\delta\hat{P}_{in} + P_{in}) + \sqrt{2}e^{-r_-}\delta\hat{P}_1^v, \quad (4.24a)$$

$$\delta\hat{Q}_B^{out} = (\delta\hat{Q}_{in} + Q_{in}) + \sqrt{2}e^{-s_-}\delta\hat{Q}_2^v. \quad (4.24b)$$

Here, we observe a fundamental limitation of the continuous-variable teleportation protocol. The input state can only be perfectly recovered under the unphysical condition of infinite squeezing ($r_-, s_- \rightarrow \infty$), which implies an infinite average number of photons and, consequently, infinite energy. In realistic conditions, finite squeezing always introduces noise into the quadratures of the teleported state, limiting the protocol's performance.

Equation 4.23 demonstrates the impact of gain miscalibration on the system. When the gain is perfectly calibrated at $\Gamma = 1$, the anti-squeezing terms disappear, leaving only the input state and the squeezing term to define the final state (Equation 4.24). However, as the gain deviates from unity, the anti-squeezing contributions grow, introducing additional noise into the system and degrading the protocol performance. At the same time, these deviations in gain also distort the input state's contribution, which can either be overestimated or underestimated. If the input state is known, it becomes possible to optimize the gain in this equation, balancing the noise contributions from each term to falsely enhance the fidelity of the system specifically for that input state.

4.2.2 Impact of Optical Losses on the Protocol

Optical setups inherently suffer from losses caused by spurious transmission, reflection, or absorption in the optical components, as well as the limited quantum efficiency of detectors. These losses cause a degradation of the quantum states being manipulated, which directly reduce the performance of the teleportation protocol [47]. Because such losses are present in all optical elements, they accumulate between the critical stages of the protocol.

Figure 16 provides a schematic representation of the optical path in the experimental setup, where losses occurring between each main stage are modeled using virtual beam splitter operations [100]. The input state, \hat{a}_{in} , is combined with Alice's field at the physical beam splitter BS-AJ, the only beam splitter in the diagram that does not correspond to a loss process. For all other beam splitters, losses are represented by the mixing of the beam with vacuum fluctuations, indicated by the superscript v . The efficiency of each loss channel is given by its transmission coefficient t_i , while the corresponding loss is given by the reflection coefficient r_i .

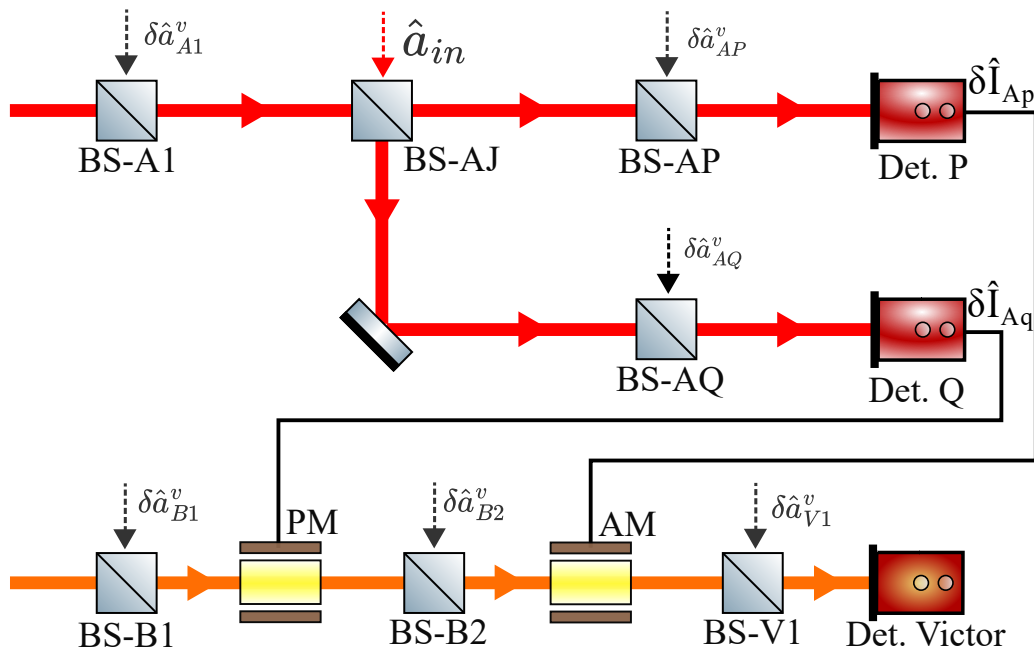


Figure 16 – Schematic representation of the optical paths for the signal and idler beams in the experiment. Beam splitter transformations are used to model the losses at each stage.

Considering the given model, the fields measured at Alice's and Victor's detectors can be described as:

$$\begin{aligned}\hat{a}_{ADetP} = & t_{A1}t_{Aj}t_{AP}(\alpha_A + \delta\hat{a}_A) - r_{Aj}t_{AP}(\alpha_{In} + \delta\hat{a}_{In}) \\ & + r_{A1}t_{Aj}t_{AP}\delta\hat{a}_{A1}^v + r_{AP}\delta\hat{a}_{AP}^v,\end{aligned}\quad (4.25a)$$

$$\begin{aligned}\hat{a}_{ADetQ} = & t_{A1}r_{Aj}t_{AQ}(\alpha_A + \delta\hat{a}_A) + t_{Aj}t_{Ax}(\alpha_{In} + \delta\hat{a}_{In}) \\ & + r_{A1}r_{Aj}t_{AQ}\delta\hat{a}_{A1}^v + r_{AQ}\delta\hat{a}_{AQ}^v.\end{aligned}\quad (4.25b)$$

$$\begin{aligned}\hat{a}_{VDet} = & t_{B1}t_{B2}t_{V1}(\alpha_B + \delta\hat{a}_B) + t_{V1}g_P(\delta\hat{P}_{ADetP} + \delta e_P) + t_{B2}t_{V1}ig_Q(\delta\hat{Q}_{ADetQ} + \delta e_Q) \\ & + r_{B1}t_{B2}t_{V1}\delta\hat{a}_{B1}^v + r_{B2}t_{V1}\delta\hat{a}_{B2}^v + r_{V1}\delta\hat{a}_{V1}^v.\end{aligned}\quad (4.25c)$$

Here, the terms $\delta e_{Q,P}$ describe the electronic noise present in the classical communication channel. This type of noise, a fundamental limitation of electronic circuits, degrades the overall performance of the protocol, as will be shown later. Additionally, the second line in each equation represents the vacuum fluctuations introduced by optical losses. Since Alice's P and Q detectors measure only their respective quadratures, the quadrature fluctuations measured at Alice's station can be written as:

$$\begin{aligned}\delta\hat{P}_{ADetP} = & t_{A1}t_{Aj}t_{AP}\delta\hat{P}_A - r_{Aj}t_{AP}(P_{In} + \delta\hat{P}_{In}) \\ & + r_{A1}t_{Aj}t_{AP}\delta\hat{P}_{A1}^v + r_{AP}\delta\hat{P}_{AP}^v,\end{aligned}\quad (4.26a)$$

$$\begin{aligned}\delta\hat{Q}_{ADetQ} = & t_{A1}r_{Aj}t_{AQ}\delta\hat{Q}_A + t_{Aj}t_{AQ}(Q_{In} + \delta\hat{Q}_{In}) \\ & + r_{A1}r_{Aj}t_{AQ}\delta\hat{Q}_{A1}^v + r_{AQ}\delta\hat{Q}_{AQ}^v.\end{aligned}\quad (4.26b)$$

At Victor's station, we perform a quantum tomography measurement, which allows access to both quadratures. As a result, the measured quadrature fluctuations at Victor are given by:

$$\begin{aligned}\delta\hat{P}_{VDet} = & t_{B1}t_{B2}t_{V1}\delta\hat{P}_B + t_{V1}g_P(\delta\hat{P}_{ADetP} + \delta e_P) \\ & + r_{B1}t_{B2}t_{V1}\delta\hat{P}_{B1}^v + r_{B2}t_{V1}\delta\hat{P}_{B2}^v + r_{V1}\delta\hat{P}_{V1}^v,\end{aligned}\quad (4.27a)$$

$$\begin{aligned}\delta\hat{Q}_{VDet} = & t_{B1}t_{B2}t_{V1}\delta\hat{Q}_B + t_{B2}t_{V1}g_Q(\delta\hat{Q}_{ADetQ} + \delta e_Q) \\ & + r_{B1}t_{B2}t_{V1}\delta\hat{Q}_{B1}^v + r_{B2}t_{V1}\delta\hat{Q}_{B2}^v + r_{V1}\delta\hat{Q}_{V1}^v.\end{aligned}\quad (4.27b)$$

To express the measured quadratures in Victor's field in terms of the input state, as well as the squeezing and anti-squeezing noise terms, we substitute Alice's measured fields from Equation 4.26 and the EPR correlations from Equation 4.21 into the measured quadrature fluctuations at Victor in Equation 4.27. The resulting quadratures measured at Victor's detector are expressed as:

$$\begin{aligned} \delta\hat{P}_{VDet} = & \frac{1}{\sqrt{2}}t_{V1}[e^{-r_-}(t_{A1}t_{Aj}t_{AP}g_P - t_{B1}t_{B2})\delta\hat{P}_1^v + e^{r_+}(t_{A1}t_{Aj}t_{AP}g_P + t_{B1}t_{B2})\delta\hat{P}_2^v] \\ & - t_{V1}r_{Aj}t_{AP}g_P(\delta\hat{P}_{In} + P_{In}) \\ & + r_{B1}t_{B2}t_{V1}\delta\hat{P}_{B1}^v + r_{B2}t_{V1}\delta\hat{P}_{B2}^v + r_{V1}\delta\hat{P}_{V1}^v + t_{V1}g_P(r_{A1}t_{Aj}t_{AP}\delta\hat{P}_{A1}^v + r_{AP}\delta\hat{P}_{AP}^v) \\ & + t_{V1}g_P\delta e_P, \end{aligned} \quad (4.28a)$$

$$\begin{aligned} \delta\hat{Q}_{VDet} = & \frac{1}{\sqrt{2}}t_{B2}t_{V1}[e^{-s_-}(t_{A1}r_{Aj}t_{AQ}g_Q + t_{B1})\delta\hat{Q}_2^v + e^{s_+}(t_{A1}r_{Aj}t_{AQ}g_Q - t_{B1})\delta\hat{Q}_1^v] \\ & + t_{B2}t_{V1}t_{Aj}t_{AQ}g_Q(\delta\hat{Q}_{In} + Q_{In}) \\ & + r_{B1}t_{B2}t_{V1}\delta\hat{Q}_{B1}^v + r_{B2}t_{V1}\delta\hat{Q}_{B2}^v + r_{V1}\delta\hat{Q}_{V1}^v + t_{B2}t_{V1}g_Q(r_{A1}r_{Aj}t_{AQ}\delta\hat{Q}_{A1}^v + r_{AQ}\delta\hat{Q}_{AQ}^v) \\ & + t_{B2}t_{V1}g_Q\delta e_Q. \end{aligned} \quad (4.28b)$$

The terms in these expressions are organized as follows: the first line addresses the squeezing and anti-squeezing noise contributions, the second line captures the input state fluctuations, the third line represents vacuum fluctuations introduced by losses, and the final line corresponds to the electronic noise. From these equations, the variance of the teleported state as measured by Victor is:

$$\begin{aligned} \Delta^2\hat{P}_{VDet} = & \frac{1}{2}T_{V1}(e^{-2r_-}|t_{A1}t_{Aj}t_{AP}g_P - t_{B1}t_{B2}|^2 + e^{2r_+}|t_{A1}t_{Aj}t_{AP}g_P + t_{B1}t_{B2}|^2) \\ & + T_{V1}R_{Aj}T_{AP}g_P^2\Delta^2\hat{P}_{In} \\ & + R_{B1}T_{B2}T_{V1} + R_{B2}T_{V1} + R_{V1} + T_{V1}g_P^2(R_{A1}T_{Aj}T_{AP} + R_{AP}) \\ & + T_{V1}g_P^2\Delta^2e_P, \end{aligned} \quad (4.29a)$$

$$\begin{aligned} \Delta^2\hat{Q}_{VDet} = & \frac{1}{2}T_{B2}T_{V1}(e^{-2s_-}|t_{A1}r_{Aj}t_{AQ}g_Q + t_{B1}|^2 + e^{2s_+}|t_{A1}r_{Aj}t_{AQ}g_Q - t_{B1}|^2) \\ & + T_{B2}T_{V1}T_{Aj}T_{AQ}g_Q^2\Delta^2\hat{Q}_{In} \\ & + R_{B1}T_{B2}T_{V1} + R_{B2}T_{V1} + R_{V1} + T_{B2}T_{V1}g_Q^2(R_{A1}R_{Aj}T_{AQ} + R_{AQ}) \\ & + T_{B2}T_{V1}g_Q^2\Delta^2e_Q, \end{aligned} \quad (4.29b)$$

where we used the fact that the variance of vacuum fluctuations is normalized to unity.

The mean quadrature values measured for the target sideband mode at Alice's and Victor's stations, as derived from Equations 4.26 and 4.28, are given by:

$$\langle\delta\hat{P}_{ADetP}\rangle = -r_{Aj}t_{AP}P_{In}, \quad \langle\delta\hat{Q}_{ADetQ}\rangle = t_{Aj}t_{AQ}Q_{In}, \quad (4.30a)$$

$$\langle\delta\hat{P}_{VDet}\rangle = -t_{V1}r_{Aj}t_{AP}g_PP_{In}, \quad \langle\delta\hat{Q}_{VDet}\rangle = t_{B2}t_{V1}t_{Aj}t_{AQ}g_QQ_{In}. \quad (4.30b)$$

In these equations, the coefficients t_{Aj} and r_{Aj} represent the splitting ratio of the beam splitter used to mix the input state. Under ideal conditions, these coefficients are equal to

$1/\sqrt{2}$. In the experiment, two separate mirrors on flip mounts are placed after the beam splitter, which mixes the input state, to direct the split light into two detectors with equal gain. Before each teleportation measurement, we adjust the flip mounts and monitor the detector readings to fine-tune the splitting ratio, ensuring it matches $t_{AJ} = r_{AJ} = 1/\sqrt{2}$.

Equation 4.30 show that the mean value of the input state measured by Alice is determined by the efficiencies t_{AP} and t_{AQ} . In the presence of losses, we can define two cases of teleportation based on how the state to be teleported is considered. The first case involves teleporting the state measured by Alice, incorporating the losses in Alice's system when defining this state. The second case focuses on teleporting the state as originally sent by Victor to Alice, disregarding any losses in Alice's system. The analysis of the protocol, as well as the associated benchmarks, varies depending on the chosen scenario. A detailed discussion of both cases follows.

4.2.2.1 State Measured by Alice: Uncorrected Losses Scenario

In this teleportation scenario, the considered input state is the one detected at Alice's station, after it has undergone all associated optical losses. This approach assumes that Alice's losses have been previously characterized and their values provided to Victor. Using this knowledge, Victor designs an input state that, after undergoing the loss transformations, results in the desired result at Alice's measurement. While this interpretation is effective for teleporting displaced coherent and thermal states, it becomes challenging for non-classical states of light, where compensating for the loss transformations during state preparation may not be possible. In this work, we refer to this scenario as Alice's uncorrected losses teleportation (AU).

Using Equation 4.30, and considering that Alice's measured mean value must be corrected for the splitting ratio of the mixing beam splitter before comparison with Victor's results, the mean values of the quadratures can be expressed as:

$$\langle \hat{P}_{V\text{Det}} \rangle = -r_{AJ}t_{V1}g_P \left(-\frac{1}{r_{AJ}} \langle P_{ADetP} \rangle \right), \quad (4.31a)$$

$$\langle \hat{Q}_{V\text{Det}} \rangle = t_{AJ}t_{B2}t_{V1}g_Q \left(\frac{1}{t_{AJ}} \langle Q_{ADetQ} \rangle \right). \quad (4.31b)$$

The teleportation gain $\Gamma_{P,Q}$ can then be defined in terms of the electronic gain $g_{P,Q}$ as [50]:

$$\Gamma_P = -r_{AJ}t_{V1}g_P = -\frac{r_{AJ} \langle \hat{P}_{V\text{Det}} \rangle}{\langle P_{ADetP} \rangle}, \quad (4.32a)$$

$$\Gamma_Q = t_{AJ}t_{B2}t_{V1}g_Q = \frac{t_{AJ} \langle \hat{Q}_{V\text{Det}} \rangle}{\langle Q_{ADetQ} \rangle}. \quad (4.32b)$$

For the unitary gain condition, the electronic gain is given by:

$$g_P = -\frac{1}{r_{Aj}t_{V1}}, \quad (4.33a)$$

$$g_Q = \frac{1}{t_{Aj}t_{B2}t_{V1}}. \quad (4.33b)$$

Incorporating the defined teleportation gain for this scenario into the variance of the fields measured at Victor's station, as given by Equation 4.29, we have:

$$\begin{aligned} \Delta^2 \hat{P}_{V\text{Det}} &= \frac{1}{2} \left(e^{-2r_-} \left| \Gamma_P \frac{t_{Aj}}{r_{Aj}} t_{A1} t_{AP} + t_{B1} t_{B2} t_{V1} \right|^2 + e^{2r_+} \left| \Gamma_P \frac{t_{Aj}}{r_{Aj}} t_{A1} t_{AP} - t_{B1} t_{B2} t_{V1} \right|^2 \right) \\ &\quad + \Gamma_P^2 T_{AP} \Delta^2 \hat{P}_{In} \\ &\quad + R_{B1} T_{B2} T_{V1} + R_{B2} T_{V1} + R_{V1} + \Gamma_P^2 \left(\frac{T_{Aj}}{R_{Aj}} R_{A1} T_{AP} + \frac{R_{AP}}{R_{Aj}} \right) \\ &\quad + \frac{\Gamma_P^2}{R_{Aj}} \Delta^2 e_P, \end{aligned} \quad (4.34)$$

$$\begin{aligned} \Delta^2 \hat{Q}_{V\text{Det}} &= \frac{1}{2} \left(e^{-2s_-} \left| \Gamma_Q \frac{r_{Aj}}{t_{Aj}} t_{A1} t_{AQ} + t_{B1} t_{B2} t_{V1} \right|^2 + e^{2s_+} \left| \Gamma_Q \frac{r_{Aj}}{t_{Aj}} t_{A1} t_{AQ} - t_{B1} t_{B2} t_{V1} \right|^2 \right) \\ &\quad + \Gamma_Q^2 T_{AQ} \Delta^2 \hat{Q}_{In} \\ &\quad + R_{B1} T_{B2} T_{V1} + R_{B2} T_{V1} + R_{V1} + \Gamma_Q^2 \left(\frac{R_{Aj}}{T_{Aj}} R_{A1} T_{AQ} + \frac{R_{AQ}}{T_{Aj}} \right) \\ &\quad + \frac{\Gamma_Q^2}{T_{Aj}} \Delta^2 e_Q. \end{aligned} \quad (4.35)$$

Here, we observe that even under unitary gain conditions, the anti-squeezing term is not necessarily zero. It becomes zero only if the signal and idler beams experience identical losses and the mixing beam splitter has a 50:50 splitting ratio. When the losses between the signal and idler beams are unbalanced, one could consider adjusting the splitting ratio to cancel the anti-squeezing term in one quadrature; however, assuming $t_{AP} = t_{AQ}$, this comes at the cost of increased anti-squeezing in the other quadrature.

To determine the quantum advantage benchmark in this scenario, we calculate the variances for the case in which the EPR state is replaced by two coherent states, defined by $r_- = r_+ = s_- = s_+ = 0$. Under this condition, and assuming a splitting ratio of $r_{Aj} = t_{Aj} = 1/\sqrt{2}$, we obtain:

$$\Delta^2 \hat{P}_{V\text{Det}}^{cl} = 1 + \Gamma_P^2 (T_{AP} \Delta^2 \hat{P}_{In} + R_{AP} + 1 + 2\Delta^2 e_P), \quad (4.36a)$$

$$\Delta^2 \hat{Q}_{V\text{Det}}^{cl} = 1 + \Gamma_Q^2 (T_{AQ} \Delta^2 \hat{Q}_{In} + R_{AQ} + 1 + 2\Delta^2 e_Q). \quad (4.36b)$$

Considering a coherent input state, we have:

$$\Delta^2 \hat{P}_{V\text{Det}}^{cl} = 1 + 2\Gamma_P^2 + 2\Gamma_P^2 \Delta^2 e_P, \quad (4.37a)$$

$$\Delta^2 \hat{Q}_{V\text{Det}}^{cl} = 1 + 2\Gamma_Q^2 + 2\Gamma_Q^2 \Delta^2 e_Q. \quad (4.37b)$$

Apart from the electronic noise term, we recover the result for the ideal case presented in Equation 4.19. In this teleportation scenario, it is unnecessary to correct for losses in the quadrature mean values measured at Alice's station, which are used in our implementation to compute the teleportation gain during data evaluation. Furthermore, the fidelity benchmark that demonstrates quantum advantage is based on the classical variance presented in Equation 4.37, which is also independent of the losses. As a result, the entire protocol analysis for this interpretation does not require knowledge of the system's loss values. This allows us to demonstrate quantum advantage directly from the acquired data. Therefore, this scenario is our first choice when presenting the teleportation results.

4.2.2.2 Victor's Prepared State: Corrected Losses Scenario

In this teleportation scenario, the considered input state is the original quantum state created by Victor before sending it to Alice. Consequently, the losses in Alice's system are not considered in the state to be teleported, which determines the gain and is used to evaluate the protocol's performance. In this work, we refer to this scenario as Alice's corrected losses teleportation (AC).

Using Equation 4.30, we have for the teleportation gain:

$$\Gamma_P = \frac{\langle \hat{P}_{V\text{Det}} \rangle}{P_{In}} = -\frac{r_{Aj} t_{AP} \langle \hat{P}_{V\text{Det}} \rangle}{\langle P_{ADetP} \rangle} = -t_{V1} r_{Aj} t_{AP} g_P, \quad (4.38a)$$

$$\Gamma_Q = \frac{\langle \hat{Q}_{V\text{Det}} \rangle}{P_{In}} = \frac{t_{Aj} t_{AQ} \langle \hat{Q}_{V\text{Det}} \rangle}{\langle Q_{ADetQ} \rangle} = t_{B2} t_{V1} t_{Aj} t_{AQ} g_Q. \quad (4.38b)$$

In the case of the unitary condition, the electronic gain can be written as:

$$g_P = -\frac{1}{t_{V1} r_{Aj} t_{AP}}, \quad (4.39a)$$

$$g_Q = \frac{1}{t_{B2} t_{V1} t_{Aj} t_{AQ}}. \quad (4.39b)$$

Comparing the obtained gain with Equation 4.32, we observe that performing the transformations $\Gamma_P \rightarrow t_{AP}\Gamma_P$ and $\Gamma_Q \rightarrow t_{AQ}\Gamma_Q$ recovers the gain for Alice's uncorrected losses scenario. Thus, these transformations can be directly applied to the earlier equations to

obtain the corresponding expressions for this case. However, for clarity and reference, the equations will be explicitly presented here. By substituting the gain in Equation 4.38 into Equation 4.29, the quadrature variances of the teleported state are calculated as:

$$\begin{aligned}\Delta^2 \hat{P}_{V\text{Det}} &= \frac{1}{2} \left(e^{-2r_-} \left| \Gamma_P t_{A1} \frac{t_{Aj}}{r_{Aj}} + t_{B1} t_{B2} t_{V1} \right|^2 + e^{2r_+} \left| \Gamma_P t_{A1} \frac{t_{Aj}}{r_{Aj}} - t_{B1} t_{B2} t_{V1} \right|^2 \right) \\ &\quad + \Gamma_P^2 \Delta^2 \hat{P}_{In} \\ &\quad + R_{B1} T_{B2} T_{V1} + R_{B2} T_{V1} + R_{V1} + \frac{\Gamma_P^2}{R_{Aj} T_{AP}} (R_{A1} T_{Aj} T_{AP} + R_{AP}) \\ &\quad + \frac{\Gamma_P^2}{R_{Aj} T_{AP}} \Delta^2 e_P,\end{aligned}\tag{4.40}$$

$$\begin{aligned}\Delta^2 \hat{Q}_{V\text{Det}} &= \frac{1}{2} \left(e^{-2s_-} \left| \Gamma_Q t_{A1} \frac{r_{Aj}}{t_{Aj}} + t_{B1} t_{B2} t_{V1} \right|^2 + e^{2s_+} \left| \Gamma_Q t_{A1} \frac{r_{Aj}}{t_{Aj}} - t_{B1} t_{B2} t_{V1} \right|^2 \right) \\ &\quad + \Gamma_Q^2 \Delta^2 \hat{Q}_{In} \\ &\quad + R_{B1} T_{B2} T_{V1} + R_{B2} T_{V1} + R_{V1} + \frac{\Gamma_Q^2}{T_{Aj} T_{AQ}} (R_{A1} R_{Aj} T_{AQ} + R_{AQ}) \\ &\quad + \frac{\Gamma_Q^2}{T_{Aj} T_{AQ}} \Delta^2 e_Q.\end{aligned}\tag{4.41}$$

The variances in the classical case, where no quantum correlations are utilized, are expressed as follows:

$$\Delta^2 \hat{P}_{V\text{Det}} = 1 + \Gamma_P \left(\Delta^2 P_{In} + \frac{T_{Aj}}{R_{Aj}} + \frac{R_{AP}}{R_{Aj} T_{AP}} + \frac{1}{R_{Aj} T_{AP}} \Delta^2 e_P \right),\tag{4.42a}$$

$$\Delta^2 \hat{Q}_{V\text{Det}} = 1 + \Gamma_Q \left(\Delta^2 Q_{In} + \frac{R_{Aj}}{T_{Aj}} + \frac{R_{AQ}}{T_{Aj} T_{AQ}} + \frac{1}{T_{Aj} T_{AQ}} \Delta^2 e_Q \right).\tag{4.42b}$$

These expressions reveal that only Alice's losses affect the performance of the classical system. This occurs because the electronic gain can be adjusted to compensate for the losses on Bob's and Victor's stations [47]. Considering a coherent input state and a splitting ratio of $r_{Aj} = t_{Aj} = 1/\sqrt{2}$, the above equations simplify to:

$$\Delta^2 \hat{P}_{V\text{Det}}^{cl} = 1 + 2 \frac{\Gamma_P^2}{T_{AP}} + 2 \frac{\Gamma_P^2}{T_{AP}} \Delta^2 e_P,\tag{4.43a}$$

$$\Delta^2 \hat{Q}_{V\text{Det}}^{cl} = 1 + 2 \frac{\Gamma_Q^2}{T_{AQ}} + 2 \frac{\Gamma_Q^2}{T_{AQ}} \Delta^2 e_Q.\tag{4.43b}$$

When compared to Equation 4.37 for the uncorrected losses scenario, the only modification is the division of the gain terms, $\Gamma_{P,Q}$, by the transmission coefficients t_{AP} and t_{AQ} . Since these transmissions are less than one, this result implies that when Alice's losses are taken into account, the classically achievable quadrature variance under the unitary gain condition will always be greater than 3.

4.2.2.3 Loss Compensation in Victor Measurements

Victor's setup, which receives the teleported state and performs the tomography measurement, is also susceptible to optical losses that can affect the fidelity of the transmitted quantum information. These losses can also be corrected during the data evaluation phase, enabling the recovery of the teleported state at the output of Bob's station. In this work, the application of this correction is referred to as the Victor corrected losses scenario.

By modeling the losses as beam splitter transformations, we can correct both the mean value and the variances of Victor's measurements to recover the expected values at Bob's station output. This is achieved using the following relations:

$$\langle \delta \hat{X}_{BLCorr} \rangle = \frac{1}{t_{V1}} \langle \delta \hat{X}_{VDet} \rangle, \quad (4.44a)$$

$$\Delta^2 \hat{X}_{BLCorr} = \frac{\Delta^2 \hat{X}_{VDet} - R_{V1}}{T_{V1}}, \quad (4.44b)$$

where \hat{X} represents either the amplitude or phase quadrature. In our formulation, this corresponds to setting $t_{V1} = 1$ and $r_{V1} = 0$ in Equation 4.28, as well as in all related derived equations. Therefore, the definitions of the gain in Equations 4.32 and 4.38 are adjusted to reflect the use of the mean value at Bob's output for comparison. As noted earlier, the classical benchmark remains unchanged by this correction, since the expected classical variances in Equations 4.36 and 4.42 are independent of Victor's losses.

4.2.3 Experimental Adjustment of Gain

To properly execute the teleportation protocol, the gain values, $\Gamma_{P,Q}$, must be precisely adjusted. In the experiment, this tuning is achieved using a variable-gain amplifier and a phase shifter in each electronic classical channel associated with each quadrature. The quantum correlations between the signal and idler cannot be used for this adjustment due to their low-noise characteristics, which provide insufficient sensitivity for optimal tuning. To overcome this limitation, we establish strong classical correlations between the fields, which serve as a reference for the gain tuning process. These correlations are generated by modulating the pump beam, which coherently transfers the modulation to both the signal and idler. Specifically, amplitude modulation is achieved using an acousto-optic modulator (AOM) by modulating the high-frequency oscillating electric signal that drives it. Phase modulation, on the other hand, is implemented via an electro-optic modulator (EOM) by directly applying the modulation voltage to the EOM. The modulation frequency matches the sideband modes being teleported, resulting in positive correlations between the quadrature values of these modes.

To perform the gain adjustment, the input state creation path of the Mach-Zehnder interferometer is first blocked. The process begins with phase modulation of the pump beam. By monitoring Victor's measurement noise levels at the analysis frequency using a spectrum analyzer, we minimize the noise by carefully tuning the variable gain and phase shifter in the phase quadrature classical channel. Once the phase gain is optimized, the same procedure is repeated, but with amplitude modulation applied to the pump beam. After completing this process, a π phase shift must be introduced to invert the signal in the phase quadrature classical channel, as will become evident in the following steps.

While the modulation and tuning of the phase and amplitude quadratures are experimentally performed sequentially, in the treatment presented below we address both simultaneously. As mentioned, the gain adjustment process introduces modulations P_M and Q_M into the signal and idler beams:

$$\hat{a}_A^{ga} = \alpha_A + \frac{1}{2} [\delta\hat{P}_A + P_M + i(\delta\hat{Q}_A + Q_M)], \quad (4.45a)$$

$$\hat{a}_B^{ga} = \alpha_B + \frac{1}{2} [\delta\hat{P}_B + P_M + i(\delta\hat{Q}_B + Q_M)]. \quad (4.45b)$$

The modulated beams pass through the system, experiencing the associated optical losses. The mean quadrature values of the fields, as measured at Alice's and Victor's stations, are given by:

$$\langle \delta\hat{P}_{ADetP} \rangle = t_{A1}t_{Aj}t_{AP}P_M, \quad (4.46a)$$

$$\langle \delta\hat{Q}_{ADetQ} \rangle = t_{Aj}r_{Aj}t_{AQ}Q_M, \quad (4.46b)$$

$$\langle \delta\hat{P}_{VDet} \rangle = t_{B1}t_{B2}t_{V1}P_M + t_{V1}g_P \langle \delta\hat{P}_{ADetP} \rangle, \quad (4.46c)$$

$$\langle \delta\hat{Q}_{VDet} \rangle = t_{B1}t_{B2}t_{V1}Q_M + t_{B2}t_{V1}g_Q \langle \delta\hat{Q}_{ADetQ} \rangle. \quad (4.46d)$$

In Victor's mean value expressions, the second term accounts for the classical channel transmitting Alice's measurement results. By substituting Alice's equation into Victor's equation, we find:

$$\langle \delta\hat{P}_{VDet} \rangle = t_{V1}(t_{B1}t_{B2} + t_{A1}t_{Aj}t_{AP}g_P)P_M, \quad (4.47a)$$

$$\langle \delta\hat{Q}_{VDet} \rangle = t_{B2}t_{V1}(t_{B1} + t_{Aj}r_{Aj}t_{AQ}g_Q)Q_M. \quad (4.47b)$$

During the gain adjustment process, the electronic gain parameters $g_{P,Q}$ are tuned to minimize the noise in Victor's measurement. The optimal tuning condition, achieved when Equation 4.47 equals zero, is given by:

$$g_P = -\frac{t_{B1}t_{B2}}{t_{A1}t_{AJ}t_{AP}}, \quad (4.48a)$$

$$g_Q = -\frac{t_{B1}}{t_{A1}r_{AJ}t_{AQ}}. \quad (4.48b)$$

This equation differs from the electronic gain under the unitary teleportation condition presented in Equations 4.33 and 4.39. Notably, the signal in g_Q is opposite to that of unitary teleportation. This discrepancy arises because the created classical correlations are positive, whereas the quantum correlations in the phase quadrature are negative. To account for this, a π phase shift is applied to this channel after the gain adjustment procedure, effectively inverting the electronic signal.

Although the adjusted gain does not perfectly match the desired gain for unitary teleportation, for a fixed beam power, the difference depends only on the system losses, which remain stable over time. This stability facilitates a straightforward calibration process. Specifically, after executing the teleportation protocol following the gain adjustment procedure, the teleportation gain $\Gamma_{P,Q}$ can be determined. Using this calculated $\Gamma_{P,Q}$, the offset between the experimentally achieved electronic gain and the theoretical values from Equations 4.33 and 4.39 can be computed. By applying this offset to subsequent gain adjustments, it is possible to achieve unitary gain conditions for the corrected and uncorrected losses scenarios of Alice and Victor. Moreover, when losses are low and the mixing beamsplitter has a 50:50 splitting ratio ($r_{Aj} = t_{Aj} = 1/\sqrt{2}$), all electronic gains (Equations 4.33 and 4.39) at the unitary condition, as well as the gain derived from the described procedure, converge to $g_Q = -g_P = \sqrt{2}$.

4.3 Evaluating the Protocol Success: Fidelity

In the development and operation of any communication process, it is essential to continuously evaluate the success of the protocol being employed. Given the inherent imperfections of practical systems, achieving flawless communication is fundamentally impossible. Consequently, it becomes necessary to define a figure of merit for the communication performance. However, when dealing with quantum states, direct measurement of the states involved is insufficient to fully characterize them or enable a comprehensive comparison between the input and output states. This limitation arises from the fundamental principles of quantum mechanics, such as the no-cloning theorem and measurement-induced state collapse, which restrict the amount of retrievable information.

To address this challenge, the involvement of an external entity, referred to here as Victor, the verifier, becomes essential. When the performance of the protocol needs to be evaluated, either for routine validation or to investigate observed anomalies, Victor

provides the input state and receives the corresponding output state. Through repeated executions of the protocol, Victor statistically reconstructs the produced quantum state using techniques such as quantum state tomography. He then compares the reconstructed state with his prior knowledge of the prepared input state. Such a comparison provides a robust framework for assessing the overall performance of the protocol, ensuring that the system functions within acceptable parameters and diagnosing deviations from expected behavior.

The fidelity is the most widely used and fundamental figure of merit for comparing two quantum states [121, 132, 133]. It provides a clear measure of the similarity between two quantum states, serving as a critical tool for evaluating the effectiveness of quantum protocols. The quantum fidelity between two states, denoted as $\hat{\rho}_1$ and $\hat{\rho}_2$, is defined by [134, 135]:

$$\mathcal{F}(\hat{\rho}_1, \hat{\rho}_2) = \left[\text{Tr} \left(\sqrt{\sqrt{\hat{\rho}_2} \hat{\rho}_1 \sqrt{\hat{\rho}_2}} \right) \right]^2. \quad (4.49)$$

The fidelity has the following key properties:

1. **Range and Equality Condition:** $0 \leq \mathcal{F}(\hat{\rho}_1, \hat{\rho}_2) \leq 1$, where $\mathcal{F}(\hat{\rho}_1, \hat{\rho}_2) = 1$ if and only if $\hat{\rho}_1 = \hat{\rho}_2$. This implies that the fidelity reaches its maximum value when the two states are identical, and its minimum when the states are completely orthogonal.
2. **Symmetry:** $\mathcal{F}(\hat{\rho}_1, \hat{\rho}_2) = \mathcal{F}(\hat{\rho}_2, \hat{\rho}_1)$. Fidelity is symmetric with respect to the two states being compared.
3. **Simplification for Pure States:** If either $\hat{\rho}_1$ or $\hat{\rho}_2$ is a pure state, fidelity simplifies to the overlap of the two states: $\mathcal{F}(\hat{\rho}_1, \hat{\rho}_2) = \text{Tr}(\hat{\rho}_1 \hat{\rho}_2)$. For pure states $|\psi\rangle$ and $|\phi\rangle$, fidelity reduces to the squared modulus of their inner product: $\mathcal{F}(\hat{\rho}_\psi, \hat{\rho}_\phi) = |\langle \psi | \phi \rangle|^2$.
4. **Invariance under Unitary Transformations:** Fidelity remains unchanged under unitary operations applied to both states: $\mathcal{F}(U\hat{\rho}_1 U^\dagger, U\hat{\rho}_2 U^\dagger) = \mathcal{F}(\hat{\rho}_1, \hat{\rho}_2)$, where U is any unitary operator. This property highlights fidelity's independence from the choice of reference frame or basis transformations.

By calculating the fidelity between the input and output states, we can rigorously assess the quality of the teleportation protocol, identify sources of error, and determine how well the quantum system preserves information. In the special case where one of the quantum states is pure, the fidelity simplifies to $\mathcal{F}(\hat{\rho}_1, \hat{\rho}_2) = \text{Tr}(\hat{\rho}_1 \hat{\rho}_2)$, as noted in item 3 above. When the Wigner function is used to represent quantum states, the following identity becomes particularly useful [69]:

$$\text{Tr}(\hat{\rho}_1 \hat{\rho}_2) = \left(\frac{\pi}{4}\right)^n \int d^{2n}x W[\hat{\rho}_1](\mathbf{x}) W[\hat{\rho}_2](\mathbf{x}), \quad (4.50)$$

where $W[\hat{\rho}](\mathbf{x})$ refers to the Wigner function associated with the density matrix $\hat{\rho}$, n corresponds to the number of modes, and \mathbf{x} represents the phase-space coordinates arranged in the vector $\mathbf{x} = (p_1, q_1, \dots, p_n, q_n)^T$. Using this identity, the teleportation fidelity for a pure input state can be expressed in terms of the Wigner functions as:

$$\mathcal{F}(\hat{\rho}_{in}, \hat{\rho}_{out}) = \left(\frac{\pi}{4}\right)^n \int d^{2n}x W[\hat{\rho}_{in}](\mathbf{x}) W[\hat{\rho}_{out}](\mathbf{x}). \quad (4.51)$$

For Gaussian states, the corresponding Wigner functions are given by:

$$W[\hat{\rho}_{\text{Gauss}}](\mathbf{x}) = \left(\frac{2}{\pi}\right)^n \frac{1}{\sqrt{\det \mathbf{V}}} \exp\left[-\frac{1}{2}(\mathbf{x} - \langle \hat{\mathbf{x}} \rangle)^T \mathbf{V}^{-1} (\mathbf{x} - \langle \hat{\mathbf{x}} \rangle)\right], \quad (4.52)$$

where $\langle \hat{\mathbf{x}} \rangle = [\langle \hat{p}_1 \rangle, \langle \hat{q}_1 \rangle, \dots, \langle \hat{p}_n \rangle, \langle \hat{q}_n \rangle]^T$ is the vector containing the mean quadrature values, while \mathbf{V} is the covariance matrix describing the quantum state, with \mathbf{V}^{-1} being its inverse.

To motivate the choice of fidelity as a performance metric for the teleportation protocol, let us examine the behavior of an observable \hat{A} . This observable can be expressed in terms of projection operators \hat{E}_α associated with eigenvalues α . For the input and output states, the probability densities of measuring the outcome α are given by:

$$P_{in}(\alpha) = \text{Tr}(\hat{\rho}_{in} \hat{E}_\alpha), \quad (4.53a)$$

$$P_{out}(\alpha) = \text{Tr}(\hat{\rho}_{out} \hat{E}_\alpha). \quad (4.53b)$$

The similarity between these two probability distributions can be quantified by their overlap, which is bounded by the fidelity [121, 136]:

$$\left(\int d\alpha \sqrt{P_{in}(\alpha) P_{out}(\alpha)} \right)^2 \geq \mathcal{F}(\hat{\rho}_{in}, \hat{\rho}_{out}), \quad (4.54)$$

this inequality is independent of the specific observable chosen. Therefore, the fidelity provides a robust lower limit for comparing the measurement outcomes of any observable for the two states.

4.3.1 Fidelity for Specific Quantum States

In this section, we present explicit analytical expressions for the teleportation fidelity when applied to specific types of input and output states. The analysis is confined

to a single Gaussian mode for both the input and output states, utilizing the single-sideband framework, in which the lower and upper sideband modes are collectively treated as a unified mode (Section 3.2.3). The discussion centers on coherent and thermal input states, as these are both fundamental to quantum optics and can be readily generated using the experimental setup at Victor's station. It is important to note that the output state is always a mixed state, therefore, the input state's purity determines if the previously discussed simplification (Equation 4.51) can be applied.

4.3.1.1 Coherent Input State

In this analysis, we consider a single-mode coherent input state characterized by a mean value $\langle \hat{\mathbf{X}}_{in} \rangle$ and a covariance matrix \mathbf{V}_{in} , defined as $\mathbf{V}_{in} = I_2$, where I_2 denotes the 2×2 identity matrix. For the output state, we begin with the assumption that its noise ellipse is aligned with the quadrature axes. This state is described by a mean value $\langle \hat{\mathbf{X}}_{out} \rangle$ and a diagonal covariance matrix:

$$\mathbf{V}_{out} = \begin{pmatrix} \alpha_{out} & 0 \\ 0 & \beta_{out} \end{pmatrix}, \quad (4.55)$$

where $\alpha_{out} = \Delta^2 \hat{P}_{out}^2$ and $\beta_{out} = \Delta^2 \hat{Q}_{out}^2$ are the variances in the respective quadratures. Since both the input and output states are single-mode ($n = 1$), and off-diagonal terms in their covariance matrices are zero, the Wigner function for these Gaussian states, as derived from Equation 4.52, is expressed as:

$$W[\hat{\rho}](X) = \frac{2}{\pi} \frac{\exp \left[-\frac{1}{2} \left(\frac{(P - \langle \hat{P} \rangle)^2}{\alpha} + \frac{(Q - \langle \hat{Q} \rangle)^2}{\beta} \right) \right]}{\sqrt{\alpha\beta}}. \quad (4.56)$$

Using the purity of the input coherent state, the fidelity is computed by integrating the product of the Wigner functions (Equation 4.51) for the input and output states:

$$\mathcal{F} = \frac{1}{\pi} \int \int dP dQ \exp \left[-\frac{1}{2} \left((P - \langle \hat{P}_{in} \rangle)^2 + (Q - \langle \hat{Q}_{in} \rangle)^2 \right) \right] \frac{\exp \left[-\frac{1}{2} \left(\frac{(P - \langle \hat{P}_{out} \rangle)^2}{\alpha_{out}} + \frac{(Q - \langle \hat{Q}_{out} \rangle)^2}{\beta_{out}} \right) \right]}{\sqrt{\alpha_{out}\beta_{out}}}. \quad (4.57)$$

By performing the integrals, the fidelity simplifies to:

$$\mathcal{F}_{C_{in}} = \frac{2}{\sqrt{(1 + \alpha_{out})(1 + \beta_{out})}} \exp \left[-\frac{1}{2} \left(\frac{(\langle \hat{P}_{out} \rangle - \langle \hat{P}_{in} \rangle)^2}{1 + \alpha_{out}} + \frac{(\langle \hat{Q}_{out} \rangle - \langle \hat{Q}_{in} \rangle)^2}{1 + \beta_{out}} \right) \right]. \quad (4.58)$$

The obtained fidelity expression reveals that the multiplicative term depends only on the variances of the teleported state, while the exponential term accounts for the difference in mean values between the input and output states. This equation accurately represents the experimental scenario in which the quadratures of the output state exhibit distinct variances. As mentioned earlier, the amount of two-mode squeezing in the shared bipartite EPR state fundamentally limits the maximum fidelity achievable in the teleportation protocol. Using Equation 4.24, which describes the lossless teleportation output state, and assuming equal squeezing parameters for the amplitude and phase quadratures ($r = r_- = s_-$), the maximum fidelity under the unitary gain condition (where input and output mean values coincide) is:

$$\mathcal{F}_{C_{in}}^{max} = \frac{1}{1 + e^{-2r}}. \quad (4.59)$$

This expression shows that perfect teleportation, characterized by unitary fidelity ($\mathcal{F} = 1$), requires infinite squeezing ($r \rightarrow \infty$), a condition that is not possible to achieve in practice.

In the experiment, a non-ideal rotation of the noise ellipse may occur in Bob's cavity, leading to a misalignment angle between the noise ellipse of the output state and the quadrature axes. The fidelity expression derived in Equation 4.58 does not account for this experimental imperfection. To address this more general scenario, we extend the fidelity expression to include an output state with non-zero off-diagonal terms in the covariance matrix:

$$\mathbf{V}_{out} = \begin{pmatrix} \alpha_{out} & \gamma_{out} \\ \gamma_{out} & \beta_{out} \end{pmatrix}, \quad (4.60)$$

where $\gamma_{out} = C(\hat{P}_{out}, \hat{Q}_{out})$ represents the covariance between the quadratures, introduced by the misaligned noise ellipse. Under these conditions, the fidelity is expressed as:

$$\mathcal{F}_{C_{in}} = \frac{2}{\sqrt{\Delta_{out}}} \exp \left[-\frac{1}{2\Delta_{out}} (\mathcal{P}_{out-in}^2 (1 + \beta_{out}) + \mathcal{Q}_{out-in}^2 (1 + \alpha_{out}) - 2\mathcal{P}_{out-in}\mathcal{Q}_{out-in}\gamma_{out}) \right], \quad (4.61)$$

where $\mathcal{P}_{out-in} = \langle \hat{P}_{out} \rangle - \langle \hat{P}_{in} \rangle$ and $\mathcal{Q}_{out-in} = \langle \hat{Q}_{out} \rangle - \langle \hat{Q}_{in} \rangle$ quantify the differences in the mean values of the quadratures, and the term $\Delta_{out} = (1 + \alpha_{out})(1 + \beta_{out}) - \gamma_{out}^2$ incorporates both variance and covariance elements of the output state.

4.3.1.2 Thermal Input State

Experimentally, an input state with excess noise in the quadratures can be generated by introducing white Gaussian noise into the electronic signal that drives the electro-optic

modulator (EOM) used for the input state creation. Such states are commonly referred to as thermal states. While this terminology is widely used, it is important to note that a thermal state is formally defined as a zero-mean Gaussian state with symmetric excess noise in both quadratures [137], as described in Section 2.1.3.2.

A feature of a thermal state is the determinant of its covariance matrix is greater than 1, which implies that the state is mixed (not pure) [69]. Consequently, the simplified approach of Equation 4.51 cannot be applied to compute the fidelity. Instead, the fidelity must be calculated using the general formalism provided in Equation 4.49. The general expression for the fidelity between two single-mode mixed Gaussian states has been derived in the literature and is presented in [138, 139]. In these conditions, the fidelity is given by:

$$\mathcal{F}_{T_{in}} = \frac{2 \exp \left[-\frac{1}{2} \left(\langle \hat{\mathbf{X}}_{out} \rangle - \langle \hat{\mathbf{X}}_{in} \rangle \right)^T (\mathbf{V}_{in} + \mathbf{V}_{out})^{-1} \left(\langle \hat{\mathbf{X}}_{out} \rangle - \langle \hat{\mathbf{X}}_{in} \rangle \right) \right]}{\sqrt{\Delta + \Theta} - \sqrt{\Theta}}, \quad (4.62)$$

where the parameters Δ and Θ depend on the covariance matrices of the states:

$$\Delta = \det(\mathbf{V}_{in} + \mathbf{V}_{out}) \geq 1, \quad (4.63a)$$

$$\Theta = [\det(\mathbf{V}_{in}) - 1][\det(\mathbf{V}_{out}) - 1]. \quad (4.63b)$$

4.3.2 Teleportation Protocol Benchmarks

Given a quantum protocol and a methodology for quantifying its performance, it is possible to establish benchmarks that characterize performance regimes where certain conditions are satisfied. In this section, we present two fidelity benchmarks for the continuous-variable teleportation protocol. The first is the classical limit, which defines the threshold at which the protocol demonstrates quantum advantage outperforming all classical alternatives. The second is the no-cloning limit, which guarantees that the best possible reconstruction of the input state resides with Bob, ensuring that no other party can possess it, a property with direct relevance for quantum cryptography.

4.3.2.1 Classical Limit

A teleportation attempt can be performed without utilizing quantum resources, i.e., without relying on an entangled state. This classical teleportation protocol can be described by assuming that the EPR station sends two coherent states to Alice and Bob stations [121]. The use of two coherent states is justified as they are the separable states that maximize fidelity in this case. In the lossless scenario described in Equation

[4.23](#), assuming no quantum correlations ($r_- = s_- = 0$) and unitary gain condition, the teleported state quadratures are expressed as:

$$\delta\hat{P}_B^{out,cl} = (\delta\hat{P}_{in} + P_{in}) + \delta\hat{P}_A + \delta\hat{P}_B, \quad (4.64a)$$

$$\delta\hat{Q}_B^{out,cl} = (\delta\hat{Q}_{in} + Q_{in}) + \delta\hat{Q}_A + \delta\hat{Q}_B. \quad (4.64b)$$

When the input is a coherent state, the variances of all the fluctuation terms are equal to one. As a result, the teleported state quadratures have the following mean values and variances:

$$\langle\delta\hat{P}_B^{out,cl}\rangle = P_{in}, \quad \langle\delta\hat{Q}_B^{out,cl}\rangle = Q_{in}, \quad (4.65a)$$

$$\Delta^2\hat{P}_B^{out,cl} = 3, \quad \Delta^2\hat{Q}_B^{out,cl} = 3. \quad (4.65b)$$

By substituting these values into the fidelity expression in [Equation 4.58](#), we find for the classical teleportation fidelity of a coherent state:

$$\mathcal{F}_{C_{in}}^{cl} = \frac{1}{2}. \quad (4.66)$$

In this result, we considered an ideal system: the states involved have no excess noise, the teleportation setup is free from optical losses and electronic noise, and the gain is perfectly adjusted to the unitary condition. Given these ideal conditions, the fidelity obtained represents the maximum achievable for a classical attempt, corresponding to the classical limit of the protocol. Achieving a fidelity greater than this classical limit indicates the utilization of quantum resources in the teleportation process. A teleportation system that surpasses this threshold has the capacity to transfer quantum states with greater accuracy than is possible with any classical method based on local states and classical communication.

We can also compare a quantum teleportation implementation with a classical approach under identical experimental conditions. This comparison allows us to demonstrate the quantum advantage in specific real-world scenarios, which are less restrictive than the idealized limit derived above. To determine the classical limit in a practical setting, we calculate the fidelity using the variances of the teleported state, assuming unitary gain and no quantum correlations between Alice's and Bob's fields. For a coherent input state and considering optical losses across the system, these variances were derived in [Section 4.2.2](#) for both uncorrected and corrected cases of Alice's losses and additional electronic noise. As noted earlier, losses at Victor's tomography measurement do not impact the classically teleported state at the proper unitary gain condition.

The maximum classical fidelity of the teleported state in Alice's uncorrected losses scenario (AU) is determined using the variances from Equation 4.37, which account for additional electronic noise. The fidelity is given by:

$$\mathcal{F}_{C_{in},AU}^{cl} = \frac{2}{\sqrt{(4 + 2\Delta^2 e_P)(4 + 2\Delta^2 e_Q)}}. \quad (4.67)$$

In the case where the electronic noise is equal in both quadratures, such that $\Delta^2 e_P = \Delta^2 e_Q = \Delta^2 e$, the fidelity simplifies to:

$$\mathcal{F}_{C_{in},AU}^{cl} = \frac{1}{2 + \Delta^2 e}. \quad (4.68)$$

These equations define the classical limit when Alice's measurement defines the input state. In this framework, optical losses on Alice's side are already factored into the input state's definition. Therefore, this classical limit is independent of her losses, with electronic noise being the only remaining imperfection considered. For low electronic noise ($\Delta^2 e \rightarrow 0$), the expression recovers the idealized classical limit of 1/2 given in Equation 4.66. Therefore, surpassing the fidelity from Equation 4.67 demonstrates a quantum advantage over a classical protocol with equivalent electronic noise. While this is an important check, the ultimate goal remains to surpass the ideal benchmark of 1/2, which represents the best possible classical performance under any circumstance.

In the case of Alice's corrected losses (AC), the quadrature variances of the classically teleported state are presented in Equation 4.43. The corresponding fidelity at unitary gain is given by:

$$\mathcal{F}_{C_{in},AC}^{cl} = \frac{2}{\sqrt{\left(2 + \frac{2+2\Delta^2 e_P}{T_{AP}}\right)\left(2 + \frac{2+2\Delta^2 e_Q}{T_{AQ}}\right)}}. \quad (4.69)$$

When assuming equal losses in amplitude and phase quadrature detection, $T_{AP} = T_{AQ} = T_{AD}$, and identical electronic noise levels, the fidelity simplifies to:

$$\mathcal{F}_{C_{in},AC}^{cl} = \frac{T_{AD}}{1 + T_{AD} + \Delta^2 e}. \quad (4.70)$$

We observe that when attempting to teleport the original input state as created by Victor, losses in Alice's system also impact the performance of the classical approach. It is important to note that the classical limits derived here are applicable only when teleportation is performed over the set of coherent states. For any other set of input states, these benchmarks must be re-evaluated to fit the properties of the chosen states.

4.3.2.2 No-Cloning Limit

A second important benchmark in the context of quantum teleportation with continuous-variables is the no-cloning limit [140, 141]. Although exceeding the classical limit verifies the use of entanglement, it does not guarantee that additional copies of the teleported state do not exist.

For instance, Alice might attempt to clone the input state by extracting partial information using a beam splitter before combining it with her share of the EPR state. Another equivalent scenario involves an eavesdropper, referred to as Eve, who has access to the classical channel and to the losses along one transmission line of the EPR state. In this case, Eve could attempt to construct her own version of the teleported state.

Exceeding the no-cloning limit guarantees that the most accurate copy of the input state resides with Bob, ensuring that no other party, such as Alice or Eve, can possess a better version of it. In the general case, where M copies of the coherent input state are produced, the no-cloning limit is expressed as:

$$\mathcal{F}_{C_{in}}^{M,\text{cloning}} = \frac{M}{2M-1}. \quad (4.71)$$

This value represents the maximum fidelity achievable if M identical copies of the teleported state exist using perfect quantum resources. Exceeding this fidelity limit implies that, among the M copies, the one in Bob's possession has a higher fidelity with the input state than the others. It is interesting to note that for an infinite amount of copies $M \rightarrow \infty$, the no-cloning limit is equal to the classical limit $\mathcal{F}_{C_{in}}^{\infty,\text{cloning}} = \mathcal{F}_{C_{in}}^{\text{cl}} = 1/2$. This result reflects the idea that any process capable of producing infinite clones is fundamentally classical, and the maximum fidelity of a classically teleportation is exactly 1/2.

In the most restrictive case of the no-cloning limit, where there are only two copies ($M = 2$), for instance, one copy with Bob and the other with Alice or Eve, the fidelity limit is given by:

$$\mathcal{F}_{C_{in}}^{2,\text{cloning}} = \frac{2}{3}. \quad (4.72)$$

Therefore, to ensure that the best existing copy of the input state is in Bob's possession, it is necessary to obtain a fidelity greater than 2/3. According to the Equation 4.59, this condition requires a minimum two-mode squeezing parameter of $r > \ln 2/2 \approx 0.35$, assuming equal squeezing in amplitude and phase $r_- = s_- = r$. Using Equation 4.5, we obtain that this condition for the two-mode squeezing is equivalent to:

$$\Delta^2 \hat{P}_- = \Delta^2 \hat{Q}_+ \leq \frac{1}{2}, \quad (4.73)$$

which implies that the subtraction of amplitude and sum of phase quadratures of the EPR state must show at least $-3dB$ of squeezing relative to the vacuum noise.

The no-cloning limit is very important for applications related to communication using quantum teleportation. Reaching this limit is desirable, but in our case, it is a secondary objective, the primary goal is to demonstrate that the quantum channel constructed between different frequencies can execute a quantum information protocol using quantum resources and achieving quantum advantage. Therefore, the classical limit is the main benchmark we use to evaluate the success of our teleportation.

Part II

Experimental Development and Results

5 EXPERIMENTAL SETUP

This chapter provides a comprehensive description of the experimental setup used in this work, focusing on both its construction and operational characteristics. A schematic diagram of the setup is presented in Figure 17. While the project was executed collaboratively, I assumed primary responsibility for all critical aspects, including decision-making, system design, construction, and performance characterization. It should be noted that the spectral filtration system for the pump beam was already operational prior to the start of this study [142, 143], the nonlinear crystal was available but uncharacterized [144], and the vacuum chamber had been constructed [59, 145]. The acquisition data boards were also accessible [143, 146], while all additional components were designed, assembled, and refined during the course of this doctoral research.

This chapter begins by introducing the primary light source used in the experiment, the Diabolo laser (532 nm), along with the procedures employed to prepare its beam as the pump source for the optical parametric oscillator (OPO). These procedures include spectral filtering of the beam using a filter cavity, which is designed to attenuate noise in the pump laser. The discussion then transitions to the central component of the experiment, the OPO, which generates intense entangled beams at widely separated frequencies that serve as the quantum resource in this study. A detailed description of the OPO components and the auxiliary systems required for its proper operation is provided. Subsequently, the chapter outlines the experimental setup for the teleportation protocol, including the preparation of the input state, the configurations of Alice's and Bob's stations, and the quantum tomography station operated by Victor. Finally, the detection system is described, encompassing the electronic signal processing and data acquisition stages, as well as the classical communication channel, essential for enabling the exchange of classical information required in the teleportation protocol.

5.1 Laser Source

The primary laser source, which is used to pump the OPO, is a commercial DPSS (diode-pumped solid-state) laser manufactured by the German company *InnoLight GmbH*, of the model *Diabolo*. It operates by utilizing two high-intensity diode lasers at 808 nm to pump a monolithic Nd:YAG (neodymium-doped yttrium aluminum garnet) crystal configured in a ring resonator setup, resulting in the generation of an intense 1064 nm laser beam. This beam's frequency is then doubled in an external cavity with a nonlinear crystal through second harmonic generation, producing an intense beam at 532 nm, which serves as the main output of the Diabolo laser. Relevant parameters of the laser can be

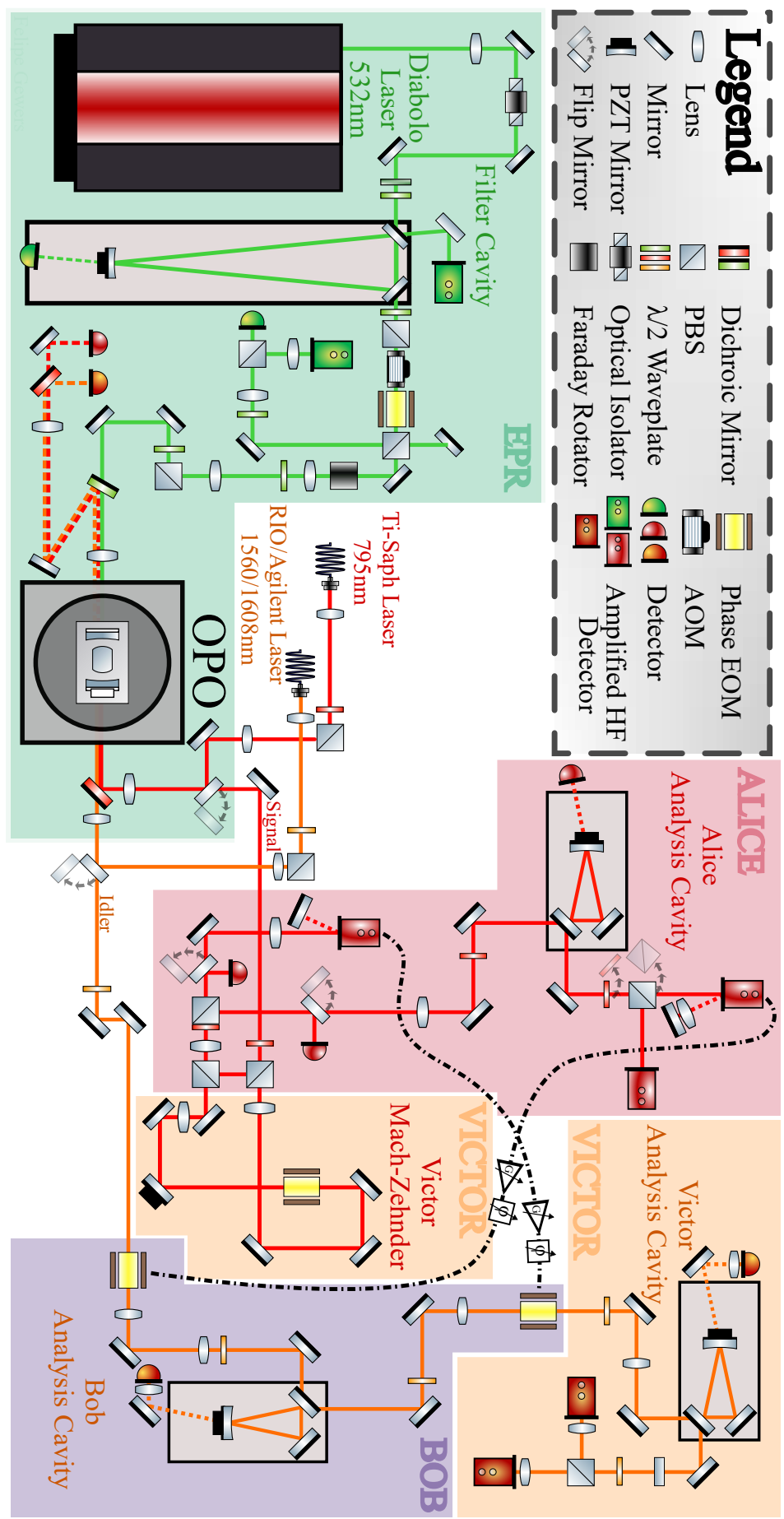


Figure 17 – Schematic of the optical setup used in the teleportation experiment.

found in Table 2.

Table 2 – Relevant parameters of the Diabolo laser, which is used as the pump for the OPO.

Diabolo laser parameter	Value
Maximum output intensity	900 mW
Wavelength	532 nm
Linewidth	1 kHz
Coherence length	> 1 km
Frequency drift	2 MHz/min
Pound-Drever-Hall lock frequency	12 MHz
Relative Intensity Noise (RIN) - Noise eater activated	< -140 dB/Hz

The stability of the frequency doubling cavity is maintained through the utilization of the Pound-Drever-Hall (PDH) locking technique [147]. This essential locking system is an integral component of the Diabolo laser and operates with a 12 MHz modulation. However, it is important to note that this modulation affects the manipulation and measurement of the sideband modes at 12 MHz and its second harmonic at 24 MHz. As a result, we avoid operating near these frequencies and use dedicated electronic filters for 12 MHz in our detection system, as further explained in the next sections.

In previous studies, our group found that although the Diabolo laser has a relatively low noise compared to other options in the laboratory, it still produces considerable noise for our needs. According to [142], the amplitude noise is only comparable to shot noise for analysis frequencies above 25 MHz. Even for these frequencies, as indicated by the ellipse rotation described in [148], we have more than 3.5 units of shot noise in the phase quadrature at 27 MHz. This excessive noise justifies the need for a filter cavity, which we will discuss in more detail later on, as a noisy pump field negatively affects the two-mode squeezing of the OPO's generated fields [92].

Considering our aim to develop a quantum channel between the 790 – 795 nm wavelength range and telecommunications bands, selecting a 532 nm laser as the pump for the OPO necessitates, due to energy conservation principles, generating the entangled counterpart in the long wavelengths L-band of the telecommunications spectrum (1565 – 1625 nm) rather than the conventional C-band (1530 – 1565 nm) [13]. This choice was made primarily due to the availability of the laser in the laboratory, but also because frequency-doubled Nd:YAG ring lasers are widely used commercially available systems known for their exceptionally low intrinsic frequency and amplitude noise levels. Additionally, these lasers offer the flexibility to achieve various power levels, ranging from submilliwatts to tens of watts [149].

The telecommunications L-band is the second primary wavelength band used for optical communication, primarily due to its relatively low attenuation in standard silica-

based optical fibers, surpassed only by the C-band. For instance, in the widely deployed *Corning SMF-28e+* optical fiber, the maximum attenuation is 0.2 dB/km at 1550 nm and 0.23 dB/km at 1625 nm, representing a difference of 15%. Additionally, the widespread availability of erbium-doped fiber amplifiers (EDFAs) optimized for the L-band further establishes it as the next preferred alternative after the C-band [150]. Moreover, multiband (C+L) open line systems, based on wavelength division multiplexing (WDM), have been extensively implemented in long-distance terrestrial networks worldwide. This approach is favored mainly because it effectively doubles the number of WDM channels that can be supported per optical fiber [151, 152].

5.1.1 Auxiliary Lasers

Throughout the project, we had two auxiliary lasers at our disposal for tasks such as optical alignment, verifying OPO cavity losses, and several other optical tests. These were a homemade Ti:sapphire laser operating at 795 nm, and a commercial diode laser operating at 1560.6 nm. Both lasers are used as the primary sources for research on rubidium atoms [25, 26], and silicon nitride micro-resonators [30] in our laboratory. A small portion of these laser beams is diverted and directed into an optical fiber, which transmits them to the teleportation experiment room.

The titanium sapphire (*Ti:Al₂O₃*) laser was assembled in the laboratory by Flávio Campopiano during his master's degree studies [153]. It is powered by a 532 nm commercial DPSS laser, specifically the *Verdi-V10* model manufactured by *Coherent*. The laser's wavelength can be tuned within the range of 730 nm to 800 nm with a linewidth of less than 0.2 MHz. By utilizing the signal from the saturated absorption spectroscopy, it is possible to precisely lock the Ti:sapphire laser at the rubidium atoms' D1 line (795 nm) [154].

The second auxiliary laser is a commercially produced diode laser fabricated by the *RIO* company, under the *ORION* model. It has a linewidth of less than 15 kHz and can be tuned to operate between 1530 nm and 1565 nm, typically operating at 1560.6 nm. In cases where a few milliwatts are not sufficient, we use an optical amplifier (EDFA - Erbium Doped Fiber Amplifier) manufactured by *Keopsys* to increase the available intensity.

We were fortunate to have temporary access to a tunable telecom laser, generously loaned by UNICAMP. The laser, a *Keysight* model 81949A, operates in the 1520–1630 nm range with a linewidth of less than 100 kHz. For our experiments, we utilized it at a wavelength of 1608 nm to characterize the cavities. Additionally, we had access to an external-cavity diode laser at 850 nm (*Vortex 6017, New Focus*), which was used exclusively for spectrometer calibration, given its spectral distance from the region of interest.

5.1.2 Filter Cavity

As mentioned earlier, our pump laser has an excessive quadrature noise, which ends up contaminating the quadratures of the fields generated by the OPO. To address this issue, we filter out the excess noise in the pump beam by using an empty high-finesse resonator, known as a filter cavity, which acts as a spectral and spatial mode filter [155]. The filter cavity is actively stabilized in resonance, transmitting the carrier while reflecting the sideband modes. The resulting transmitted field exhibits heavily suppressed sidebands, with both amplitude and phase noise reaching the fundamental shot-noise limit.

The filter cavity, as illustrated in Figure 18a, adopts a traveling-wave design with a three-mirror ring configuration. The input and output plane mirrors have a manufacturer-specified reflectivity of 99.1(1)% at a wavelength of 532 nm for S-polarized light and an angle of incidence (AOI) between 43° and 45°. The third mirror is a concave spherical high-reflective (HR) mirror with a 1 m radius of curvature and a reflectivity exceeding 99.9% for near-normal incidence (AOI close to 0°). All mirrors were produced by *ATFilms*, and the plane mirrors have an anti-reflective (AR) coating on their back surface. This configuration ensures optimal transmission at resonance by closely approximating the impedance-matching condition. The ideal impedance match, also known as critical coupling, is achieved when the input mirror's transmission equals the cumulative transmission of all other cavity elements, including both useful losses, such as the transmission of the output mirror, and spurious losses, such as scattering inside the cavity and transmission through the HR spherical mirror. Under this ideal condition, all incident light at resonance is either transmitted or dissipated within the cavity [156].

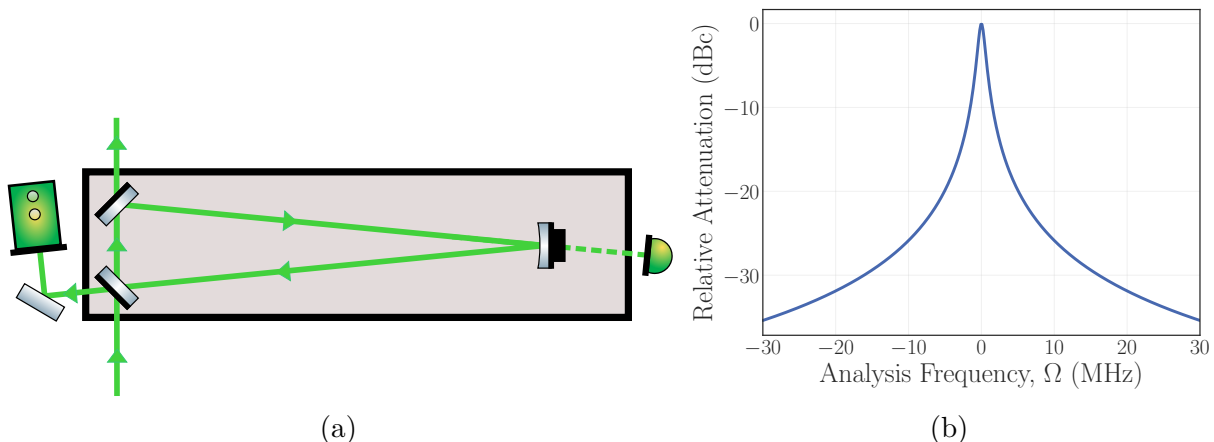


Figure 18 – (a) Filter cavity schematic. The reflection is measured and the signal is sent to the locking system. The transmission of the spherical mirror is used for alignment, and the filtered transmission is used as a pump for the OPO. (b) Spectral transmission of the cavity for a resonant carrier, showing significant attenuation of the sidebands. This plot is based on the Lorentzian transmission profile and the measured parameters of the filter cavity.

The spherical mirror is mounted on a hollow piezoelectric transducer (PZT), which tunes the cavity's resonance frequency by adjusting its position in response to an applied voltage. Moreover, the PZT can be used to actively stabilize the cavity at resonance by counteracting fluctuations in the optical path length due to mechanical vibrations or environmental changes, such as air density variations from currents or acoustic noise. Such stabilization is essential for maintaining reliable cavity performance despite external disturbances.

The cavity has a geometric round-trip perimeter of $1.019(3)$ m. This relatively large length was chosen to reduce the cavity's bandwidth. To minimize the impact of air current waves and other environmental disturbances, the cavity is enclosed within an acrylic housing and mounted on a base composed of three distinct material layers, enhancing vibration isolation. A continuous airflow is introduced into the enclosure to maintain positive pressure, effectively preventing external particles from entering and keeping the cavity clean for extended periods. The filter cavity as described here was originally constructed by Alessandro Villar during his Ph.D. [142] and later improved for higher finesse by Antonio Coelho during his Ph.D. [143].

The Pound-Drever-Hall (PDH) locking technique is used to stabilize the filter cavity at resonance [147]. The system was implemented using the 12 MHz phase modulation from the Diabolo laser locking system as a reference. As part of this work, the locking system was upgraded by integrating the *STEMlab 125-14* FPGA board from *Red Pitaya* and automating the stabilization process with the open-source *Python Red Pitaya Lockbox (PyRPL)* software [157, 158]. The automation consists of two steps: side-of-fringe locking to approach resonance, followed by a PDH step for precise stabilization. The system includes a monitoring mechanism for rapid locking and automatic recovery from external disturbances. Additionally, the flexibility to fine-tune PID controls and implement custom digital filters via *PyRPL* significantly enhanced the locking system's stability and robustness [159].

Figure 18b shows the sideband attenuation effect when the carrier is resonant with the filter cavity. The curve is derived from the measured cavity parameters, revealing a relative attenuation of $-29.39(3)$ dBc at 15 MHz, the frequency at which the teleportation protocol was implemented. This level of attenuation exceeds the expected laser noise at this frequency, allowing us to treat the states in the ± 15 MHz sidebands and higher frequencies as being effectively vacuum states. A summary of the key measured parameters for the filter cavity is presented in Table 3. The reported uncertainties apply exclusively to this characterization, which was performed over a short timescale consisting of three measurements of several tens of milliseconds. These values do not account for performance deviations occurring over longer periods.

Table 3 – Summary of the filter cavity parameters for the 532 nm laser beam at S-polarization.

Filter Cavity Parameter	Value
Finesse	258.9(4)
Bandwidth (FWHM)	1.019(3) MHz
Free spectral range	263.8(7) MHz
Q factor	560(2) $\times 10^6$
Geometric perimeter	1137(3) mm
Waist radius	289.62(6) μm
Rayleigh length	495.3(2) mm
Stability criterion	0.432(2)
Total roundtrip losses	2.397(4)%
Transmission at resonance	51.6(9)%
Attenuation at 15 MHz relative to carrier	-29.39(3) dBc
Pound-Drever-Hall modulation frequency	12 MHz

5.2 Optical Parametric Oscillator

The optical parametric oscillator (OPO) generates the quantum resource required for the teleportation protocol. This device consists of an optical cavity containing a nonlinear medium and operates on the principle of parametric down-conversion, where a high-frequency pump beam is converted into two lower-frequency beams known as signal and idler [87]. The process conserves energy, while the conservation of momentum is governed by the phase-matching condition within the nonlinear medium, as discussed in more detail in Section 2.2. Under proper operating conditions, the signal and idler fields exhibit the strong quantum correlations characteristic of entanglement. Specifically, their collective state is well approximated by a two-mode squeezed state, presented in Section 2.1.3.4. This global quantum state is defined by reduced noise on certain joint quadratures, such as the difference between the signal and idler amplitudes, to a level below the standard quantum noise limit [90, 124]. This robust entanglement is the critical resource that makes the teleportation protocol possible.

In the experiment, we adopted the Fabry-Perot (or linear) cavity configuration, consisting of two mirrors, as illustrated in Figure 2. The mirrors, manufactured by *Layertec*, were configured such that the input mirror was partially reflective for the pump beam, while the output mirror was partially reflective for the signal and idler beams. This type of OPO is referred to as triply resonant, or TROPO, because the pump, signal, and idler beams all resonate simultaneously inside the cavity.

The choice of using the Fabry-Perot configuration avoids additional losses from extra mirrors and allows for a smaller perimeter, resulting in a larger bandwidth, which is desirable for the OPO. An alternative approach involves polishing the crystal surfaces and applying coatings to function as spherical mirrors. When both crystal surfaces undergo this

treatment, the resulting cavity is called monolithic, whereas treating a single surface results in a semi-monolithic cavity. This method enables the creation of even more compact cavities and reduces losses due to transmission on the crystal surfaces. However, this approach is significantly more expensive than mirrors, and the monolithic version adds extra difficulty in controlling the cavity's optical path independently of the crystal temperature, which can be achieved for small deviations by applying pressure over the crystal, but this is far from the range of operation of a PZT-coupled mirror [160, 161].

Both OPO mirrors are plane-concave with a curvature radius of 10.00(5) mm and transverse diameter of 7.75(10) mm, as specified by the manufacturer. The input mirror has a coating on the spherical surface with a reflectivity of $R_{in,S2}^p = 75(5)\%$ for the pump at 532 nm, and $R_{in,S2}^{s,i} > 99.9\%$ for the signal in the range of 790 – 800 nm, and the idler in the range of 1603 – 1613 nm. The output mirror is coated to provide $R_{out,S2}^p > 99.9\%$ for the pump and $R_{out,S2}^{s,i} = 95(1)\%$ for signal and idler. Both mirrors have an anti-reflection coating on their plane surface with transmission $T_{in/out,S1} < 0.25\%$ for the partially reflective wavelengths.

At the center of the cavity, we have a type-0 periodically poled potassium titanium oxide phosphate (PPKTP) crystal, manufactured by the Israeli company *Raicol Crystals*. This second-order nonlinear crystal was selected for its high second-order nonlinear coupling coefficient $\chi^{(2)}$ and excellent transparency at the desired wavelengths [162]. The crystal measures 15 mm in length, with anti-reflection coatings applied to its surfaces along the length, with a transmission of $T_{532,795,1608\text{nm}} > 99.5\%$. Figure 19 illustrates a schematic of the crystal, including its dimensions and axes. Table 4 presents the specifications of the crystal provided by the manufacturer.

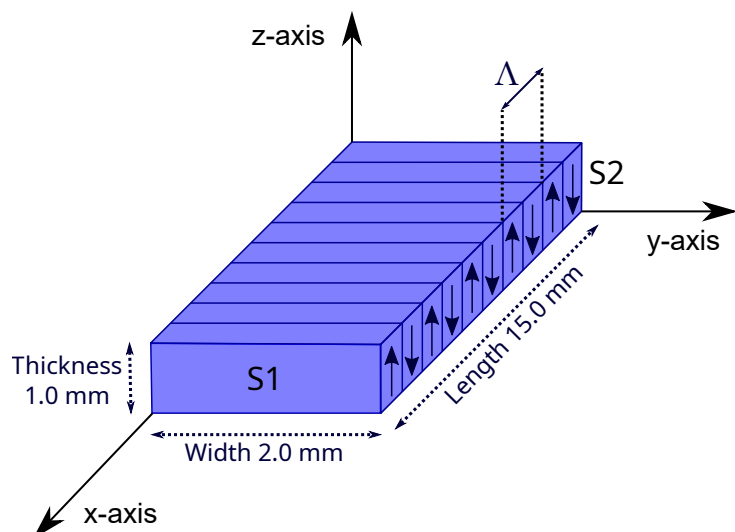


Figure 19 – Schematic representation of the PPKTP crystal, optimized for efficient conversion of light polarized along the z-axis. The surfaces S1 and S2 have anti-reflection coatings, with reflectivity of $R < 0.5\%$ at wavelengths of 532 nm, 795 nm, and 1608 nm.

Table 4 – Specifications of the PPKTP crystal as provided by the manufacturer, Raicol.

PPKTP Crystal Parameter	Value
Length	15 mm
Aperture	$1 \times 2 \text{ mm}^2$
Period Λ	$10 \mu\text{m}$
Surface transmission	> 99.5% @532, 795, 1608 nm
Transparency range	350 - 4000 nm
Bulk Absorption	< 100 ppm/cm @1064 nm < 1000 ppm/cm @532 nm
Gray tracking (due to GRIIRA, 600 sec ppm/cm*)	2000
Laser induced damage threshold (10 ns pulse, 10 Hz)	600 MW/cm ² @1064 nm 300 MW/cm ² @1064 nm 20 MW/cm ² @532 nm
Average power density	
Typical resistivity (Ωcm^2)	10^7

* Depends on the infrared absorption in the crystal when exposed to 532 nm radiation. This parameter reflects the gray-tracking resistance, which correlates with the crystal's lifetime; lower values indicate a longer lifetime.

We utilize the collinear type-0 phase-matching process, where all three interacting waves (pump, signal, and idler) propagate in the same direction as the pump and share the same polarization. This differs from type-I or type-II processes, in which the interacting waves exhibit distinct polarizations. The choice of a type-0 crystal is motivated by its ability to effectively utilize the significantly larger d_{33} nonlinear coefficient (much larger than the off-diagonal coefficients), which can be accessed only if all the interacting waves are polarized in the same direction [163, 164]. Since birefringent phase-matching cannot be employed to compensate for dispersion in this scenario, we adopt a quasi-phase-matching strategy to achieve the collinear process based on the d_{33} nonlinear coefficient, more specifically with $d_{eff} = 2d_{33}/\pi$ [165]. In periodically poled quasi-phase-matching, the crystal lattice is engineered with a periodic structure of period Λ (Figure 19), enabling efficient energy transfer along the crystal for the signal and idler fields and overcoming the phase-matching limitations of standard KTP crystals. For our crystal, the specified poling period is about $10 \mu\text{m}$.

The output mirror is coupled to a hollow PZT actuator, model *HPSt 15014-1012 VS22*, produced by *Piezomechanik*. Both the input and output mirrors are attached to kinematic mounts, models *Polaris-K1S5* and *Polaris-K1S4*, respectively, from *Thorlabs*, selected for their high mechanical stability and compatibility with vacuum environments. The crystal is positioned on a five-axis kinematic stage, model *PY005*, also from *Thorlabs*. All components are mounted on a robust aluminum structure to ensure the correct beam height and provide mechanical and thermal stability, with custom adaptation parts designed to securely attach the mirrors, the PZT, the two kinematic mounts, and the kinematic stage. Figure 20a shows an exploded view of the assembly, and Figure 20b provides a

photograph of the OPO assembly in operation.

5.2.1 Cavity Characterization

To achieve a larger cavity bandwidth, we constructed the OPO with a compact cavity design, having a geometric length of 24.0(6) mm. This length was carefully determined by comparing the resonant transverse modes of both the pump and auxiliary lasers [88], along with the crystal's refractive indices calculated using Sellmeier equations [166, 167]. Given that the crystal itself is 15 mm long, the surfaces of the mirrors are at a distance of 4.5(3) mm from the crystal. After accounting for refraction, the effective cavity length for the pump beam is 16.9(6) mm, defining a waist radius of 25(1) μm and a Rayleigh length of 6.8 mm. The Kleinman-Boyd focal condition defines the optimum waist size for maximum efficiency in the parametric amplification process with Gaussian beams [168], the focal parameter, ξ , is defined as:

$$\xi = \frac{\ell}{kw^2} = \frac{\ell c}{2\pi n\omega w^2}, \quad (5.1)$$

where ℓ is the crystal length, k is the wavenumber inside the medium, and w is the waist. Optimal efficiency is achieved when the Kleinman-Boyd condition $\xi_p = \xi_s = \xi_i = 2.84$ is satisfied, which, in our setup, corresponds to a pump waist of $w_p^{kb} = 15.4 \mu\text{m}$. The waist obtained is reasonably close to w_p^{kb} , and considering that the regime of good focusing condition is robust over a broad range, we expect only a minor threshold increase compared to the ideal scenario [169].

We conducted a comprehensive characterization of the OPO cavity across the relevant wavelength regions, utilizing both the pump laser and auxiliary lasers to examine the cavity's performance. This approach provided detailed insights into the cavity's spectral response, allowing us to experimentally evaluate how well the actual cavity parameters align with the expected design specifications. Given the high reflectivity of the input mirror at the auxiliary wavelengths, we injected the auxiliary beams into the cavity through the output mirror instead, allowing us to bypass the reflectivity limitations of the input mirror (Figure 17).

The characterization was performed by measuring the cavity transmission and reflection below threshold while scanning across one free spectral range [170]. During the measurements, the crystal was maintained at approximately 20°C using water cooling, with the laser beams set to S-polarization along the crystal's z-axis (Figure 19). The results are presented in the Table 5, with expected losses calculated based on the specifications of the mirror and crystal coatings. The uncertainties reflect only the measurements presented here, these values may vary over time due to factors such as gray-tracking [171], contamination

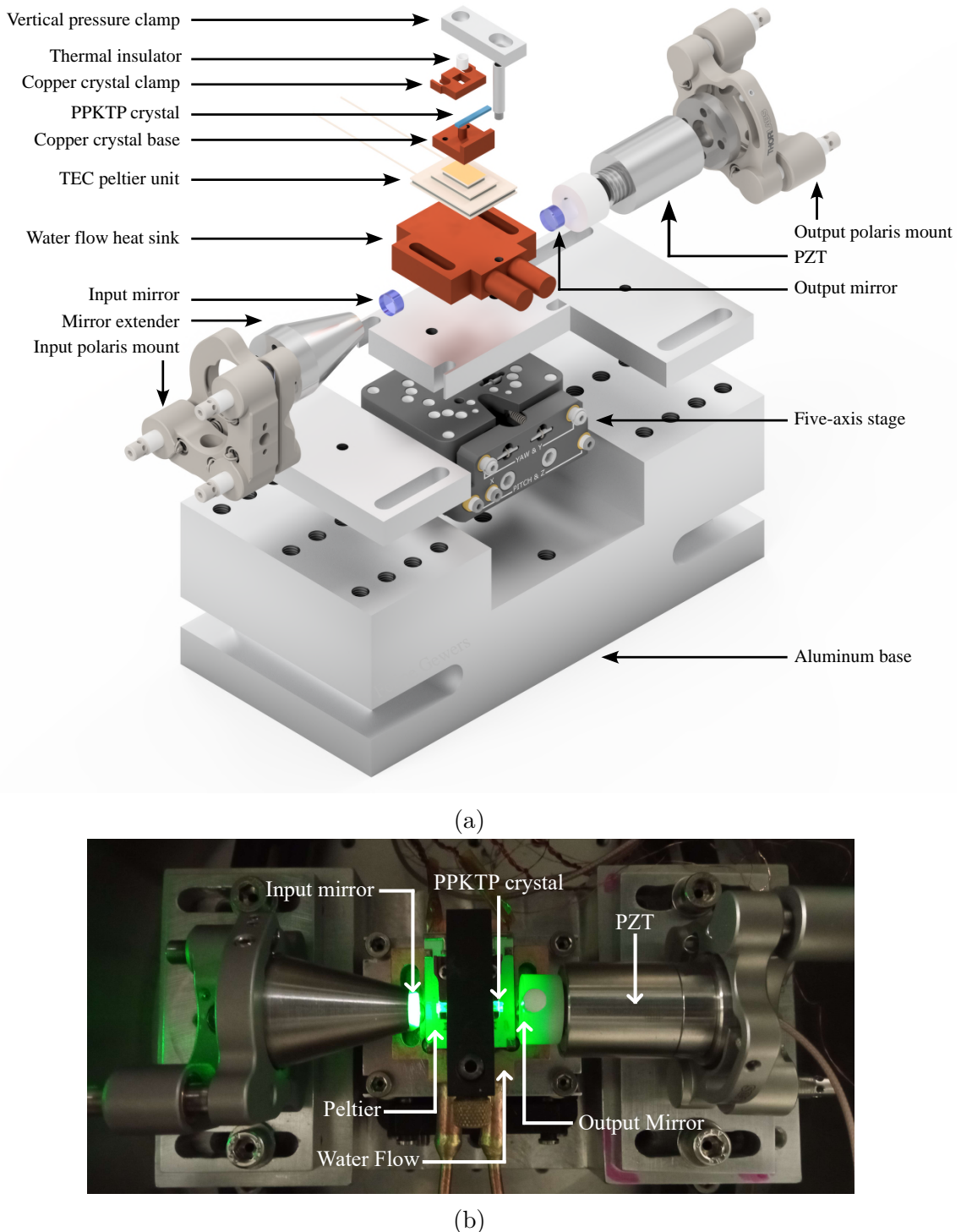


Figure 20 – (a) Exploded view of the OPO assembly, illustrating the detailed arrangement of its components. The model was created using *Autodesk Inventor* software, primarily to verify the alignment and spacing of the components, ensuring precise integration and operation. The models for the kinematic mounts, five-axis stage, and Peltier element were obtained from their respective manufacturers. (b) Photograph of the OPO assembly in operation, illustrating the setup with all components in place. The vertical pressure clamp was later replaced with an aluminum component, as shown in the exploded model.

on optical surfaces, and misalignment caused by thermal expansion and contraction, as well as mechanical stress.

Table 5 – Experimentally determined parameters of the OPO cavity with the crystal at approximately 20°C for the S-polarization aligned with the crystal z-axis. Expected values were calculated based on the specifications of the mirrors and crystal.

OPO cavity parameter	Diabolo (532nm)	Ti-saph (795nm)	RIO (1560.6nm)	Agilent (1608nm)
Finesse	17.07(8)	82.9(2)	70.9(1)	80.2(2)
Bandwidth - FWHM (MHz)	235(4)	49.4(9)	58(1)	51.6(9)
Free spectral range (GHz)	4.02(7)	4.09(7)	4.14(7)	4.14(7)
Intensity enhancement	5.43(3)	26.37(5)	22.56(4)	25.53(6)
Q factor ($\times 10^6$)	2.87(5)	7.9(1)	3.44(6)	3.75(7)
Effective geometric length (mm)	16.9(6)	17.1(6)	17.2(6)	17.2(6)
Optical path length (mm)	37.3(6)	36.7(6)	36.2(6)	36.2(6)
Waist radius (μm)	25(1)	30(1)	41(2)	42(2)
Focal parameter	2.2(2)	2.3(2)	2.4(2)	2.4(2)
Rayleigh length in the crystal (mm)	6.8(6)	6.5(6)	6.3(6)	6.3(6)
Stability criterion	0.48(9)	0.51(9)	0.52(9)	0.53(9)
Total roundtrip losses (%)	30.7(1)	7.30(1)	8.48(1)	7.53(2)
Coupler transmission (%)	27.7(5)	6.5(1)	6.7(2)	5.7(2)
Spurious losses (%)	4.2(7)	0.8(1)	1.9(2)	1.9(2)
Expected roundtrip total losses (%)	27(5)	7(2)	8(2)	7(2)
Expected coupler transmission (%)	25(5)	5(1)	6(1)	5(1)
Expected spurious losses (%)	< 2.1	< 2.1	< 2.1	< 2.1
Refractive index [166, 167]	1.8887(1)	1.8451(1)	1.8155(1)	1.8144(1)

An important aspect of this characterization is the evaluation of spurious losses at the wavelength of the generated beams, as these losses significantly impair the entanglement between them [92, 172]. Based on the coating specifications, we expected spurious losses of less than 2.1% for all involved wavelengths. While the measured spurious losses for the pump inside the cavity are higher than expected, as long as these losses do not propagate to the generated fields, they will only increase the oscillation threshold, requiring a higher pump intensity into the OPO. For the generated beams, the spurious losses are within expected limits, suggesting that there are no issues with the system alignment or coating performance in that spectral region. Being dependent on the intracavity gain and losses, the OPO oscillation threshold is highly sensitive to several factors, including the crystal's laser-induced damage state, external alignment conditions, and environmental stresses. In particular, operating in vacuum at sub-zero temperatures can introduce mechanical stress, potentially leading to internal misalignments. For the configuration detailed above, the oscillation threshold of the pump beam ranged from 8 mW to 18 mW, as measured outside of the vacuum chamber window.

In this work, we generate our quantum states in the above threshold regime, which

offers significant advantages with some drawbacks. Specifically, the quantum fields are produced in the sideband modes alongside an intense carrier, which can be used as a local oscillator (LO) for the detection process. This approach eliminates the need for a separate high-intensity local oscillator beam with a fixed phase relation to the generated fields. Moreover, since we operate at widely separated frequencies, deriving the local oscillators from the main carrier laser allows us to avoid the complexity of using two independent lasers that would need to be phase-locked to the pump. In more versatile setups, it also removes the necessity of an additional OPO to generate either the local oscillators or the pump beam [173]. Another key benefit is that the local oscillator, generated alongside the sideband modes, shares the same spatial mode, eliminating effective losses due to mode mismatch between the local oscillator and the measured field.

Operating above threshold naturally enables the use of the resonator-assisted auto-homodyne detection technique, discussed in detail in Section 3.3 [112]. This method offers the significant advantage of measuring the noise difference between the upper and lower sidebands, allowing access to an element of the covariance matrix that standard homodyne detection cannot reach. However, the primary drawback of this regime is the observed reduction in the squeezing levels compared to the below threshold regime, mainly due to phase noise introduced by the coupling of the carrier with phonons in the crystal [123].

The intensities of the three interacting fields in the OPO above threshold, while scanning the PZT, are shown in Figure 21. The pump intensity was measured using a Faraday rotator on the reflection from the OPO, while the signal and idler were measured via the small fields leaking through the OPO's input mirror (Figure 17). These small fields allowed us to monitor the generated beams without introducing losses after the OPO. Additionally, they served as intensity references for stabilizing the analysis cavities at a specific detuning, ensuring that the locked target detuning remains unaffected by intensity fluctuations of the generated fields.

The OPO cavity bandwidths for both the signal and idler are approximately 50 MHz. We designed the cavity to be as compact as was suitable; therefore, further increasing the bandwidth would require a higher transmission output coupler. However, this change would also increase the circulating pump power required to reach the oscillation threshold. Maintaining a lower circulating pump power is desirable for several reasons. It reduces coupling with thermal phonons in the crystal, thereby decreasing the phase noise they induce [123]. Additionally, the green-induced infrared absorption (GRIIRA) effect depends on the circulating power of green light (532 nm), so minimizing this power helps mitigate GRIIRA-related losses [174]. A lower pump power also extends the crystal's lifetime by reducing gray-tracking effects [171, 175], which are forms of laser-induced damage to the crystal structure that can accumulate over long-term use.

In our system, the gray-tracking remains an issue, and its severity is intensified by

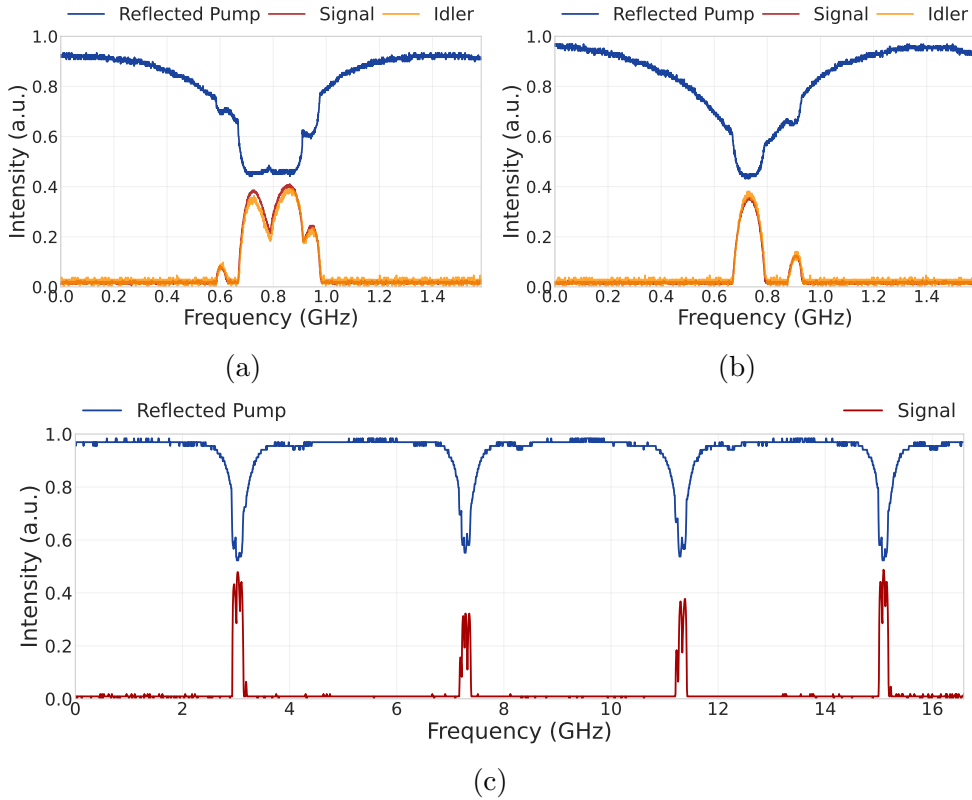


Figure 21 – Intensities of the three interacting fields in the OPO above threshold during PZT scanning. (a, b) Two distinct pump resonance profiles are presented. (c) A broader scan showing multiple cavity resonances. For all plots, the x-axis is normalized using the cavity’s free spectral range (FSR), and the y-axis intensity values are scaled for clarity, with peak values adjusted for improved visualization.

several factors: the specific pump wavelength, the focused spot size inside the crystal, the polarization aligned with the crystal’s z-axis, the use of a periodically poled crystal, and prolonged operation at low temperatures [171, 174]. Over the course of weeks, we observe a gradual increase in the OPO oscillation threshold, suggesting progressive crystal damage. To mitigate this, we periodically adjust the crystal position slightly, changing the region through which the pump beam propagates.

5.2.2 Temperature Dynamics

The presence of thermal phonons within the crystal induces random fluctuations in the refractive index (or permittivity), scattering light from the carrier into sideband modes and generating additional phase noise in the three fields involved (pump, signal, and idler) [123]. This effect is temperature-dependent, making it desirable to operate the crystal at low temperatures to reduce spurious phase noise that can impair the quantum measurements. To address this, we designed a crystal with a poling period optimized for phase-matching the conversion $532\text{ nm} \rightarrow 795\text{ nm} + 1608\text{ nm}$ at sub-zero temperatures.

We characterized the wavelength of the generated signal beam as a function of the crystal temperature. The temperature readings were obtained using a $10\text{ k}\Omega$ NTC thermistor (*GA10K3MCD1, TE Connectivity*) inserted into the crystal holder. For the wavelength measurement, we used a fiber optic spectrometer (*USB4000, Ocean Optics*), which was calibrated using the Ti:Sapphire laser locked to the 795 nm rubidium D1 line [176]. Since the spectrometer's range is limited to below 1 μm , the idler beam wavelengths were not measured directly but were instead calculated via the energy conservation principle of the parametric down-conversion process.

The results of this characterization are shown in Figure 22. From this data, we determined that the desired signal wavelength of 795 nm is achieved when the crystal is at a temperature of $T_{795,1608\text{nm}} = -45.7(3)^\circ\text{C}$. As an alternative tuning mechanism, the crystal can also be slightly rotated to change the effective poling period, reducing the temperature needed to generate the desired wavelengths if phonon noise remains an issue.

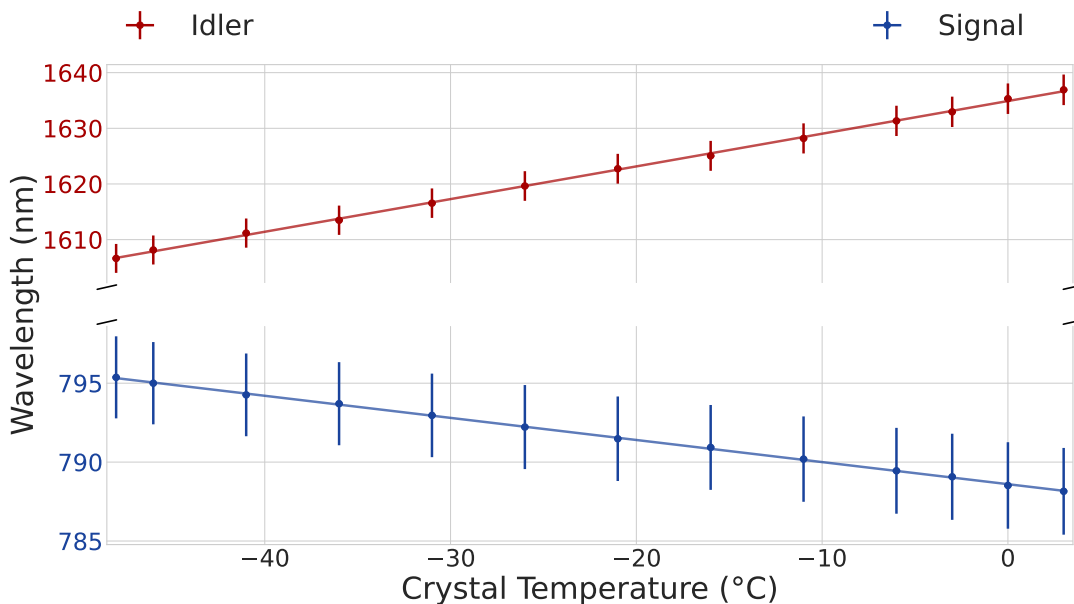


Figure 22 – Experimental characterization of the dependence of signal and idler wavelengths on crystal temperature. The line corresponds to the linear fit performed on the corresponding experimental points.

To control the crystal temperature, we refined the system design originally implemented in previous projects within our research group [59, 60, 95]. This was achieved using a multi-stage thermoelectric module, model *SP2402*, manufactured by *Marlow*, which operates based on the Peltier effect. According to the specifications, the thermoelectric module can have a maximum temperature variation of $\Delta T_{max} = 109^\circ\text{C}$, when operating in nitrogen and with the hot surface maintained at 27°C . A constant-temperature water flow from a thermoelectric chiller (*T257P, ThermoTek*) is used to cool the hot side of the Peltier device. Both the crystal holder and the water circulation component are made of copper to ensure optimal thermal conductivity. The interfaces between these components

are filled with *Apiezon H* vacuum grease (from *M&I Materials*), which has a thermal conductivity of 0.216 W/mK at 20°C. To maintain vertical pressure between the thermal components, we used a vertical clamp, focusing the pressure on a small point on the crystal holder base using a thermal insulator (made of teflon) to prevent heat transfer through the clamp. The temperature control assembly is shown in Figure 20.

To achieve precise temperature stabilization, we utilize a thermoelectric cooling (TEC) temperature controller, model *TEC-1162* from *Meerstetter Engineering*, which regulates the temperature to the millikelvin level. The controller adjusts the Peltier element based on temperature data obtained from the thermistor attached to the crystal holder. It also features an auto-tuning function that optimally determines the PID parameters, which vary significantly depending on the operating temperature and pressure conditions.

To monitor the temperature within the system, we use digital thermometers (model *MT-455A* from *Minipa*) connected to four standard K-type thermocouples placed inside the vacuum chamber: one inserted into the crystal holder, one attached to the OPO input mirror, one on the intermediate surface of the Peltier, and one on the water flow component. Additionally, two more thermocouples are positioned outside the chamber, attached to the water inlet and outlet. This arrangement of thermocouples allows for a comprehensive evaluation of the thermal dynamics across the entire system.

With the implementation of this system, we achieved a minimum crystal temperature of -62.7°C , which generated signal and idler wavelengths of 797.4(6) nm and 1598(3) nm, respectively. However, operation at this temperature required a Peltier current near its maximum limit, making continuous use inadvisable. For stable, long-term performance, a crystal temperature above -55°C is recommended. The main results presented in this work were obtained with the crystal maintained at approximately -41.5°C . At this temperature, the system demonstrated excellent long-term stability, and the generated signal and idler wavelengths of 794.4(6) nm and 1611(3) nm, respectively, were compatible with our desired wavelengths.

As the temperature of the crystal decreases, water vapor in the surrounding air condenses on the crystal surface, causing significant losses that prevent proper OPO operation. The temperature at which condensation becomes an issue depends on the ambient temperature and humidity, with a noticeable increase in the oscillation threshold typically occurring around 5°C . To achieve the desired temperatures, it is necessary to control the OPO environment. To address this, we mounted the OPO inside a vacuum chamber and implemented a system designed to operate at low pressures, as described below.

5.2.3 Vacuum System

The OPO vacuum chamber, shown in Figure 23b, is composed of three main components: an aluminum base, a stainless steel flanged chamber wall, and a stainless steel lid. These components are sealed together using two rubber O-rings to ensure proper isolation. The chamber has eight ports, consisting of six KF-50 flanges and two KF-16 flanges. Two of the KF-50 ports are fitted with windows to allow the beams to enter and exit the chamber. These windows, manufactured by *Layertec*, have surfaces equipped with anti-reflective coatings, providing a transmission efficiency of $T_{532,795,1608\text{nm}} > 99.5\%$. The chiller supplies water to the vacuum chamber through a spiral copper tube installed via a KF-50 flange. Copper was selected for its superior compatibility with vacuum conditions, and the spiral design ensures sufficient flexibility to avoid exerting mechanical stress on the crystal's kinematic stage.

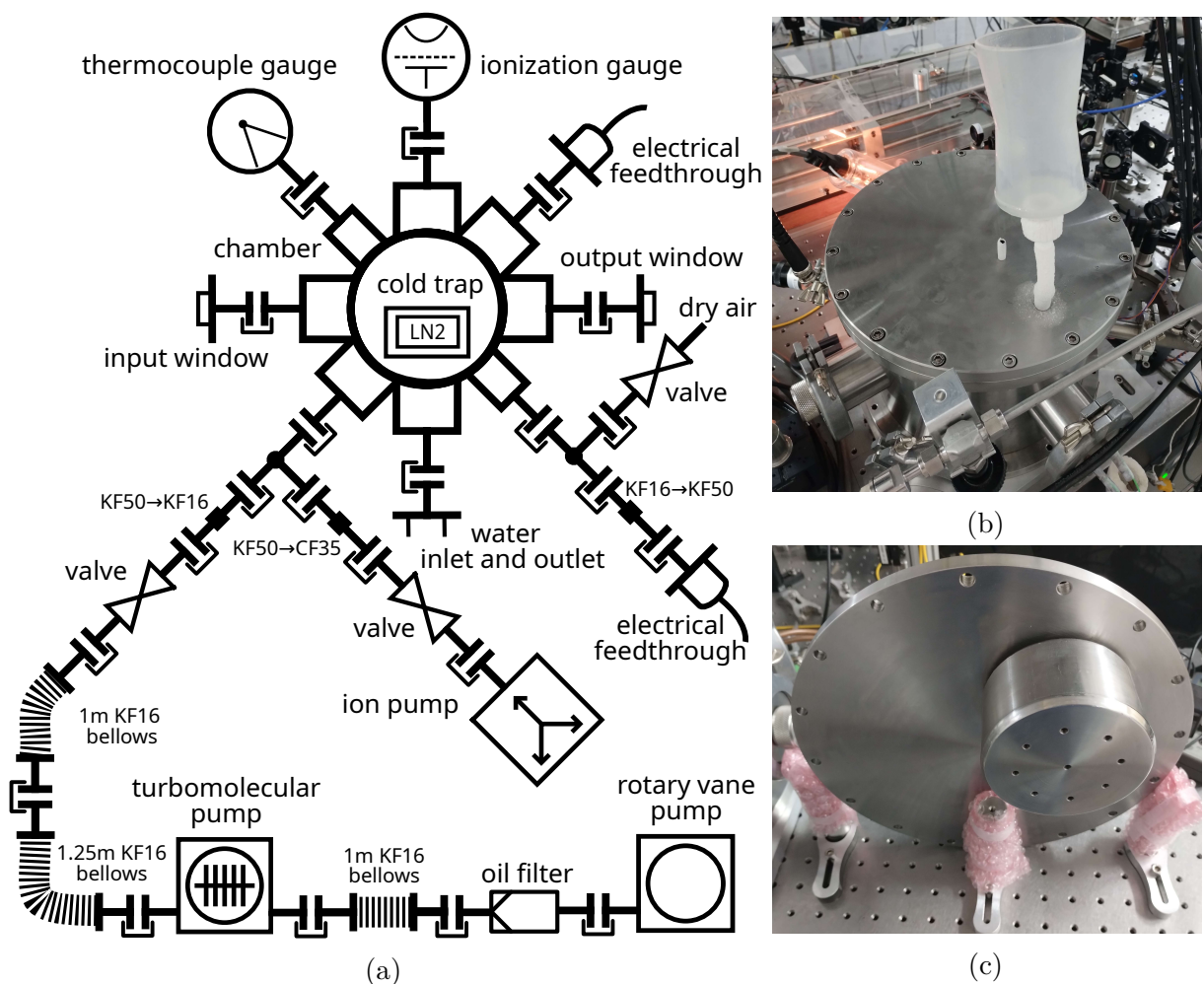


Figure 23 – (a) A 2D schematic illustrating the final configuration of the OPO vacuum system. (b) A photograph of the vacuum chamber. In this setup, the compressed air system for introducing liquid nitrogen into the trap was not used; instead, a silicone funnel was utilized. (c) A photograph of the modified chamber lid, designed to function as a cryopump.

Vacuum is achieved using a combination of four pumps: a mechanical pump (*SD 40, Varian*), a turbomolecular pump (*Turbo-V 70, Varian*), a custom cryogenic trap built in-house, and an ion pump (*VacIon Plus 25 Diode*) paired with the *Minivac Controller*, both manufactured by *Varian*. To monitor the chamber pressure, we utilize two gauges, each suited for a specific pressure range, both connected to the *senTorr* gauge controller manufactured by *Varian*. For rough vacuum measurements, spanning from 1×10^{-3} Torr to atmospheric pressure (7.6×10^2 Torr), a thermocouple gauge tube (*531, Varian*) is used. For high-vacuum pressures, ranging from 1×10^{-8} Torr to 1×10^{-3} Torr, we used a Bayard-Alpert ionization gauge (*RG75K, Veeco*). All additional vacuum components, excluding pumps and gauges, are manufactured by *Agilent*.

The mechanical pump is connected to the turbomolecular pump via a small, flexible KF-16 bellows, providing the necessary pre-vacuum for the turbo pump to operate. Initially, the mechanical and turbo pump system was located in the same room as the experiment and connected to the chamber through a 1-meter-long KF-50 bellows. This configuration allowed us to reach a pressure of 1.0×10^{-4} Torr; however, condensation was still observed around -41.5°C . To resolve this issue, we designed and built a cryogenic trap cooled by liquid nitrogen (*LN₂*, with a temperature of 77 K, or -196.15°C). For this purpose, we modified the chamber lid to include a small compartment with an inlet for the liquid nitrogen and an outlet for the evaporated gas, as shown in Figure 23c. The liquid nitrogen, stored in a 30 L dewar (*EG&G Ortec*), is delivered to the compartment through a silicone tube, with compressed air being used as the driver to induce the flow of nitrogen. Using the cryogenic trap, we achieved a pressure of 1.6×10^{-6} Torr, effectively preventing condensation at temperatures down to -62.7°C .

However, with the vacuum pumps operating in the same room as the experiment, stabilizing the OPO in resonance was not possible due to significant noise at 1.27 kHz, corresponding to the turbomolecular pump's rotational speed of 76,000 rpm. Although various mitigation strategies were attempted, none proved effective. The final solution was to relocate the pumps to an adjacent room, connecting them to the vacuum chamber via two long KF-16 bellows passed through a hole in the wall. The hole was sealed with expanding polyurethane foam to reduce acoustic transmission and secure the bellows in place. However, this configuration introduced trade-offs: the increased distance, smaller bellows diameter, and additional junctions reduced vacuum performance, leading to longer pumping times and limiting the chamber pressure to a minimum of 6.1×10^{-4} Torr using both pumps. With the cryogenic trap, we achieved a pressure of 8.0×10^{-5} Torr, but even at that pressure we noticed condensation on the crystal after several hours of operation.

Therefore, to improve the vacuum level, we performed baking (at 180°C) and reinstalled an old ion pump from the lab [177]. To extend the ion pump's operating life, it is ideal to activate it at pressures below 1.0×10^{-4} Torr, so the cryogenic trap is still

required to reach the necessary pressure levels before turning on the ion pump. Even once the ion pump is running, the liquid nitrogen supply to the cryogenic trap must remain active. In this final configuration (in the schematic in Figure 23a), with all four pumps running, we can achieve a pressure of 7×10^{-6} Torr, which prevents condensation at all temperatures at which we operate the crystal. It is important to note that the pressure values reported were measured after several hours of pumping and at least one day following the chamber's closure and initial pumping, as the system requires time to stabilize after opening the chamber.

5.2.4 Locking System

An optical cavity operating in resonance with a monochromatic beam requires precise control of either the light's frequency or the optical distance between the mirrors. This is because the resonance condition requires the round-trip acquired phase to be an integer multiple of 2π [156]. This precise control in real time is typically achieved through a servo system that employs a negative feedback loop, which uses an error signal to compare the desired resonance condition with the actual cavity length or frequency, and adjusts the parameters accordingly [178]. This approach ensures that the optical cavity remains locked in resonance, maintaining accurate and reliable performance over time.

To stabilize the OPO cavity in the resonance condition where the pump, signal, and idler beams are resonant within the cavity, we apply the Pound-Drever-Hall (PDH) technique to the pump beam [147]. Since the OPO is a linear cavity, the reflected beam follows the same path as the incident beam. To deflect and measure the reflected beam, we use two polarizing beam splitters (PBSs) with a Faraday rotator and a $\lambda/2$ waveplate placed between them (Figure 17), effectively creating an optical isolator. For all the locking electronic signal generation and processing, as well as for the locking control, we use a *STEMlab 125-14* FPGA board, developed by *Red Pitaya* [157]. The automation of the locking process was achieved using the board alongside the open-source software *Python Red Pitaya Lockbox (PyRPL)*, developed by the Laboratoire Kastler Brossel (LKB) [158].

In contrast to the strategy used in the filter cavity, where an external reference signal and error signal generation were involved, here the entire process is managed by the *Red Pitaya* board. The board generates a 26 MHz sine wave, which is sent to a phase electro-optic modulator (EOM), model *LM0202* by *Qioptiq LINOS*, creating a small phase modulation in the pump beam. The reflected beam is split using a $\lambda/2$ waveplate and a PBS, with both outputs measured. A silicon switchable gain detector (*PDA36A, Thorlabs*) is used for the DC signal, while a homemade detector with a silicon PIN photodiode (*S5973-02, Hamamatsu*) measures the HF signal. The use of two separate detectors is due to the *Red Pitaya* board's requirement for an input signal within the ± 1 V range, so decoupling the detectors allows us to optimize each signal for its respective input range.

The FPGA board demodulates the measured HF signal using the generated sine wave as a reference, producing the PDH error signal. An internal PID controller then uses this error signal to adjust the resonance by controlling the PZT of the OPO cavity. The automated locking procedure consists of two main steps: a side-of-fringe step that initially locks the cavity near resonance using the DC signal, followed by a PDH step that locks the system at resonance. This approach, together with a monitor that detects when the cavity drifts out of resonance, enables rapid locking and automatic recovery to the locked state in the event of any disturbance taking the system out of stability.

When operating above threshold, the reflection peak deviates from a perfect Lorentzian shape (Figure 21), leading to distortion in the PDH error signal. To ensure proper locking at the correct position, the phase of the reference signal must be adjusted during the demodulation process to accurately shape the PDH error signal. Additionally, the resonance conditions for the signal and idler beams in the cavity do not necessarily coincide with those of the pump beam. During OPO cavity scanning, the maximum generation occurs at positions that differ from the pump resonance peaks (Figure 21). Therefore, achieving optimal generation with the OPO locked to the pump resonance requires selecting the appropriate pump resonance peak and fine-tuning the crystal temperature to maximize the signal and idler intensities [179].

The thermal phonon-induced phase noise in the OPO above threshold increases with the pump power relative to the oscillation threshold $\sigma = P_0^{in}/P_{th}$ [92, 123]. To minimize this additional noise and preserve the quantum correlations, it is desirable to operate the system as close to the threshold as possible. However, under these conditions, the OPO locking system becomes increasingly unstable and more challenging to maintain. Despite these difficulties, with our stabilization system, we successfully achieved stable OPO operation at a pump power 10% above the threshold ($\sigma = 1.1$).

5.3 Teleportation Stations

In this section, the technical details of the optical components associated with each station in the continuous-variable teleportation protocol will be presented. The discussion will emphasize the intricate design and precise alignment of the optical setup, addressing the challenges and critical considerations involved in manipulating quantum states for the teleportation process. The generated signal and idler beams are separated using a dichroic mirror (*DMLP950* from *Thorlabs*) and directed to different stations, which will be described in detail subsequently.

5.3.1 Victor: Input State Station

The verifier of the protocol, Victor, is responsible for creating the quantum state to be teleported. This work is centered on the teleportation of Gaussian states, with a primary focus on coherent states. The input state is prepared by extracting a small fraction of the signal beam, approximately 0.5% – 1%, to ensure that the sideband mode in this portion can be well approximated by a vacuum state. The creation process involves a phase displacement operation and a rotation operation, resulting in a coherent state with a non-zero mean value.

5.3.1.1 Phase Displacement Operation

The phase displacement operation is performed using a phase EOM, model *LM0202* by *Qioptiq LINOS*. We drive the EOM with a 15 MHz sinusoidal signal, corresponding to our analysis frequency, from the *Tektronix AFG1022* function generator. This process modulates the phase of the laser field, applying a quantum displacement operation to the sideband modes at a spectral offset from the vestigial carrier equal to the modulation frequency [72]. It is crucial that the modulation generator remains in phase with the demodulation electronic local oscillators (Section 3.1.2); otherwise, the measurement of the quadratures of the teleported state will rotate over time. To ensure this, we synchronize the generators by configuring one to follow the reference clock of the other. Victor is responsible for both generating the input state and performing the tomography of the teleported state. As a result, the phase information remains local to Victor and does not need to be shared with the other parties involved in the protocol.

Any noise present in the electronic signal from the function generator is transferred to the created quantum state. As a result, a noisy signal would produce a thermal state instead of a coherent one [180]. While the system can teleport any quantum state in the field quadratures, teleporting a thermal state is less desirable. During the initial teleportation measurements, we encountered issues with the input state deviating from a coherent state. This was mitigated by properly impedance-matching the function generator to the EOM and operating it below 1 V_{PP}, where the noise relative to the carrier is significantly reduced.

5.3.1.2 Mach-Zehnder Interferometer

A Mach-Zehnder interferometer (MZI) configuration is used to manipulate the phase relationship between the displaced sideband modes and the intense carrier of Alice’s beam, effectively performing a rotation operation, as detailed in Section 3.4.3. Due to space limitations, our MZI setup is asymmetric, with one arm being considerably longer than the

other (Figure 24a), which necessitates a lens-based mode-matching system in the longer arm to ensure optimal beam overlap at the output. To maximize beam overlap while aligning the longer path, we use Alice's analysis cavity as a reference. The transmission profile of the cavity provides more precise and detailed information about the alignment compared to relying solely on the interferometer's visibility, enabling a more accurate and efficient alignment process, and the simultaneous mode matching of both fields. Additionally, a half-wave plate and a PBS are used to control the intensity of light in each arm. Since the signal beam intensity from the OPO is relatively low, this adjustment is crucial to ensure sufficient beam intensity in both arms for proper alignment.

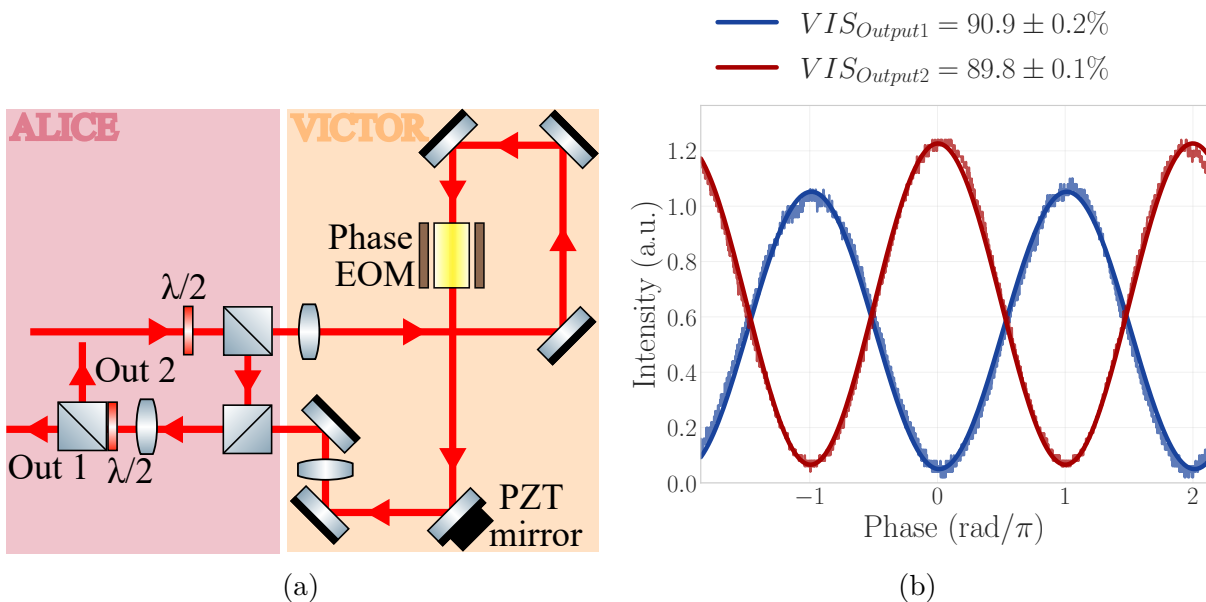


Figure 24 – (a) Schematic of the asymmetric Mach-Zehnder interferometer used to generate the state for teleportation. (b) Plot showing the visibility of the interferometer for both output ports, when the input PBS splitting ratio is set to 50:50.

At the output of the interferometer, the two beams have different polarizations. To combine them, a PBS aligns them collinearly, followed by a half-wave plate and another PBS to enable their interference. This strategy functions correctly only for a 50:50 splitting ratio. To verify this, we use two mirrors mounted on a flip mechanism followed by two detectors (*PDA36A, Thorlabs*), as shown in Figure 17. This verification specifically evaluates the PBS's splitting ratio, ignoring any additional losses from other parts of the experiment. By setting the splitting ratio of the input PBS to 50:50, the visibility at both outputs was measured, as shown in Figure 24b, achieving a maximum visibility of 90.9(2)%.

The interferometer's phase control is achieved using a PZT-mounted mirror. For each phase, a corresponding rotation angle is applied, resulting in a distinct input state, with the displacement being distributed differently across the amplitude and phase quadratures

(Section 3.4.3). To ensure the input state remains constant throughout the protocol execution, we stabilize the phase of the interferometer. To achieve this, we use the small interference fringe signal at the DC output of Alice’s amplitude quadrature detector as the error signal and implement a simple side-of-fringe locking technique. While the side-of-fringe technique prevents locking the interferometer at the maximum or minimum points of the interference fringe, this limitation can be readily overcome by utilizing the error signal from the phase quadrature detector, in which the interference fringe is $\pi/2$ shifted.

To ensure the selected locked phase remains stable against signal beam intensity fluctuations, we use the small signal from the transmission of the signal beam through the input mirror of the OPO cavity as a reference. This reference signal is then processed through a custom-built electronic device, where a gain and offset are applied, and the resulting signal is subtracted from the interference fringe. With correct calibration of the parameters, the final error signal will fluctuate around the locking point in accordance with the intensity variations, effectively keeping the phase constant. The error signal is sent to a *Red Pitaya STEMlab 125-14* FPGA board, which controls the PZT-mounted mirror. Using the *PyRPL* software, we adjust the PID control parameters and automate the locking procedure to restore stability in the event of significant deviations [157, 158].

5.3.2 Alice Station

Alice is responsible for receiving the input state, combining it with her share of the entangled state, measuring both orthogonal quadratures, and transmitting the resulting information to Bob over a classical channel. It is important to highlight that Alice possesses limited information about the input state, thanks to the noisy input of the signal field, and any attempt to gain more knowledge would degrade the protocol’s fidelity [141]. The interference between the beam containing the input state and Alice’s beam occurs using a 50:50 beam splitter, as explained in the previous section. One of the resulting outputs is directed toward the amplitude quadrature measurement, while the other is sent to the phase quadrature measurement. A schematic of Alice’s experimental setup is shown in Figure 25a.

5.3.2.1 Alice’s Analysis Cavity

The amplitude quadrature measurement is straightforward and can be performed using a photodiode detector, as by definition the intensity fluctuations carry the noise information of this quadrature. In contrast, the measurement of the orthogonal phase quadrature requires a more sophisticated approach, involving the introduction of a $\pi/2$ phase shift between the carrier, the local oscillator, and the sidebands at the analysis

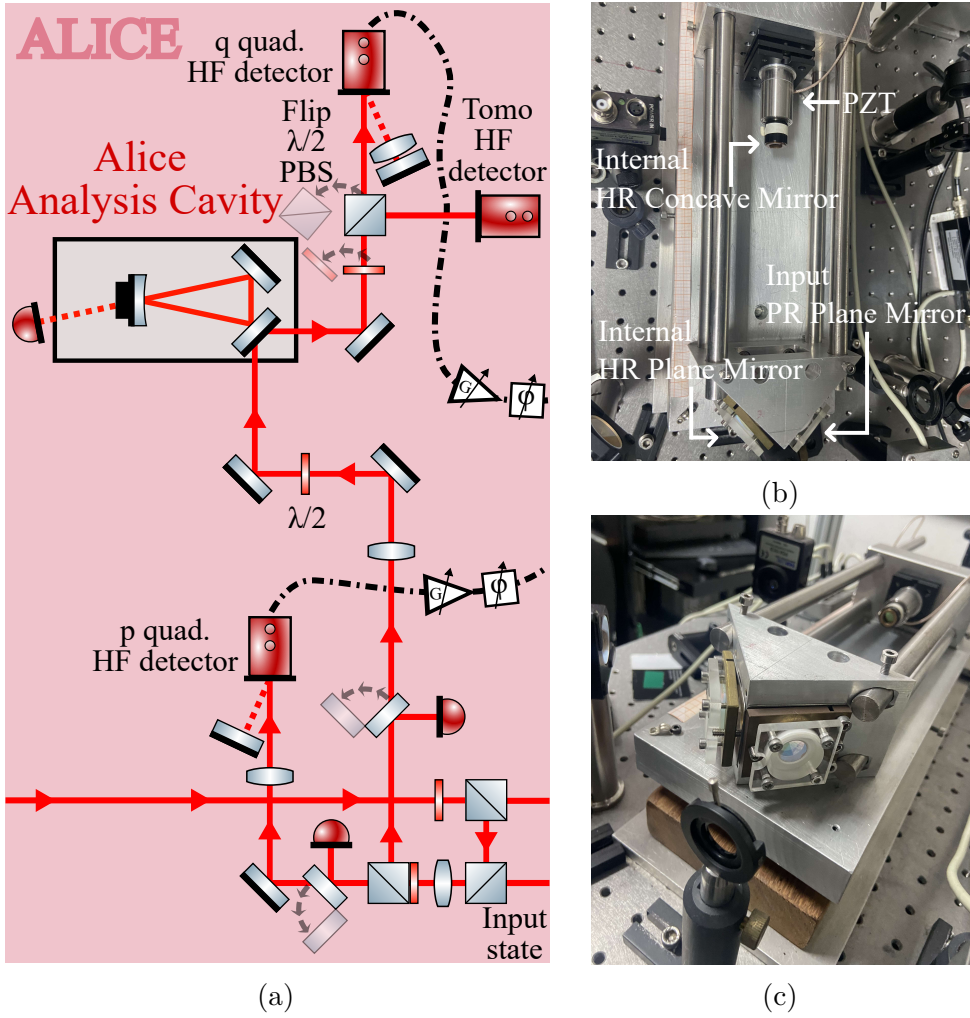


Figure 25 – (a) Schematic of Alice’s experimental setup, illustrating the interference of the beam containing the input state and Alice’s beam at a 50:50 beam splitter and the subsequent measurements of amplitude and phase quadratures. (b) and (c) Photographs of one of the custom-designed analysis cavities.

frequency [107]. This phase shift is implemented using the dispersive properties of an optical resonator, as detailed in Section 3.3. Depending on the cavity’s detuning, the carrier and its symmetric sidebands undergo distinct phase shifts, determined by their relative frequencies within the resonance profile [112]. An optical cavity specifically designed for such measurements is referred to as an *analysis cavity*. Since we aim at measuring spectral components that are not resonant in the cavity, and losses are highly detrimental to quantum states, it is natural to measure the cavity’s reflection. A triangular cavity is particularly well-suited for this purpose, as it represents the simplest design that allows convenient access to the reflected beam. Unlike a filter cavity (Section 5.1.2), which focuses on maximizing the power of the transmitted beam, this design eliminates the need for an output plane mirror. Instead, both the spherical and internal plane mirrors are designed for high reflectivity, while the coupling plane mirror, which reflects the incident field, is partially reflective.

The cavity consists of one concave mirror and two plane mirrors, all supplied by *Layertec* and coated for the 790-800 nm wavelength range. According to the manufacturer, the internal concave and plane mirrors have a reflectivity of $R_{\text{internal},S2} > 99.9\%$, with the concave mirror having a radius of curvature of 1.00(1) m. The input mirror is partially reflective, with $R_{\text{in},S2} = 95(1)\%$, while its external surface has an anti-reflective coating of $R_{\text{in},S1} < 0.3\%$. The reflectivity values for the plane mirrors are specified for an angle of incidence of 45°, whereas the concave mirror is designed for angles of 0° – 10°, all specified for S-polarization, which is perpendicular to the plane defined by the optical table.

The three analysis cavities in this experiment share a common custom design, with an aluminum structure that allows angular adjustments of the plane mirrors and positional adjustments of the spherical mirror (Figures 25c and 25b). The mount rests on a base comprising three layers—wood, rubber, and aluminum—designed to attenuate mechanical vibrations. An acrylic enclosure protects the cavities, maintaining cleanliness and minimizing airflow disturbances. Additionally, a hollow piezoelectric transducer (PZT) is coupled to the spherical mirror, enabling fine adjustments to its position.

The same electronic system is used to control the resonance conditions of all three analysis cavities. Resonance stabilization relies on the vestigial transmission signal from the spherical mirror, detected using a standard switchable-gain detector from *Thorlabs*. Specifically, for Alice's cavity, the silicon-based detector model *PDA36A* is utilized. To ensure the stabilized detuning is robust against pump power fluctuations, we follow the same procedure used in the Mach-Zehnder interferometer locking scheme for Alice and Bob cavities. This process involves measuring the small signal field transmitted through the OPO's input mirror and using it as a reference. A carefully calibrated gain and offset are applied to this signal before it is subtracted from the analysis cavity transmission via a custom-designed electronic module. The resulting signal serves as the error signal for active stabilization.

The processed transmission signal is sent to a *Red Pitaya STEMlab 125-14* FPGA board, where PID parameters and digital filters are adjusted using the *PyRPL* library to automate locking. For the analysis cavities, we use a simple side-of-fringe locking method to stabilize them at the phase-to-amplitude detuning point. We developed a Python script to integrate the locking mechanisms of the filter cavity, OPO, Mach-Zehnder interferometer, and analysis cavities. This script interfaces with the *PyRPL* object of each system, enabling access to their individual locking visual interfaces and facilitating coordinated adjustments when necessary.

We conducted a detailed characterization of the optical cavity using the OPO with its crystal maintained at different temperatures and the Ti-saph laser. By analyzing the Gouy phase shift between the resonant fundamental mode and the first-order vertical Hermite-Gaussian mode, we determined the cavity perimeter to be 413(5) mm [181]. This

value is consistent with the expected result and corresponds to a free spectral range of 729(6) MHz. The characterization, performed using the signal beam with the OPO's crystal set at -41.5°C (emitting 794.4(6) nm) and the Ti-saph laser locked to the rubidium's D1-line at 795 nm, is detailed in Table 6. The cavity parameters align with the expected values, including the input coupler transmission and internal losses, which match the company specifications. The Ti-saph laser visibility was not optimized, as it was used only for cavity characterization, but its measured value was used in the parameter estimation calculations. The stated uncertainty corresponds to a single characterization measurement. The characterizations with both sources were performed on different dates, which can explain the differences, given that the alignment condition and cleanliness of the cavity change over time.

Table 6 – Parameters of Alice's analysis cavity, experimentally determined for S-polarization. The phase-to-amplitude quadrature conversion values are calculated for the analysis frequency of 15 MHz

Alice's analysis cavity parameter	OPO -41.5°C 794.4(6)nm	Ti-saph 795nm
Finesse	118.5(2)	114(2)
Bandwidth - FWHM (MHz)	6.13(8)	6.4(1)
Intensity enhancement	37.71(8)	19.8(8)
Q factor ($\times 10^6$)	63.3(8)	34(1)
Waist radius (μm)	319.7(7)	320.0(7)
Rayleigh length (mm)	405(2)	405(2)
Visibility (%)	98(1)	66(4)
Total roundtrip losses (%)	5.17(1)	5.39(7)
Coupler transmission (%)	5.07(1)	5.25(7)
Spurious losses (%)	0.105(9)	0.138(9)
Reflectivity in resonance (%)	92.2(6)	90.2(6)
Minimum analysis frequency to fully retrieve phase (MHz)	8.7(1)	9.0(2)
Detuning for phase-to-amplitude conversion (MHz)	3.28(4)	3.43(6)
Percent of the transmission peak for the conversion (%)	46.6(1)	46.5(1)
Carrier reflectivity at the conversion (%)	96.4(3)	97.2(2)
Upper sideband reflectivity at the conversion (%)	99.79(2)	99.46(4)
Lower sideband reflectivity at the conversion (%)	99.50(4)	95.2(6)

For complete phase-to-amplitude quadrature noise conversion, the condition $\Omega > \sqrt{2}\Delta\omega_{acav}$ must be fulfilled, where Ω represents the analysis frequency, and $\Delta\omega_{acav}$ denotes the cavity bandwidth [103, 107]. In this regime, a detuning can be chosen so that only the carrier interacts significantly with the cavity, undergoing an approximate $\pi/2$ phase shift, while the sidebands are mostly reflected. In other words, only the carrier, which serves as the local oscillator, is attenuated, with minimal vacuum noise contribution mixing into the sidebands. As indicated in Table 6, the reflectivity for the sidebands at the phase-to-amplitude conversion detuning is nearly 100%, with minimal associated losses.

The minimum analysis frequency needed to fully retrieve the phase quadrature information using Alice's cavity is $\Omega_{min} = \sqrt{2}\Delta\omega_{acav} = 8.7(1)$ MHz. This value, along with the minimum frequencies for the other analysis cavities, guided our choice for the lower bound of the analysis frequency used in our system. On the other hand, the upper bound is set by the OPO's spectral half-width at half-maximum, 24.7(5) MHz for signal beam, since frequencies higher than this result in a significant reduction in quantum correlations. Within this range, we aim to select the analysis frequency as low as possible to maximize the available quantum resources, considering the Lorentzian profile of the OPO cavity. However, the Diabolo laser exhibits strong intrinsic phase modulation at 12 MHz, which persists even after passing through the filter cavity. To avoid saturation of our electronic signals, a filtering process was implemented, which affected the ± 2 MHz range around the 12 MHz, rendering it unusable for analysis. As a result, we opted for an analysis frequency of 15 MHz.

5.3.2.2 Alice's Detection Schemes

At Alice's station, we use three homemade detectors designed for high-fidelity measurement of HF signals (Figure 25c). During the teleportation protocol, two of these detectors are in operation: one is responsible for measuring the amplitude quadrature, while the second, located after the analysis cavity's reflection, is used to measure the phase quadrature. The photodiodes (*PC10-7 TO* from *First Sensor*) used in the detectors have a protective curved glass window that reflects a small percentage of the incident light. To minimize this reflection loss, we use a mirror to retroreflect the beam back into the detector.

To characterize our quantum resource, we perform quantum tomography of the four-mode global state, comprising the two sideband modes of the signal and idler beams. During this measurement, we adjust the waveplates to direct the full intensity of the signal beam into the analysis cavity. At the output of the cavity, a waveplate and a PBS on a flip mount (see Figure 25a) are used to divide the beam into two paths. We then measure the state quadratures using the phase detector and the third detector, both configured in a balanced detection scheme to simultaneously capture shot noise values.

5.3.2.3 Optical Losses

Optical losses are highly detrimental to continuous-variable quantum resources. To address this, the experimental setup following the OPO was carefully designed to minimize losses, constrained by the practicality of the system operation and the available optical components. Despite these efforts, the final setup incorporates numerous optical components, which inevitably introduce a significant level of loss. Additional care was

taken to prevent unnecessary losses through regular cleaning of the system.

The signal beam losses through the system were characterized by measuring its intensity at several key positions, with multiple measurements taken at each location to ensure reliable statistical estimates. These measurements were conducted using a silicon photodiode power sensor (*S121C*, *Thorlabs*) in combination with the *Thorlabs PM003148* power meter electronics. To account for intensity fluctuations in the OPO output fields, we simultaneously monitored, using an oscilloscope, the power meter signal and two reference signals: the idler beam intensity, measured at Victor's station, and the signal beam transmitted through the OPO's input mirror.

The transmission efficiency from the OPO output to the point after the PBS, which splits the signal beam for orthogonal quadrature measurements, is estimated as $\eta_{OPO,mix}^s = 80.5(5)\%$. From the PBS to the detectors measuring the amplitude and phase quadratures, the efficiencies are $\eta_{mix,pdet}^s = 98.5(5)\%$ and $\eta_{mix,qdet}^s = 91.5(5)\%$, respectively. Consequently, the total transmission efficiencies from the OPO output to the detectors are $\eta_{OPO,pdet}^s = 79.3(6)\%$ for the amplitude quadrature and $\eta_{OPO,qdet}^s = 73.7(6)\%$ for the phase quadrature. Including the intrinsic efficiency of the photodetector, the total transmission is $\eta_{OPO,pmeas}^s = 70.2(6)\%$ for amplitude and $\eta_{OPO,qmeas}^s = 66.2(5)\%$ for phase measurements.

5.3.3 Bob Station

Bob receives Alice's amplitude and phase noise measurement signals through two classical channels and applies a displacement operation on the corresponding quadrature of his share of the EPR state, conditioned on these measurements. By using the quantum correlations between Alice's and Bob's fields, this feedforward mechanism cancels excess noise in Bob's state while adding the input state mean value and noise. In the perfect correlation scenario, with infinite squeezing, all the quantum noise in the Bob's EPR state is compensated, leaving in the teleported state only the input state information. For finite squeezing, the teleportation fidelity is inherently limited but still exceeds the capabilities of any classical method by effectively utilizing quantum resources.

A detailed schematic of Bob's experimental setup is presented in Figure 26. To determine the losses for the idler beam, we employed the same measurement approach as used for the signal beam. The final transmission efficiency for the idler field, calculated from the OPO to just after the second EOM, was found to be $\eta_{OPO,2EOM}^i = 81.7(1)\%$.

5.3.3.1 Conditioned Displacement Operation

To implement the displacement operation at Bob's station, two electro-optic modulators (EOMs) are employed as phase modulators. These devices are used to independently

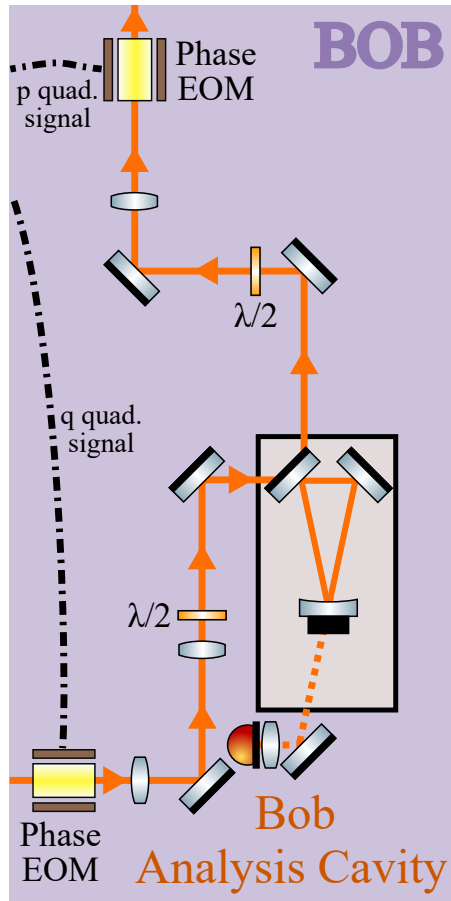


Figure 26 – Schematic of Bob’s experimental setup, illustrating the arrangement of optical components.

modulate the phase and amplitude quadratures of the optical field. However, because phase EOMs inherently modulate only the phase quadrature, achieving amplitude quadrature modulation requires an intermediate conversion step. The conversion between phase and amplitude quadratures is performed using an analysis cavity, which is carefully locked at the point where the phase-to-amplitude quadrature conversion is optimized. This step ensures that the second phase EOM can effectively modulate the original amplitude quadrature, enabling precise control over both quadratures required for the conditioned displacement operation.

As a result, the final teleported state is rotated relative to the carrier. Specifically, the information encoded in the input state’s amplitude and phase quadratures is transferred to the teleported state’s phase and amplitude quadratures, respectively. However, this is not a significant issue since the phase relationship can be restored through a local rotation operation. For instance, this can be achieved by locking Victor’s cavity at the phase-to-amplitude conversion detuning, a routine step performed during the optimization of the amplitude classical channel gain.

The decision to use two phase EOMs, rather than a combination of a phase EOM and an amplitude EOM, was driven by the need to minimize spurious noise in the system.

Amplitude EOMs based on Pockels cells are susceptible to crosstalk, unintentionally introducing small modulations in the phase quadrature while modulating the amplitude quadrature. Such crosstalk would elevate noise levels in the teleported state, compromising the fidelity of the teleportation process. Other amplitude modulation approaches we explored were also problematic: they either exhibited crosstalk, introduced significant optical losses, or failed to meet our bandwidth requirements. By exclusively employing phase EOMs, we eliminated these concerns, though it required the additional effort of building and stabilizing another analysis cavity.

We utilize two phase electro-optic modulators (EOMs) of model *PM-C-BB*, produced by *Qioptiq LINOS*. Each EOM consists of a Brewster-cut MgO-LiNbO₃ crystal. According to the manufacturer, these modulators exhibit a transmission efficiency of TEOM > 98% for wavelengths within the 680–2000 nm range. Due to the small clear aperture of 1.5 mm and the lateral beam offset introduced by the Brewster angle cut, careful consideration of the EOM characteristics is crucial when performing mode matching for the optical cavities. A waveplate is required before each EOM to serve two purposes. First, it optimizes the alignment of the polarization axis with the crystal axis, minimizing spurious polarization modulation and the resulting amplitude modulation. Second, it addresses polarization-dependent transmission: the experiment is designed to use S-polarized light to reduce losses, but for practical operation of the EOM (to ensure the propagation offset is lateral rather than vertical), maximum transmission is achieved with P-polarization.

5.3.3.2 Bob's Analysis Cavity

The analysis cavity at Bob's station is specifically designed to operate at the phase-to-amplitude conversion detuning. Its design is similar to Alice's cavity, utilizing the same triangular optical configuration, mounting system design (Figures 25c and 25b), and electronic locking approach, with separate electronic devices dedicated to this cavity. The cavity transmission is measured using an InGaAs switchable gain detector (*PDA10CS*, *Thorlabs*). To ensure the locked detuning remains robust against pump variations, the reference signal for the subtraction system is derived from the transmission of the idler beam through the OPO's input mirror, which is measured using a detector of the same model.

The mirrors used in Bob's cavity, manufactured by *Layertec*, are identical to those employed in Victor's cavity. The high-reflective (HR) concave mirror is specified with a reflectivity of $R_{\text{int,conc}}^i > 99.9\%$ for wavelengths from 1603 to 1613 nm, designed for angles of incidence between 0° and 10°, with a radius of curvature of 1.00(1) m. The internal HR plane mirror has a reflectivity of $R_{\text{int,pl}}^i > 99.8\%$ for 1500–1650 nm at 45° incidence and S-polarization. A partially reflective input plane mirror specified for a 45° angle of incidence was not available for the wavelength of interest. To address this limitation,

we requested simulation results from *Layertec* for coatings previously ordered, spanning various wavelengths and angles of incidence. Through interpolation, we identified that a mirror designed for $R = 96(1)\%$ at 1608 nm, S-polarization, and incidence angles between 0° and 10° , would achieve a reflectivity of $R_{\text{coup,pl}}^i = 94(1)\%$ at 43° AOI. Although we decided to use this mirror as it met our requirements, it is important to note that its reflectivity is highly sensitive to small changes in angle, as it was not optimized for this specific incidence.

We performed a detailed characterization of the cavity using the OPO-generated idler field at several wavelengths and auxiliary telecom lasers: the RIO at 1560.6 nm and the Agilent at 1608.0 nm. The measured cavity perimeter is 455(7) mm, corresponding to a free spectral range of 659(10) MHz. The experimentally determined parameters, presented in Table 7, show good agreement with the expected values. Although the visibility for the auxiliary lasers was not optimized, it was accounted for in the analysis.

Table 7 – Experimentally measured parameters of Bob’s analysis cavity for S-polarization, with phase-to-amplitude quadrature conversion values calculated at 15 MHz analysis frequency.

Bob’s analysis cavity parameter	OPO –41.5°C	Agilent 1608nm	RIO 1560nm 1611(3)nm
Finesse	95.4(2)	107.8(4)	153.0(7)
Bandwidth - FWHM (MHz)	6.9(1)	6.1(1)	4.31(7)
Intensity enhancement	30.36(5)	34.3(1)	48.7(2)
Q factor ($\times 10^6$)	27.8(4)	31.4(5)	45.5(7)
Waist radius (μm)	464(1)	463(1)	456(1)
Rayleigh length (mm)	419(2)	419(2)	419(2)
Visibility (%)	98.4(8)	73(1)	68(1)
Total roundtrip losses (%)	6.37(1)	5.66(2)	4.02(2)
Coupler transmission (%)	6.32(4)	5.61(2)	3.98(2)
Spurious losses (%)	0.05(4)	0.05(1)	0.04(1)
Reflectivity in resonance (%)	97(2)	96.6(9)	96.0(4)
Minimum analysis frequency to fully retrieve phase (MHz)	9.8(2)	8.6(1)	6.1(1)
Detuning for phase to amplitude conversion (MHz)	3.86(6)	3.31(5)	2.22(4)
Percent of the transmission peak for the conversion (%)	44.5(1)	46.0(1)	48.4(1)
Carrier reflectivity at the conversion (%)	98(1)	98.4(4)	98.0(2)
Upper sideband reflectivity at the conversion (%)	99.89(8)	99.91(2)	99.94(1)
Lower sideband reflectivity at the conversion (%)	99.7(2)	99.78(6)	99.89(1)

5.3.4 Victor: State Tomography Station

Victor receives the teleported state and, since he created the input state, he is the only party in the experiment who knows what the state is. By running the experiment multiple times with the same input state, he can perform quantum tomography to

reconstruct the teleported state and evaluate the protocol's success. In this experiment, success is measured by fidelity, with the 50% benchmark serving as the threshold for demonstrating a quantum advantage over any classical method, as discussed in more detail in Section 4.3.2. Figure 27 presents a detailed schematic of the optical setup used for quantum tomography, consisting of an analysis cavity and a balanced detection scheme to implement the auto-homodyne technique. The transmission efficiency at Victor's station, measured in the same run as Bob's station, from the output of the second EOM to the detectors, was determined as $\eta_{2EOM, det}^i = 91.4(1)\%$. Including the intrinsic efficiency of the photodetectors, this value is reduced to $\eta_{2EOM, meas}^i = 78.1(1)\%$. The reported values represent an average over the efficiencies associated with each of the detectors used in Victor's balanced detection. The total measured efficiency from the OPO to the detectors, incorporating quantum efficiency, is given by $\eta_{OPO, meas}^i = 63.8(1)\%$.

The balanced detection setup consists of two custom-built detectors, each of them utilizing photodiodes (*ETX 500T* from *Epitaxx*) featuring planar windows. During testing, we found that removing the window reduced optical losses but significantly shortened the diodes' operational lifetime. Consequently, we chose to keep the windows in place. Additionally, we decided not to redirect the small fraction of reflected light back onto the photodiode. This choice was driven by the diode's limited active area (0.785 mm^2), which makes precise alignment and focusing of the reflected beam challenging. Furthermore, our finding that reflection losses at the window and photodiode chip were minimal allowed for a simplified optical design without the need for complex reflection management.

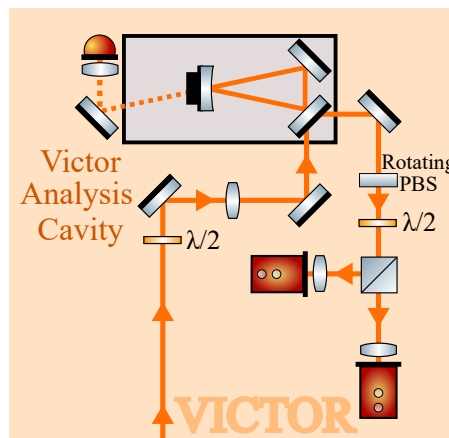


Figure 27 – Schematic of the optical setup at the second Victor station for quantum tomography, featuring an analysis cavity and a balanced detection scheme to implement the auto-homodyne technique.

5.3.4.1 Victor's Analysis Cavity

The primary function of Victor's analysis cavity is to perform quantum tomography (Section 3.3). This involves scanning the cavity detuning around a resonance peak using

the PZT actuator coupled to the concave mirror. Additionally, stabilizing the cavity at the phase-to-amplitude conversion detuning is essential during the gain adjustment of the amplitude quadrature classical channel. Consequently, implementing locking electronics was also necessary.

The cavity was constructed following the same design as the Alice and Bob cavities, utilizing the same mirrors as Bob's cavity and the same detector model to measure its transmission. Since stabilization is only required for a short period and not during measurements, no signal processing strategy using a reference signal was implemented to make the stabilized detuning robust to pump intensity variations. The experimental results from the cavity characterization are presented in Table 8. The cavity's perimeter was determined to be 479(6) mm, corresponding to a free spectral range of 626(8) MHz, aligning with our expectations.

Table 8 – The experimentally determined Victor's analysis cavity parameters for S-polarized light, with phase-to-amplitude quadrature conversion calculated at a 15 MHz analysis frequency.

Victor's analysis cavity parameter	OPO	Agilent	RIO
	–41.5°C	1608nm	1560nm
	1611(3)nm		
Finesse	91.9(2)	118.6(3)	134.3(5)
Bandwidth - FWHM (MHz)	6.81(9)	5.28(7)	4.66(6)
Intensity enhancement	29.25(5)	37.8(1)	42.8(2)
Q factor ($\times 10^6$)	28.2(4)	36.3(5)	42.2(6)
Waist radius (μm)	469(1)	467(1)	460(1)
Rayleigh length (mm)	427(2)	427(2)	427(2)
Visibility (%)	98.5(7)	81(1)	83(1)
Total roundtrip losses (%)	6.61(1)	5.16(1)	4.57(2)
Coupler transmission (%)	6.15(7)	4.88(2)	4.19(3)
Spurious losses (%)	0.48(7)	0.29(1)	0.40(2)
Reflectivity in resonance (%)	74(4)	79.1(6)	69(2)
Minimum analysis frequency to fully retrieve phase (MHz)	9.6(1)	7.5(1)	6.59(9)
Detuning for phase to amplitude conversion (MHz)	3.48(4)	2.64(3)	2.21(3)
Percent of the transmission peak for the conversion (%)	48.9(1)	50.0(1)	52.6(1)
Carrier reflectivity at the conversion (%)	87(2)	89.6(3)	83.5(8)
Upper sideband reflectivity at the conversion (%)	99.1(1)	99.54(2)	99.43(3)
Lower sideband reflectivity at the conversion (%)	97.9(3)	99.09(4)	98.99(6)

Victor and Bob analysis cavities exhibit a spurious Hänsch-Couillaud effect, characterized by a resonance-dependent polarization shift [182]. We attribute this to the birefringence of the input mirror's reflection and to small deviations from a planar cavity alignment. The primary consequence is that the carrier, when interacting with the cavity and experiencing the associated phase shift, also undergoes a tiny polarization change. This results in incomplete mode overlap of the carrier with the total reflected sidebands, effectively introducing losses for the quantum states we aim to measure. A secondary minor

issue arises in the balanced detection scheme: by dividing the beam with a $\lambda/2$ waveplate and a PBS, the polarization shift disrupts the 50:50 beam balance during the resonance scan, preventing the simultaneous acquisition of the shot noise level. To mitigate these effects, we employed a polarizing beam splitter (PBS) on a rotating mount (Figure 27) to purify the polarization component of the carrier aligned with the reflected sidebands, eliminating the transverse residual polarization component. The PBS angle is optimized by maximizing transmission with the cavity out of resonance.

5.4 Detection system and classical communication

This section provides technical details of the detection system and the classical communication channel, both essential components of the teleportation protocol. It presents the design and operation of the employed photodiode-based detectors, including their role in separating and amplifying the acquired signal components. The section also explores the signal processing architecture of the data acquisition system, detailing how signals are digitized and filtered for optimal performance. Additionally, it addresses the design principles of the classical channels and outlines the procedures for gain calibration and phase alignment, necessary for accurate transmission and reconstruction of the teleported quantum state.

5.4.1 Detectors

The quantum state measurements are performed using photodiode-based detectors operating in photoconductive mode. These semiconductor devices produce a photocurrent in response to the incident optical field. The generated photocurrent can be expressed in time as $I(t) = \langle I(t) \rangle + \delta I(t)$, where $\langle I(t) \rangle$ is the mean photocurrent (low-frequency DC component), and $\delta I(t)$ represents the fluctuations (high-frequency HF component). The detector circuits are custom-designed, all sharing the same architecture. Within each circuit, the photocurrent is separated into DC and HF components using a first-order filter with a 600 kHz cut-off frequency, then the DC component is converted into voltage by a load resistance, and this resulting voltage is amplified. The HF component is converted into voltage signals and amplified via a transimpedance amplifier (TIA) [100]. These detectors provide independent access to both signal components, each with different gains. The resulting output voltages can be expressed in terms of the photocurrent operator as:

$$V_{\text{DC}}(t) = g_{\text{DC}} \langle \hat{I}(t) \rangle = g_{\text{DC}} |\alpha(t)|^2, \quad (5.2a)$$

$$\delta V_{\text{HF}}(t) = g_{\text{HF}} \delta \hat{I} + \delta e(t) = g_{\text{HF}} |\alpha(t)| \delta \hat{X}(t) + \delta e(t). \quad (5.2b)$$

Here, g_{DC} and g_{HF} represent the DC and HF gains, respectively, incorporating all proportionality constants and electronic properties of the detector to ensure the validity of the equality. The term $\alpha(t)$ describes the complex amplitude of the field, $\delta\hat{X}(t)$ represents the accessible quadrature fluctuations of the field, and $\delta e(t)$ accounts for the inherent electronic dark noise, commonly referred to as Johnson-Nyquist thermal noise [183]. This dark noise at Alice's station can severely impact the teleportation protocol by directly coupling with Bob's field during state reconstruction. This issue justified our design choice at Alice's station: when measuring the amplitude and phase quadratures, we opted against balanced detection for acquiring the corresponding shot noise value. This decision was made to prevent the summation of dark noise from each detector, which would otherwise degrade performance.

The three detectors for the signal beam were meticulously constructed to achieve near-identical performance, utilizing the same photodiodes and identical electronic components. Similarly, the two detectors for the idler beam were designed with the same principles. Despite these efforts, slight variations in detector responses were unavoidable. To address this, precise characterization and successive fine-tuning were conducted to optimize their performance. Any remaining discrepancies were corrected digitally whenever possible, as described in greater detail in the following sections.

For the signal beam measurement, we used a silicon-based PIN photodiode, model *PC10-7 TO*, manufactured by *First Sensor*. This photodiode has a circular active area of 10 mm^2 and operates with a reverse bias of 70 V, implying a capacitance of approximately 5.5 pF. The amplifier in the detector circuit is configured for a $1 \text{ mA} \rightarrow 1 \text{ V}$ conversion for the low-frequency (DC) signal.

The idler beam measurement utilized an InGaAs-based PIN photodiode, model *ETX 500T*, produced by *Epitaxx*. This device has a circular active region with a diameter of 0.5 mm, giving an effective area of 0.785 mm^2 . A reverse bias of 15 V was used, resulting in a capacitance of 15 pF. For this detector, the amplifier is designed to perform a $1.91 \text{ mA} \rightarrow 1 \text{ V}$ photocurrent-to-voltage conversion for the DC signal.

The detection process in optical detectors is inherently probabilistic, not unitary, meaning that not all incident photons are converted into measurable signals. The quantum efficiency (η_{QE}) quantifies this limitation by describing the average proportion of photons successfully converted into charge carriers (electrons or holes). The quantum efficiency, defined in terms of experimentally measurable quantities such as photocurrent and incident optical power, is given by [184]:

$$\eta_{QE} = \left(\frac{hc}{e\lambda} \right) \frac{I_{\text{ph}}}{P_{\text{opt}}}. \quad (5.3)$$

Where I_{ph} refers to the generated photocurrent, P_{opt} is the power of the incident optical

signal, λ denotes the wavelength of the incident light, and e , h , and c correspond to the elementary charge, Planck's constant, and the speed of light in vacuum, respectively. To measure the performance of our detectors and account for the losses in the detection procedure, we determined the quantum efficiency for all the detectors. For the signal detectors, we obtained efficiencies of $\eta_{Ap} = 86.60(4)\%$, $\eta_{Aq} = 89.88(4)\%$, and $\eta_{\text{Tomo}} = 86.20(4)\%$. For the idler, the efficiencies are $\eta_{V1} = 83.2(1)\%$ and $\eta_{V2} = 87.75(7)\%$. Figure 28 illustrates the fits for the detectors involved in the teleportation protocol.

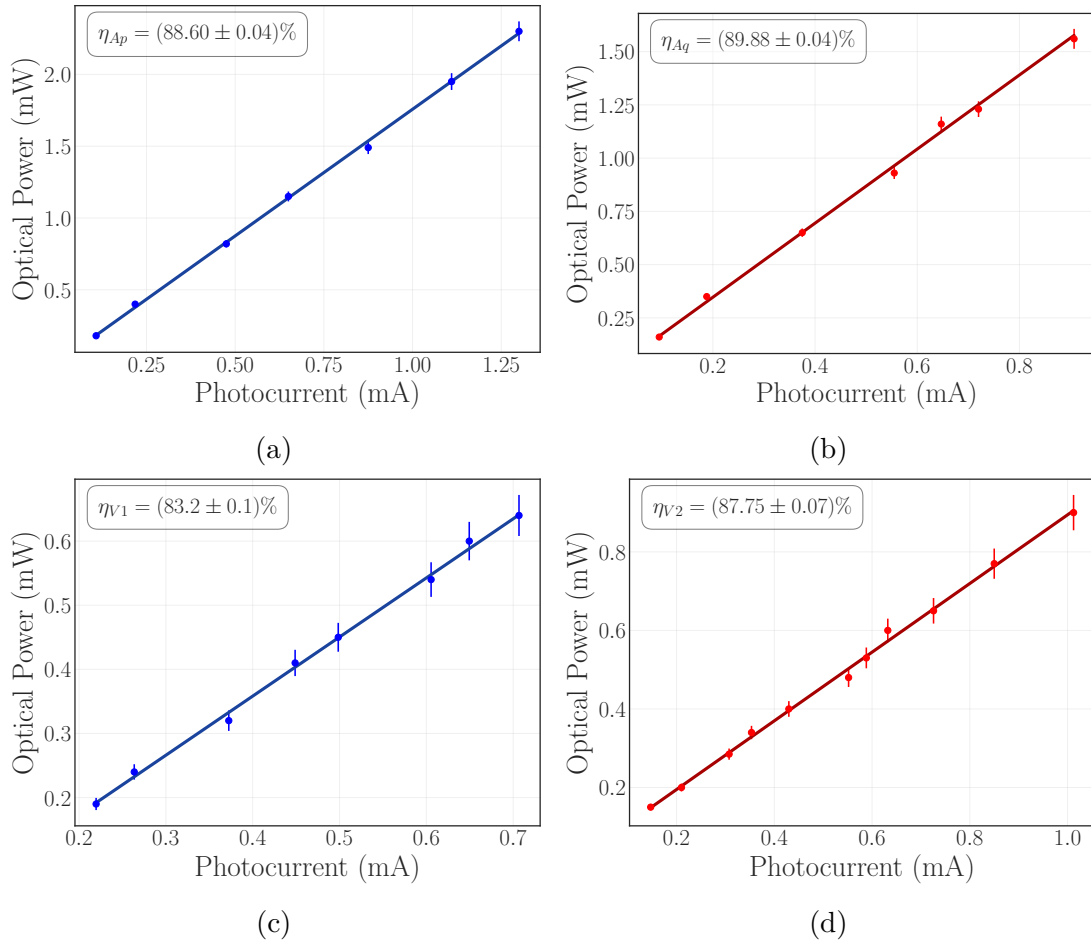


Figure 28 – Quantum efficiency characterization for the detectors in the teleportation protocol: (a) Alice's amplitude quadrature detector, (b) Alice's phase quadrature detector, and (c, d) Victor's detectors used in the balanced detection scheme. The error bars were calculated using the uncertainty specifications provided by *Thorlabs* for the power meters *S121C* (signal) and *S122C* (idler).

5.4.2 Demodulation and Data Acquisition

The high-frequency (HF) component of Alice's detectors is split into two paths using a power splitter (*ZSC-2-1*, manufactured by *Mini-Circuits*). One path is directed to the classical communication channel of the teleportation protocol, while the other is connected to the data acquisition system. For Victor's detectors, the HF signals are

transmitted directly to the data acquisition system. A schematic diagram illustrating the signal processing workflow for both data acquisition and classical communication is shown in Figure 29. The figure shows the teleportation protocol setup. For two-field quantum tomography, cables are rerouted from Alice's amplitude detector to the tomography detector (located after the analysis cavity). This rerouting enables the balanced detection scheme, and the classical channel feed-forward is also disconnected. Since accurate correlation measurements between these electronic signals rely heavily on phase alignment, all intermediate cables were selected to have identical lengths. Their propagation delays were tested and calibrated using a function generator and an oscilloscope to ensure minimal phase discrepancies.

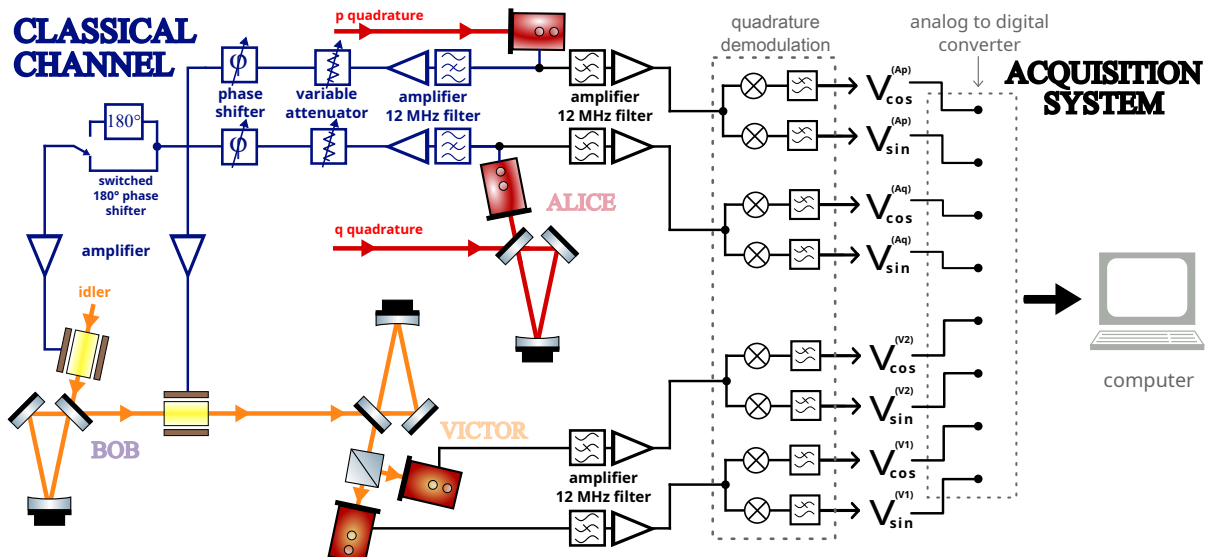


Figure 29 – Schematic diagram of the electronic signal processing system for HF signals detected at Alice and Victor stations. At Alice's station, the HF signal is split into two paths: one for the acquisition system and the other for teleportation classical communication. At Victor's station, the entire signal is sent to the acquisition system. For data acquisition, HF signals are amplified, filtered with a 12 MHz band-cut filter, and processed through a quadrature demodulation system. These demodulated signals are digitized using an ADC board and saved to a computer. The two classical communication channels include preamplifiers with 12 MHz band-cut filters, variable attenuators and phase shifters for precise teleportation gain adjustment, and final amplifiers before driving Bob's EOMs. The phase quadrature channel also includes a switched inverter (π phase shifter) before the final amplifier.

For data acquisition, each HF signal is amplified by a custom-built amplifier with an integrated 200 kHz bandwidth active filter. The filter suppresses the 12 MHz frequency component, as illustrated in the power spectrum in Figure 30. This suppression is necessary because the Diabolo laser stabilizes the second harmonic generation (SHG) cavity using a 12 MHz signal. The strong modulation of this signal requires additional filtering, even after the filter cavity, to avoid saturating the electronic devices. After amplification and filtering,

the HF signals are directed to a quadrature demodulation system, a signal processing technique designed to extract amplitude and phase information from a modulated carrier signal.

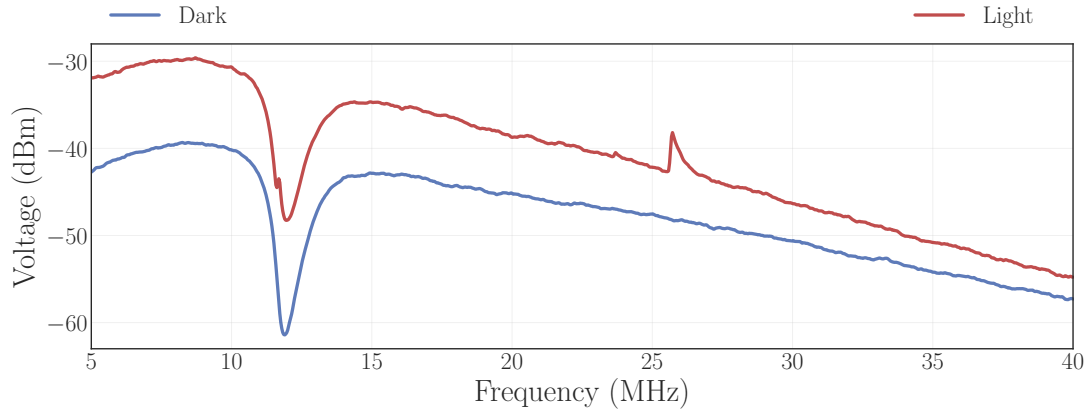


Figure 30 – The power spectrum of Alice’s phase quadrature detector is shown after the amplification and filtering step. The blue curve represents the detector’s response without incident light, while the red curve corresponds to a 1.12 mW beam from the OPO at -41.5°C (794.4(6) nm). Distinct spectral features include active filtering around 12 MHz, the pump laser stabilization modulation peak at 12 MHz and its second harmonic at 24 MHz, and the modulation at 26 MHz, used for stabilizing the OPO. The measurements were conducted using the *Keysight EXA N9010B* spectrum analyzer, configured with a resolution bandwidth (RBW) of 30 kHz, video bandwidth (VBW) of 1 kHz, and an average of 100 repetitions for improved signal clarity.

The analog quadrature demodulation process is implemented by splitting each signal into two distinct paths using a power splitter (*ZSC-2-1, Mini-Circuits*). These two signals are then processed by a custom-designed electronic device, where each is mixed with an electronic local oscillator operating at the analysis frequency (15 MHz) and phase-shifted by $\pi/2$ relative to the other (in quadrature). A low-pass filter with a bandwidth of 300 kHz is subsequently applied to the resulting signals. The local oscillators are generated by an *Agilent 81150A* function generator, clock-synchronized with the function generator used during the displacement operation for input state preparation (Section 5.3.1). Through quadrature demodulation, the high-frequency signal is decomposed into two low-frequency orthogonal components: the in-phase (I) and quadrature-phase (Q) components, referred to here as the cosine and sine components [185]. These low-frequency signals are compatible with the bandwidth of our analog-to-digital converter (ADC) boards and are subsequently transmitted to them for data acquisition. By recovering both the amplitude and phase of the electronic signal, the quadrature demodulation procedure enables digital correction of the phase shift between the measured electronic signals from Alice’s and Victor’s detectors. This shift arises due to differences in the capacitances of their photodiodes. The details of this compensation are described in terms of the covariance matrix elements in Section 3.3.5.

We use two 8-channel ADC boards (*PCI-6133*) paired with *BNC-2110* connectors, both from *National Instruments*, which are directly connected to the computer, offering a total of 16 available measurement channels for data acquisition. The channels are allocated as follows: four channels record the DC components of the custom-built detectors used during a measurement, eight channels capture the sine and cosine components of the HF demodulated signals, two channels measure the transmission of the analysis cavities, and the final two channels monitor the pump beam. Specifically, one channel measures a small fraction of the pump beam directed toward the OPO, and the other measures the pump light reflected by the OPO. The voltage data is acquired at a rate of 600 kS/s (samples per second). Since our measurements involve scanning the detuning of the analysis cavities and collecting a large number of data points to correlate with the detuning position, the process is relatively slow. Each measurement takes 750 ms, resulting in 450,000 voltage samples per channel. To address artifacts associated with classical communication, as will be detailed in the following sections, a 6th-order digital Butterworth low-pass filter with a cutoff frequency of 100 kHz is applied to the digitized signal, effectively narrowing the spectral range of the post-demodulation filter.

For shot noise characterization, we use a balanced detection scheme, which allows for simultaneous measurement of field fluctuations and the corresponding shot noise value. The theoretical description of this detection scheme is provided in Section 3.1.1. The setup involves splitting the beam into two equal-power parts using a $\lambda/2$ waveplate and a polarizing beam splitter (PBS). Each beam is then directed to a photodetector, ensuring precise and balanced detection. This approach requires the electronic signals from the two detectors to experience identical gain and phase shifts during signal processing. Despite designing the electronic processing units with matched components and architecture, minor residual differences remain. To mitigate these discrepancies in gain, we conduct a calibration procedure before each measurement, evaluating the balance of the high-frequency (HF) gain in the acquisition system. Figure 31 presents the HF response, expressed as the standard deviation of the HF electronic signal, for sine and cosine demodulations at both detectors, across different balanced beam intensities. Based on this calibration, we correct for any gain mismatch by digitally scaling one signal, such as signal (1), by the relative gain factor:

$$g_{\text{rel}}^{(2,1)} = \frac{g_{\text{HF}}^{(2)}/g_{\text{HF}}^{(1)}}{g_{\text{DC}}^{(2)}/g_{\text{DC}}^{(1)}}. \quad (5.4)$$

As illustrated by the initial points in the plots of Figure 31, measured under dark conditions with no incident light, a portion of the observed fluctuations arises from electronic noise. Figure 32 displays the signal-to-noise ratio (SNR) of the acquisition system, defined as:

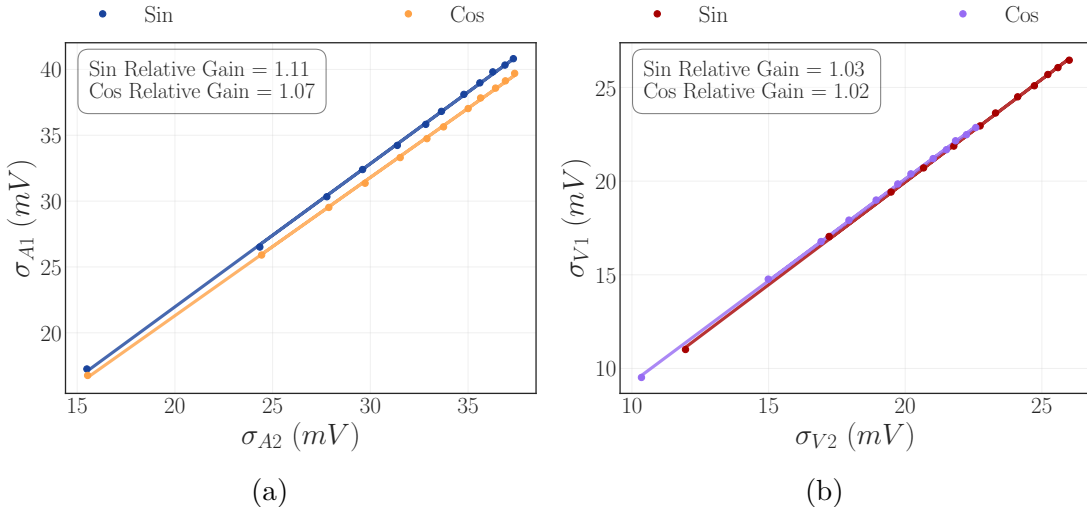


Figure 31 – Comparison of the standard deviation of the high-frequency (HF) signal from the detector pairs for the (a) signal and (b) idler fields, measured after the complete acquisition system. The measurements were conducted at an analysis frequency of 15 MHz, with the nonlinear crystal maintained at -41.5°C (794.4(6) nm and 1611(3) nm). The first data points represent the "dark" condition, where no incident light is present, corresponding to electronic noise.

$$\text{SNR} = \Delta^2 V_{HF} / \Delta^2 e, \quad (5.5)$$

where $\Delta^2 V_{HF}$ represents the variance of the measured signal and $\Delta^2 e$ corresponds to the variance of the electronic noise, expressed as a function of the incident beam power. For the protocol to be executed correctly, the signal-to-noise ratio (SNR) must be carefully managed. While working near the oscillation threshold maximizes quantum resources, the low power of the generated beams significantly degrades the SNR, making the data more prone to errors. Consequently, it is crucial to identify a balance that optimizes the SNR of the acquisition system while maintaining the benefits of operating close to the threshold.

5.4.3 Classical channel

Classical communication is a critical component of the teleportation protocol, operating as the mechanism through which Alice's measurement results are transmitted to Bob for the reconstruction of the teleported state. Alice's joint measurement produces two distinct outcomes: one corresponding to the amplitude quadrature and the other to the phase quadrature. These results are transmitted to Bob over two separate classical channels. The finite speed of this transmission, constrained by the speed of light, ensures compliance with the no-signaling theorem, which prohibits faster-than-light information transfer [120].

Upon receiving the measurement results, Bob uses them to drive the electro-

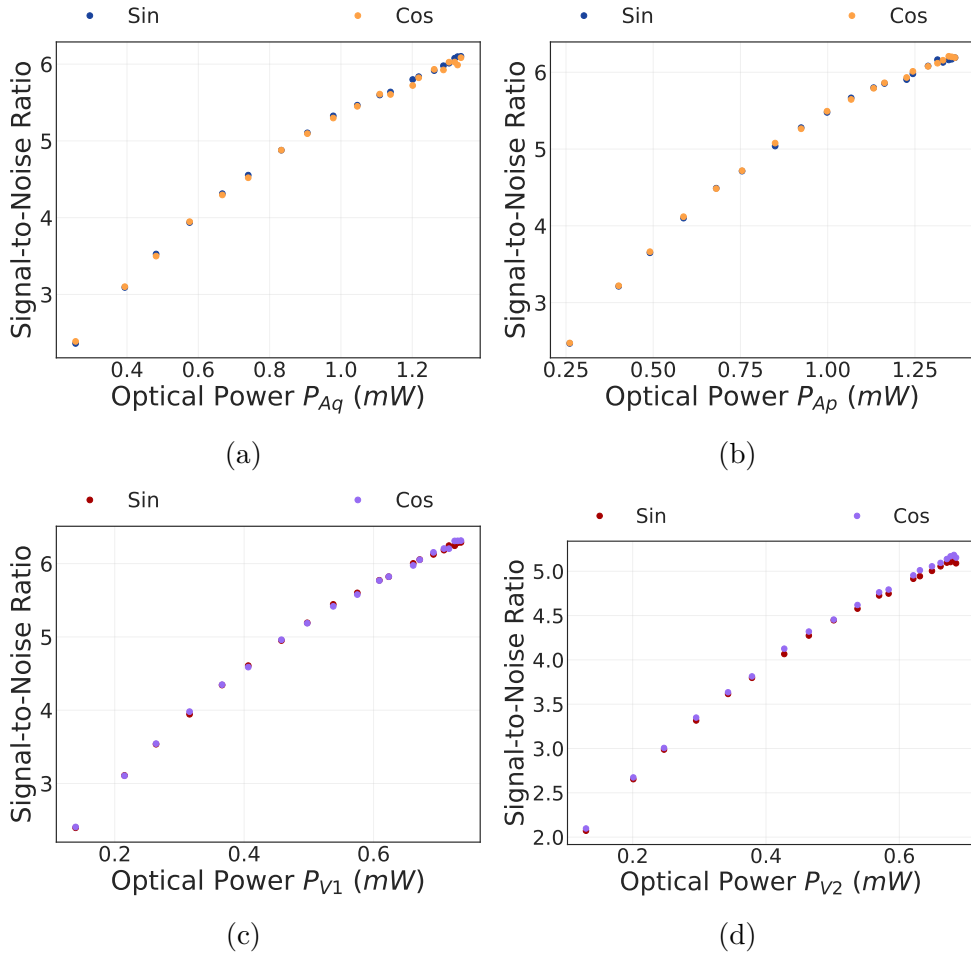


Figure 32 – Signal-to-noise ratio (SNR) of the acquisition system in the teleportation protocol as a function of incident optical power. Results are shown for (a) Alice’s phase quadrature detector, (b) Alice’s amplitude quadrature detector, and (c, d) Victor’s detectors. Measurements were taken at an analysis frequency of 15 MHz, with the PPKTP crystal maintained at -41.5°C (wavelengths: 794.4(6) nm and 1611(3) nm).

optic modulators (EOMs) responsible for performing the displacement operations. Each classical channel incorporates an associated variable electronic gain (g_Q for the amplitude quadrature and g_P for the phase quadrature) and an electronic phase shifter (ϕ_Q and ϕ_P) to account for two key factors: the difference in voltage ranges between the measured signals and the voltages required to control the EOMs, and the phase shifts introduced by the communication line. These complex electronic gains are directly related to the teleportation normalized gains, $\Gamma_P = \langle \hat{P}_{\text{out}} \rangle / \langle \hat{P}_{\text{in}} \rangle$ and $\Gamma_Q = \langle \hat{Q}_{\text{out}} \rangle / \langle \hat{Q}_{\text{in}} \rangle$, which are defined for each quadrature in terms of the mean values of the input state and the teleported state [50]. A more detailed discussion of the teleportation gain can be found in Section 4.2.2. The gain serves as a critical interface between the quantum and classical domains of the protocol, ensuring the appropriate scaling and adjustment of the classical signals. Under the condition of unitary gain ($\Gamma_Q, \Gamma_P = 1$), Bob’s displacement operation, driven by Alice’s classical results, reproduces all input coherent states at a constant fidelity, a key feature

that establishes the protocol's state-independence. Thus, the proper calibration of these gains is essential for achieving optimal performance of the teleportation protocol.

For classical communication, the directed HF signals are preamplified and filtered at 12 MHz using a custom-built amplifier, analogous to the one employed in the acquisition system pathway. Following this step, a variable attenuator (*EVA-23-75+*, *Mini-Circuits*) and a 0° to 360° phase shifter (*SCPHS-13.6+*, *Mini-Circuits*) are applied to both channels to fine-tune the signal. In the phase quadrature channel, the signal is divided by a power splitter (*ZSCJ-2-1+*, *Mini-Circuits*). One of the splitter's outputs introduces a π phase shift relative to the other. By selecting between these outputs, the splitter operates as a switched signal inverter. The electronic signals are then amplified using a 24 dB *ZHL-3A* amplifier (*Mini-Circuits*) and subsequently coupled to Bob's EOMs. Our approach to implementing variable gain involves a fixed amplification stage complemented by a variable attenuator. Both the attenuator and phase shifter are regulated by a control voltage, which can be supplied either internally or externally in our configuration. In all cases, we use a set of potentiometers to manually fine-tune their parameters. For the variable attenuator, the control voltage is supplied externally, enabling dynamic adjustments to the gain settings during teleportation measurements. The components of the classical channel are depicted in the schematic shown in Figure 29.

To adjust the gain parameters, we introduce strong classical correlations into the generated beams, as the quantum correlations we aim to optimize are subtler and provide a weaker signal, making fine-tuning more challenging. This is accomplished by modulating the pump beam at the analysis frequency, which, during the parametric down-conversion process, transfers coherently the modulation to the generated beams, thus establishing correlations between them. For amplitude modulation, we use an acousto-optic modulator (AOM) with a center frequency of 200 MHz (model *AOMO 3200-124*) driven by the *1200AF-AEF0-1.0 RF* driver, both manufactured by *Crystal Technology*. By modulating the amplitude of the AOM's driving frequency, the intensity of the deflected field is controlled, leading to a modulation of the amplitude of the transmitted zero-order mode. The AOM is positioned after the filter cavity and is also used to automatically adjust the pump power during the shot noise calibration measurement. For phase modulation, we use the same electro-optic modulator (EOM, model *LM0202*, *Qioptiq LINOS*) employed for PDH stabilization of the OPO (Section 5.2.4). A power splitter (model *ZSC-2-1*, *Mini-Circuits*) combines the modulation signal with the 26 MHz stabilization signal. The modulation electronic signal at the analysis frequency (15 MHz) used in both devices is generated by an *Agilent 81150A* function generator, which is controlled via LabView software on the computer.

The teleportation gain adjustment procedure is performed before each teleportation measurement. For this, the system must already be prepared, including locking Alice

and Bob's analysis cavities at the phase-to-amplitude conversion point and splitting the signal beam between amplitude and phase detection. During the procedure, all the light at Victor's station is directed to a single detector to enhance the signal, which is then monitored using a spectrum analyzer (*Keysight EXA N9010B*) centered at the analysis frequency. Simultaneously, the light from the Mach-Zehnder responsible for creating the input state is blocked (Figure 24a). The process starts with adjusting the gain of the phase quadrature classical channel. This involves maintaining Victor's cavity out of resonance, activating phase modulation in the pump, and adjusting the phase shifter and attenuation in the channel to suppress the modulation in the idler beam (Figure 29). Since the phase correlation induced by modulating the pump beam is positive, while the quantum phase correlation is negative (Equation 4.20), it is necessary to shift the phase by π . This adjustment is implemented via the switched signal inverter by altering the output port of the power splitter.

Once the gain of the phase quadrature classical channel has been adjusted, we initiate the procedure for the amplitude quadrature channel. To do so, we deactivate the phase modulation and enable amplitude modulation in the pump, and Victor's analysis cavity is stabilized at the phase-to-amplitude conversion point. We then again fine-tune the phase and attenuation in the amplitude channel to suppress modulation in the idler field. Using this approach, we achieve suppression of 60 dB in phase modulation and 40 dB in amplitude modulation. As detailed in Section 4.2.3, due to losses in various parts of the experiment, this process does not perfectly set the system to the unitary gain condition ($\Gamma_Q, \Gamma_P = 1$). However, it does correctly align the channel's electronic phase shift and brings the electronic gain close to the unitary condition. Because the deviation depends only on system losses, the electronic gain can be adjusted by applying a calibrated offset after a few teleportation runs, enabling unitary gain to be achieved for both channels simultaneously.

During the gain adjustment procedure, spurious modulation peaks were observed near the analysis frequency, indicating undesired artifacts in the system. These peaks exhibited dependence on the tuning of the phase shifter and variable attenuator, with both their frequency and amplitude varying accordingly. Figure 33a illustrates these anomalies, showing distinct peaks around the primary modulation at the analysis frequency of 15 MHz. Even after proper gain adjustment (orange curve), residual noise persisted near the analysis frequency. Furthermore, analysis of the demodulated HF signal spectrum, obtained via fast Fourier transform (FFT), revealed corresponding artifact peaks in Victor's measurements during the teleportation protocol, coinciding with the activation of the classical channel. These results point to the presence of additional noise sources or coupling effects within the classical channel that are potentially responsible for generating these observed artifacts.

Analysis of data from teleportation protocol executions revealed that these artifacts

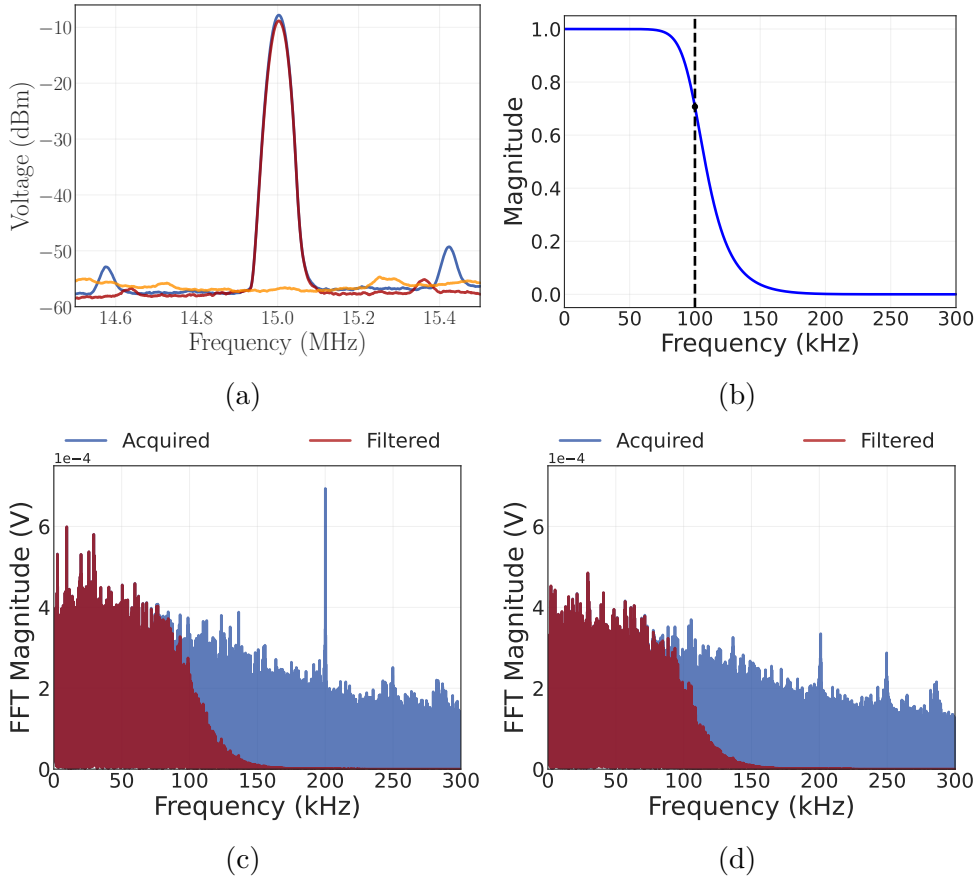


Figure 33 – (a) The curves correspond to the idler beam measured at Victor’s station during the teleportation gain adjustment. The red and blue curves show the classical phase correlations before the adjustment procedure, while the orange curve shows the result after. Spurious modulation peaks are observed near the analysis frequency of 15 MHz, indicating undesired artifacts dependent on the tuning of the phase shifter and variable attenuator. The orange curve shows that residual noise persists even after proper gain adjustment. The spectrum analyzer was set with a 30 kHz RBW, 1 kHz VBW, and the curve represents an average of 100 samples. (b) Transfer function of the 100 kHz 6th-order digital Butterworth low-pass filter applied to the demodulated HF channels using Python’s SciPy library. (c) and (d) FFT spectra of the demodulated HF signal measured at Victor’s station during a teleportation execution before and after applying the digital filter. The DC peak is omitted for clarity.

consistently appear in the 150–300 kHz range. To resolve this, we opted to filter these technical artifacts, effectively narrowing the low-pass filter in the demodulation step. This low-pass filter defines the bandwidth of the sideband modes in which the quantum states are manipulated during the experiment. Given that the affected signal falls well within the bandwidth of our ADC, using an analog filter was unnecessary. A digital filter was preferred instead, offering the dual advantages of increased flexibility in filter design and the assurance that all channels are processed with an identical transfer function. Therefore, in all presented results, a 100 kHz 6th-order digital Butterworth low-pass filter was applied to the demodulated HF channels using the SciPy library in Python [186, 187]. The transfer function of this filter is shown in Figure 33b. Additionally, Figures 33c and 33d show FFT examples of the demodulated HF signal measured at Victor’s station before and after applying the filter. The DC peak has been omitted from these spectra to improve readability. While the main conclusions of the study remained valid without filtering, its use enhanced the data quality.

6 EXPERIMENTAL RESULTS

In this chapter, we present the experimental results, along with the data analysis steps and the characterizations performed to achieve them. Initially, we provide an overview of the data analysis process and define the notation employed throughout the chapter. We then describe the shot noise calibration procedure, a critical step in our quantum measurements, and elaborate on the information it provides. Following this, we present the results of a quantum tomography measurement designed to characterize the global state produced by the OPO and propagated through the system. The chapter concludes with the results of the first demonstration of multicolor quantum teleportation in the continuous-variable domain.

6.1 Data Analysis and Shot Noise Calibration

In this section, we explore the principles of data analysis applied to our measurement results. We define the notation for the acquired voltages and their connection to the theoretical concepts discussed in previous sections. Additionally, we will discuss the shot noise calibration process, which is performed before each measurement session. This calibration not only reveals the dependence of shot noise on the incident power for each detector but also provides valuable insights into the overall system performance.

6.1.1 Overview of the Data Analysis Approach

After acquiring data from the detectors and the demodulation system using analog-to-digital converters (ADC) controlled via LabVIEW software, we proceed to analyze the data using a custom Python script. The variables corresponding to each acquired data channel from the ADCs and their associated notations, as used in this chapter, are summarized in Table 9. When the detectors are in dark conditions, meaning no light is incident on them, the symbol V is replaced with e in the notation to indicate electronic noise. Furthermore, during teleportation measurements, the notations for Alice's detectors are altered, with $A1$ being redefined as AQ for phase quadrature and $A2$ as AP for amplitude quadrature measurements.

The first step in the data analysis process is to apply a digital low-pass filter to the acquired HF signals, as described in Section 5.4.3. The 100 kHz 6th-order Butterworth low-pass filter is implemented using the SciPy Signal module (`scipy.signal`) in Python [187, 188]. Next, we digitally compensate for any differences in the HF gains of the signal and idler balanced detection, following the procedure detailed in Section 5.4.2. Subsequently,

Table 9 – The table summarizes the variables corresponding to each acquired data channel from the analog-to-digital converters and their associated notations as used in this chapter. The final three rows correspond to the DC signals from detectors measuring: transmission through the spherical HF mirror in both analysis cavities, a deflected fraction of the incident pump beam, and the pump beam’s reflection from the OPO.

Detector	Frequency Band	Demodulation	Beam		
			Signal (Alice)	Idler (Victor)	Pump
Measurement Detector 1	HF	Sine	$V_{sin}^{A1}(t)$	$V_{sin}^{V1}(t)$	-
		Cosine	$V_{cos}^{A1}(t)$	$V_{cos}^{V1}(t)$	-
	DC	-	$V_{DC}^{A1}(t)$	$V_{DC}^{V1}(t)$	-
Measurement Detector 2	HF	Sine	$V_{sin}^{A2}(t)$	$V_{sin}^{V2}(t)$	-
		Cosine	$V_{cos}^{A2}(t)$	$V_{cos}^{V2}(t)$	-
	DC	-	$V_{DC}^{A2}(t)$	$V_{DC}^{V2}(t)$	-
Analysis Cavity	DC	-	$V_{cav}^A(t)$	$V_{cav}^V(t)$	-
Incident OPO	DC	-	-	-	$V_{inc}^{pump}(t)$
Reflection OPO	DC	-	-	-	$V_{ref}^{pump}(t)$

we compute the sum and difference of the balanced HF detected signals for each beam, defined as:

$$V_{\text{dem}}^{S+}(t) = V_{\text{dem}}^{S1}(t) + V_{\text{dem}}^{S2}(t), \quad (6.1a)$$

$$V_{\text{dem}}^{S-}(t) = V_{\text{dem}}^{S1}(t) - V_{\text{dem}}^{S2}(t), \quad (6.1b)$$

$$e_{\text{dem}}^{S+}(t) = e_{\text{dem}}^{S1}(t) + e_{\text{dem}}^{S2}(t), \quad (6.1c)$$

$$e_{\text{dem}}^{S-}(t) = e_{\text{dem}}^{S1}(t) - e_{\text{dem}}^{S2}(t), \quad (6.1d)$$

where $\text{dem} \in \{\sin, \cos\}$, and $S \in \{A, V\}$.

For the DC values, we first determine the representation to be used. The options are to use the raw voltage, convert it to photocurrent using detector specifications, or calculate the incident optical power from the characterized quantum efficiency. We then sum the balanced DC values using the chosen representation.

If the measurement under analysis includes a time-varying feature, such as a scanning analysis cavity during a quantum tomography measurement, the acquired data must be divided into distinct sections. The number of sections into which the 450,000 acquired points are divided depends on how the features of interest are distributed over the measurement’s time frame. For instance, if the cavity scan is slow and spans the entire range, fewer divisions can be used, allowing each section to contain more data points. Conversely, if the scan is fast, more divisions are needed to capture rapid changes and

avoid averaging out the features of interest, at the cost of higher statistical fluctuations.

Next, we compute the statistical properties of the data, or for each segment if the data is divided. This involves calculating the mean of both the HF and DC values, along with the variance of the HF values. For the mean values, we estimate the uncertainties by calculating the standard deviation of the mean using the following formula [189]:

$$\sigma_{mean} = \frac{\sigma_{sample}}{\sqrt{N}}, \quad (6.2)$$

where σ_{sample} is the standard deviation of the sample set, and N is the number of samples. For a sufficiently large sample size, the variance of a normal distribution, which follows a Chi-squared distribution, can be well approximated by a normal distribution according to the central limit theorem. In this case, its uncertainty is estimated as [190]:

$$\sigma_{var} = \frac{\sqrt{2}\sigma_{sample}^2}{\sqrt{N-1}}. \quad (6.3)$$

To analyze the quantum correlations between two modes or perform system diagnostics, we also compute the covariance of the measured signals.

Using the calculated signal statistics, we proceed to derive the accessed quadrature statistics in physically meaningful units. This process involves accounting for and subtracting the electronic noise contributions and normalizing the acquired voltage. Equation 5.2b establishes the relationship between the detected HF voltage and the temporal photocurrent operator introduced in the theoretical Chapter 3. After demodulation, the measured high-frequency (HF) voltages contain the quadrature information of the symmetric and antisymmetric combinations of the two sideband modes, as described in Equation 3.30. Considering that the electronic noise is uncorrelated with any other measured signal, the normalized mean and variance of the accessed quadratures are defined as follows:

$$\langle \hat{I}_{\text{dem}}^S \rangle = \langle \hat{x}_{\text{dem}}^S \rangle = \frac{\langle V_{\text{dem}}^{S+} \rangle - \langle e_{\text{dem}}^{S+} \rangle}{\sqrt{\Delta^2 V_{\text{Shot,dem}}^{S+}}} \quad (6.4a)$$

$$\Delta^2 \hat{I}_{\text{dem}}^S = \Delta^2 \hat{x}_{\text{dem}}^S = \frac{\Delta^2 V_{\text{dem}}^{S+} - \Delta^2 e_{\text{dem}}^{S+}}{\Delta^2 V_{\text{Shot,dem}}^{S+}}, \quad (6.4b)$$

where $\text{dem} \in \{\sin, \cos\}$, and $S \in \{A, V\}$.

The covariance between these operators is then calculated as:

$$C(\hat{I}_{\text{dem}}^S, \hat{I}_{\text{dem}'}^{S'}) = C(\hat{x}_{\text{dem}}^S, \hat{x}_{\text{dem}'}^{S'}) = \frac{C(V_{\text{dem}}^{S+}, V_{\text{dem}'}^{S'+})}{\sqrt{\Delta^2 V_{\text{Shot,dem}}^{S+} \Delta^2 V_{\text{Shot,dem}'}^{S'+}}}, \quad (6.5)$$

where $\text{dem}, \text{dem}' \in \{\sin, \cos\}$, and $S, S' \in \{A, V\}$.

Here, $\Delta^2 V_{\text{Shot}}$ represents the shot noise variance, corresponding to the fluctuations observed when measuring a coherent state in the same sideband modes of a beam with the same intensity as the incident beam [100]. To obtain the shot noise in the absence of a coherent state with matching specifications to the measured beam, the balanced detection scheme is used, we employ the balanced detection scheme described in Section 3.1.1.

In the balanced detection scheme, the sum of the two signals corresponds to the total intensity of the beam, containing all the information about the field under measurement, as indicated by the + subscript in Equations 6.4 and 6.5. On the other hand, subtracting the signals cancels any excess noise in the field, resulting in a residual signal with variance equal to the shot noise, as demonstrated in Section 3.1.1. This approach enables normalization of the measured field noise by the shot noise in a single measurement. Specifically, the shot noise variance, as measured in the balanced detection scheme, is expressed as:

$$\Delta^2 V_{S+}^{\text{Shot,dem}} = \Delta^2 V_{\text{Shot,dem}}^{S-} - \Delta^2 e_{\text{dem}}^{S-} \quad (6.6)$$

During teleportation, each of Alice's detectors measures a different quadrature, making it impossible to use a balanced detection scheme to directly determine the shot noise. We opted against using two balanced detection schemes, one for each quadrature, to minimize the electronic dark noise transferred to Bob's field during the conditioned displacement operations. To overcome this, we first calibrate the shot noise, a process detailed later in this text. These calibrated values are then used for shot noise normalization during the teleportation data analysis. Since quadrature information is extracted from individual detectors rather than their sum, the subscript + in Equations 6.4 and 6.5 should be changed to represent the specific detector.

In this work, we focus on the teleportation of a single sideband mode, which comprises both the upper and lower sidebands. This formalism is used without loss of generality, as the information encoded in both sidebands is equivalent. According to the stationary condition in Equation 3.36b, the variances of the photocurrent operator for sine and cosine demodulations are equal in the stationary regime: $\Delta^2 \hat{I}_{\sin}^S = \Delta^2 \hat{I}_{\cos}^S$. Consequently, the symmetric and antisymmetric quadrature variances are identical, implying that the variance of the single sideband mode quadrature also matches these values (Equation 3.62). Thus, the variance of the measured quadrature, accessed via the balanced detection scheme, is given by:

$$\Delta^2 \hat{X}_S = \frac{\Delta^2 V_{\text{dem}}^{S+} - \Delta^2 e_{\text{dem}}^{S+}}{\Delta^2 V_{\text{dem}}^{S-} - \Delta^2 e_{\text{dem}}^{S-}}, \quad (6.7)$$

To obtain the single sideband quadrature mean value, it is necessary to obtain the amplitude of the detected HF signal at the analysis frequency before the demodulation procedure. During the quadrature demodulation process, this amplitude information is preserved and encoded within the sine and cosine components. The mean value of the single sideband mode accessed quadrature is expressed as:

$$\langle \hat{X}_S \rangle = \frac{1}{\sqrt{2}} \sqrt{\langle \hat{I}_{\text{sin}}^S \rangle^2 + \langle \hat{I}_{\text{cos}}^S \rangle^2} = \frac{1}{\sqrt{2}} \sqrt{\langle \hat{x}_{\text{sin}}^S \rangle^2 + \langle \hat{x}_{\text{cos}}^S \rangle^2} \quad (6.8a)$$

$$= \frac{1}{\sqrt{2}} \sqrt{\left(\frac{\langle V_{\text{sin}}^{S+} \rangle - \langle e_{\text{sin}}^{S+} \rangle}{\sqrt{\Delta^2 V_{\text{Shot,sin}}^{S+}}} \right)^2 + \left(\frac{\langle V_{\text{cos}}^{S+} \rangle - \langle e_{\text{cos}}^{S+} \rangle}{\sqrt{\Delta^2 V_{\text{Shot,cos}}^{S+}}} \right)^2}. \quad (6.8b)$$

After processing the acquired signal by subtracting the electronic noise and normalizing by the shot noise, the next steps depend on the specific analysis objective. For instance, when measuring two fields, we can directly compute the sum and difference of their measured quadratures, which are described as:

$$\Delta^2 \hat{X}_{\pm} = \Delta^2 \left(\frac{\hat{X}_A \pm \hat{X}_V}{\sqrt{2}} \right) = \frac{1}{2} (\Delta^2 \hat{X}_A + \Delta^2 \hat{X}_V) \pm C(\hat{X}_A, \hat{X}_V), \quad (6.9)$$

When both fields are measured using balanced detection, and no phase difference exists between the HF electronic signals obtained from the detection of the signal and idler beams, we have:

$$\begin{aligned} \Delta^2 \hat{X}_{\pm} &= \frac{1}{2} \left(\frac{\Delta^2 V_{\text{dem}}^{A+} - \Delta^2 e_{\text{dem}}^{A+}}{\Delta^2 V_{\text{Shot,dem}}^{A+}} + \frac{\Delta^2 V_{\text{dem}}^{V+} - \Delta^2 e_{\text{dem}}^{V+}}{\Delta^2 V_{\text{Shot,dem}}^{V+}} \right) \pm \frac{C(V_{\text{dem}}^{A+}, V_{\text{dem}}^{V+})}{\sqrt{\Delta^2 V_{\text{Shot,dem}}^{A+} \Delta^2 V_{\text{Shot,dem}}^{V+}}} \\ &= \frac{1}{2} \left(\frac{\Delta^2 V_{\text{dem}}^{A+} - \Delta^2 e_{\text{dem}}^{A+}}{\Delta^2 V_{\text{dem}}^{A-} - \Delta^2 e_{\text{dem}}^{A-}} + \frac{\Delta^2 V_{\text{dem}}^{V+} - \Delta^2 e_{\text{dem}}^{V+}}{\Delta^2 V_{\text{dem}}^{V-} - \Delta^2 e_{\text{dem}}^{V-}} \right) \pm \frac{C(V_{\text{dem}}^{A+}, V_{\text{dem}}^{V+})}{\sqrt{(\Delta^2 V_{\text{dem}}^{A-} - \Delta^2 e_{\text{dem}}^{A-})(\Delta^2 V_{\text{dem}}^{V-} - \Delta^2 e_{\text{dem}}^{V-})}}. \end{aligned} \quad (6.10)$$

In our case, the capacitance difference in the photodiodes at Alice and Bob's detectors causes a phase difference in the detected HF signals. To compensate for this, the above expression is modified to:

$$\Delta^2 \hat{X}_\pm = \frac{1}{2} \left(\frac{\Delta^2 V_{\text{dem}}^{A+} - \Delta^2 e_{\text{dem}}^{A+}}{\Delta^2 V_{\text{Shot,dem}}^{A+}} + \frac{\Delta^2 V_{\text{dem}}^{V+} - \Delta^2 e_{\text{dem}}^{V+}}{\Delta^2 V_{\text{Shot,dem}}^{V+}} \right) \\ \pm \sqrt{\left(\frac{C(V_{\text{dem}}^{A+}, V_{\text{dem}}^{V+})}{\sqrt{\Delta^2 V_{\text{Shot,dem}}^{A+} \Delta^2 V_{\text{Shot,dem}}^{V+}}} \right)^2 + \left(\frac{C(V_{\text{dem}}^{A+}, V_{\text{dem}_q}^{V+})}{\sqrt{\Delta^2 V_{\text{Shot,dem}}^{A+} \Delta^2 V_{\text{Shot,dem}_q}^{V+}}} \right)^2}, \quad (6.11)$$

where $\text{dem}, \text{dem}_q \in \{\sin, \cos\}$ with $\text{dem} \neq \text{dem}_q$.

The difference between Equation 6.10 and the phase-compensated Equation 6.11 lies in the covariance term. In the phase-compensated equation, we applied the relations derived in Section 3.3.5 and enforced the imaginary component of the spectral matrix to be zero. While this approach is not used for a complete quantum tomography, it is the most suitable method for measuring a single quadrature. Using Equation 6.11, we can determine the squeezing in the difference of amplitude quadratures between the signal and idler in all shot noise calibration measurements. The observed squeezing provides valuable information about the state of the quantum resources involved and serves as an initial guess for fitting the covariance matrix elements.

For simple fitting tasks, such as linear regression, we use the *curve_fit* function from Scipy Optimize module (*scipy.optimize*) [187]. For more complex fits, such as those used to extract covariance matrix elements, we utilize the *minimize* function from LMFit library (*lmfit*) [191]. Built on Scipy Optimize, LMFit offers a more intuitive framework for defining the fitting parameters, as well as their associated properties and constraints. Additionally, LMFit simplifies the process of simultaneous multi-curve fitting, allowing parameters to be estimated from multiple curves at the same time. For instance, when analyzing the teleportation measurements across different gain values, LMFit enables us to account for all datasets collectively, ensuring a robust determination of the cavity-dependent parameters. For all the fits in this work, we utilize least-squares minimization to estimate the model parameters. To propagate uncertainties in our calculations, we use the library "Uncertainties: a Python package for calculations with uncertainties" (*uncertainties*) [192]. In this process, the variables are defined with their respective uncertainties, and the covariances between the variables are also included when applicable, for instance, when the uncertainties are obtained from the outputs of the fitting procedures.

6.1.2 Shot Noise Calibration

Before each round of measurements, we conduct a shot noise calibration measurement. This calibration is a crucial preparatory step for the teleportation measurement, in which a balanced detection scheme is not used at Alice's station in order to reduce the electronic noise transferred to Bob. The process also determines the gain relationship of

the high-frequency (HF) electronics, a parameter essential for applying the digital HF gain correction described in Section 5.4.2. In addition to its calibration role, this procedure provides important diagnostics of the system's performance, including the evaluation of the signal-to-noise ratio, the OPO threshold, the degree of amplitude squeezing, and the verification of stationary operating conditions.

The procedure for calibrating shot noise begins by setting all three analysis cavities out of resonance and blocking the Mach-Zehnder interferometer used for creating the input state. At Alice's and Victor's stations, the beam is split in a 50:50 ratio between the detectors by adjusting the half-wave plate positioned before the PBS. At Alice's station, the choice of detectors depends on the measurement objective after the calibration. For two-field quantum state tomography, the detectors positioned after Alice's cavity are used. For quantum teleportation, the amplitude and phase quadrature detectors are utilized (Figure 17).

With detection properly balanced, the calibration is performed using a custom LabVIEW software. The software controls the function generator, which sends signals to the acousto-optic modulator (AOM) in the pump beam path. By applying DC voltages to the AOM driver, we regulate the energy transferred from the zeroth-order diffraction to higher orders, enabling precise control of the pump power. The calibration involves measuring the balanced beams at various pump powers, with the final measurement taken with the pump set below the threshold for a dark acquisition. For each pump power, we acquire 450,000 data points over a duration of 750 ms. Since the data is uniform, it is analyzed as described in Section 6.1.1, without partitioning. The data analysis process starts by applying the digital HF filter, correcting the HF gain, and calculating the signal-to-noise ratio (SNR) for the acquired signal, as detailed in Section 5.4. Following this, the shot noise is calculated according to Equation 6.6, based on the subtraction of the HF-demodulated voltages while accounting for the contribution of electronic noise. As an illustrative example, we present in this section a shot noise calibration, with the OPO crystal stabilized at approximately -41.5°C and an analysis frequency of 15 MHz. The calibration, shown in Figure 34, presents the shot noise values in terms of the sum of the detectors' DC components, which are here converted into incident optical power using the characterized quantum efficiency of the detectors (Figure 28), providing a more intuitive and meaningful representation of the data.

The linear relationship observed in the shot noise calibration data presented in Figure 34 provides strong evidence that the measured noise corresponds to true shot noise. This linearity aligns with theoretical expectations, where shot noise variance scales proportionally with the incident optical power, as predicted by Equation 3.17. The agreement between the experimental data and this fundamental characteristic confirms the validity of the calibration process and the reliability of the measurement setup in

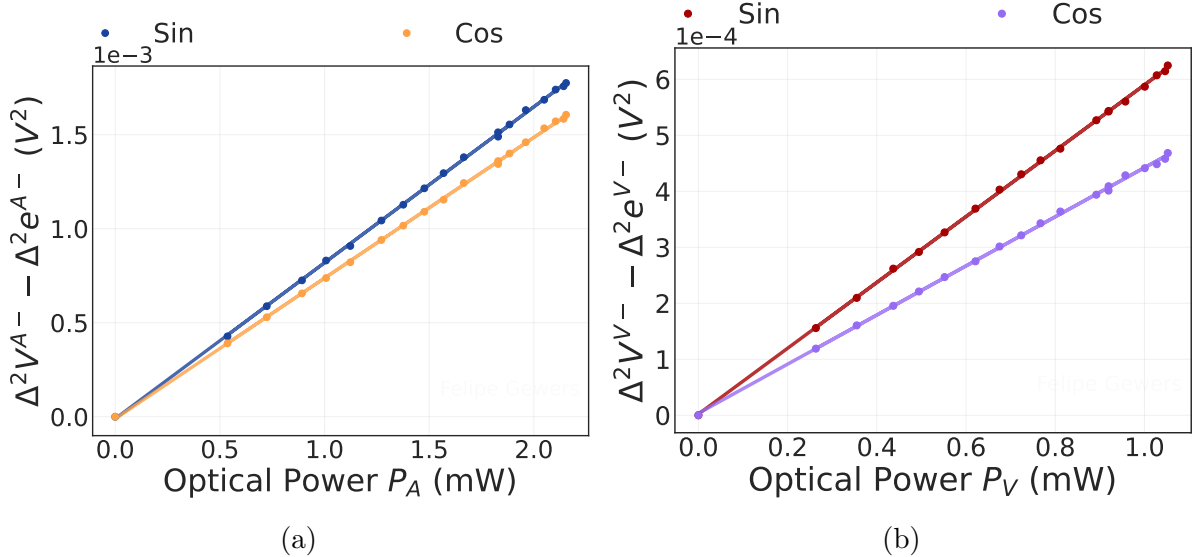


Figure 34 – Shot noise calibration results obtained with the OPO crystal stabilized at approximately $-41.5^\circ C$ and an analysis frequency of 15 MHz. The variances, referring to the shot noise fluctuations, are plotted against the DC components, converted into incident optical power using the characterized quantum efficiency of the detectors.

isolating the shot noise contribution. The linear coefficient from this calibration is used to determine the shot noise variance based on the acquired DC value, when balanced detection is not employed. This shot noise variance is used to normalize the measured field HF signal's variance, while its square root is used to normalize the mean value. The resulting normalized parameter is then expressed in shot noise units (s.n.u.).

As shown in Figure 21c, the oscillation threshold of the Optical Parametric Oscillator (OPO) depends on the specific pump resonance peak used for cavity stabilization. To minimize this threshold, we aim to stabilize the cavity on the resonance that produces the highest signal and idler intensities. However, thermal effects and occasional loss of lock can lead to stabilization on alternative resonance peaks with different threshold values. Therefore, it is valuable to determine the oscillation threshold using the acquired data. During shot noise calibration, the threshold is estimated by plotting the DC voltages from the Alice and Victor detectors against a measured fraction of the incident pump power. Figure 35 illustrates this fitting procedure. On the upper x-axis, the incident pump power at the OPO is presented, which is derived from a calibration correlating the measured fraction of pump light with direct measurements from a power meter. The threshold is estimated by fitting the data to the expression [87, 193, 194]:

$$P_{s,i} = 4P_{th}K_{OPO}^{s,i} \left(\sqrt{\frac{P_{pump}}{P_{th}}} - 1 \right), \quad (6.12)$$

where $P_{s,i}$ is the power of the signal or idler, P_{pump} is the coupled pump power, P_{th} is

the oscillation threshold, and $K_{OPO}^{s,i}$ is a parameter dependent on the signal and idler wavelengths and the useful and spurious losses of the OPO. From this measurement, the OPO oscillation threshold was determined to be 14.32(1) mW.

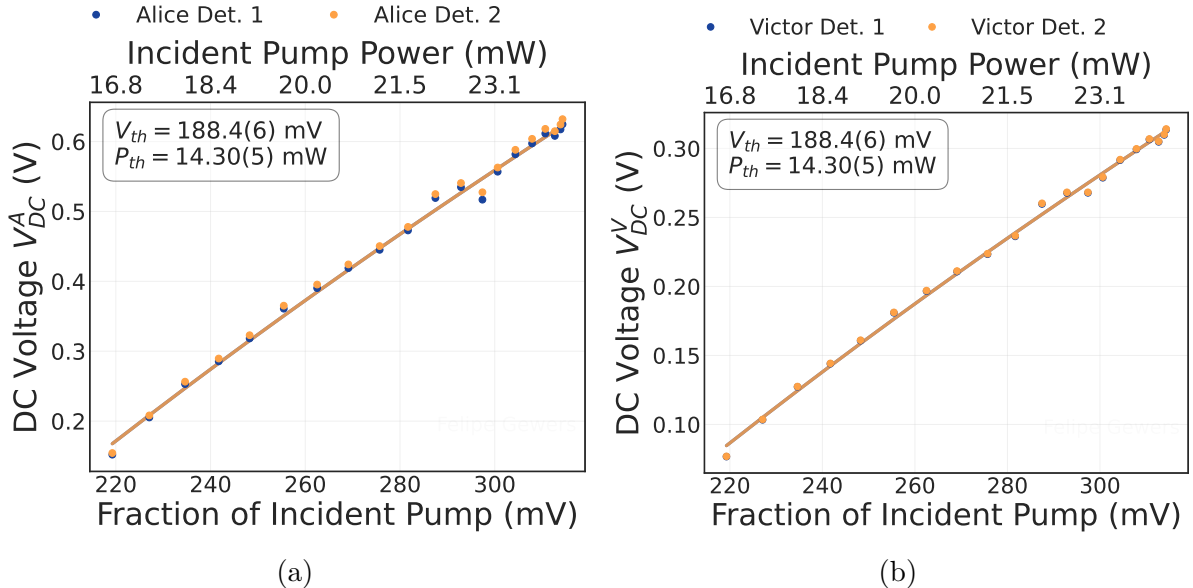


Figure 35 – The detector voltage for the generated signal and idler is plotted against a monitor voltage proportional to the incident pump power. As both voltages are proportional to optical power, the data can be fit with Equation 6.12 (solid curve). The threshold is determined from the x-intercept, which provides a voltage that corresponds to the threshold pump power.

During the shot noise calibration, we access the amplitude quadrature of the signal and idler quantum state, given that all analysis cavities are set off-resonance preserving the original phase relationship between the carrier and sidebands. The measurement of these quadratures provides an initial evaluation of the quantum resources in the system. By comparing the acquired values to the expected range for the squeezing in the subtraction of amplitude quadrature, we can identify potential issues with the system if the measurements deviate significantly. Figure 36 shows the variance of the amplitude quadrature measured at Alice’s and Victor’s stations and their covariances for sine and cosine demodulations, as a function of the incident optical power. The upper x-axis shows the normalized pump amplitude, $\sqrt{\sigma} = \sqrt{P_{\text{pump}}/P_{\text{th}}}$, which is the square root of the pump power normalized to the OPO oscillation threshold. The observed decrease in amplitude quadrature variances with increasing pump power, as shown in Figures 36a and 36b for the signal and idler, respectively, has been previously reported in other works on OPOs operating above threshold [172], confirming the expected behavior. The presence of a nonzero covariance between the cosine and sine terms, as depicted in Figure 36d, is absent in previous studies by our group [59, 94], where identical detectors were employed for signal and idler measurements. This observed covariance arises from electronic artifacts, specifically due to the use of photodiodes with differing capacitances. Using the obtained

variances and covariances in Equation 6.11, we calculate the variance for the subtraction and sum of the amplitude quadratures of the signal and idler, as shown in Figure 37. The measured squeezing in the subtraction of the amplitude quadratures is $-1.77(1)$ dB for sine demodulation and $-1.714(9)$ dB for cosine demodulation, with their close agreement confirming the expected consistency in the system's performance.

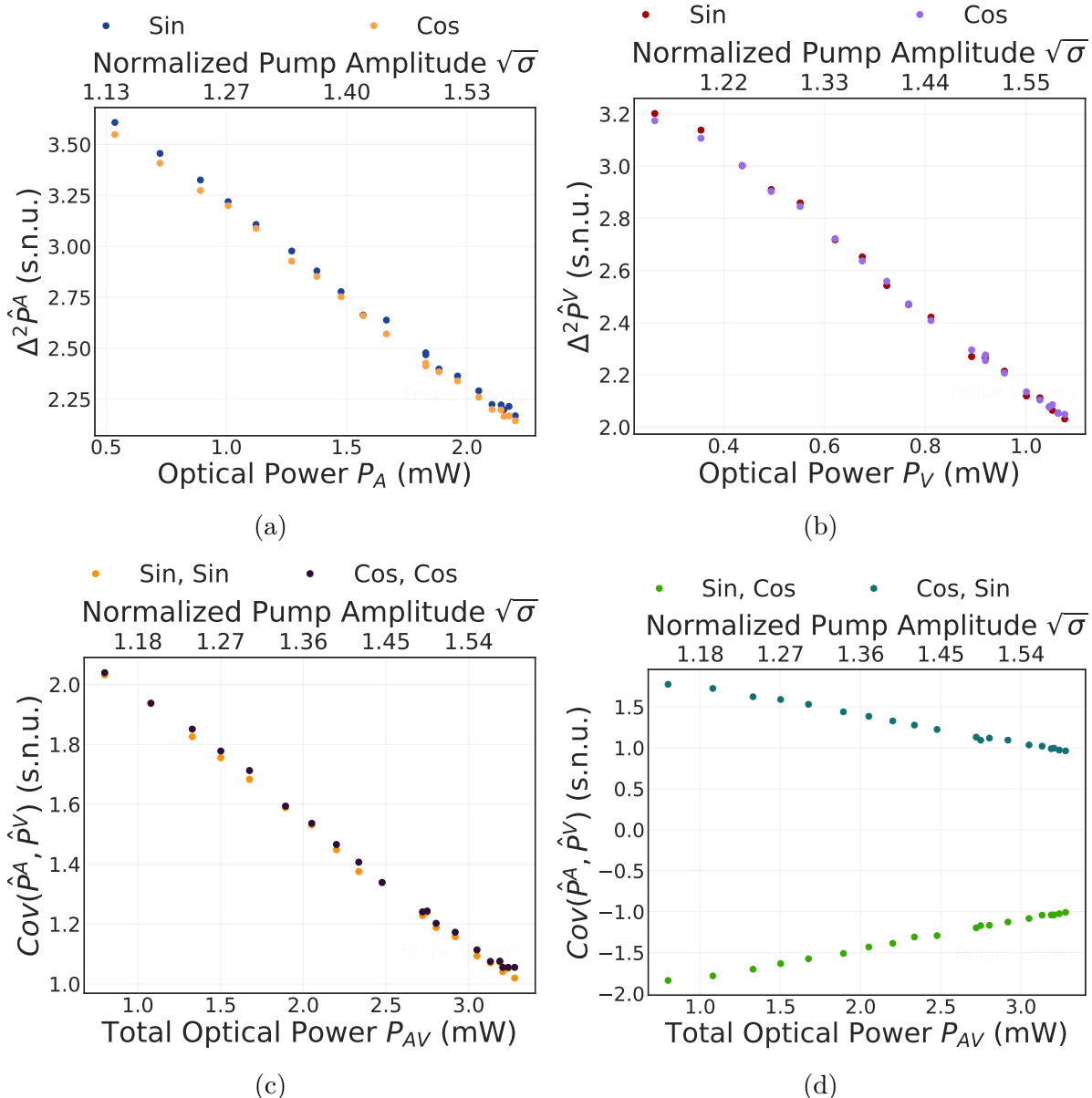


Figure 36 – Variances and covariances of the amplitude quadratures of the signal and idler fields, shown for both sine and cosine demodulations, as functions of the incident optical power and the normalized pump power. The data were obtained during shot noise calibration by measuring the generated fields at various pump powers, with the OPO crystal temperature set to -41.5°C and an analysis frequency of 15 MHz.

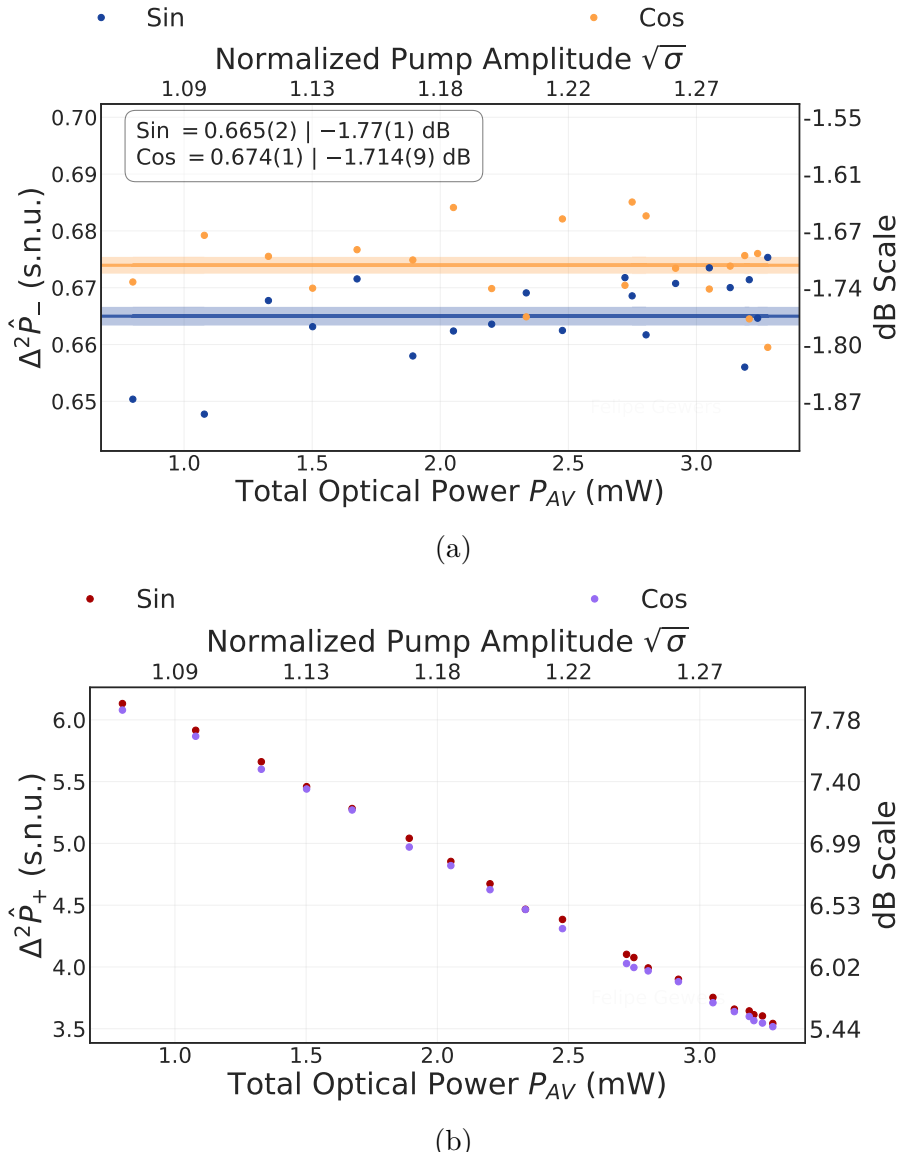


Figure 37 – Variances of the subtraction and sum of the amplitude quadratures of the signal and idler fields are plotted as functions of the incident optical power and the normalized pump power. The values were obtained during the shot noise calibration by measuring the generated fields at different pump powers, with the OPO crystal temperature set to -41.5°C and an analysis frequency of 15 MHz, and without correcting for losses.

We verify the stationarity conditions of the obtained spectral photocurrents, as described for one mode in Equation 3.36b and for two modes in Equation 3.40 [107]. Figure 38 presents these results, demonstrating that all stationarity absolute values remain below the acceptable limit of 0.1 s.n.u. In our system, the electronic local oscillator (eLO) used for demodulation is not phase-locked with the optical sidebands of interest. Over the short duration of a single data point acquisition ($\approx 1.7 \mu\text{s}$), phase diffusion between the eLO and sidebands is negligible. However, when examining the quantum state, we require statistical information derived from a much larger set of single measurements. Over this extended timescale, phase diffusion introduces significant mixing between the \hat{I}_{\sin} and \hat{I}_{\cos} components, as discussed in Section 3.1.3.2. As a result, the stationarity condition of the spectral photocurrents does not reflect the quantum state's stationarity [111]. Nonetheless, verifying photocurrent stationarity remains an important diagnostic. It confirms the orthogonality of the quadrature demodulation process. A stationarity value deviating from zero indicates that the sine and cosine components of the eLO experience unequal phase shifts in the demodulation electronics, resulting in overlap and cross-contamination of the demodulated signals if the demodulation components deviate from exact in-quadrature operation.

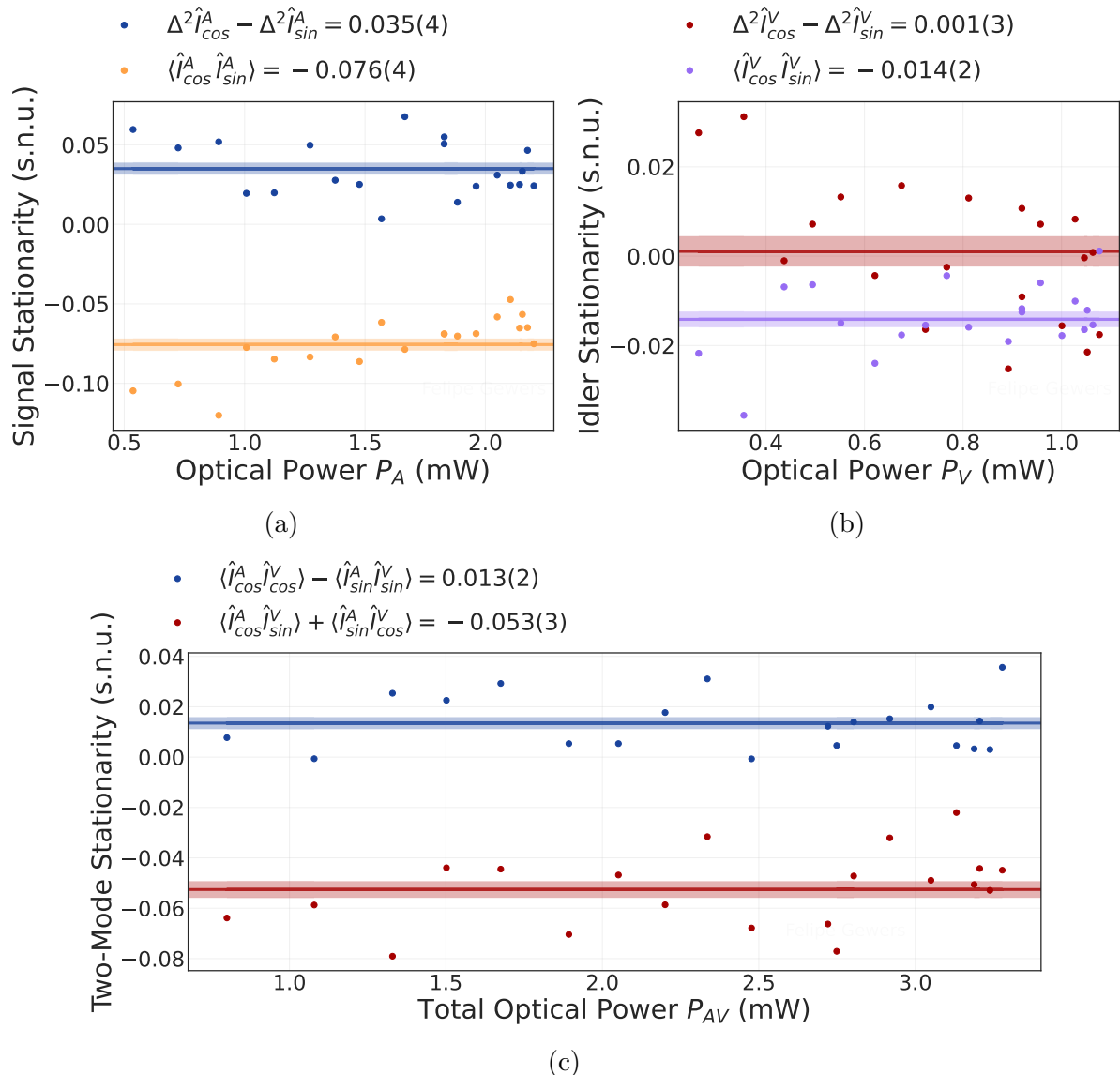


Figure 38 – Stationarity conditions of the measured spectral photocurrents. Absolute values remain below 0.1 s.n.u., confirming compliance with the predefined acceptability criteria and validating the demodulation process. These values were calculated from the same measurement data used in the previous analysis presented in this section.

To verify the stationarity condition even in the presence of phase mixing between the eLO and the optical local oscillator (LO), we analyze the higher-order moments of the acquired spectral photocurrent. Specifically, we evaluate Fisher's kurtosis, defined as:

$$Kur_F[A] = \frac{\mu_4}{\sigma^4} - 3 \quad (6.13)$$

where μ_4 represents the fourth central moment of the random variable A , and σ denotes its standard deviation. With the exception of highly specific non-Gaussian quantum states, which are improbable to occur without deliberate design, a spectral photocurrent characterized by Fisher's kurtosis equal to zero (mesokurtic) strongly indicates that the underlying quantum state is compatible with a Gaussian state [111]. If the quantum state being measured is Gaussian and the Fisher kurtosis of the spectral photocurrent is zero, it follows that the measured state exhibits the stationary property. This means the stationary condition is satisfied in the pure quantum measurement scenario when the eLO and LO are phase-locked. Figure 39 illustrates the Fisher kurtosis computed for the photocurrents obtained during the shot noise calibration discussed in this section. The near-zero values strongly indicate that the quantum state is Gaussian compatible and satisfies the stationary property.

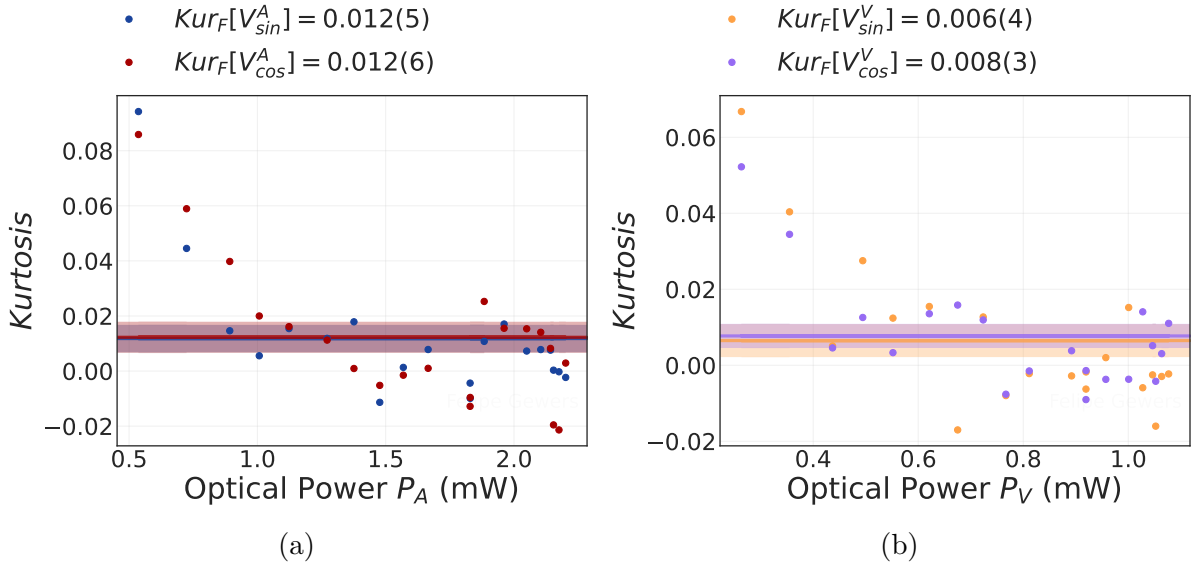


Figure 39 – Fisher kurtosis values computed for the spectral photocurrents obtained during the shot noise calibration. The near-zero values indicate that the underlying quantum state is compatible with a Gaussian state and satisfies the stationarity condition. These values derive from the same data as the preceding analysis in this section.

6.2 Quantum Resource Characterization: EPR State Tomography

To measure the quantum resources at the final stage of our experimental setup, we perform quantum state tomography on the fields at Alice's and Bob's stations. This allows us to reconstruct the full 8×8 covariance matrix in the symmetric/antisymmetric basis (\mathcal{S}/\mathcal{A}), providing a complete characterization of the composite quantum state (Section 3.2.2). Our primary focus is on the entanglement between these field quadratures, as its precise characterization informs us about the expected performance of the teleportation protocol. Moreover, the characterization itself is inherently significant, as the use of an optical parametric oscillator (OPO) to generate signal and idler fields in such a distant spectral range (infrared and telecom) under above-threshold operation is uncommon in quantum optics experiments. To our knowledge, no prior study has provided a full characterization, investigating individual sideband modes, of the generated quantum state within the continuous-variable description under these conditions. Therefore, while the tomography described in this section is not our primary result, it remains a significant contribution of this work.

The procedure for performing this measurement begins by tuning Bob's analysis cavity out of resonance and blocking the input state creation in the Mach-Zehnder interferometer. This ensures that no external interference affects the measurement process. Next, Alice's entire optical field is directed toward her analysis cavity, where both the phase detector and tomography detector, positioned after the cavity, are used in a balanced detection scheme. Subsequently, the balanced detection systems following both Alice's and Victor's analysis cavities are carefully adjusted using a half-wave plate to achieve a precise 50 : 50 splitting ratio. Once the splitting ratio is properly set, we perform shot noise calibration following the methodology described in the previous section. This calibration is used to implement HF gain correction, as the shot noise normalization here is directly derived from the balanced detection scheme. Once the initial procedure is established, the measurement is conducted by scanning the analysis cavities around the resonance peak. The quantum tomography process comprises three sequential measurements: first, both cavities are synchronously scanned around the resonance while data is acquired. Next, Victor's cavity is held out of resonance while Alice's is scanned. Finally, the configuration is reversed. This approach is essential for precise estimation of the covariance between the accessed quadratures during cavity scanning while also providing additional data to enhance the accuracy of the covariance matrix fitting (Section 3.3.3).

The scanning process is driven by an electronic ramp signal applied to the PZTs at a frequency of 0.67 Hz, which is compatible with the measurement time of 750 ms, as only one side of the ramp is relevant. The LabVIEW software triggers a custom-built electronic system that controls the ramp's direction, first applying it to both cavities, then to each individually, while simultaneously acquiring data for each configuration. For

proper synchronous scanning, the transmission peaks of the cavities must overlap. This alignment is achieved by manually adjusting the gain and offset of the electronic ramp sent to the PZTs. However, the combination of thermal effects, which induce peak drift over time, and the inherent limitations of manual tuning makes perfect overlap difficult to achieve in some cases. Nevertheless, provided the misalignment is not excessive, our data analysis procedure remains effective for evaluating the covariance matrix, though the resulting uncertainty increases.

6.2.1 Reconstruction of the Two-Field Covariance Matrix

This section presents a detailed analysis of a specific tomographic measurement. For this measurement, the OPO's crystal was maintained at -38.5°C , generating signal and idler fields at wavelengths of 794(6) nm and 1612(3) nm, respectively. The incident pump power before the vacuum chamber was 26.48(2) mW against an oscillation threshold of 16.6(3) mW, leading to a normalized pump power of $\sigma = 1.59(3)$. At the balanced detectors, the total measured power was 2.06(1) mW for the signal beam and 1.14(1) mW for the idler beam. The measurements were performed using an analysis frequency of 15 MHz. Additionally, we computed the signal-to-noise ratio, verified the stationary conditions, and analyzed the kurtosis of the acquired signal in the tomography measurement. These values agree with theoretical expectations and are presented in Appendix B.

Figure 40 presents the transmissions and reflections from the analysis cavities during the tomography measurement for all three scanning conditions. The data were fitted using a Lorentzian model. The datasets for each field and scan configuration were analyzed simultaneously, with the constraint that the cavity parameters remain consistent across all fits. The peak center position in time defines the zero-detuning point for each curve, while the fitted bandwidth determines the normalized detuning relevant to the covariance c-functions (Section 3.3). The impedance matching factor d (Equation 3.73) serves as an initial guess for the covariance elements fit. Since the reflection signal was noisy, d was not fixed but was constrained and validated post-fit to prevent significant deviations.

The acquired temporal dataset, comprising 450,000 voltage values per channel and scan configuration, is partitioned into 1800 segments, each containing 250 data points, over which the statistical analyses are conducted. Using Equation 6.11, we compute the variance of the subtracted and summed accessed quadratures during the tomography measurement for the three scanning configurations. Figure 41 presents the obtained variances in this subspace for both sine and cosine demodulations. As expected for a stationary process, the variances exhibit similar values for both demodulations. Notably, when both cavities are out of resonance, we observe squeezing in the subtraction of the accessed amplitude quadratures. However, for the sum of quadratures in the synchronous scanning configuration, we do not

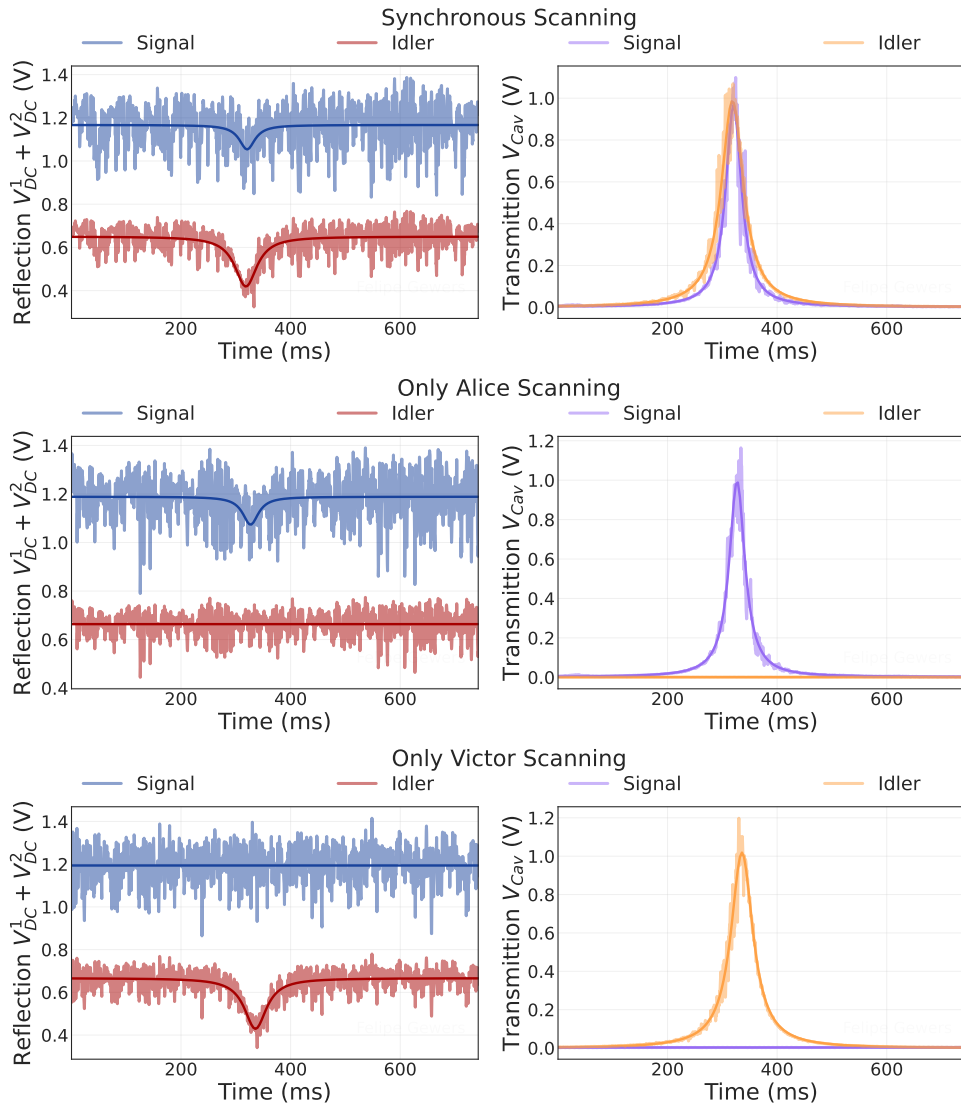


Figure 40 – The transmission and reflection signals from the analysis cavities during the tomography measurement for the three scanning configurations. Top: Both cavities scanned synchronously. Middle: Alice's cavity is scanned while Victor's remains out of resonance. Bottom: The inverse configuration, where Victor's cavity is scanned while Alice's remains out of resonance. The data is fitted using a Lorentzian curve while enforcing identical cavity parameters across all cases.

observe a variance below the shot noise level, which would be indicative of squeezing in the sum of phase quadratures. This discrepancy arises because, during the scanning process, we do not simultaneously measure the complete phase quadrature for both fields. Several factors may contribute to this effect, including differences in the bandwidths of the analysis cavities and imperfect overlap of the resonance peaks during the cavity scan (Figure 40). However, the covariance element fitting properly incorporates these considerations, allowing us to access the squeezing in the sum of phase quadratures.

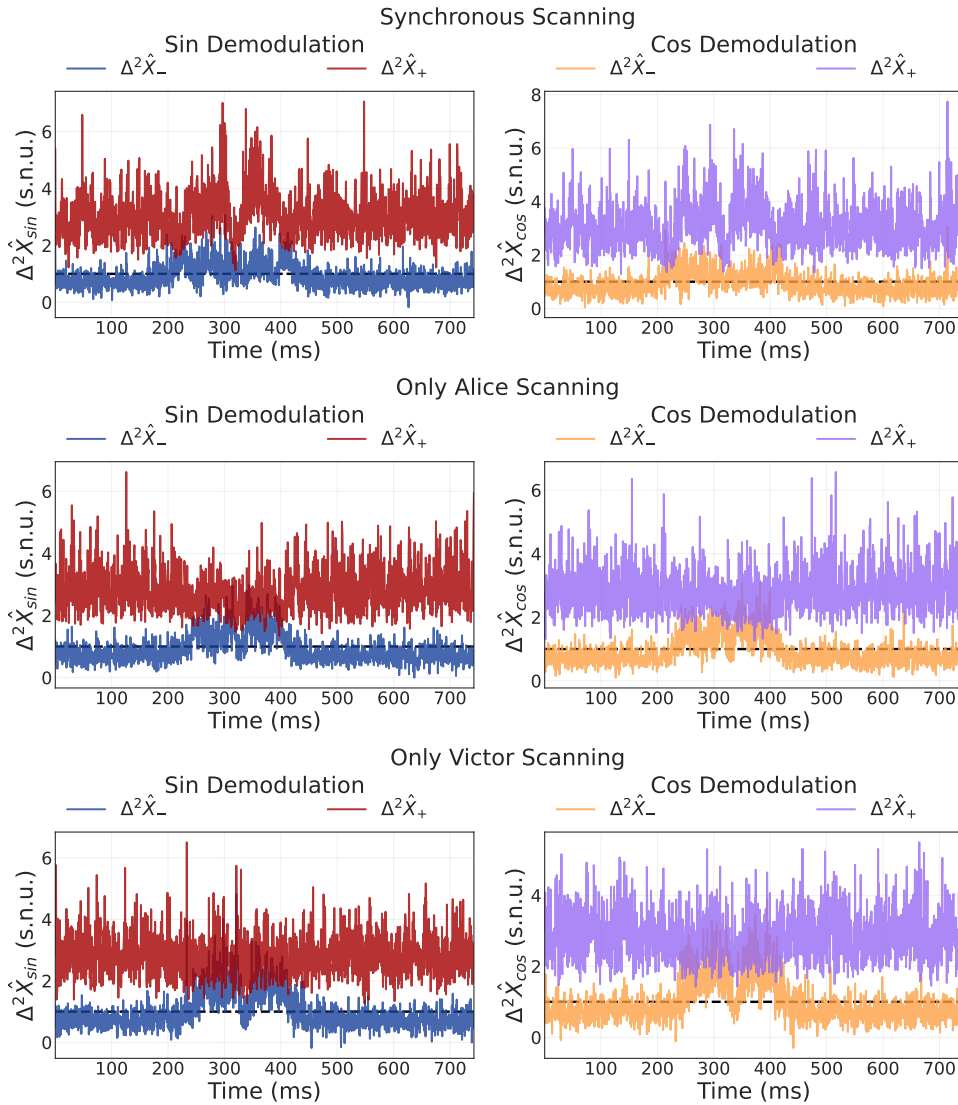


Figure 41 – Variance of the subtracted and summed accessed quadratures for the three scanning configurations. The results are shown for both sine and cosine demodulation components.

Figure 42 displays the normalized variance of each accessed quadrature during scans for both demodulation components, expressed in shot noise units. Similarly, Figure 43 presents the real and imaginary components of the cross-correlations, also normalized to shot noise units. To fully characterize the covariance matrix, we perform a fit on these curves, with the fitted curves presented in the figures. According to the Wiener-Khinchin theorem (Section 3.1.3) for stationary processes, these variances correspond to the normalized spectral noise density of the photocurrent when the mean quadrature values are zero. In our analysis, we extract the mean values of the accessed quadratures during the scan and find them to be consistent with zero, as expected for a state generated by the OPO when the target sideband modes of the pump field are in vacuum state [84, 87].

The fitting procedure utilizes Equation 3.99 for the single-field covariance elements and Equation 3.105 for the two-field elements, both of which account for potential spatial mode mismatches in the analysis cavities. The process involves the simultaneous minimization of the 18 acquired curves: six corresponding to the signal field's variances, six to the idler field's variances (each considering sine and cosine demodulations across the three scanning configurations), and six to the real and imaginary cross-correlations across all scanning configurations. This simultaneous approach ensures consistency in the extracted covariance elements and cavity parameters. Since the fit involves a large number of parameters, it is essential to carefully choose the initial values and constrain those that can be independently determined to ensure reliable estimation. For this purpose, we use the average of the difference between the amplitude quadratures when the cavities are out of resonance (Figure 41) to establish a constraint relation between the amplitude variances (α^s, α^i) and their cross-correlation terms (μ, η). This average is computed over all scan configurations and demodulation components.

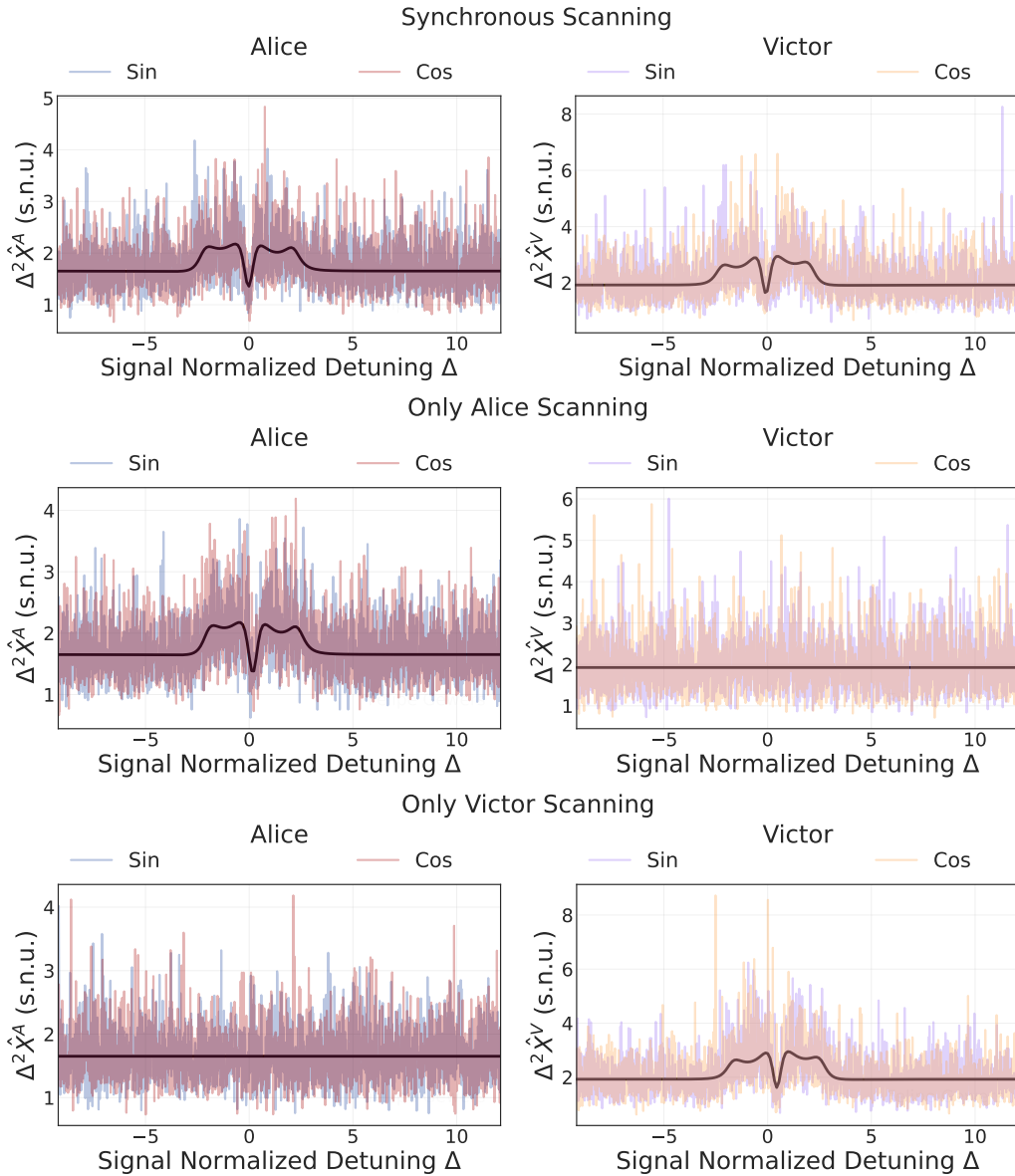


Figure 42 – Normalized variance of the accessed quadratures for the signal and idler fields across different scan configurations, considering both sine and cosine demodulation components, and expressed in shot noise units. The fitting follows the theoretical model used to extract the single-field covariance elements. The measurement was performed at a crystal temperature of -38.5°C , with a normalized pump power of $\sigma = 1.59(3)$, and an analysis frequency of 15 MHz.

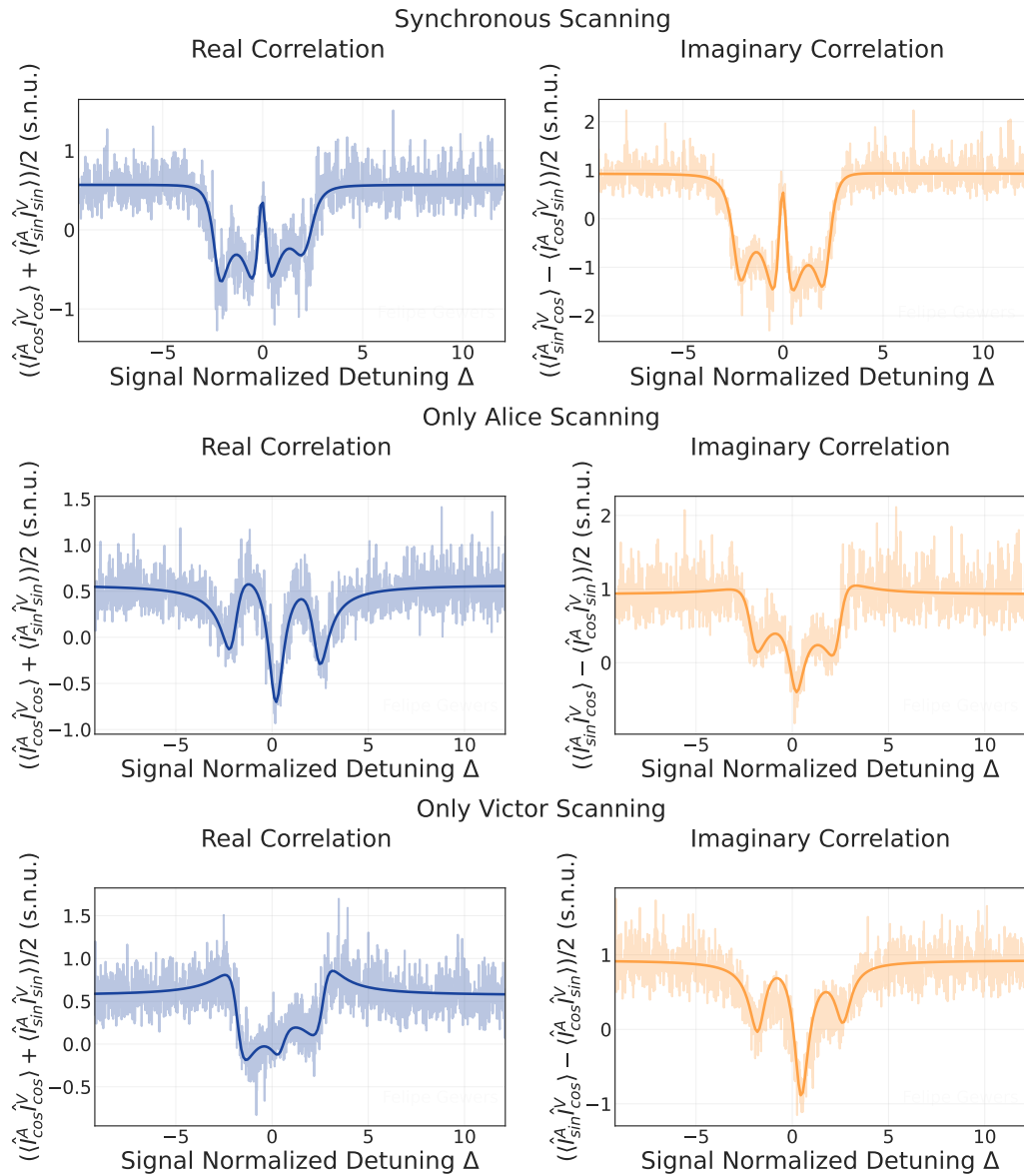


Figure 43 – Normalized real and imaginary cross-correlations between the signal and idler accessed quadratures across the three scan configurations and expressed in shot noise units. The fitted data follows the theoretical model used to extract the two-field covariance elements.

The covariance matrix elements of the signal and idler local Gaussian states, as defined in Section 3.2, are presented in Table 10. Analyzing the values, we observe that the phase quadrature exhibits higher noise levels than the amplitude quadrature. This increased noise is primarily due to thermal phonon-induced phase noise from the crystal when the OPO operates above threshold [123]. Furthermore, the noise ellipse is well aligned with the quadrature axes, as indicated by the near-zero value of the γ parameter. Additionally, the energy distribution in the sidebands is well balanced, given that the δ parameter is also compatible with zero [107].

Table 10 – Covariance matrix elements of the signal and idler local Gaussian states, obtained via the quantum tomography measurement. The first column lists the covariance symbols defined in Section 3.2.1. The second and third columns present the corresponding elements in terms of the symmetric and antisymmetric quadratures, as well as the single sideband mode or semiclassical quadratures, respectively. The last two columns provide the obtained values in shot noise units.

Covariance symbol	\mathcal{S}/\mathcal{A} quadrature basis	Semiclassical quadratures	Signal (s) (s.n.u)	Idler (i) (s.n.u)
α	$\Delta^2 \hat{p}_s, \Delta^2 \hat{q}_a$	$\Delta^2 \hat{P}$	1.65(1)	1.93(1)
β	$\Delta^2 \hat{q}_s, \Delta^2 \hat{p}_a$	$\Delta^2 \hat{Q}$	2.5(1)	3.3(1)
γ	$C(\hat{p}_s, \hat{q}_s), -C(\hat{p}_a, \hat{q}_a)$	$Re[C(\hat{P}, \hat{Q})]$	0.05(4)	-0.06(4)
δ	$C(\hat{p}_s, \hat{q}_a), C(\hat{q}_s, \hat{p}_a)$	$Im[C(\hat{P}, \hat{Q})]$	0.0(2)	0.1(2)

The covariance elements describing the correlations between the two fields are presented in Table 11. A mismatch in the capacitance of the photodiodes used to detect the signal and idler beams introduces an electronic phase discrepancy, resulting in a mixing of certain covariance elements. Specifically, this mismatch couples the real and imaginary parts of the semiclassical covariance elements, or equivalently, it mixes the covariance elements confined to the symmetric (\mathcal{S}) or antisymmetric (\mathcal{A}) quadratures with those describing correlations between these quadratures. To compensate for this effect, we apply the electronic phase rotation correction procedure described in Section 3.3.5, determining the phase angle φ_e by minimizing the imaginary components of the semiclassical covariance matrix, which are expected to be close to zero [107]. This optimization results in an electronic phase of $\varphi_e = -0.36\pi$ rad = -64.8° , with the corrected values displayed in the final column of the table.

By analyzing the covariance values and their corresponding uncertainties in Table 11, we observe that the uncertainty in the covariance of phase quadratures is significantly higher than that of amplitude quadratures. This effect arises because both phase quadratures are accessible for a limited subset of data points and are not fully measured simultaneously. Furthermore, with the exception of the first two rows, all other parameters have values close

Table 11 – Covariance matrix elements related to the correlations between signal and idler quantum states, obtained via the quantum tomography measurement. The last two columns display the measured values and the electronically phase-corrected values, respectively, both expressed in shot noise units.

Symbol	\mathcal{S}/\mathcal{A} quadrature basis	Semiclassical quadratures	Measured value (s.n.u)	Phase corrected (s.n.u)
μ	$C(\hat{p}_s^{(s)}, \hat{p}_s^{(i)}), C(\hat{q}_a^{(s)}, \hat{q}_a^{(i)})$	$Re[C(\hat{P}^{(s)}, \hat{P}^{(i)})]$	0.57(2)	1.08(1)
ν	$C(\hat{q}_s^{(s)}, \hat{q}_s^{(i)}), C(\hat{p}_a^{(s)}, \hat{p}_a^{(i)})$	$Re[C(\hat{Q}^{(s)}, \hat{Q}^{(i)})]$	-0.7(1)	-2.0(1)
ξ	$C(\hat{p}_s^{(s)}, \hat{q}_s^{(i)}), -C(\hat{q}_a^{(s)}, \hat{p}_a^{(i)})$	$Re[C(\hat{P}^{(s)}, \hat{Q}^{(i)})]$	-0.05(7)	0.15(7)
ζ	$C(\hat{q}_s^{(s)}, \hat{p}_s^{(i)}), -C(\hat{p}_a^{(s)}, \hat{q}_a^{(i)})$	$Re[C(\hat{Q}^{(s)}, \hat{P}^{(i)})]$	0.03(7)	0.14(7)
η	$C(\hat{q}_a^{(s)}, \hat{p}_s^{(i)}), -C(\hat{p}_s^{(s)}, \hat{q}_a^{(i)})$	$Im[C(\hat{P}^{(s)}, \hat{P}^{(i)})]$	0.93(1)	-0.15(2)
τ	$C(\hat{q}_s^{(s)}, \hat{p}_a^{(i)}), -C(\hat{p}_a^{(s)}, \hat{q}_s^{(i)})$	$Im[C(\hat{Q}^{(s)}, \hat{Q}^{(i)})]$	-1.9(1)	-0.1(1)
κ	$C(\hat{p}_s^{(s)}, \hat{p}_a^{(i)}), C(\hat{q}_a^{(s)}, \hat{p}_s^{(i)})$	$Im[C(\hat{P}^{(s)}, \hat{Q}^{(i)})]$	0.18(7)	0.12(7)
λ	$-C(\hat{q}_s^{(s)}, \hat{q}_a^{(i)}), -C(\hat{p}_a^{(s)}, \hat{p}_s^{(i)})$	$Im[C(\hat{Q}^{(s)}, \hat{P}^{(i)})]$	0.14(7)	0.03(7)

to zero and are statistically compatible with zero considering a three-standard-deviation range. This suggests that our quantum state exhibits strong symmetry, with minimal correlations between orthogonal semiclassical quadratures.

To ensure the validity of the obtained covariance matrix as a quantum state in compliance with the uncertainty principle for the quadratures of the field, it is essential to conduct a verification process. As discussed in Section 2.1.2, this verification can be accomplished by analyzing the symplectic eigenvalues. Following the methodology described in Equation 2.16, the symplectic eigenvalues of the measured covariance matrix are:

$$\begin{aligned} \nu_1 &= 1.351, & \nu_2 &= 1.460, \\ \nu_3 &= 1.954, & \nu_4 &= 2.138. \end{aligned} \quad (6.14)$$

The fact that all symplectic eigenvalues exceed unity confirms that the reconstructed information about the measured state is physically valid and satisfies the uncertainty principle.

6.2.2 Entanglement and Predicted Teleportation Fidelity

The complete covariance matrix obtained from our measurements fully characterizes the four-mode quantum state, which consists of the upper and lower sidebands of the signal and idler fields. A full characterization from the covariance matrix alone is possible

because the state is Gaussian with zero mean quadrature values. The Gaussian nature is supported by observing zero kurtosis (Section 3.1.3.2), while the zero mean is confirmed by directly accessing the quadrature values in our measurements.

From the complete covariance matrix, we can extract important features of the generated quantum state. In the context of quantum teleportation, entanglement assumes a crucial role, serving as the essential resource for achieving quantum advantage in the protocol. Specifically, we focus on the Duan-Giedke-Cirac-Zoller (DGCZ) criterion, which quantifies entanglement through amplitude quadrature correlations and phase quadrature anti-correlations [81], as detailed in Section 2.1.4.1. In this context, the variances of the difference in amplitude quadratures and the sum of phase quadratures, expressed in terms of covariance matrix elements, are given by:

$$\Delta^2 \hat{P}_- = \Delta^2 \hat{p}_s^{(-)} = \frac{1}{2} [\Delta^2 \hat{p}_s^{(s)} + \Delta^2 \hat{p}_s^{(i)} - 2C(\hat{p}_s^{(s)}, \hat{p}_s^{(i)})] = \frac{1}{2} [\alpha^{(s)} + \alpha^{(i)} - 2\mu], \quad (6.15a)$$

$$\Delta^2 \hat{Q}_+ = \Delta^2 \hat{q}_s^{(+)} = \frac{1}{2} [\Delta^2 \hat{q}_s^{(s)} + \Delta^2 \hat{q}_s^{(i)} + 2C(\hat{q}_s^{(s)}, \hat{q}_s^{(i)})] = \frac{1}{2} [\beta^{(s)} + \beta^{(i)} + 2\nu]. \quad (6.15b)$$

According to the DGCZ criterion, a bipartite quantum state is certified as entangled if it satisfies the following inequality:

$$\frac{\Delta^2 \hat{P}_- + \Delta^2 \hat{Q}_+}{2} < 1. \quad (6.16)$$

The computed variances in the subtraction and sum space, obtained from the measured covariance matrix described in the previous section, are presented in Table 12. A value below one for $\Delta^2 \hat{P}_-$ and $\Delta^2 \hat{Q}_+$ indicates quantum noise squeezing in these quadrature combinations. As a direct consequence, the conjugate quadratures $\Delta^2 \hat{P}_+$ and $\Delta^2 \hat{Q}_-$ exhibit increased noise, corresponding to the expected anti-squeezing in the orthogonal quadratures [71]. A comparison with the shot noise calibration results in Figure 37 reveals a decrease in the observed amplitude squeezing, indicating a reduction in system performance. This degradation is attributed to higher optical losses from several factors: gray-tracking in the crystal, the overall alignment and cleanliness of the experiment, and the sensitivity of the idler photodetector and optical coatings to small wavelength deviations. These deviations occurred because the crystal was maintained at -38.5°C for this measurement, rather than the more optimal -41.5°C . The lower squeezing coefficient for the sum of phase quadratures, $\Delta^2 \hat{Q}_+$, relative to its amplitude counterpart, $\Delta^2 \hat{P}_-$, results from phase noise contamination induced by thermal noise in the crystal's phonons [123]. The uncertainty in the sum of phase quadratures suggests that within a one-sigma range, squeezing may not be present. Nevertheless, as indicated by the value below one in the last row of the table, the DGCZ criterion is violated by 2.5 standard deviations, confirming entanglement with strong statistical significance.

Table 12 – The first four rows show the variances of the signal and idler quadratures in the sum and subtraction spaces, where values below one indicate quantum noise squeezing. The last row presents the DGCZ criterion, with a value smaller than one confirming entanglement between the fields.

Term	Value (s.n.u)	dB (s.n.u)
$\Delta^2 \hat{P}_-$	0.71(2)	-1.48(9)
$\Delta^2 \hat{Q}_+$	0.9(2)	-0.5(8)
$\Delta^2 \hat{P}_+$	2.87(2)	4.57(2)
$\Delta^2 \hat{Q}_-$	5.0(2)	7.0(1)
$\frac{\Delta^2 \hat{P}_- + \Delta^2 \hat{Q}_+}{2}$	0.80(8)	-1.0(4)

In the context of entanglement, it is insightful to analyze the entanglement between the four modes corresponding to the individual sidebands. To do so, we employ the Peres–Horodecki, or PPT (positive partial transpose), criterion, introduced in Section 2.1.4.2, by considering different bipartitions of these four modes [83]. Table 13 presents the PPT criterion values for bipartitions in both the symmetric/antisymmetric (\mathcal{S}/\mathcal{A}) and upper/lower ($\pm\Omega$) sideband bases. The notation used here is as follows: s and i denote the signal and idler fields, while the subscripts s and a represent the symmetric and antisymmetric modes, and $-$ and $+$ denote the lower and upper sideband modes. Furthermore, the symbol \times denotes that the modes on one side of it are transposed, while the modes on the other side remain unchanged. A bipartition is entangled if the minimum symplectic eigenvalue of the PPT matrix is less than one. Our results indicate that in both bases, all but one bipartition exhibit entanglement, which is consistent with theoretical predictions. This is expected, as energy conservation dictates that photon pairs are always generated either in the signal’s lower sideband (s_-) and idler’s upper sideband (i_+) or in the signal’s upper sideband (s_+) and idler’s lower sideband (i_-).

We estimate the predicted fidelity of the teleportation protocol when the generated state acts as the quantum channel between Alice and Bob. This estimation is derived by naively using Equation 4.58, which applies to a coherent input state, utilizing the variance values provided in Table 12. The input state is assumed to be a coherent state with a mean amplitude given by $\alpha_{in} = \sqrt{\langle \hat{P} \rangle^2 + \langle \hat{Q} \rangle^2}/2$, and both quadratures with equal mean values, $\langle \hat{P} \rangle = \langle \hat{Q} \rangle$. The quadrature variances of the output state can be estimated in terms of the teleportation gain Γ using Equation 4.23. This estimation incorporates the input state properties as well as the squeezing and anti-squeezing parameters derived from the variances presented in Table 12. Notably, no corrections for optical losses are applied in this prediction.

Figure 44 shows the expected evaluated fidelity as a function of the teleportation gain Γ for different input state amplitudes α_{in} . It can be observed that when the gain is

Table 13 – PPT criterion values for different bipartitions of the four-mode system, analyzed in both the symmetric/antisymmetric (\mathcal{S}/\mathcal{A}) and upper/lower ($\pm\Omega$) sideband bases. A bipartition is considered entangled if the minimum symplectic eigenvalue of the PPT matrix is less than one.

\mathcal{S}/\mathcal{A} PPT Bipartition	Minimum Symplectic Eigenvalue	$\pm\Omega$ PPT Bipartition	Minimum Symplectic Eigenvalue
$s_s \times s_a i_s i_a$	0.76	$s_- \times s_+ i_- i_+$	0.72
$s_a \times s_s i_s i_a$	0.76	$s_+ \times s_- i_- i_+$	0.78
$i_s \times s_s s_a i_a$	0.76	$i_- \times s_- s_+ i_+$	0.77
$i_a \times s_s s_a i_s$	0.76	$i_+ \times s_- s_+ i_-$	0.74
$s_s s_a \times i_s i_a$	0.74	$s_- s_+ \times i_- i_+$	0.74
$s_s i_s \times s_a i_a$	1.43	$s_- i_- \times s_+ i_+$	0.67
$s_s i_a \times s_a i_s$	0.76	$s_- i_+ \times s_+ i_-$	1.25

non-unitary, the evaluated fidelity improves for certain input states while decreasing for others. Only under unitary gain does the system teleport any unknown input state with equal fidelity, ensuring fairness without requiring prior knowledge of the input state. For the unitary gain condition, the expected fidelity based on the presented measurement is $\mathcal{F}_{exp} = 56(2)\%$, indicating quantum advantage in the teleportation protocol. Notably, this prediction does not incorporate the imaginary components of the spectral matrix, even though their inclusion could slightly enhance fidelity. In the teleportation execution, this improvement is feasible due to the ability to adjust individual electronic phase shifters in the classical feedforward process for amplitude and phase quadratures.

Achieving an expected fidelity of $\mathcal{F}_{exp} = 56(2)\%$ under the suboptimal conditions discussed in this section provided strong evidence of our system's capability for quantum teleportation. This result motivated the execution of the full teleportation protocol, which is described in the following section. Furthermore, additional tomography measurements performed with the fully assembled system yielded similar conclusions, demonstrating the reproducibility of the results presented in this chapter.

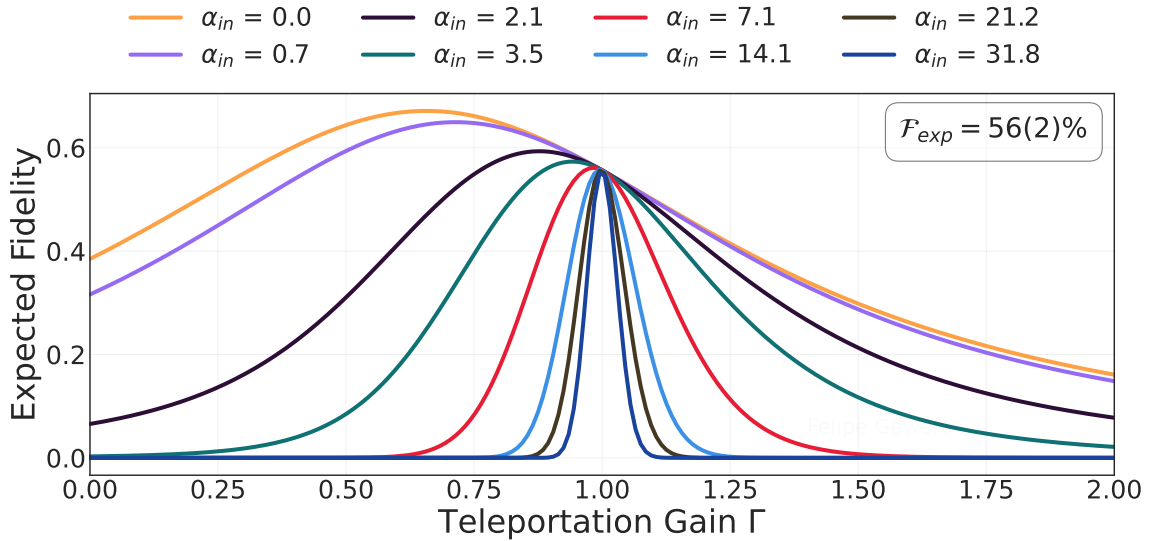


Figure 44 – Predicted fidelity for the teleportation as a function of the teleportation gain Γ , for several coherent input states. The prediction is based on the measured squeezing and anti-squeezing coefficients, without accounting for optical losses. At the unitary gain, the expected fidelity is 56(2)%, indicating quantum advantage.

6.3 Execution of the CV Quantum Teleportation Protocol

This section presents the results from our implementation of the continuous-variable (CV) quantum teleportation protocol between the infrared and telecommunication frequency bands. To the best of our knowledge, this is the first successful implementation of this protocol to surpass the classical limit across optical modes at such distant regions of the spectrum. Additionally, this achievement marks the first demonstration of CV quantum teleportation that exceeds the classical benchmark using bright fields generated by an optical parametric oscillator (OPO) operating in the above-threshold regime. These findings not only expand the scope of CV quantum teleportation but also pave the way for the development of quantum information protocols across a broader range of the optical spectrum, with potential implications for long-distance quantum communication and hybrid quantum systems.

The preparation procedure begins with the signal field. We first adjust the half-wave plate before the Mach-Zehnder interferometer to ensure that less than 1% of the beam is used for input state creation. Next, we fine-tune the splitting ratio of the PBS at Alice’s station (which mixes the optical states) to achieve an exact 50:50 beam distribution between amplitude and phase detections. Subsequently, we calibrate the gain and offset of custom-made electronic signal subtractors for the transmission signals from Alice’s and Bob’s cavities, as well as the Mach-Zehnder interference signal. Each signal is subtracted from an intensity reference to generate the error signal for active stabilization, ensuring that cavity detuning and interferometer phase remain constant despite intensity fluctuations.

We then stabilize both Alice’s and Bob’s cavities at the phase-to-amplitude conversion detuning and also stabilize the Mach-Zehnder interferometer at an arbitrary phase. Finally, using a spectrum analyzer, we adjust the gain as described in Section 5.4.3 and fine-tune the splitting ratio at Victor’s station to ensure balanced detection before starting the measurement.

The protocol’s measurement involves quantum state tomography at Victor’s station for different values of the teleportation gain. For each gain, we measure the teleportation of both a displaced coherent input state and a vacuum input state. This allows us to both verify whether the displacement operation introduces noise and determine the gain for vacuum state teleportation. A LabVIEW program controls and automates the measurements, managing both data acquisition and electronic signals. The teleportation gain is tuned by stepping the bias voltage on the classical channel attenuator in 0.075 V increments (full operational range: 0 – 8 V). For each gain, two measurements are performed: one with the modulating signal to the EOM in Victor’s Mach-Zehnder interferometer turned off, and another with it on. The automated measurement process minimizes the time between measurements of the displaced coherent and vacuum input states, reducing the risk of significant system fluctuations, which can still be detected during data analysis if they occur. While each teleportation run comprises 40 tomography measurements (20 each for the coherent and vacuum input states), the results presented here are derived from a select subset. This approach streamlined the data analysis and enhanced visualization. We excluded measurements where the teleportation gain deviated significantly from unity, as these were not relevant for characterizing the protocol’s performance.

The discussion begins with a detailed analysis of a single teleportation execution, including the intermediate data used to characterize the protocol and verify proper system operation. We then present the results from two additional teleportations, using different input states, to demonstrate the system’s versatility. One of these was performed on the same day as the detailed analysis to confirm the short-term robustness of the results over a timescale where system parameters are stable.

6.3.1 Teleported State Reconstruction

This section describes the data analysis procedure for reconstructing the teleported state and presents the corresponding results. The measurements were performed at an analysis frequency of 15 MHz with the PPKTP nonlinear crystal stabilized at -41.5°C . The pump power was 23.6(3) mW against an oscillation threshold of 14.9(3) mW, resulting in a normalized pump power of $\sigma = 1.58(2)$. Under these conditions, the generated signal and idler wavelengths were 794.4(6) nm and 1611(3) nm, respectively, and their total measured powers were 2.71(1) mW and 1.45(1) mW. In this protocol execution, we varied the teleportation gain by adjusting the bias voltage of the amplitude quadrature’s classical

channel while keeping the phase quadrature channel stable. When data from a single tomography measurement is shown in this section, it represents the teleportation of a displaced coherent input state for which the gain was set as close as possible to the unitary condition. Our full characterization involved 40 tomography measurements, however, for better visualization, we present a subset of 26 here. It's important to note that no values have been corrected for optical losses, as these corrections are addressed in a later section.

Figure 45 shows the sum of the acquired DC signals ($V_{DC}^1 + V_{DC}^2$) and the transmission of the analysis cavities (V_{cav}) at Alice's and Victor's stations during a measurement. As shown in the figure, Victor's cavity was scanned to perform quantum state tomography, while Alice's signals remained constant, demonstrating effective stabilization of both Alice's analysis cavity and Mach-Zehnder interferometer. To obtain consistent values for Victor's cavity parameters, the signals were fitted using a Lorentzian model, taking all 40 tomography measurements into account simultaneously. Compared to the previous teleportation experiment conducted in the laboratory, we observe a significant improvement in OPO stability during the teleportation measurement [59, 60]. This enhancement was achieved through improvements in the stabilization strategy and, most importantly, because our crystal exhibits significantly lower levels of gray-tracking than the one used previously. Figure 46 shows the signal-to-noise ratio, as defined in Equation 5.5, for the demodulated HF voltages acquired during the same measurement. A reduction in SNR is observed at Victor's cavity resonance due to destructive interference between the carrier field, which undergoes a phase shift inside the cavity, and mismatched modes that are only reflected.

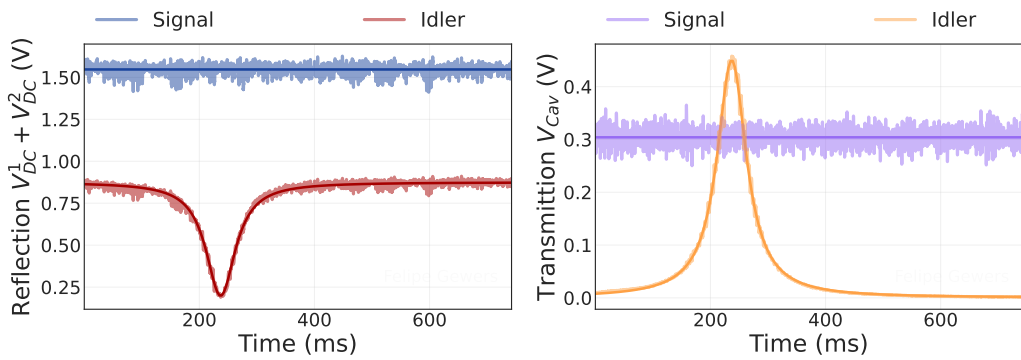


Figure 45 – Transmission and reflection intensity signals from Alice's (signal) and Victor's (idler) analysis cavities during a teleportation measurement. Alice's cavity remained stabilized, while Victor's cavity was scanned to perform quantum state tomography.

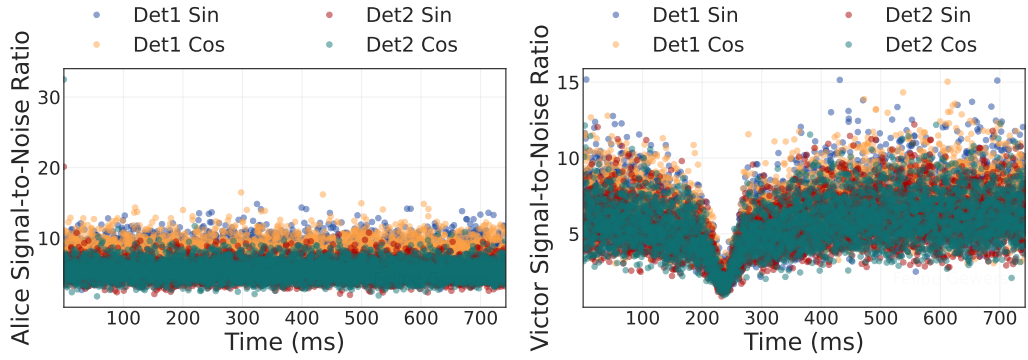


Figure 46 – Signal-to-noise ratio (SNR), which was calculated using the variance of the demodulated high-frequency signals obtained during the teleportation measurement.

6.3.1.1 Teleportation Quadrature Variances

Since we exclusively work with Gaussian states, reconstructing the teleported state requires obtaining both the first and second moments of the normalized quadratures. These moments correspond to the quadrature mean vector and the covariance matrix, which together provide a complete description of the Gaussian state. This section describes the data analysis process used to extract the covariance matrix elements of the teleported state from the measured quadrature data. It should be noted that here, the shot noise normalization relies on the shot noise calibration curve, such as the one shown in Figure 34, which is obtained prior to the teleportation execution. The calibration curve is used to convert the measured DC voltage into the corresponding shot noise value. This is necessary because Alice’s station lacks a balanced detection setup for simultaneous shot noise measurement, a design choice made to avoid transferring additional electronic noise to Bob.

The high-frequency signals at Alice’s station are recorded before transmission through the classical channel. To illustrate how the mean variance is obtained, Figure 47 first shows the data from a single measurement with a displaced coherent input state, the lines represent the calculated mean variance for each demodulation component. To verify the input state’s quality, we compute the variance of the amplitude and phase quadratures for both a displaced coherent input state (Figure 48a) and a vacuum input state (Figure 48b). The values are plotted as a function of the bias voltage applied to the amplitude quadrature’s classical channel, with one voltage setting being measured twice: once at the beginning of the process and again in the middle. As shown in Figure 48c, the difference in variance between the two cases is nearly zero. This result indicates that the displacement operation does not introduce additional noise to the sidebands. It therefore confirms that the input is a true coherent state, based on the initial assumption that the sideband modes begin in a vacuum state.

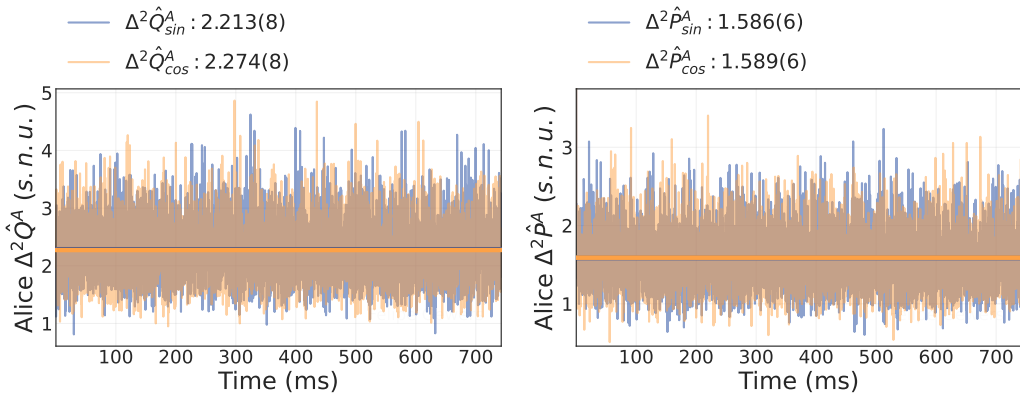


Figure 47 – Variance of the amplitude and phase quadratures for both demodulation components measured at Alice’s station. The measurement corresponds to the teleportation gain nearest to the unitary condition with a displaced coherent input state.

To extract the covariance matrix elements of the teleported state at Victor station, we apply the same data analysis procedure described in Section 6.2.1 for the single-field tomography. The fitting model is described by Equation 3.99, where the cost function is minimized simultaneously across all the sine and cosine demodulation components from the 40 measurements. Initial cavity parameters for the fit are taken from previous characterizations and the fitting results from the DC data presented in Figure 45. The variance of the accessed quadratures for both demodulation components, during Victor’s cavity scan, is shown in Figure 49. The cavity parameters obtained from this fit are listed in Table 14 and show good agreement with other characterizations performed around the same time. The cavity bandwidth and impedance matching factor values indicate a lower finesse than expected (Table 8), likely due to dust on the cavity mirrors.

The parameters in Table 14 show that the ratio between the analysis frequency and the cavity bandwidth is smaller than $\sqrt{2}$. As a consequence, the phase variance observed in Figure 49 underestimates the total phase variance due to it being affected by internal cavity losses. Our model, however, properly accounts for these losses. After considering the losses, the actual phase variance is confirmed to remain below the 3 shot noise unit limit, thus demonstrating a quantum advantage, as will be shown in the next sections. Interestingly, the reduced impedance matching factor improves the sensitivity of the tomography measurement to the δ parameter (Equation 3.95) of the covariance matrix, a value found to be compatible with zero for the data presented here. The reduced noise at zero-detuning is a known effect caused by destructive interference between the carrier field coupled into the cavity and reflected mismatch modes. This is properly accounted for in our model, as discussed in Section 3.3.4.

Figure 50 shows the covariance matrix elements of the teleported state as a function of the electronic gain in the amplitude classical feedforward channel. It presents the results

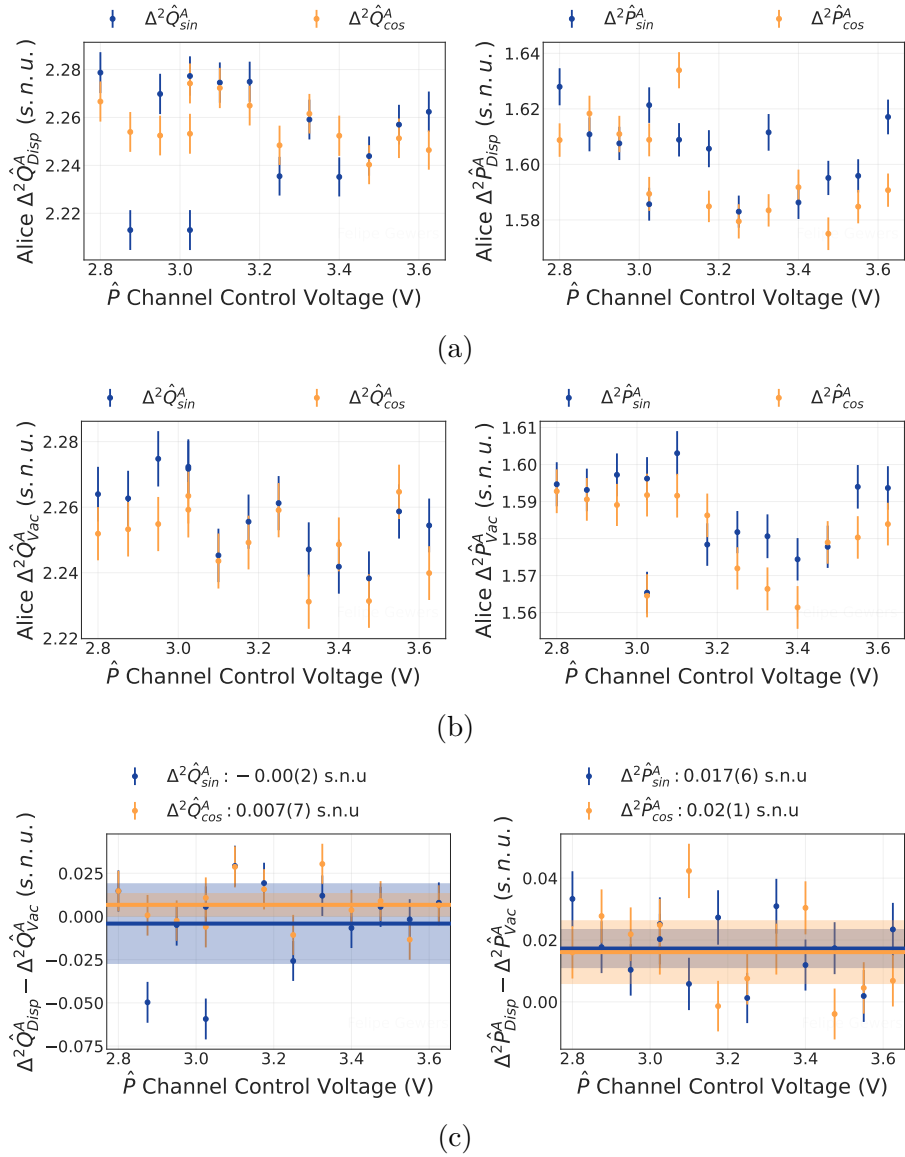


Figure 48 – Mean variances of the amplitude and phase quadratures measured at Alice’s station for all measurements near the unitary gain. (a) Variances for the displaced coherent input state. (b) Variances for the vacuum input state. (c) Difference between the variances of the displaced coherent state and the vacuum state.

Table 14 – Parameters of the Victor’s analysis cavity obtained from the fitting procedure used to extract the teleported state covariance matrix elements.

Analysis Cavity Parameter	Value
Cavity bandwidth (MHz)	11.85(2)
Normalized cavity bandwidth ($\Omega_{af}/\Delta\omega_{acav}$)	1.26(1)
Impedance matching factor d	0.227(1)
Spatial mismatch factor f^2	0.099(1)

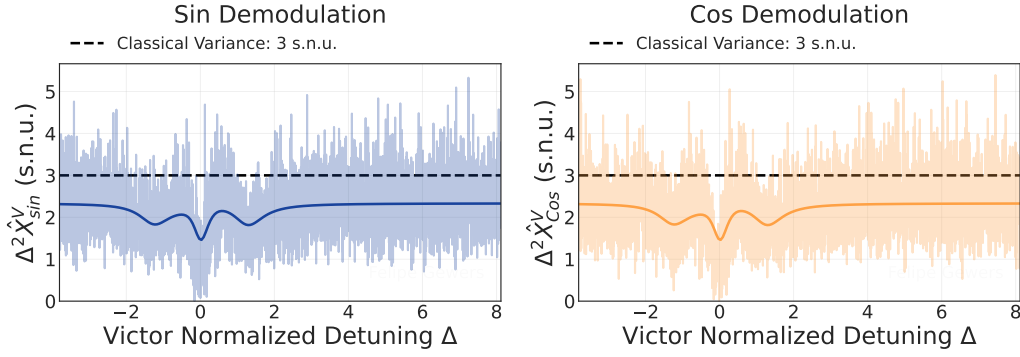


Figure 49 – Measured variance of the sine and cosine demodulation components of the accessed quadrature at Victor station as a function of normalized detuning. The data corresponds to the tomography of a teleported displaced coherent state at a gain close to unity.

for the case of displaced coherent input states (Figure 50a) and vacuum input states (Figure 50b), with the difference between them shown in Figure 50c. As previously mentioned, in our experimental setup, the teleported state exhibits quadrature swapping. This is demonstrated by the constant measured amplitude noise $\alpha^V = \Delta^2 \hat{P}^V$, while the phase noise $\beta^V = \Delta^2 \hat{Q}^V$ increases quadratically with the amplitude channel electronic gain. Examining the differences in the covariance elements shows that all values remain close to zero, except for β^V , which increases significantly at high electronic gain levels. This increase is likely caused by non-linear effects in the amplitude classical channel, where the stronger modulation of the displaced input state introduces greater noise compared to unmodulated or weakly modulated signals. Importantly, differences higher than 0.2 s.n.u are observed outside the region associated with unitary gain.

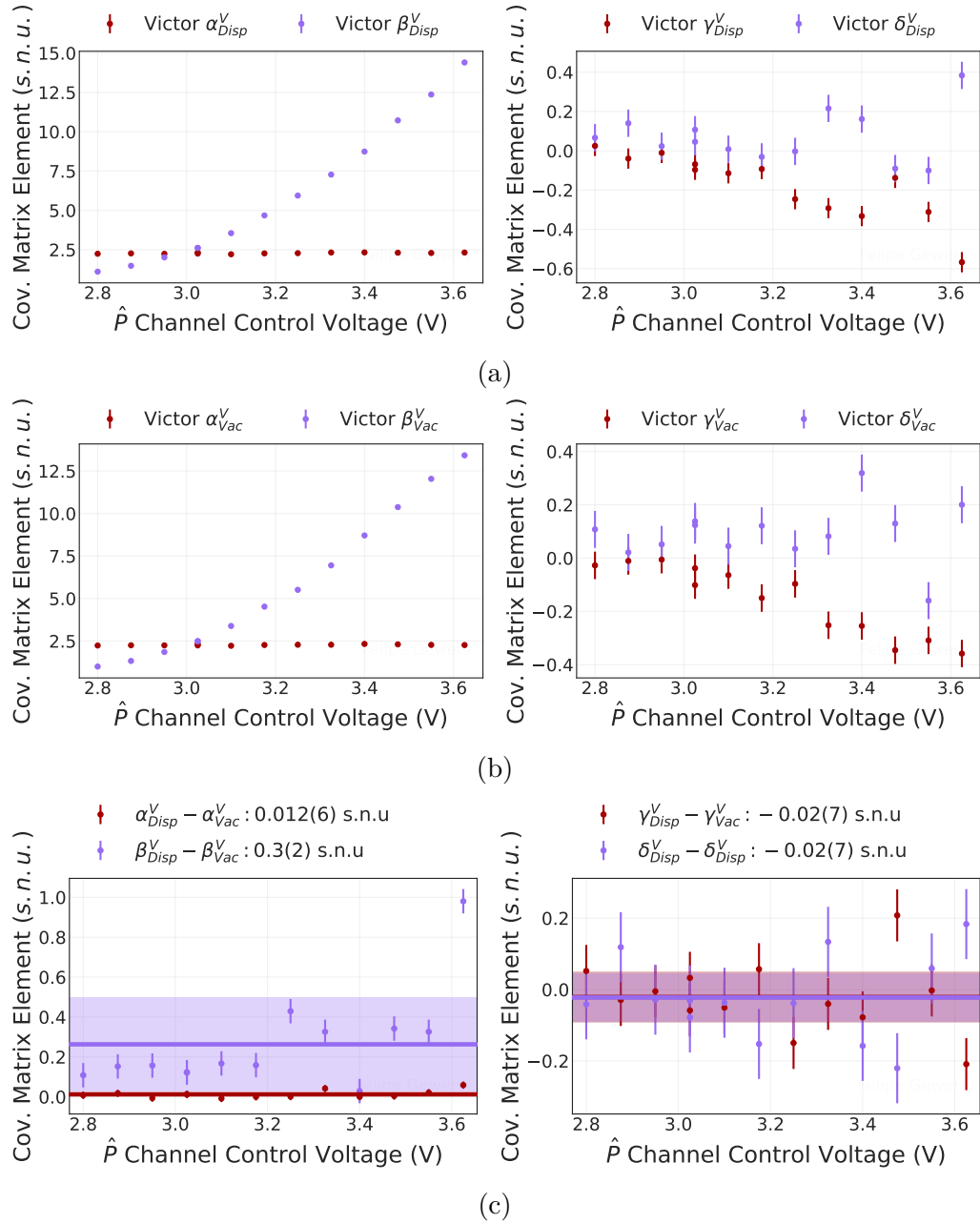


Figure 50 – Covariance matrix elements of the teleported state as a function of the electronic gain in the amplitude classical channel. (a) Teleported displaced coherent state. (b) Teleported vacuum state. (c) Difference between the covariance elements of the teleported displaced coherent state and the teleported vacuum state.

6.3.1.2 Teleportation Quadrature Mean Values

Characterizing the mean quadrature values is essential not only for the complete reconstruction of the teleported Gaussian state but also for determining the teleportation gain, as defined in Section 4.2.2. A crucial point must be emphasized regarding our measurement basis. For conceptual simplicity, our theoretical description often uses a single sideband mode representation in terms of the \hat{P} and \hat{Q} quadratures. In practice, however, the protocol teleports the individual sideband modes, with the actual measurements of the demodulation components being associated with the symmetric (\mathcal{S}) and antisymmetric (\mathcal{A}) quadrature basis, as given in Equation 3.30.

For the variances, the noise is evenly distributed across both electronic quadratures of the measured signal, leading to equal variances in both bases, $\Delta^2 \hat{P} = \Delta^2 \hat{p}_s = \Delta^2 \hat{q}_a$ and $\Delta^2 \hat{Q} = \Delta^2 \hat{q}_s = \Delta^2 \hat{p}_a$, as shown in Table 10. However, for the mean values, each component of the quadrature demodulation procedure directly recovers the corresponding component of the electronic signal amplitude. Consequently, the mean values of the single sideband quadratures are determined from the mean values of the \mathcal{S}/\mathcal{A} quadratures, as described in Sections 3.4, using the following relation:

$$\langle \hat{P} \rangle = \sqrt{\frac{\langle \hat{p}_s \rangle^2 + \langle \hat{q}_a \rangle^2}{2}}, \quad (6.17a)$$

$$\langle \hat{Q} \rangle = \sqrt{\frac{\langle \hat{q}_s \rangle^2 + \langle \hat{p}_a \rangle^2}{2}}. \quad (6.17b)$$

The mean quadrature values of the input state, which are required to compute the teleportation gain, are inferred from the measurements performed at Alice's station. To retrieve these input state values, a correction must be applied to the measured data. This correction accounts for the effect of the beam splitter that mixes the input state with Alice's share of the EPR pair, based on its transmission and reflection coefficients. Since the splitting ratio is balanced, this correction involves simply multiplying the acquired mean quadrature value by $\sqrt{2}$ for the phase measurement and by $-\sqrt{2}$ for the amplitude measurement. Figure 51 shows the mean \mathcal{S}/\mathcal{A} quadrature values of the displaced coherent input state, derived from correcting Alice's measurements.

Figure 52a shows the mean quadrature values of the input state for all measurements performed with a displaced coherent input state. The scattering in the data is an expected artifact. The measured \mathcal{S}/\mathcal{A} quadrature mean values depend on the phase relationship between the electronic local oscillator (eLO) used in quadrature demodulation and the electronic modulation signal responsible for the input state displacement, as demonstrated in Equation 3.135 [66]. Since the function generator for the modulation signal is frequently turned on and off to teleport a vacuum input state, this phase relationship changes between

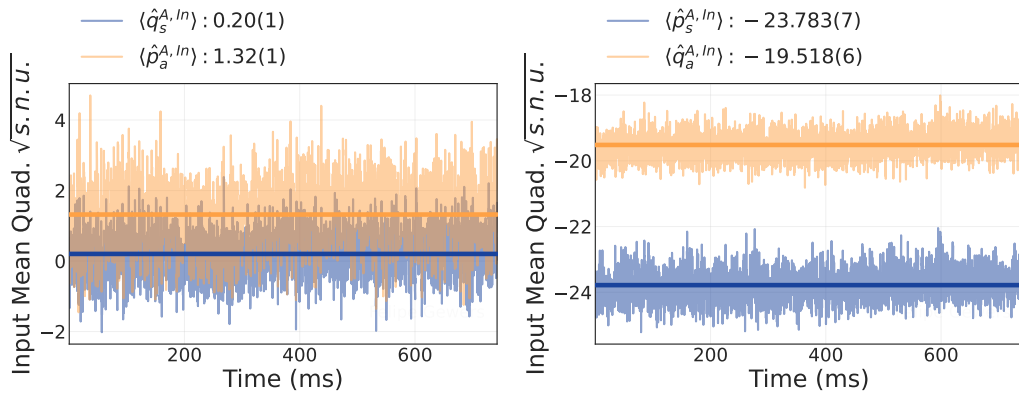


Figure 51 – Mean quadrature values of the displaced coherent input state obtained from Alice’s measurements. The data represents the closest case to unitary teleportation gain, with no correction for optical losses applied.

measurements, which explains the observed scattering. However, this variation is not an issue, as the phase relation remains constant during each individual measurement, as shown by the constant mean value in Figure 51. More importantly, the calculated single sideband mean quadrature values are, by design, unaffected by this phase shift, as described by Equation 6.17. Figure 52b presents these values. The figure reveals that the input state has a significantly larger displacement in the amplitude quadrature than in the phase quadrature. This asymmetry is a direct consequence of the phase at which the Mach-Zehnder interferometer was stabilized. Adjusting the interferometer phase changes how the displacement is distributed across the quadratures, as discussed in Section 3.4.3.

To obtain the quadrature mean vector for the teleported state, we again perform a simultaneous fitting minimization over all sine and cosine demodulation components from the 40 tomography measurements. For this procedure, the cavity parameters are fixed to the values previously determined from the variance fitting (Table 14). The fitting model itself is based on the spectral photocurrent in the auto-homodyne detection scheme with spatial mismatches (Equation 3.92). This expression is normalized by the square root of the shot noise term (Equation 3.98), while the vacuum state terms are assumed to have a zero mean value. An example of the data from a single cavity scan, to which the model is fit, is shown in Figure 53. The final results for all displaced coherent state measurements are summarized in Figure 54. This figure presents the mean values in two equivalent forms: the directly fitted results in the measured \mathcal{S}/\mathcal{A} basis (Figure 54a) and the corresponding calculated values for the single sideband quadratures (Figure 54b). The mean value of the phase quadrature scales linearly with the control voltage, while the amplitude quadrature remains constant.

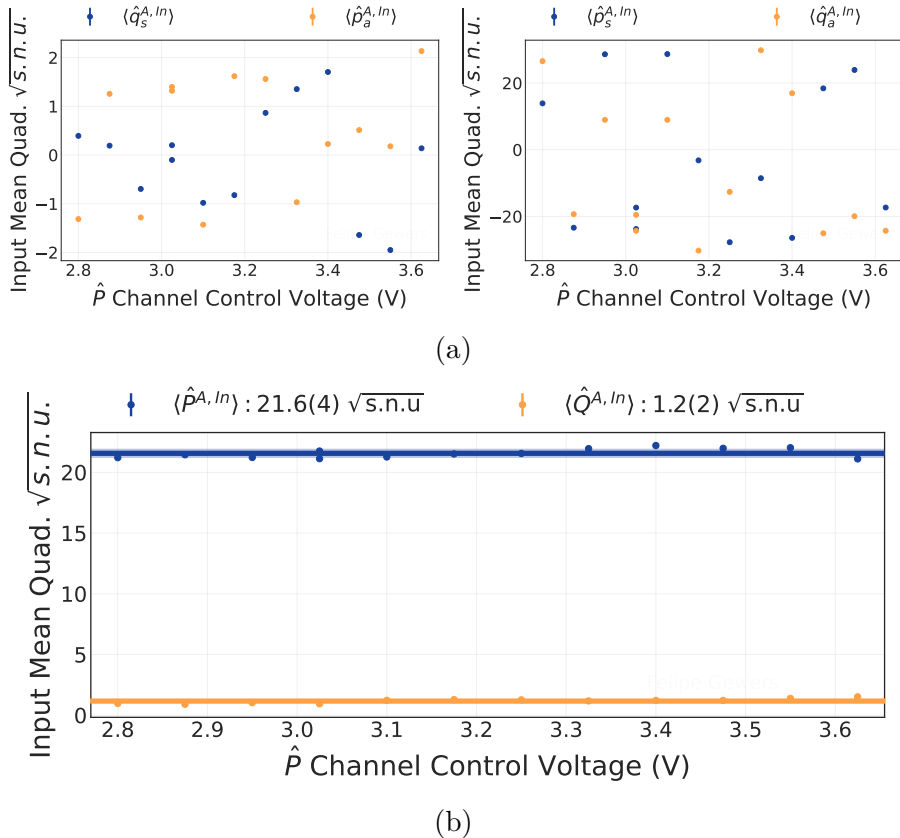


Figure 52 – (a) Mean quadrature values of the coherent displaced input state in the \mathcal{S}/\mathcal{A} quadrature basis for all measurements. (b) Corresponding single sideband mean quadrature values, showing greater displacement along the amplitude quadrature compared to the phase quadrature.

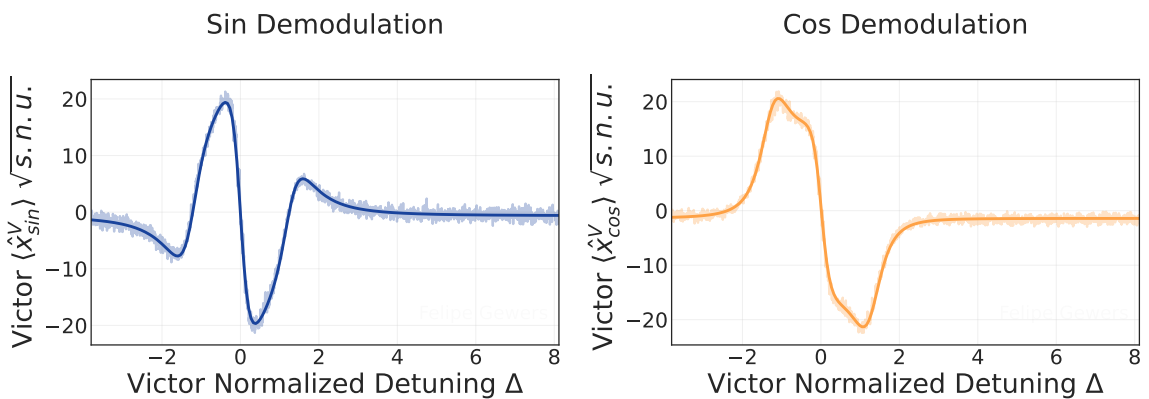


Figure 53 – Mean values of the sine and cosine demodulation signals obtained during Victor's analysis cavity scan. The quantum tomography corresponds to the teleported displaced coherent state with a teleportation gain near unitary. From the fitting procedure, the symmetric and antisymmetric quadrature mean values were extracted.

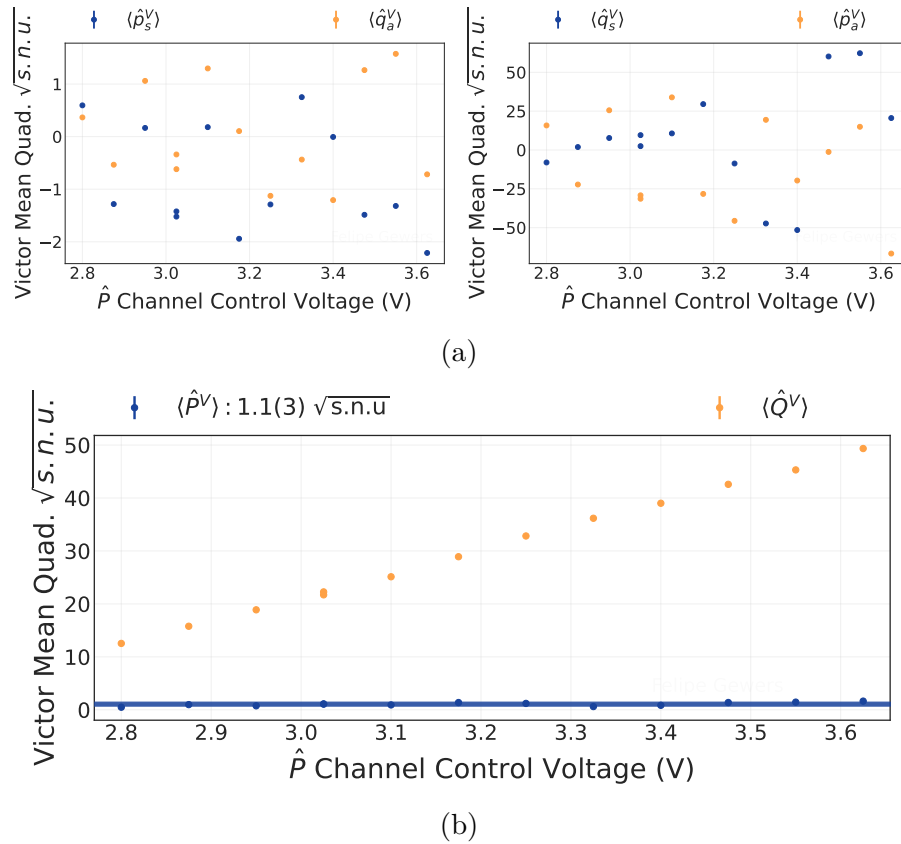


Figure 54 – (a) Teleported state mean \mathcal{S}/\mathcal{A} quadrature values from the tomography measurements using a displaced coherent input state. (b) The corresponding mean quadrature values in the single sideband basis.

6.3.2 Evaluating Protocol Performance

Having fully characterized the first and second statistical moments (the mean vectors and covariance matrices) of both the input states and the corresponding output states across a range of gain settings, we can now proceed with a comprehensive evaluation of the teleportation protocol’s performance. This section presents the core results of this analysis. It is important to establish upfront that the following evaluation is based on the raw previously presented data and does not account for optical losses. The impact and correction of these losses will be addressed in a subsequent section. Our performance evaluation involves two key steps. First, we detail the method used to extract the experimental teleportation gain, which parameterizes the classical channel, from the relationship between the input and output mean quadrature values. Second, we use the characterized states to calculate the fidelity, a primary measure of the protocol’s success. We will analyze this fidelity as a function of the teleportation gain to determine the optimal operating point of our system and assess its performance against classical benchmarks.

6.3.2.1 Teleportation Gain Determination

The teleportation gain for a given quadrature can be expressed as the ratio between the mean quadrature value of the teleported state and that of the input state: $\Gamma_{\hat{X}} = \langle \hat{X}^{Out} \rangle / \langle \hat{X}^{In} \rangle$ [122]. The unitary gain condition corresponds to the case where the teleportation gains for both quadratures are equal to one: $\Gamma_{\hat{P}} = \Gamma_{\hat{Q}} = 1$. Under this condition, the teleportation process is unbiased and consistent for all input states, ensuring that any arbitrary unknown coherent state is teleported with the same fidelity [132]. In practical implementations, however, it is often challenging to precisely tune both teleportation gains to the unitary condition simultaneously due to physical limitations of the system. The objective is to adjust both gains as close to unity as possible, minimizing bias in the protocol and ensuring that all input states are teleported with consistent accuracy and fairness. Since the vacuum state teleportation has zero mean values in its quadratures by definition, it cannot be used to determine the teleportation gain. Therefore, this section focuses on the teleportation attempts using displaced coherent input states.

Figure 55a presents a direct comparison between the mean quadrature values of the displaced coherent input state (shown in Figure 52b) and the resulting teleported state (from Figure 54b), without correcting for optical losses. Since our teleportation implementation swaps the transmitted quadrature information, the mean values of the teleported quadratures are compared with their orthogonal equivalent of the input state. The right panel of the figure compares the input phase quadrature $\langle \hat{Q}^A \rangle$, against the output amplitude quadrature $\langle \hat{P}^V \rangle$. In this plot, we observe a crossing point where the mean values closely match, indicating operation at nearly unitary gain $\Gamma_{\hat{P}} \approx 1$ for the amplitude classical channel. The left panel compares the input amplitude quadrature $\langle \hat{P}^A \rangle$ against the output phase quadrature $\langle \hat{Q}^V \rangle$. The gain for this channel was set to be close to unity, during the gain calibration step, and was intended to be maintained at this value throughout the measurement. However, visible fluctuations in the mean values indicate that the effective gain varied during data acquisition. These instabilities are attributed to the lower signal-to-noise ratio associated with the small input state's phase quadrature mean value, minor fluctuations in the optical cavity locking systems, and potential electronic cross-talk within the control system. Nevertheless, as will be presented in more detail later, it was still possible to achieve teleportation instances where the gains for both quadratures were simultaneously close to unity.

Figure 55b shows a comparison based on the mean field magnitude, defined as $|\alpha| = \sqrt{\langle \hat{P} \rangle^2 + \langle \hat{Q} \rangle^2}/2$. This parameter serves as a compact measure that combines information from both quadratures. The left panel in Figure 56 presents the teleportation gain for each channel, which accounts for our protocol's quadrature-swapping nature. The right panel presents the effective gain, Γ , defined as the ratio of the output and input mean field magnitudes, $\Gamma = |\alpha^V|/|\alpha^A|$. Without any correction for optical losses, the

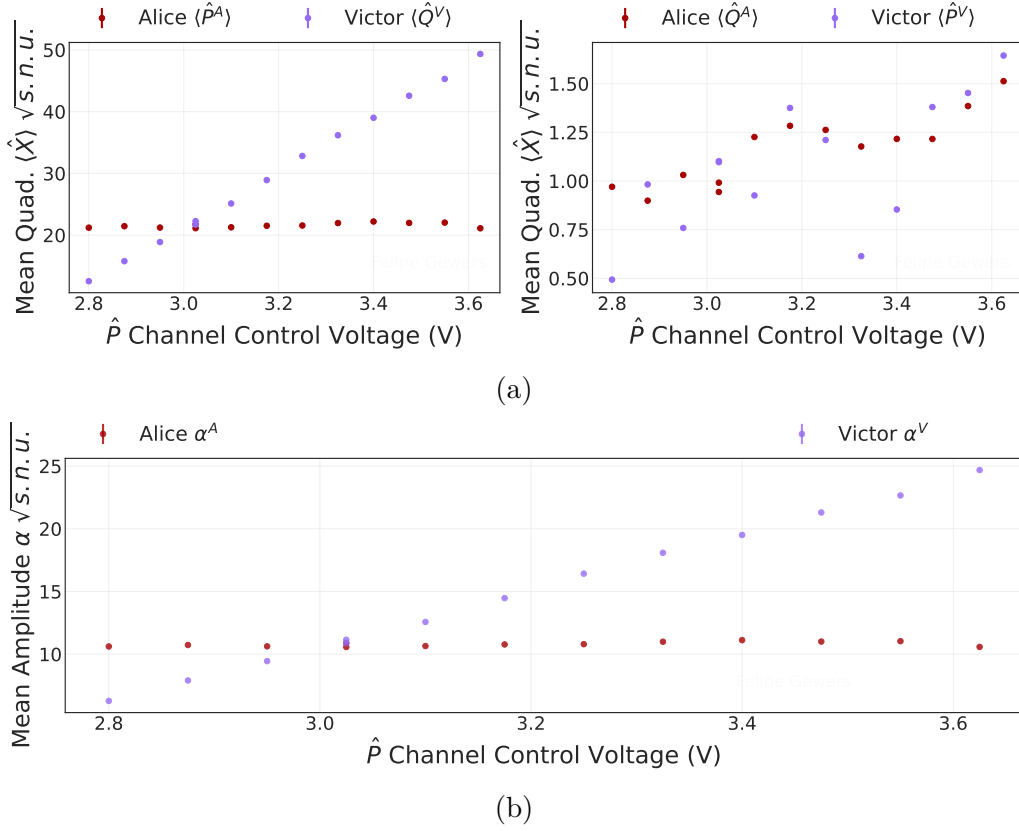


Figure 55 – Comparison of the mean values between the displaced coherent input state and teleported state in terms of the amplitude classical channel's control voltage, without correcting for optical losses. (a) Mean values of the input and teleported orthogonal quadratures: $\langle \hat{P} \rangle$ and $\langle \hat{Q} \rangle$. (b) Corresponding mean absolute value of the field amplitude $|\alpha| = \sqrt{\langle \hat{P}^2 \rangle + \langle \hat{Q}^2 \rangle / 2}$.

measurement with a teleportation gain closest to unity occurs at:

$$\Gamma_{\hat{P}} = \Gamma_{\langle \hat{Q}^V \rangle, \langle \hat{P}^A \rangle} = \frac{\langle \hat{Q}^V \rangle}{\langle \hat{P}^A \rangle} = 1.024(1), \quad (6.18a)$$

$$\Gamma_{\hat{Q}} = \Gamma_{\langle \hat{P}^V \rangle, \langle \hat{Q}^A \rangle} = \frac{\langle \hat{P}^V \rangle}{\langle \hat{Q}^A \rangle} = 1.16(2), \quad (6.18b)$$

$$\Gamma = \frac{|\alpha^V|}{|\alpha^A|} = 1.024(1). \quad (6.18c)$$

The effective gain Γ offers the advantage of a single parameter for plotting fidelity, and we will use it for this purpose in the following sections. However, relying on it alone can be misleading. A value of $\Gamma = 1$ does not guarantee that the individual gains for each quadrature are also unity (i.e., $\Gamma_{\hat{P}} = 1$ and $\Gamma_{\hat{Q}} = 1$). This discrepancy can lead to a significant overestimation of the true protocol fidelity. For instance, if an input state has a very small mean value for one of its quadratures (e.g., $\langle \hat{P}^A \rangle \approx 0$), the gain for that channel ($\Gamma_{\hat{P}}$) will have little impact on the value of the effective gain Γ . In such a case, a near-unity

effective gain could mask a poorly performing individual channel. Therefore, although Γ is useful for a simplified visualization, a rigorous performance evaluation requires analyzing the individual gains, $\Gamma_{\hat{P}}$ and $\Gamma_{\hat{Q}}$, separately.

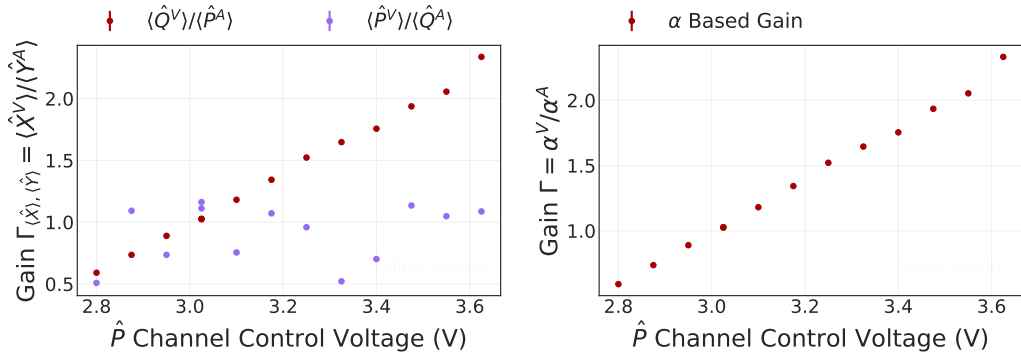


Figure 56 – Measured teleportation gain values as a function of control voltage, without applying corrections for optical losses. Left: Gain derived from the individual quadrature ratio. Right: Gain derived from the mean field magnitude ratio.

6.3.2.2 Teleportation Fidelity

Having established the teleportation gain, we now evaluate the protocol’s performance by calculating the fidelity. The fidelity, computed using Equation 4.61, quantifies the quantum state overlap between the displaced coherent input state and the teleported output state. This calculation is based on two components: the mean quadrature values of both states and the covariance matrix of the teleported state, including the parameter γ , which accounts for any misalignment of the noise ellipse relative to the measurement axes. For a vacuum input state, this same equation is used, but with zero mean quadrature values, as expected.

Table 15 presents the quadrature values of the displaced coherent input state and the corresponding teleported state, without considering optical losses. The results shown are for the teleportation measurement with the gain closest to unity. For the displaced input state, we achieved a teleportation fidelity of $\mathcal{F}_{Disp} = 55.4(4)\%$. This fidelity exceeds the perfect classical limit of 50%, which represents the maximum possible fidelity for a teleportation protocol executed without quantum resources. The observed fidelity surpasses this classical benchmark by more than 13 standard deviations, providing compelling evidence of the successful implementation of a quantum-enhanced teleportation protocol. For the vacuum state teleportation, we achieved a fidelity of $\mathcal{F}_{Vac} = 58.8(4)\%$, providing stronger statistical evidence of the quantum advantage of our implementation. The better performance for the vacuum state can be attributed to two main factors. First, the fidelity calculation for displaced states is more sensitive to small deviations from unitary gain (an effect visible in Figure 44). Second, the displaced state measurement

suffered from a small amount of excess noise attributed to the electronics of the classical channel, as shown in Figure 50c.

Table 15 – Quadrature values of the displaced coherent input and corresponding teleported state without accounting for optical losses. The results are shown for the teleportation gain closest to unity: $\Gamma_{\hat{P}} = 1.024(1)$, $\Gamma_{\hat{Q}} = 1.16(2)$ and $\Gamma = 1.024(1)$. The measured teleportation fidelity of $\mathcal{F}_{Disp} = 55.4(4)\%$ exceeds the classical limit of 50% by over 13 standard deviations, demonstrating quantum advantage.

Input State	Value	Output State	Value
Magnitude $ \alpha^{In} $	$10.888(2) \sqrt{s.n.u}$	Magnitude $ \alpha^{Out} $	$11.15(1) \sqrt{s.n.u}$
$\langle \hat{P}^{In} \rangle$	$21.755(5) \sqrt{s.n.u}$	$\langle \hat{Q}^{Out} \rangle$	$22.27(2) \sqrt{s.n.u}$
$\langle \hat{Q}^{In} \rangle$	$0.94(1) \sqrt{s.n.u}$	$\langle \hat{P}^{Out} \rangle$	$1.097(9) \sqrt{s.n.u}$
$\alpha^{In} = \Delta^2 \hat{P}^{In}$	$1 s.n.u$	$\beta^{Out} = \Delta^2 \hat{Q}^{Out}$	$2.61(4) s.n.u$
$\beta^{In} = \Delta^2 \hat{Q}^{In}$	$1 s.n.u$	$\alpha^{Out} = \Delta^2 \hat{P}^{Out}$	$2.33(1) s.n.u$
$\gamma^{In} = C(\hat{P}^{In}, \hat{Q}^{In})$	$0 s.n.u$	$-\gamma^{Out} = C(\hat{Q}^{Out}, \hat{P}^{Out})$	$0.10(5) s.n.u$

Figure 57a shows the teleportation fidelity around unitary gain for a displaced coherent input state as a function of the effective gain Γ , while Figure 57b presents the corresponding fidelity for a vacuum input state. In both plots, the red curve is generated from the theoretical model (Equations 4.34 and 4.61) to serve as a guide to the eye that illustrates the expected trend. While the curve shows good qualitative agreement, obtaining a robust quantitative fit for the model’s parameters proved challenging. During the optimization process, we encountered issues with local minima and parameter ambiguity, likely due to the high number of free parameters relative to the available data points. A more reliable fit could be achieved by constraining certain parameters with independently measured values, an approach planned for future work.

This result confirms the success of our implementation and its quantum advantage, as it outperforms any classical strategy for transferring an unknown coherent state. The violation of the classical limit was consistently observed across multiple runs, with higher fidelity values being achieved, as will be shown in subsequent sections. This demonstrates that the quantum advantage we report is both reproducible and reliable. Notably, this analysis does not account for electronic noise from the classical communication channel. Although this noise is small in the relevant gain range for this measurement, its presence still degrades the maximum achievable fidelity.

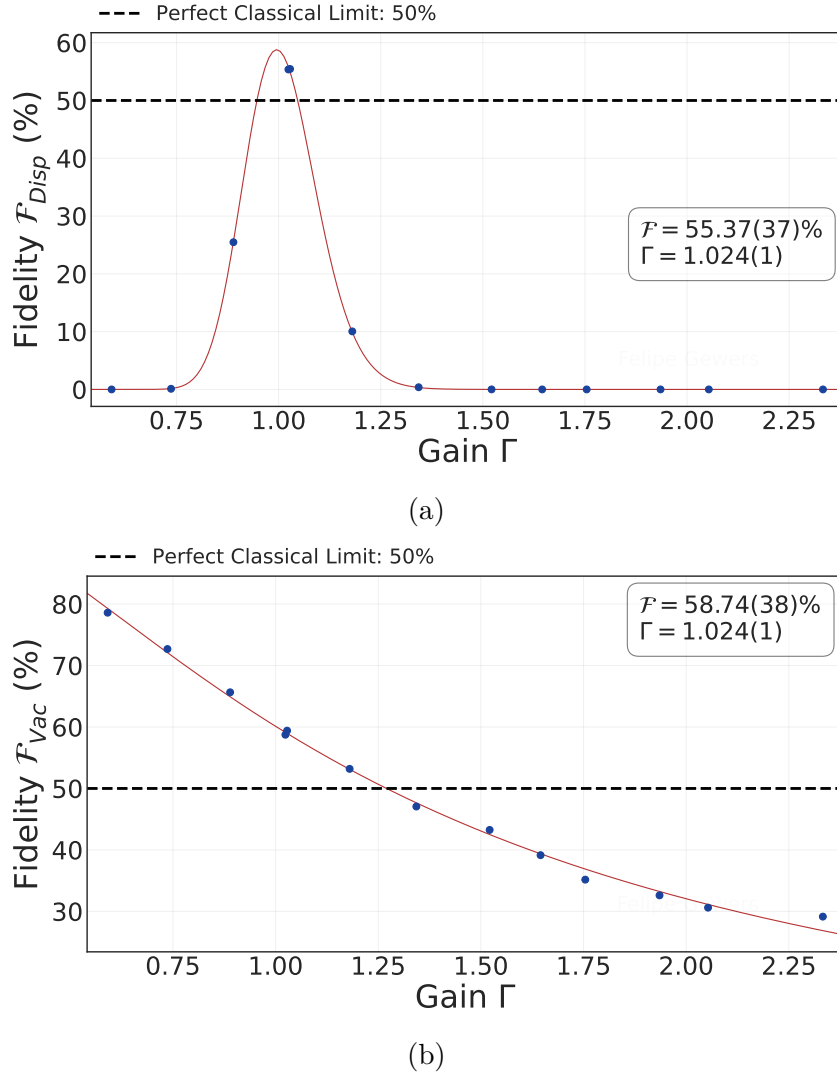


Figure 57 – Teleportation fidelity as a function of the effective gain Γ , without correction for optical losses. (a) Fidelity for a displaced coherent input state. (b) Fidelity for a vacuum input state. The red curves are generated from the theoretical model to illustrate the expected trend and serve as guides to the eye.

6.3.3 Considering Losses

The conclusions obtained in the previous sections did not account for optical losses in our experimental setup. Correcting for these losses is particularly significant at Alice's station, as they directly influence the interpretation of the input state, as discussed in Section 4.2.2. Consequently, the preceding analysis effectively benchmarked the teleported state against the attenuated input state as measured by Alice's detection apparatus, rather than the ideal state prepared by Victor. This distinction arises from optical losses in the transmission path and the limited quantum efficiency of the detectors. Despite this, the established quantum advantage of the protocol remains valid, since any classical strategy would be bound by the same 50% fidelity limit under the same interpretation.

To verify the fidelity of the teleported state with respect to the state originally sent

by Victor, we use the fact that optical losses attenuate the mean quadrature values of a coherent state but do not alter its fundamental quantum noise characteristics. Consequently, we apply a correction to the mean quadrature values obtained from Alice's measurements using the following relation [100]:

$$\langle \hat{X}_C \rangle = \frac{\langle \hat{X} \rangle}{\sqrt{\eta}}, \quad (6.19)$$

where the subscript C denotes the loss-corrected quadrature value, and η represents the total detection efficiency. This efficiency accounts for both optical path transmission and the photodetector's intrinsic quantum efficiency, and it is related to the overall loss μ by $\eta = 1 - \mu$. Since the teleportation gain is defined by the ratio of mean quadrature values, any correction applied to these values necessarily modifies the estimated gain, and potentially shifts the tomography measurement for which the gain is closest to unity. Visually, applying this correction to the data in Figure 55a increases the input state's mean values, thereby changing the crossing point that signifies unitary gain. Notably, accounting for Alice's losses results in a lower fidelity value. This is an expected outcome, as benchmarking against a perfect, lossless input state is a more demanding test for any protocol, whether quantum or classical.

Table 16 summarizes the optical losses characterized along the paths at Alice's and Victor's measurement stations, as well as the total losses, which incorporate the photodetectors' quantum efficiencies as calibrated in Figure 28. The correction for Alice's losses is based on the optical path from the outputs of the polarizing beam splitter (PBS), where the input state is mixed, to the detector for each respective quadrature (see Figure 25a). For Victor, the correction is defined by the optical path from the output of the second electro-optic modulator (EOM) at Bob's station, where the teleported state is reconstructed, to his detectors (see Figure 27). The optical losses were measured under conditions consistent with the presented results, including maintaining the non-linear crystal at the same temperature to ensure closely matched operating wavelengths. More details about the losses measurement procedure are provided in Section 5.3. The reported values for Victor represent the average total efficiency of both detectors in the balanced detection scheme, offering a reliable estimate of the attenuation affecting the teleported state.

Table 16 – Characterized optical losses along the measurement paths at Alice’s and Victor’s stations. The total losses incorporate the quantum efficiencies of the photodetectors. These values were used to apply the loss correction to the teleportation data.

Considered Range	Efficiency η (%)	Losses μ (%)
From the mixture BS to Alice’s \hat{P} detector	98.5(5)	1.5(5)
From the mixture BS to Alice’s \hat{P} detector, considering its quantum efficiency	87.3(4)	12.7(5)
From the mixture BS to Alice’s \hat{Q} detector	91.5(4)	8.5(4)
From the mixture BS to Alice’s \hat{Q} detector, considering its quantum efficiency	82.2(4)	17.8(4)
From Bob’s second EOM output to Victor’s detectors	91.4(1)	8.6(1)
From Bob’s second EOM output to Victor’s detectors, considering its quantum efficiency	78.1(1)	21.9(1)

Figure 58 presents the teleportation results after correcting for Alice’s losses. Specifically, Figure 58a shows the corrected mean values, Figure 58b displays the resulting effective gain Γ , and Figure 58c shows the fidelity values for a displaced coherent input state. At the gain closest to unity, we achieved a fidelity of $\mathcal{F}_{Disp}^{AC} = 52.1(4)\%$, which exceeds the perfect classical limit by more than 5 standard deviations. The small deviation from unitary gain in the amplitude channel limited the maximum fidelity that was achieved. The classical limit under identical experimental losses is shown as a purple dotted line, computed using Equation 4.67, and corresponds to $\mathcal{F}_{Classic}^{AC} = 45.9(2)\%$. Table 17 summarizes the input and teleported states quadrature values at the gain value closest to unity. For the vacuum input state, shown in Figure 58d, the fidelity reached $\mathcal{F}_{Vac}^{AC} = 59.4(3)\%$. This value is considerably higher, partly because the fidelity calculation for a vacuum state tends to overestimate performance when the gain is less than one. However, the data clearly shows that the fidelity remains well above 50% for gain greater than one, confirming a non-classical result. The obtained values indicate that the teleportation process allows for the accurate reconstruction of the input state, as originally sent by Victor to Alice, with a fidelity exceeding the perfect classical limit of 50%.

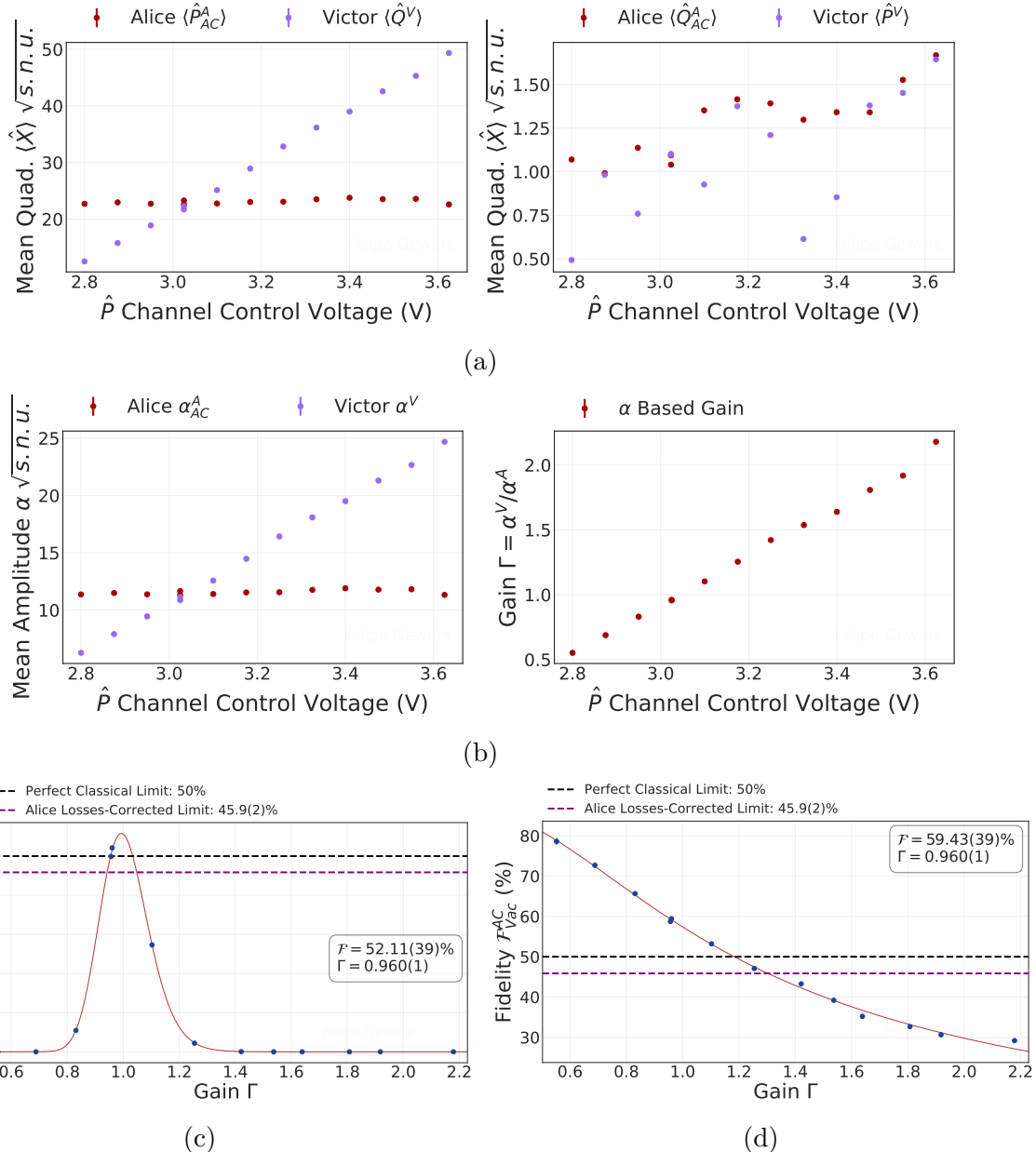


Figure 58 – Teleportation results after correcting for Alice’s losses. (a) Comparison of the mean quadrature values. (b) Effective teleportation gain Γ post-correction. (c) Fidelity for the displaced coherent input state. (d) Fidelity for the vacuum input state. The purple dotted line represents the classical limit under the same experimental losses.

Table 17 – Quadrature values of the displaced coherent input and teleported states in Alice’s corrected losses scenario. The fidelity between these states is $\mathcal{F}_{Disp}^{AC} = 52.1(4)\%$, with a teleportation gain of $\Gamma_{\hat{P}}^{AC} = 0.960(1)$, $\Gamma_{\hat{Q}}^{AC} = 1.01(1)$ and $\Gamma^{AC} = 0.960(1)$.

Alice’s Corrected Losses Scenario			
Input State	Value	Output State	Value
Magnitude $ \alpha_{AC}^{In} $	$11.320(3) \sqrt{s.n.u}$	Magnitude $ \alpha^{Out} $	$10.87(1) \sqrt{s.n.u}$
$\langle \hat{P}_{AC}^{In} \rangle$	$22.613(6) \sqrt{s.n.u}$	$\langle \hat{Q}^{Out} \rangle$	$21.71(2) \sqrt{s.n.u}$
$\langle \hat{Q}_{AC}^{In} \rangle$	$1.09(1) \sqrt{s.n.u}$	$\langle \hat{P}^{Out} \rangle$	$1.102(9) \sqrt{s.n.u}$
$\Delta^2 \hat{P}_{AC}^{In}$	$1 s.n.u$	$\Delta^2 \hat{Q}^{Out}$	$2.62(4) s.n.u$
$\Delta^2 \hat{Q}_{AC}^{In}$	$1 s.n.u$	$\Delta^2 \hat{P}^{Out}$	$2.26(1) s.n.u$
$C(\hat{P}_{AC}^{In}, \hat{Q}_{AC}^{In})$	$0 s.n.u$	$C(\hat{Q}^{Out}, \hat{P}^{Out})$	$0.07(5) s.n.u$

By correcting for optical losses in Victor’s tomography station, we can retrieve the teleported state as reconstructed by Bob, before being affected by losses in Victor’s measurement process. This requires correcting not only the mean value of the teleported state, as described in Equation 6.19, but also its covariance matrix elements using the following relations [100]:

$$\Delta^2 \hat{X}_C = \frac{\Delta^2 \hat{X} - 1}{\eta} + 1, \quad (6.20a)$$

$$C(\hat{P}_C, \hat{Q}_C) = \frac{C(\hat{P}, \hat{Q})}{\eta}. \quad (6.20b)$$

Notably, in classical teleportation attempts, fidelity remains unchanged when correcting for optical losses after the input state is reconstructed, as can be verified using the correction expressions in Equations 4.32 and 4.36. Therefore, this transformation does not affect the classical fidelity limit.

Figures 59a and 59b show the fidelity values after correcting for losses at Victor’s station for both the displaced coherent and vacuum input states, respectively. Table 18 presents the corresponding quadrature values for the displaced input state at effective gain closest to unity. After applying this correction, the calculated fidelity for the displaced input state was $\mathcal{F}_{Disp}^{VC} = 57.7(5)\%$, while the value for the vacuum input state was $\mathcal{F}_{Vac}^{VC} = 59.9(5)\%$. However, a closer inspection of the individual gain parameters reveals a critical flaw in this specific result. The loss correction shifts the gains to $\Gamma_{\hat{P}}^{VC} = 1.007(1)$ and $\Gamma_{\hat{Q}}^{VC} = 0.83(1)$. While the amplitude quadrature channel gain is nearly perfect, the phase quadrature channel gain is significantly less than one. When a channel’s gain is this low, and the corresponding input quadrature has a small mean value, the calculated fidelity becomes an overestimation of the true performance, as illustrated in Figure 44.

Therefore, the fidelity value for this particular scenario cannot be trusted as a reliable metric of successful state reconstruction. This highlights the importance of analyzing individual channel gains, as a high fidelity score, even with a unity effective gain, can be misleading if the underlying channel gains are not both close to unity.

Figures 59c and 59d present the fidelity results when accounting for losses at both Alice's and Victor's stations. Table 19 provides the quadrature values for the displaced states in this scenario. In this fully corrected case, it was not possible to obtain a fidelity exceeding the classical limit for the displaced coherent input state. This occurred because no measurement was sufficiently close to unitary gain for both channels after the correction, and the gain balance was further compromised, yielding values of $\Gamma_{\hat{P}}^{AC,VC} = 0.940(1)$ and $\Gamma_{\hat{Q}}^{AC,VC} = 0.76(1)$. However, the specific outcomes related to correcting Victor's losses do not invalidate the overall success of the presented teleportation execution. This is because the protocol's electronic gains were specifically optimized for the state as measured after it experienced losses at Victor's station, not for this retroactively corrected scenario. While correcting for Victor's losses and recovering the state information after reconstruction in Bob's station is an interesting consideration, it is not particularly relevant here. As established previously, correcting for losses at the output does not change the classical fidelity limit. The key conclusions of this characterization are drawn from the uncorrected and the Alice's corrected losses cases. Those results remain valid and successfully demonstrate the quantum advantage of our implementation of the continuous-variable teleportation protocol.

Table 18 – Quadrature values of the displaced coherent input state and teleported state after correcting for losses at Victor's station, showing a fidelity of $\mathcal{F}_{Disp}^{VC} = 57.7(5)\%$ for a teleportation gain of $\Gamma_{\hat{P}}^{VC} = 1.007(1)$, $\Gamma_{\hat{Q}}^{VC} = 0.83(1)$ and $\Gamma^{VC} = 1.007(1)$.

Victor's Corrected Losses Scenario			
Input State	Value	Output State	Value
Magnitude $ \alpha^{In} $	$10.636(3) \sqrt{s.n.u}$	Magnitude $ \alpha_{VC}^{Out} $	$10.69(1) \sqrt{s.n.u}$
$\langle \hat{P}^{In} \rangle$	$21.227(5) \sqrt{s.n.u}$	$\langle \hat{Q}_{VC}^{Out} \rangle$	$21.37(3) \sqrt{s.n.u}$
$\langle \hat{Q}^{In} \rangle$	$1.031(7) \sqrt{s.n.u}$	$\langle \hat{P}_{VC}^{Out} \rangle$	$0.86(1) \sqrt{s.n.u}$
$\Delta^2 \hat{P}^{In}$	$1 s.n.u$	$\Delta^2 \hat{Q}_{VC}^{Out}$	$2.30(6) s.n.u$
$\Delta^2 \hat{Q}^{In}$	$1 s.n.u$	$\Delta^2 \hat{P}_{VC}^{Out}$	$2.59(2) s.n.u$
$C(\hat{P}^{In}, \hat{Q}^{In})$	$0 s.n.u$	$C(\hat{Q}_{VC}^{Out}, \hat{P}_{VC}^{Out})$	$0.01(7) s.n.u$

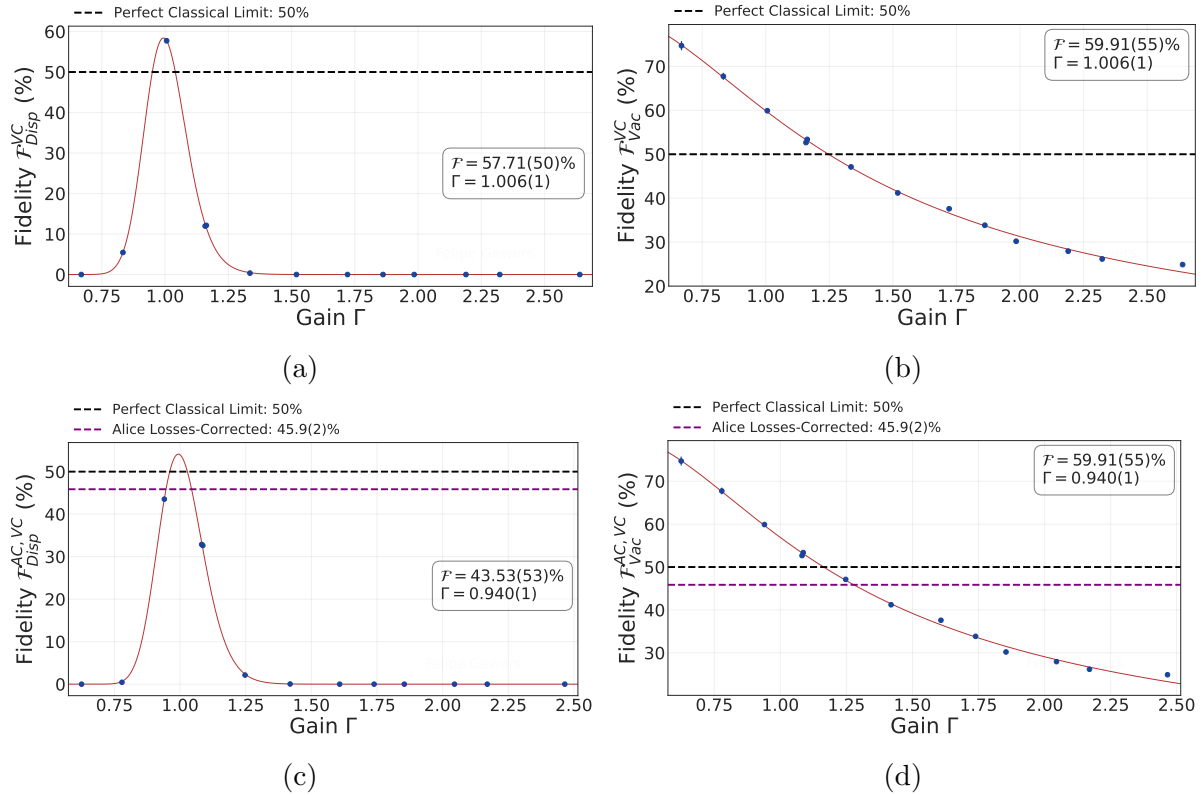


Figure 59 – Fidelity of the teleported state after correcting for Victor’s tomography station optical losses. (a) and (b) show the fidelity results after correcting only for Victor’s losses for the displaced coherent and vacuum input states, respectively. (c) and (d) present fidelity results after correcting for both Alice’s and Victor’s losses simultaneously.

Table 19 – Quadrature values of the input and teleported states after losses correction at both Alice’s and Victor’s stations. The fidelity between the states is $\mathcal{F}_{Disp}^{AC,VC} = 43.5(5)\%$, measured at a teleportation gain of $\Gamma_{\hat{P}}^{AC,VC} = 0.940(1)$, $\Gamma_{\hat{Q}}^{AC,VC} = 0.76(1)$ and $\Gamma^{AC,VC} = 0.940(1)$.

Alice’s and Victor’s Corrected Losses Scenario			
Input State	Value	Output State	Value
Magnitude $ \alpha_{AC}^{In} $	$11.375(3) \sqrt{s.n.u}$	Magnitude $ \alpha_{VC}^{Out} $	$10.69(1) \sqrt{s.n.u}$
$\langle \hat{P}_{AC}^{In} \rangle$	$22.722(6) \sqrt{s.n.u}$	$\langle \hat{Q}_{VC}^{Out} \rangle$	$21.37(3) \sqrt{s.n.u}$
$\langle \hat{Q}_{AC}^{In} \rangle$	$1.137(8) \sqrt{s.n.u}$	$\langle \hat{P}_{VC}^{Out} \rangle$	$0.86(1) \sqrt{s.n.u}$
$\Delta^2 \hat{P}_{AC}^{In}$	$1 s.n.u$	$\Delta^2 \hat{Q}_{VC}^{Out}$	$2.30(6) s.n.u$
$\Delta^2 \hat{Q}_{AC}^{In}$	$1 s.n.u$	$\Delta^2 \hat{P}_{VC}^{Out}$	$2.59(2) s.n.u$
$C(\hat{P}_{AC}^{In}, \hat{Q}_{AC}^{In})$	$0 s.n.u$	$C(\hat{Q}_{VC}^{Out}, \hat{P}_{VC}^{Out})$	$0.01(7) s.n.u$

6.3.4 Additional Teleportation Executions

To provide a more comprehensive characterization of our teleportation protocol, this section presents two additional experimental characterizations of teleportation protocol. While many measurements were performed, these two were selected to complement the preceding discussion by highlighting the protocol's robustness and versatility. The following subsections serve distinct purposes. The first demonstrates the short-term stability and reproducibility of our system by presenting a characterization taken on the same day as the execution detailed previously. For this run, the classical channel gains resulted in a violation of the classical limit across all loss-correction scenarios. The second subsection presents an execution with a significantly different input state. Here, the characterization was achieved by carefully scanning and adjusting both classical channel gains simultaneously. By demonstrating success across different input states and operational conditions, these results corroborate the robustness of our implementation and its capability to faithfully teleport arbitrary coherent states of small amplitude.

6.3.4.1 Short-Term Reproducibility and Stability

To demonstrate the short-term stability of our experimental setup, we present a teleportation characterization performed on the same day as the previously detailed run. Between these two measurements, all main stabilization systems, including the optical parametric oscillator (OPO), were disengaged for a standard measurement of dark noise conditions. Despite this significant disturbance, the input state and key protocol parameters remained consistent upon re-stabilization. This demonstrates that not only the quantum advantage is reproducible, but also the overall system is robust against significant short-term disturbances. In this characterization, the classical limit was violated under all four analysis scenarios used to correct for optical losses at Alice's and Victor's stations. This was achieved with well-balanced channel gains, avoiding the issue presented in the previous characterization where one channel's gain was significantly below unity.

The measurement was performed under conditions nearly identical to the previous one, using an analysis frequency of 15 MHz with the nonlinear crystal stabilized at -41.5°C , which generated a signal at 794(4) nm and an idler at 1611(3) nm. However, the measured power was slightly lower, at 2.31(1) mW for the signal and 1.15(1) mW for the idler. The cavity parameters obtained from the fits were compatible with those from the previous measurement presented in Table 14. Figure 60 shows the quadrature variances and mean values measured at Alice's station during the teleportation of a displaced coherent input for the gain closest to unity, without any loss correction. Figure 61 presents the corresponding values obtained by scanning Victor's analysis cavity during the tomography measurement, along with the fit used to extract the first and second moments of the teleported state.

Notably, the variance of this teleported state remains below the classical limit of 3 shot noise units throughout the entire scan, a finding confirmed by the fitting results.

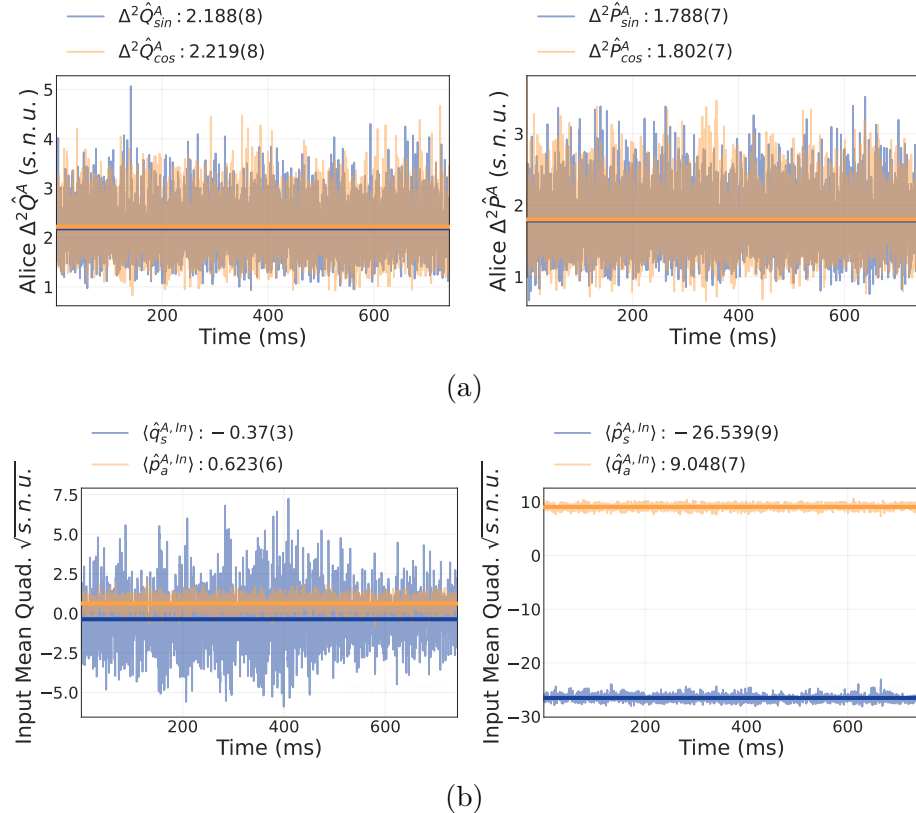


Figure 60 – Measured variances (a) and mean values (b) at Alice’s station during the teleportation of a displaced coherent input. These data correspond to the measurement with the gain closest to unity, which is calculated without correction for optical losses.

The teleportation gain is determined by the ratio between the mean quadrature values of the teleported state and the corresponding displaced input state. Figure 62a illustrates this comparison as a function of the control voltage applied to the amplitude quadrature classical feedforward channel, while also accounting for the quadrature swapping inherent to our protocol. Consistent with the characterization described in the previous sections, fluctuations associated with the classical phase channel are still observable in the data. Despite these fluctuations, it was possible to simultaneously achieve a near-unitary gain condition ($\Gamma_P, \Gamma_Q \approx 1$) for both channels, a result that holds even after accounting for optical losses. Figure 62b presents the calculated gains for each individual quadrature channel alongside the effective gain derived from the total field magnitude.

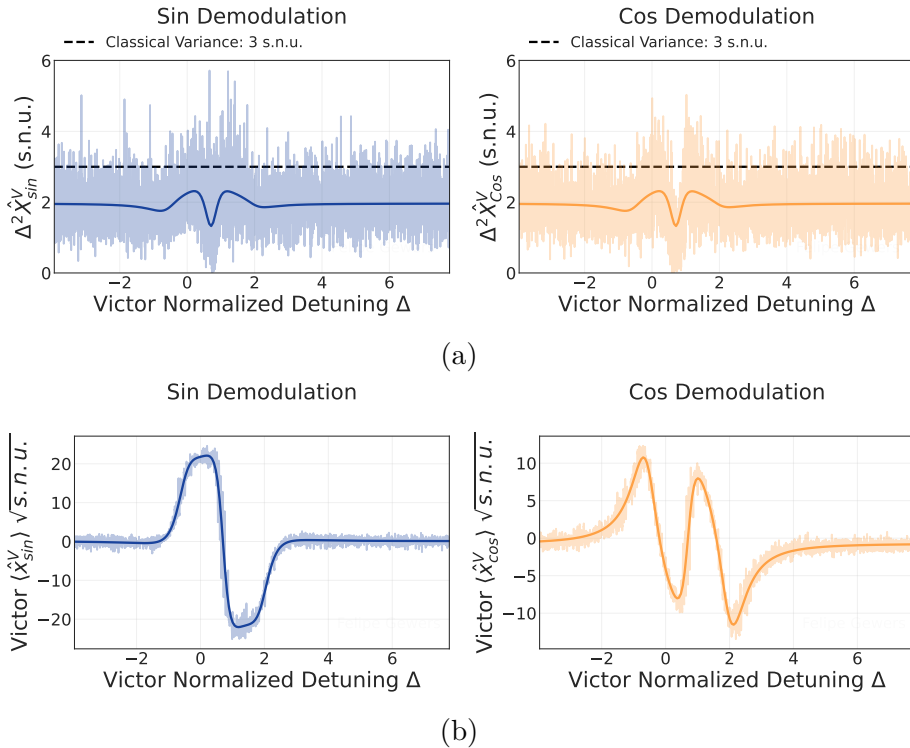


Figure 61 – Measured quadrature variances (a) and mean values (b) of the displaced teleported state during Victor’s quantum tomography. The measurement corresponds to the gain closest to unity, and the data are presented without correction for optical losses.

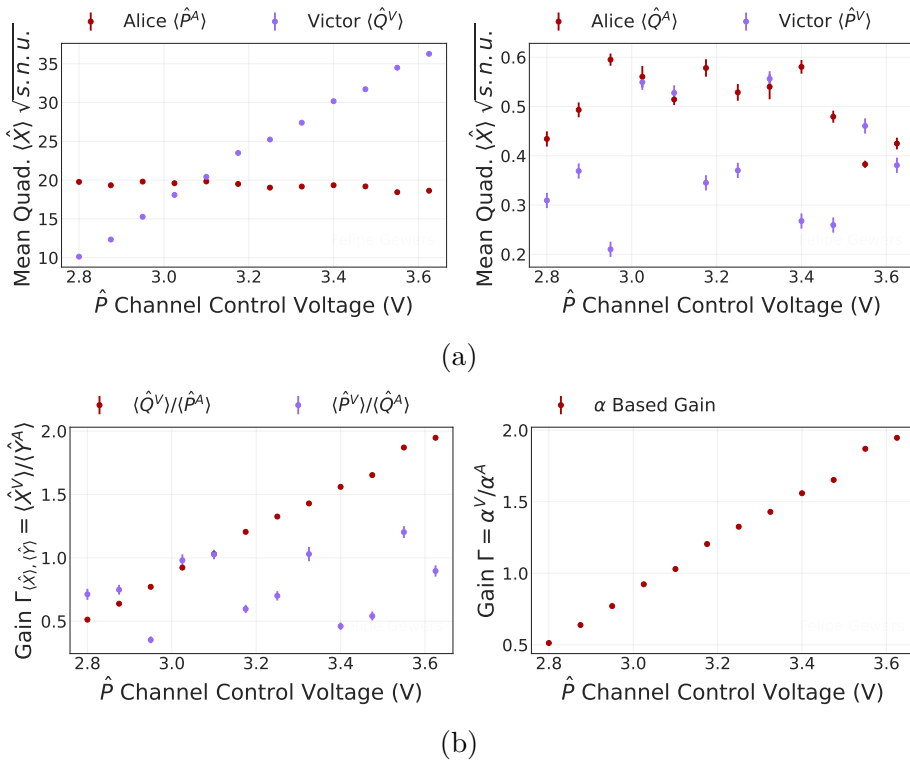


Figure 62 – Comparison of mean quadrature values (a) and the resulting teleportation gain (b) for a displaced coherent input state, plotted against the control voltage of the amplitude channel.

Table 20 summarizes the key results of the characterization. It presents the teleportation fidelity for both displaced and vacuum input states, the associated channel gains, and the moments of the input and output states for the displaced input state. The results are presented for two distinct scenarios: the uncorrected losses scenario, which uses the raw measurement data, and the Alice's corrected losses (AC) scenario, which compensates for optical losses within Alice's detection apparatus, using the values presented in Table 17. Figure 63 complements this by plotting the teleportation fidelity as a function of the effective gain Γ .

For the teleportation of a displaced coherent state in the uncorrected losses scenario, we achieved a fidelity of $\mathcal{F}_{Disp} = 55.8(4)\%$ (Figure 63a). This result surpasses the optimal classical teleportation fidelity of 50% by more than 13 standard deviations, providing clear evidence of a quantum advantage. This performance is consistent with the previous characterization presented in Section 6.3.2.2, demonstrating the robustness of our experimental setup. The measurement was performed with the quadrature gains well-balanced and slightly above unity: $\Gamma_{\hat{P}} = 1.030(2)$, $\Gamma_{\hat{Q}} = 1.03(4)$ and $\Gamma = 1.030(2)$. Under these same optimal gain conditions, the teleportation of a vacuum state yields a fidelity of $\mathcal{F}_{Vac} = 60.0(4)\%$ (Figure 63b). This fidelity is a reliable benchmark for the protocol's performance, given that the gains are well-balanced and greater than one, and constitutes an even stronger violation of the classical limit. As in the previous characterization, the fidelity difference between the two input states arises because the vacuum fidelity is less sensitive to small gain variations and is not affected by the additional electronic noise affecting more strongly modulated quadratures.

The Alice's corrected losses fidelity for the displaced input state is $\mathcal{F}_{Disp}^{AC} = 53.8(5)\%$ (Figure 63c). This violates the classical limit by more than 7 standard deviations, again showing that our system can outperform a perfect classical strategy even when accounting for experimental losses. Interestingly, in this specific run, the same teleportation measurement was closest to unity gain for both the uncorrected and Alice's corrected scenarios. Therefore, as seen in Table 20, only the input state values and the parameters derived from them (gains and fidelity) change between the two cases. Since the vacuum fidelity calculation does not depend on the input state's mean values, its value remains $\mathcal{F}_{Vac}^{AC} = 60.0(4)\%$ (Figure 63d). However, this value is an overestimation of the true performance under this scenario. The actual teleportation quality is determined by the corrected gain, which is less than one, indicating the classical channel configuration was not optimal (see Figure 44).

Table 20 – Teleportation parameters for the second presented experimental run, showing results for both the uncorrected and Alice’s corrected losses (AC) cases. All values correspond to the measurement with gain closest to unity for each respective scenario.

Parameter	Uncorrected Losses	Alice’s Corrected Losses (AC)
<i>Performance Metrics</i>		
Displaced Input Fidelity \mathcal{F}_{Disp}	55.8(4)%	53.8(5)%
Vacuum Input Fidelity \mathcal{F}_{Vac}	60.0(4)%	60.0(4)%
<i>Gain Parameters</i>		
Amplitude Channel Gain $\Gamma_{\hat{P}}$	1.030(2)	0.962(2)
Phase Channel Gain $\Gamma_{\hat{Q}}$	1.03(4)	0.93(3)
Effective Gain Γ	1.030(2)	0.962(2)
<i>Input State</i>		
Magnitude $ \alpha^{In} $	9.917(3) $\sqrt{s.n.u}$	10.615(3) $\sqrt{s.n.u}$
Mean Amplitude $\langle \hat{P}^{In} \rangle$	19.827(6) $\sqrt{s.n.u}$	21.223(7) $\sqrt{s.n.u}$
Mean Phase $\langle \hat{Q}^{In} \rangle$	0.51(1) $\sqrt{s.n.u}$	0.57(1) $\sqrt{s.n.u}$
<i>Output State</i>		
Magnitude $ \alpha^{Out} $	10.21(2) $\sqrt{s.n.u}$	10.21(2) $\sqrt{s.n.u}$
Mean Phase $\langle \hat{Q}^{Out} \rangle$	20.42(4) $\sqrt{s.n.u}$	20.42(4) $\sqrt{s.n.u}$
Mean Amplitude $\langle \hat{P}^{Out} \rangle$	0.53(2) $\sqrt{s.n.u}$	0.53(2) $\sqrt{s.n.u}$
Phase Variance $\Delta^2 \hat{Q}^{Out}$	2.97(4) $s.n.u$	2.97(4) $s.n.u$
Amplitude Variance $\Delta^2 \hat{P}^{Out}$	1.96(1) $s.n.u$	1.96(1) $s.n.u$
Covariance $C(\hat{Q}^{Out}, \hat{P}^{Out})$	-0.06(5) $s.n.u$	-0.06(5) $s.n.u$

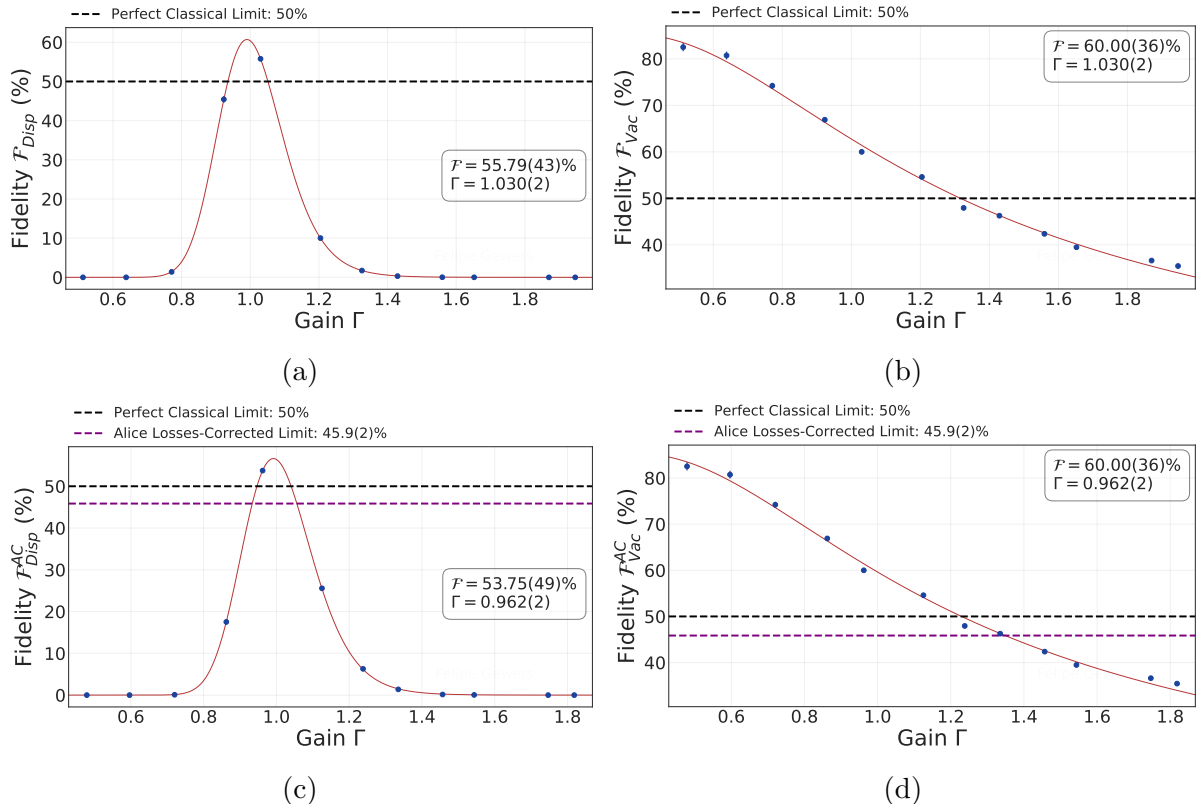


Figure 63 – Teleportation fidelity plotted as a function of the effective gain, Γ . The top panels, (a) and (b), present the fidelity for displaced and vacuum input states, respectively, calculated from the raw data without loss correction. The bottom panels, (c) and (d), show the corresponding fidelities after applying corrections for detection losses at Alice’s station.

Table 21 presents the teleportation results for the Victor's corrected losses (VC) scenario, which mathematically corrects for detection losses at Victor's station. As mentioned, this correction allows us to infer the properties of the teleported state as it was reconstructed by Bob, before its transmission to Victor for measurement. The table also includes the scenario where detection losses at both Alice's and Victor's stations are corrected (AC,VC). Figure 64 shows the teleportation fidelity as a function of the effective gain Γ for these two cases.

For these scenarios, the measurements were performed with well-balanced gains close to unity. The largest deviation from unity was the phase channel gain for the VC case, $\Gamma_Q^{VC} = 1.11(5)$. Although a gain greater than one is not optimal, it does not lead to an artificial overestimation of the fidelity compared to the ideal unitary condition. When correcting only for losses at Victor's station, we achieved a fidelity of $\mathcal{F}_{Disp}^{VC} = 53.1(7)\%$ for the displaced input state and $\mathcal{F}_{Vac}^{VC} = 61.2(5)\%$ for the vacuum input state. When fully correcting for all detection losses, the fidelity for the displaced state improved to $\mathcal{F}_{Disp}^{AC,VC} = 57.0(6)\%$, while the vacuum state fidelity remained unchanged at $\mathcal{F}_{Vac}^{AC,VC} = 61.2(5)\%$. All of these results surpass the classical limit with high statistical significance. Therefore, the measurements demonstrate that our system successfully teleports quantum states with a fidelity unachievable by classical means. This holds true whether we define the final state as the one arriving at Victor's detectors or infer its properties at Bob's station, immediately after recreation. This comprehensive analysis confirms that the quantum advantage is maintained across different stages of the teleportation process.

Table 21 – Teleportation parameters for the second presented experimental run, showing results for the Victor’s corrected losses (VC) and for the fully corrected losses (AC,VC) cases. All values correspond to the measurement with gain closest to unity for each respective scenario.

Parameter	Victor’s Corrected Losses (VC)	Both Corrected Losses (AC,VC)
<i>Performance Metrics</i>		
Displaced Input Fidelity \mathcal{F}_{Disp}	53.1(7)%	57.0(6)%
Vacuum Input Fidelity \mathcal{F}_{Vac}	61.2(5)%	61.2(5)%
<i>Gain Parameters</i>		
Amplitude Channel Gain $\Gamma_{\hat{P}}$	1.044(2)	0.976(2)
Phase Channel Gain $\Gamma_{\hat{Q}}$	1.11(5)	1.01(5)
Effective Gain Γ	1.044(2)	0.976(2)
<i>Input State</i>		
Magnitude $ \alpha^{In} $	9.804(5) $\sqrt{s.n.u}$	10.495(5) $\sqrt{s.n.u}$
Mean Amplitude $\langle \hat{P}^{In} \rangle$	19.60(1) $\sqrt{s.n.u}$	20.98(1) $\sqrt{s.n.u}$
Mean Phase $\langle \hat{Q}^{In} \rangle$	0.56(2) $\sqrt{s.n.u}$	0.62(2) $\sqrt{s.n.u}$
<i>Output State</i>		
Magnitude $ \alpha^{Out} $	10.24(2) $\sqrt{s.n.u}$	10.24(2) $\sqrt{s.n.u}$
Mean Phase $\langle \hat{Q}^{Out} \rangle$	20.47(4) $\sqrt{s.n.u}$	20.47(4) $\sqrt{s.n.u}$
Mean Amplitude $\langle \hat{P}^{Out} \rangle$	0.62(2) $\sqrt{s.n.u}$	0.62(2) $\sqrt{s.n.u}$
Phase Variance $\Delta^2 \hat{Q}^{Out}$	2.53(5) $s.n.u$	2.53(5) $s.n.u$
Amplitude Variance $\Delta^2 \hat{P}^{Out}$	2.25(2) $s.n.u$	2.25(2) $s.n.u$
Covariance $C(\hat{Q}^{Out}, \hat{P}^{Out})$	-0.08(6) $s.n.u$	-0.08(6) $s.n.u$

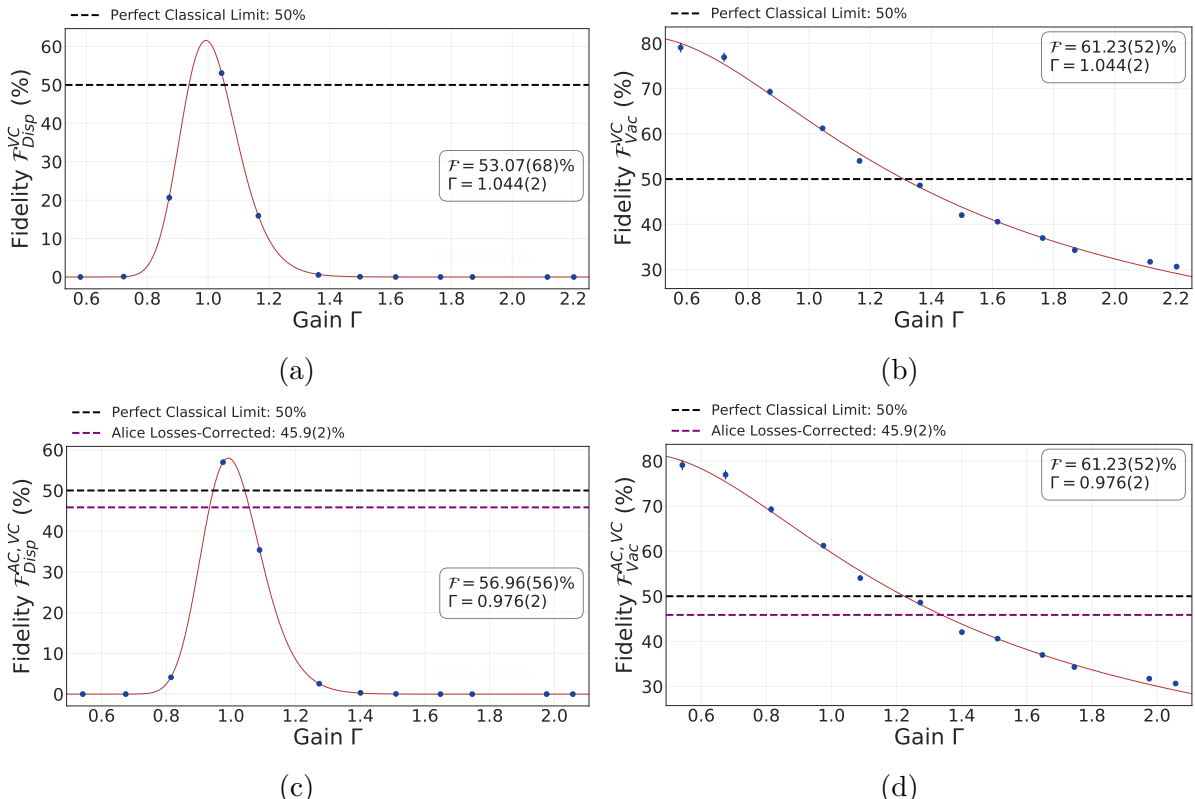


Figure 64 – Teleportation fidelity under two different loss-correction schemes. The top panels, (a) and (b), illustrate the fidelity for displaced and vacuum states, respectively, when accounting only for losses at Victor’s station. The bottom panels, (c) and (d), present the fidelity for the same input states when losses at both Alice’s and Victor’s stations are corrected simultaneously.

6.3.4.2 Teleportation via Simultaneous Gain Scanning

To showcase the versatility of our system, this subsection presents a teleportation characterization using a different input state, one with a much larger component in the phase quadrature compared to the previously presented runs. This demonstration corroborates the concept that our system is capable of teleporting any unknown, small-amplitude coherent state. For this characterization, we varied the teleportation gain by simultaneously scanning the electronic gains of both the amplitude and phase classical channels. This tuning procedure, although more difficult to implement experimentally, allows us to correct for different optical losses without significantly compromising the gain balance between the quadrature channels. Therefore, achieving the quantum limit under these conditions further confirms the capabilities of our protocol for various inputs and operational settings.

This characterization was performed several weeks after the previously presented results, and several small improvements were made to the system in the meantime. During these measurements, the pump power was 23.4(2) mW against an oscillation threshold of 13.6(2) mW, resulting in a normalized pump power of $\sigma = 1.73(3)$. The PPKTP crystal temperature was stabilized at the same temperature as previous runs (-41.5°C), generating a signal field at 794.4(6) nm and an idler field at 1611(3) nm, with respective measured powers of 2.41(1) mW and 1.22(1) mW. Figure 65 presents the sum of the measured DC signals and the transmission of the analysis cavities at Alice’s and Victor’s stations during a tomography measurement. For this run, the parameters of Victor’s analysis cavity were aligned more closely with the expected design values, featuring a measured bandwidth of 7.56(2) MHz and an impedance matching factor of $d = 0.856(1)$. These values, together with the analysis frequency of 15 MHz, imply a normalized bandwidth of $\Omega_{af}/\Delta\omega_{acav} = 1.985(6)$. As this value is higher than $\sqrt{2}$, it indicates that the cavity can measure the complete phase quadrature without being affected by internal losses.

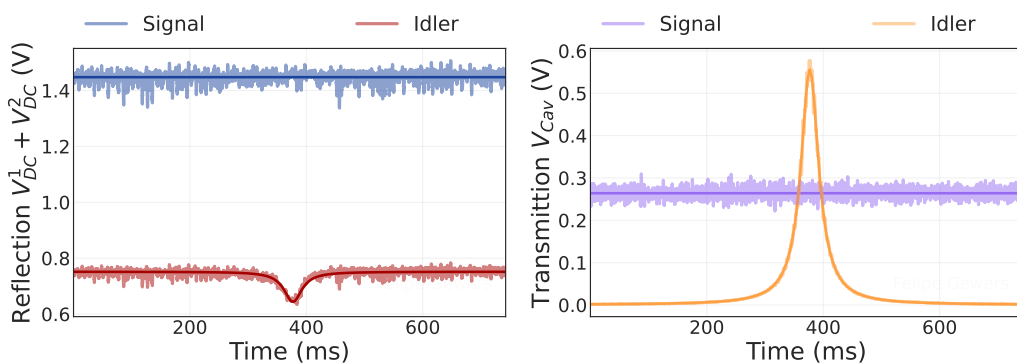


Figure 65 – Transmission and reflection intensity signals from Alice’s (signal) and Victor’s (idler) analysis cavities during a teleportation measurement. Alice’s cavity remained stabilized, while Victor’s cavity was scanned to perform quantum state tomography.

The presentation of the results in this section follows the same pattern as the previous one. Figure 66 shows the quadrature variances and mean values measured at Alice's station for the displaced coherent input state and gain closest to unity. Figure 67 presents the corresponding quadrature values measured at Victor's station by scanning the analysis cavity during the quantum tomography procedure, along with the fitted curve. Notably, the amplitude quadrature's variance was near the classical limit, preventing the extraction of quantum advantage from the phase quadrature correlations, likely due to spurious electronic noise. Despite this limitation, high fidelities and overall quantum advantage were still demonstrated. Figure 68a shows the comparison of the quadrature mean values as a function of the bias voltage applied to the variable attenuator in both classical channels. Figure 68b presents the calculated gains, where the synchronous and balanced tuning is evident.

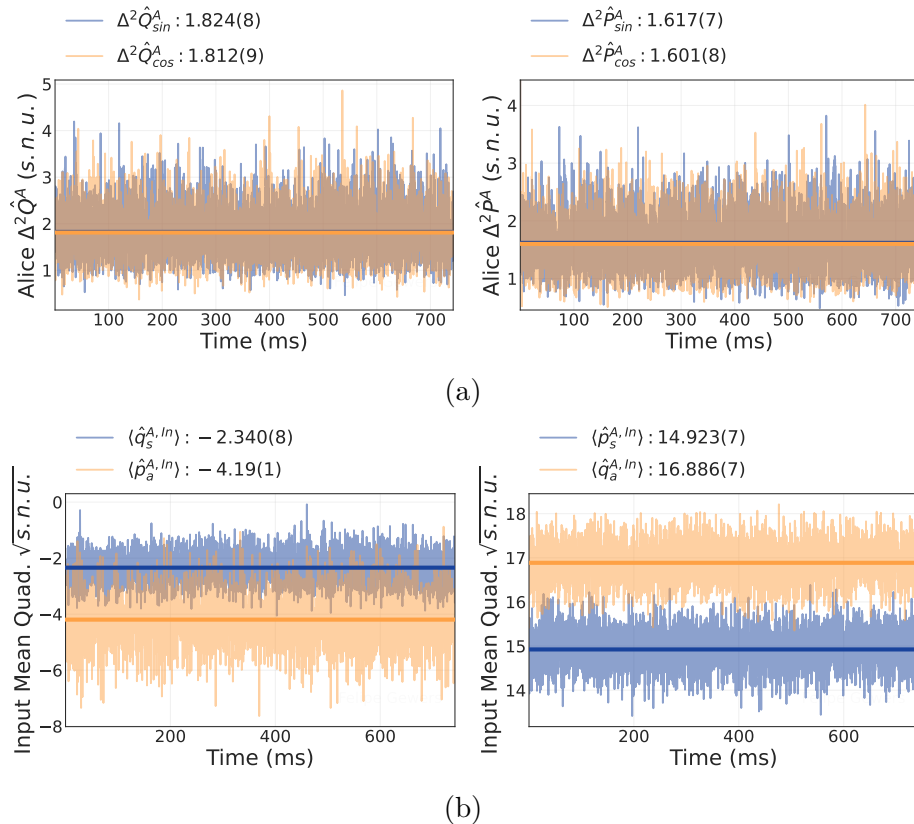


Figure 66 – Measured variances (a) and mean values (b) for a displaced coherent input state at Alice's station. The data shown are from the measurement with a gain closest to unity without correction for optical losses.

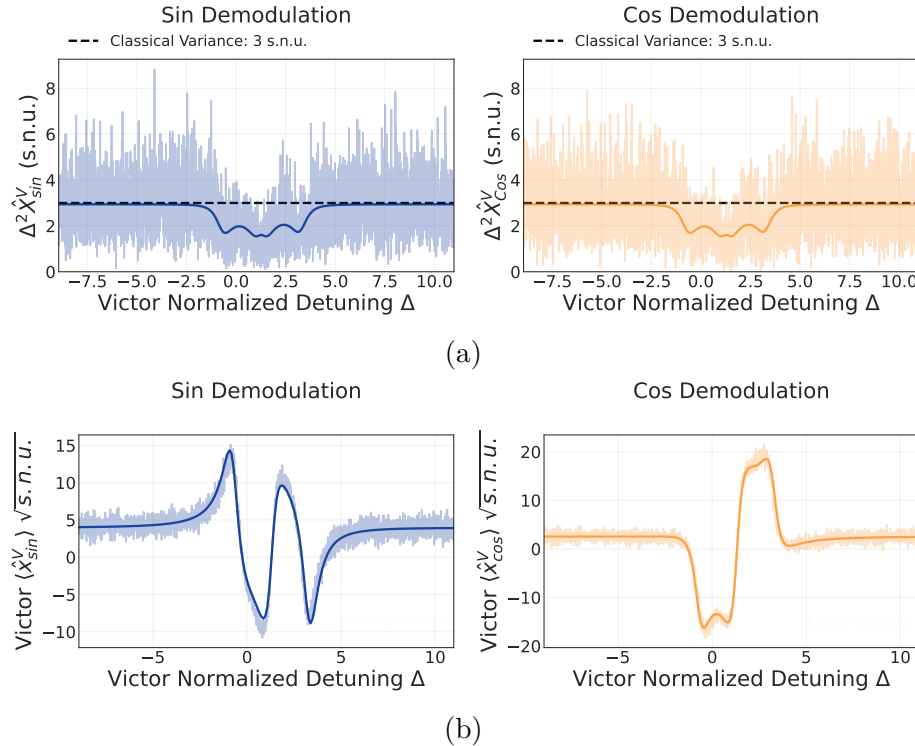


Figure 67 – Measured quadrature variances (a) and mean values (b) of the displaced teleported state during the tomography scan. The data are uncorrected for losses and correspond to the gain setting closest to unity.

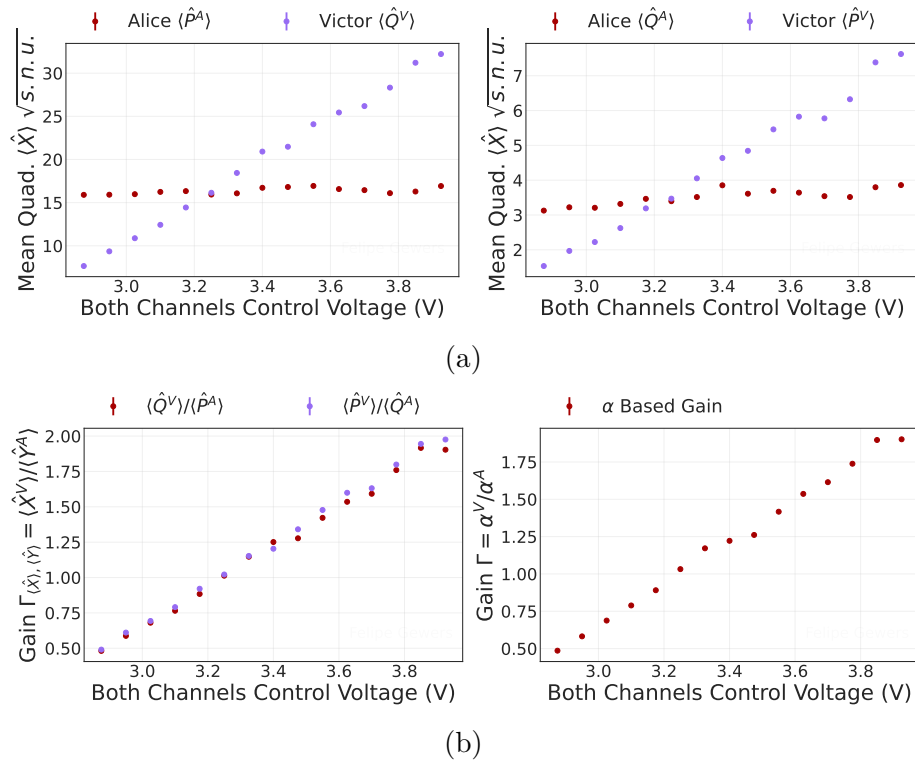


Figure 68 – Mean quadrature values (a) and the resulting teleportation gain (b) for a displaced coherent input state, plotted as a function of the control voltage for the amplitude and phase classical channels.

Table 22 presents the teleportation results for the uncorrected and Alice's corrected losses (AC) scenarios, while Figure 69 presents the fidelity as a function of the effective gain for these cases. The applied corrections were calculated using the values from Table 17. In the uncorrected scenario, the acquired fidelities for the displaced and vacuum input states are identical: $\mathcal{F}_{Disp} = \mathcal{F}_{Vac} = 57.1(8)\%$. This value is higher than in previous uncorrected runs and surpasses the classical limit by more than 8 standard deviations. The equality of the fidelities indicates that the teleportation gain was precisely tuned to the unitary condition. In contrast, for the scenario correcting Alice's losses, no measurement was performed with a gain close to unity. Consequently, the fidelity achieved in this case did not surpass the classical limit.

Table 22 – Teleportation parameters for the third presented experimental run, showing results for both the uncorrected and Alice's corrected losses (AC) cases. All values correspond to the measurement with gain closest to unity for each respective scenario.

Parameter	Uncorrected Losses	Alice's Corrected Losses (AC)
<i>Performance Metrics</i>		
Displaced Input Fidelity \mathcal{F}_{Disp}	57.1(8)%	49.1(5)%
Vacuum Input Fidelity \mathcal{F}_{Vac}	57.1(8)%	57.1(8)%
<i>Gain Parameters</i>		
Amplitude Channel Gain $\Gamma_{\hat{P}}$	1.013(1)	0.943(1)
Phase Channel Gain $\Gamma_{\hat{Q}}$	1.022(3)	0.933(3)
Effective Gain Γ	1.013(1)	0.943(1)
<i>Input State</i>		
Magnitude $ \alpha^{In} $	8.146(3) $\sqrt{s.n.u}$	8.753(4) $\sqrt{s.n.u}$
Mean Amplitude $\langle \hat{P}^{In} \rangle$	15.935(5) $\sqrt{s.n.u}$	17.108(7) $\sqrt{s.n.u}$
Mean Phase $\langle \hat{Q}^{In} \rangle$	3.40(1) $\sqrt{s.n.u}$	3.72(1) $\sqrt{s.n.u}$
<i>Output State</i>		
Magnitude $ \alpha^{Out} $	8.256(1) $\sqrt{s.n.u}$	8.256(1) $\sqrt{s.n.u}$
Mean Phase $\langle \hat{Q}^{Out} \rangle$	16.144(2) $\sqrt{s.n.u}$	16.144(2) $\sqrt{s.n.u}$
Mean Amplitude $\langle \hat{P}^{Out} \rangle$	3.469(1) $\sqrt{s.n.u}$	3.469(1) $\sqrt{s.n.u}$
Phase Variance $\Delta^2 \hat{Q}^{Out}$	2.06(8) $s.n.u$	2.06(8) $s.n.u$
Amplitude Variance $\Delta^2 \hat{P}^{Out}$	2.94(2) $s.n.u$	2.94(2) $s.n.u$
Covariance $C(\hat{Q}^{Out}, \hat{P}^{Out})$	0.03(7) $s.n.u$	0.03(7) $s.n.u$

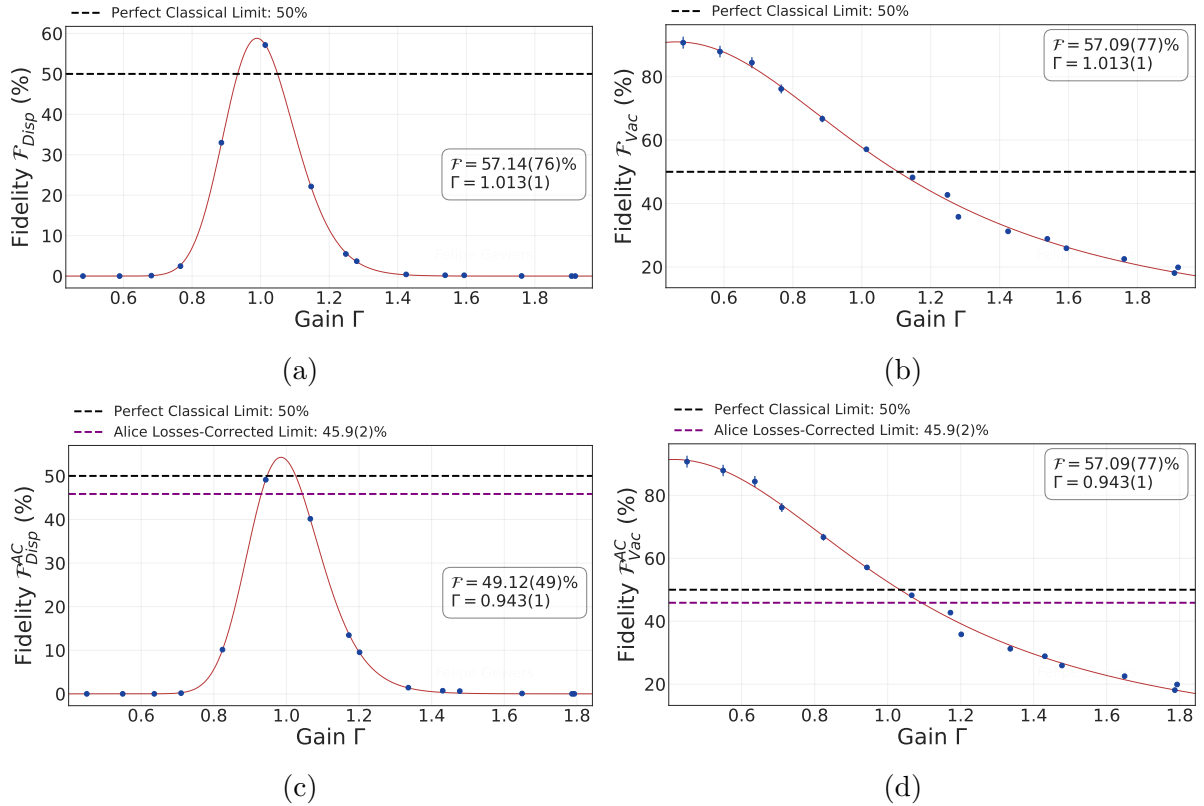


Figure 69 – Teleportation fidelity plotted as a function of the effective gain, Γ . The top panels show the raw data fidelity for displaced coherent (a) and vacuum (b) input states, while the bottom panels, (c) and (d), show the corresponding fidelities after applying corrections for detection losses at Alice’s station.

Table 23 presents the results for the scenarios correcting for Victor’s detection losses and for both Alice’s and Victor’s losses simultaneously, while Figure 70 shows the corresponding fidelity as a function of gain. When correcting for losses at Victor’s station, we obtain a fidelity of $\mathcal{F}_{Disp}^{VC} = 60(1)\%$ for the displaced input state and $\mathcal{F}_{Vac}^{VC} = 61(1)\%$ for the vacuum state. Both values violate the classical limit with high statistical significance, surpassing it by more than 9 standard deviations. In contrast, when correcting for losses at both stations, no measurement was performed with a properly adjusted teleportation gain close to unity. Consequently, the fidelity achieved in this case did not violate the classical limit.

The results from this and the preceding sections consistently demonstrate a quantum advantage across various experimental conditions and for different input states. We have confirmed that our system teleports quantum states with a fidelity that surpasses the classical limit, which is the best possible performance achievable without quantum resources. This work therefore marks a significant milestone: the first successful implementation of continuous-variable quantum teleportation using entanglement between different frequency bands.

Table 23 – Teleportation parameters for the third presented experimental run, showing results for the Victor’s corrected losses (VC) and for the fully corrected losses (AC,VC) cases. All values correspond to the measurement with gain closest to unity for each respective scenario.

Parameter	Victor’s Corrected Losses (VC)	Both Corrected Losses (AC,VC)
<i>Performance Metrics</i>		
Displaced Input Fidelity \mathcal{F}_{Disp}	60(1)%	42.0(5)%
Vacuum Input Fidelity \mathcal{F}_{Vac}	61(1)%	51.0(8)%
<i>Gain Parameters</i>		
Amplitude Channel Gain $\Gamma_{\hat{P}}$	1.000(1)	1.068(1)
Phase Channel Gain $\Gamma_{\hat{Q}}$	1.042(3)	1.056(3)
Effective Gain Γ	1.001(1)	1.068(1)
<i>Input State</i>		
Magnitude $ \alpha^{In} $	8.349(3) $\sqrt{s.n.u}$	8.753(4) $\sqrt{s.n.u}$
Mean Amplitude $\langle \hat{P}^{In} \rangle$	16.335(5) $\sqrt{s.n.u}$	17.108(7) $\sqrt{s.n.u}$
Mean Phase $\langle \hat{Q}^{In} \rangle$	3.46(1) $\sqrt{s.n.u}$	3.72(1) $\sqrt{s.n.u}$
<i>Output State</i>		
Magnitude $ \alpha^{Out} $	8.365(4) $\sqrt{s.n.u}$	9.341(5) $\sqrt{s.n.u}$
Mean Phase $\langle \hat{Q}^{Out} \rangle$	16.336(8) $\sqrt{s.n.u}$	18.265(9) $\sqrt{s.n.u}$
Mean Amplitude $\langle \hat{P}^{Out} \rangle$	3.609(2) $\sqrt{s.n.u}$	3.925(2) $\sqrt{s.n.u}$
Phase Variance $\Delta^2 \hat{Q}^{Out}$	2.91(3) $s.n.u$	2.4(1) $s.n.u$
Amplitude Variance $\Delta^2 \hat{P}^{Out}$	1.8(1) $s.n.u$	3.49(3) $s.n.u$
Covariance $C(\hat{Q}^{Out}, \hat{P}^{Out})$	0.04(9) $s.n.u$	0.04(9) $s.n.u$

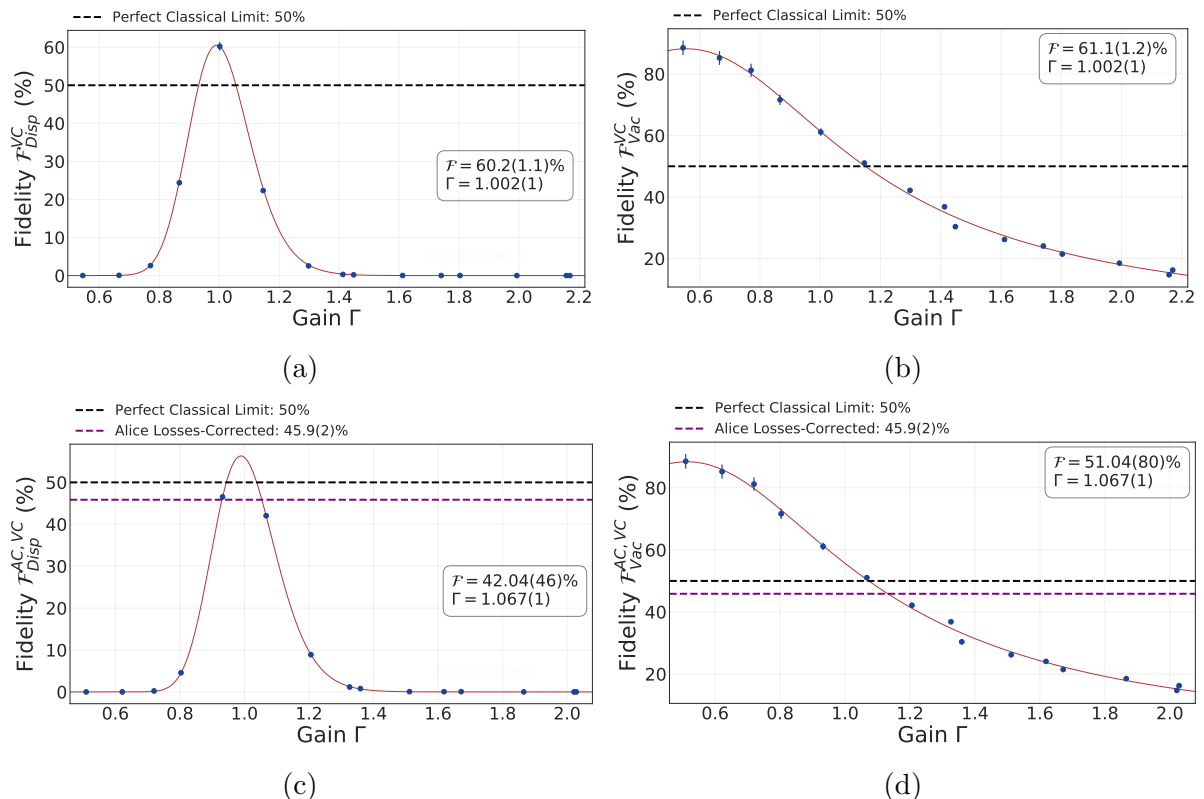


Figure 70 – Teleportation fidelity for displaced coherent, (a) and (c), and vacuum, (b) and (d), input states under two losses correction schemes. The top panels show fidelity when correcting for losses at Victor’s station only. The bottom panels show fidelity when correcting for losses at both Alice’s and Victor’s stations.

7 CONCLUSION AND PERSPECTIVES

This work marks an important advancement in the development of quantum communication technologies, particularly for hybrid quantum networks. We have successfully developed a triply resonant optical parametric oscillator (TROPO) operating above threshold, a unique source capable of generating intense, entangled optical fields at widely separated frequencies. The precise generation of a signal field in the near-infrared at 794.4(6) nm and an idler field in the telecommunications L-band at 1611(3) nm is not arbitrary: these wavelengths are strategically chosen for their compatibility with disparate yet promising quantum platforms. The signal wavelength aligns with the D1 line of rubidium atoms, a leading candidate for robust continuous-variable quantum memories [23, 24], while the idler wavelength's placement within the telecommunications band ensures efficient long-distance quantum communication and seamless integration with silicon nitride integrated photonics, a highly promising platform for scalable quantum optical information processing [28, 56]. Our laboratory actively researches both of these platforms, with established expertise on hot rubidium vapor cells and integrated silicon nitride microring resonators, which allows us to directly integrate this source into novel hybrid systems [25–27, 30].

An achievement of this work is the first detailed characterization of individual sideband modes of signal and idler fields generated by an above-threshold optical parametric oscillator (OPO) at such widely separated frequencies. To achieve this, we employed the auto-homodyne technique [66], a method well-established within our research group [94, 112, 172]. Our measurements demonstrated robust entanglement not only between the single sideband modes of the signal and idler fields but also, remarkably, across multiple bipartitions of their individual sideband modes. These findings provide new insights into the intricate phase and amplitude noise dynamics inherent to triply resonant optical parametric oscillators, particularly when maintaining resonance for all three fields despite their substantial frequency separation.

Leveraging this characterized source of two-mode entangled states, we performed the first unconditional continuous-variable quantum teleportation across distinct frequency bands. We successfully teleported a displaced coherent state from the near-infrared (794.4(6) nm) to the telecommunications band (1611(3) nm). This achievement is quantified by a fidelity of $\mathcal{F}_{Disp} = 57.1(8)\%$ for a teleportation gain of $\Gamma = 1.013(1)$, when not considering optical losses. Crucially, even after accounting for losses at Alice's station, we achieved a fidelity significantly above the classical limit at $\mathcal{F}_{Disp}^{AC} = 53.8(3)\%$ with a gain of $\Gamma^{AC} = 0.962(2)$. Both fidelity values decisively surpass the perfect classical limit of 50%, providing irrefutable evidence of quantum advantage in our implementation of the

teleportation protocol, a feat fundamentally impossible without the utilization of quantum resources [119, 121]. This result also represents the first instance of quantum teleportation employing an above-threshold OPO to violate the classical limit, marking a profound step towards the realization of large-scale hybrid quantum networks capable of interfacing specialized quantum platforms operating at disparate wavelengths.

Beyond the demonstration, this experiment and the prior work from our group [59, 60] are the only teleportation implementations to utilize the auto-homodyne technique for quantum state tomography. This distinctive approach opens an exciting avenue for future research: the possibility of teleporting individual sidebands containing different quantum states, a scheme that could effectively double the transferable modal capacity of the quantum channel. Future investigations will rigorously explore this enhanced capability. Furthermore, a highly promising direction involves the teleportation of more complex quantum states, such as states exhibiting a negative Wigner function, across these disparate frequency bands. Achieving this will require meticulous modifications to the input state preparation system and a significant enhancement of the protocol's fidelity by minimizing optical losses, both throughout the setup and, critically, within the TROPO cavity itself.

In the context of the quantum internet, our demonstration of a cross-band teleportation-based quantum channel, compatible with both rubidium's D1 line and telecommunication bands, is specifically relevant for continuous-variable quantum repeaters based on alkaline atom quantum memories [8, 9]. Such repeaters are essential for overcoming the inherent decoherence and loss encountered in long-distance quantum communication, leveraging quantum memories, entanglement distillation, and teleportation [17, 19, 20]. To further advance these quantum network applications, the immediate next step involves precisely stabilizing the frequency of the signal field to the rubidium D1-line, enabling robust and precise coupling with the atomic physical system. A compelling future demonstration would be the teleportation of a quantum state, initially stored within a Rubidium cloud, to the telecommunication wavelength. Another intriguing avenue involves utilizing entangled states generated from four-wave mixing (FWM) in atomic ensembles and performing entanglement swapping with the entangled states generated by our OPO.

BIBLIOGRAPHY

- [1] Jonathan P. Dowling and Gerard J. Milburn. [Quantum Technology: The Second Quantum Revolution](#). In: *Philosophical Transactions of the Royal Society of London. Series A: Mathematical, Physical and Engineering Sciences* 361.1809 (Aug. 2003). Ed. by A. G. J. MacFarlane, pp. 1655–1674. ISSN: 1364-503X, 1471-2962 (cit. on p. 27).
- [2] Lars Jaeger. [The Second Quantum Revolution: From Entanglement to Quantum Computing and Other Super-Technologies](#). Cham: Springer International Publishing, 2018. ISBN: 978-3-319-98823-8 (cit. on p. 27).
- [3] Ivan H. Deutsch. [Harnessing the Power of the Second Quantum Revolution](#). In: *PRX Quantum* 1.2 (Nov. 2020), p. 020101. ISSN: 2691-3399 (cit. on p. 27).
- [4] Peter W. Shor. [Polynomial-Time Algorithms for Prime Factorization and Discrete Logarithms on a Quantum Computer](#). In: *SIAM Review* 41.2 (Jan. 1999), pp. 303–332. ISSN: 0036-1445, 1095-7200 (cit. on p. 27).
- [5] Dorit Aharonov. [Quantum Computation](#). In: *Annual Reviews of Computational Physics VI*. Vol. Volume 6. Annual Reviews of Computational Physics. WORLD SCIENTIFIC, Mar. 1999, pp. 259–346. ISBN: 978-981-02-3563-5 (cit. on p. 27).
- [6] Michael A. Nielsen and Isaac L. Chuang. [Quantum Computation and Quantum Information](#). 10th anniversary edition. Cambridge: Cambridge university press, 2010. ISBN: 978-1-107-00217-3 (cit. on pp. 27, 44).
- [7] Miralem Mehic et al. [Quantum Key Distribution: A Networking Perspective](#). In: *ACM Computing Surveys* 53.5 (Sept. 2021), pp. 1–41. ISSN: 0360-0300, 1557-7341 (cit. on p. 27).
- [8] H. J. Kimble. [The Quantum Internet](#). In: *Nature* 453.7198 (June 2008), pp. 1023–1030. ISSN: 0028-0836, 1476-4687 (cit. on pp. 27, 28, 250).
- [9] Stephanie Wehner, David Elkouss, and Ronald Hanson. [Quantum Internet: A Vision for the Road Ahead](#). In: *Science* 362.6412 (Oct. 2018), eaam9288. ISSN: 0036-8075, 1095-9203 (cit. on pp. 27, 28, 250).
- [10] Vittorio Giovannetti, Seth Lloyd, and Lorenzo Maccone. [Advances in Quantum Metrology](#). In: *Nature Photonics* 5.4 (Apr. 2011), pp. 222–229. ISSN: 1749-4885, 1749-4893 (cit. on p. 27).
- [11] Hugo Defienne et al. [Advances in Quantum Imaging](#). In: *Nature Photonics* 18.10 (Oct. 2024), pp. 1024–1036. ISSN: 1749-4885, 1749-4893 (cit. on p. 27).

- [12] Jonathan Roslund et al. **Wavelength-Multiplexed Quantum Networks with Ultrafast Frequency Combs**. In: *Nature Photonics* 8.2 (Feb. 2014), pp. 109–112. ISSN: 1749-4885, 1749-4893 (cit. on p. 28).
- [13] Peter J. Winzer, David T. Neilson, and Andrew R. Chraplyvy. **Fiber-Optic Transmission and Networking: The Previous 20 and the next 20 Years [Invited]**. In: *Optics Express* 26.18 (Sept. 2018), p. 24190. ISSN: 1094-4087 (cit. on pp. 28, 139).
- [14] Angela Sara Cacciapuoti et al. **Quantum Internet: Networking Challenges in Distributed Quantum Computing**. In: *IEEE Network* 34.1 (Jan. 2020), pp. 137–143. ISSN: 0890-8044, 1558-156X (cit. on p. 28).
- [15] H.-J. Briegel et al. **Quantum Repeaters: The Role of Imperfect Local Operations in Quantum Communication**. In: *Physical Review Letters* 81.26 (Dec. 1998), pp. 5932–5935. ISSN: 0031-9007, 1079-7114 (cit. on p. 28).
- [16] Fabian Furrer and William J. Munro. **Repeaters for Continuous-Variable Quantum Communication**. In: *Physical Review A* 98.3 (Sept. 2018), p. 032335. ISSN: 2469-9926, 2469-9934 (cit. on p. 28).
- [17] Kaushik P. Seshadreesan, Hari Krovi, and Saikat Guha. **Continuous-Variable Quantum Repeater Based on Quantum Scissors and Mode Multiplexing**. In: *Physical Review Research* 2.1 (Mar. 2020), p. 013310. ISSN: 2643-1564 (cit. on pp. 28, 30, 250).
- [18] Koji Azuma et al. **Quantum Repeaters: From Quantum Networks to the Quantum Internet**. In: *Reviews of Modern Physics* 95.4 (Dec. 2023). ISSN: 0034-6861, 1539-0756 (cit. on p. 28).
- [19] Josephine Dias and T. C. Ralph. **Quantum Repeaters Using Continuous-Variable Teleportation**. In: *Physical Review A* 95.2 (Feb. 2017), p. 022312. ISSN: 2469-9926, 2469-9934 (cit. on pp. 28, 250).
- [20] Josephine Dias et al. **Quantum Repeater for Continuous-Variable Entanglement Distribution**. In: *Physical Review A* 102.5 (Nov. 2020), p. 052425. ISSN: 2469-9926, 2469-9934 (cit. on pp. 28, 250).
- [21] S. Tanzilli et al. **A Photonic Quantum Information Interface**. In: *Nature* 437.7055 (Sept. 2005), pp. 116–120. ISSN: 0028-0836, 1476-4687 (cit. on p. 29).
- [22] V. Krutyanskiy et al. **Telecom-Wavelength Quantum Repeater Node Based on a Trapped-Ion Processor**. In: *Physical Review Letters* 130.21 (May 2023). ISSN: 0031-9007, 1079-7114 (cit. on p. 29).
- [23] M. Hosseini et al. **High Efficiency Coherent Optical Memory with Warm Rubidium Vapour**. In: *Nature Communications* 2.1 (Feb. 2011), p. 174. ISSN: 2041-1723 (cit. on pp. 29, 249).

- [24] Mark Bashkansky, Fredrik K. Fatemi, and Igor Vurgaftman. [Quantum Memory in Warm Rubidium Vapor with Buffer Gas](#). In: *Optics Letters* 37.2 (Jan. 2012), pp. 142–144. ISSN: 1539-4794 (cit. on pp. 29, 249).
- [25] A. Montaña Guerrero et al. [Quantum Noise Correlations of an Optical Parametric Oscillator Based on a Nondegenerate Four Wave Mixing Process in Hot Alkali Atoms](#). In: *Physical Review Letters* 125.8 (Aug. 2020), p. 083601. ISSN: 0031-9007, 1079-7114 (cit. on pp. 29, 140, 249).
- [26] A. Montaña Guerrero et al. [Continuous Variable Entanglement in an Optical Parametric Oscillator Based on a Nondegenerate Four Wave Mixing Process in Hot Alkali Atoms](#). In: *Physical Review Letters* 129.16 (Oct. 2022), p. 163601. ISSN: 0031-9007, 1079-7114 (cit. on pp. 29, 140, 249).
- [27] R. L. Rincón Celis et al. [Hidden Entanglement in Twin Beams Generated through Optical Parametric Amplification in Hot Alkali Atoms](#). Jan. 2025. arXiv: 2501.06136 [quant-ph] (cit. on pp. 29, 249).
- [28] Daniel J. Blumenthal et al. [Silicon Nitride in Silicon Photonics](#). In: *Proceedings of the IEEE* 106.12 (Dec. 2018), pp. 2209–2231. ISSN: 0018-9219, 1558-2256 (cit. on pp. 29, 249).
- [29] Wei Luo et al. [Recent Progress in Quantum Photonic Chips for Quantum Communication and Internet](#). In: *Light: Science & Applications* 12.1 (July 2023), p. 175. ISSN: 2047-7538 (cit. on p. 29).
- [30] Roger Alfredo Kögler et al. [Quantum State Tomography in a Third-Order Integrated Optical Parametric Oscillator](#). In: *Optics Letters* 49.11 (June 2024), p. 3150. ISSN: 0146-9592, 1539-4794 (cit. on pp. 29, 140, 249).
- [31] Xiao-Min Hu et al. [Progress in Quantum Teleportation](#). In: *Nature Reviews Physics* 5.6 (May 2023), pp. 339–353. ISSN: 2522-5820 (cit. on p. 29).
- [32] S. Pirandola et al. [Advances in Quantum Teleportation](#). In: *Nature Photonics* 9.10 (Oct. 2015), pp. 641–652. ISSN: 1749-4885, 1749-4893 (cit. on pp. 29, 30, 103).
- [33] Robert Raussendorf and Hans J. Briegel. [A One-Way Quantum Computer](#). In: *Physical Review Letters* 86.22 (May 2001), pp. 5188–5191. ISSN: 0031-9007, 1079-7114 (cit. on p. 29).
- [34] C. Ryan-Anderson et al. [High-Fidelity Teleportation of a Logical Qubit Using Transversal Gates and Lattice Surgery](#). In: *Science* 385.6715 (Sept. 2024), pp. 1327–1331. ISSN: 0036-8075, 1095-9203 (cit. on p. 29).
- [35] J. Borregaard et al. [Super Sensitivity and Super Resolution with Quantum Teleportation](#). In: *npj Quantum Information* 5.1 (Feb. 2019), p. 16. ISSN: 2056-6387 (cit. on p. 29).

- [36] I. Marcikic et al. [Long-Distance Teleportation of Qubits at Telecommunication Wavelengths](#). In: *Nature* 421.6922 (Jan. 2003), pp. 509–513. ISSN: 0028-0836, 1476-4687 (cit. on pp. 29, 30).
- [37] T. Opatrný, G. Kurizki, and D.-G. Welsch. [Improvement on Teleportation of Continuous Variables by Photon Subtraction via Conditional Measurement](#). In: *Physical Review A* 61.3 (Feb. 2000). ISSN: 1050-2947, 1094-1622 (cit. on p. 30).
- [38] P. T. Cochrane, T. C. Ralph, and G. J. Milburn. [Teleportation Improvement by Conditional Measurements on the Two-Mode Squeezed Vacuum](#). In: *Physical Review A* 65.6 (May 2002). ISSN: 1050-2947, 1094-1622 (cit. on p. 30).
- [39] Daniel Gottesman, Alexei Kitaev, and John Preskill. [Encoding a Qubit in an Oscillator](#). In: *Physical Review A* 64.1 (June 2001). ISSN: 1050-2947, 1094-1622 (cit. on p. 30).
- [40] Mikkel V. Larsen et al. [Fault-Tolerant Continuous-Variable Measurement-based Quantum Computation Architecture](#). In: *PRX Quantum* 2.3 (Aug. 2021). ISSN: 2691-3399 (cit. on p. 30).
- [41] Warit Asavanant and Akira Furusawa. [Optical Quantum Computers: A Route to Practical Continuous Variable Quantum Information Processing](#). AIP Publishing LLC Melville, New York, Jan. 2022. ISBN: 978-0-7354-2404-3 (cit. on p. 30).
- [42] Warit Asavanant et al. [Switching-Free Time-Domain Optical Quantum Computation with Quantum Teleportation](#). In: *Physical Review A* 107.3 (Mar. 2023). ISSN: 2469-9926, 2469-9934 (cit. on p. 30).
- [43] Charles H. Bennett et al. [Teleporting an Unknown Quantum State via Dual Classical and Einstein-Podolsky-Rosen Channels](#). In: *Physical Review Letters* 70.13 (Mar. 1993), pp. 1895–1899. ISSN: 0031-9007 (cit. on pp. 30, 101).
- [44] Dik Bouwmeester et al. [Experimental Quantum Teleportation](#). In: *Nature* 390.6660 (Dec. 1997), pp. 575–579. ISSN: 1476-4687 (cit. on p. 30).
- [45] Samuel L. Braunstein and H. J. Kimble. [Teleportation of Continuous Quantum Variables](#). In: *Physical Review Letters* 80.4 (Jan. 1998), pp. 869–872. ISSN: 0031-9007, 1079-7114 (cit. on pp. 30, 103, 112).
- [46] A. Furusawa et al. [Unconditional Quantum Teleportation](#). In: *Science* 282.5389 (Oct. 1998), pp. 706–709. ISSN: 0036-8075, 1095-9203 (cit. on pp. 30, 103, 114).
- [47] T. C. Zhang et al. [Quantum Teleportation of Light Beams](#). In: *Physical Review A* 67.3 (Mar. 2003), p. 033802. ISSN: 1050-2947, 1094-1622 (cit. on pp. 30, 116, 122).
- [48] Warwick P. Bowen et al. [Experimental Investigation of Continuous-Variable Quantum Teleportation](#). In: *Physical Review A* 67.3 (Mar. 2003), p. 032302. ISSN: 1050-2947, 1094-1622 (cit. on pp. 30, 112).

- [49] Mitsuyoshi Yukawa, Hugo Benichi, and Akira Furusawa. [High-Fidelity Continuous-Variable Quantum Teleportation toward Multistep Quantum Operations](#). In: *Physical Review A* 77.2 (Feb. 2008), p. 022314. ISSN: 1050-2947, 1094-1622 (cit. on p. 30).
- [50] Hidehiro Yonezawa, Takao Aoki, and Akira Furusawa. [Demonstration of a Quantum Teleportation Network for Continuous Variables](#). In: *Nature* 431.7007 (Sept. 2004), pp. 430–433. ISSN: 0028-0836, 1476-4687 (cit. on pp. 30, 119, 177).
- [51] Nobuyuki Takei et al. [High-Fidelity Teleportation beyond the No-Cloning Limit and Entanglement Swapping for Continuous Variables](#). In: *Physical Review Letters* 94.22 (June 2005), p. 220502. ISSN: 0031-9007, 1079-7114 (cit. on p. 30).
- [52] Shuntaro Takeda et al. [Entanglement Swapping between Discrete and Continuous Variables](#). In: *Physical Review Letters* 114.10 (Mar. 2015). ISSN: 0031-9007, 1079-7114 (cit. on p. 30).
- [53] Nobuyuki Takei et al. [Experimental Demonstration of Quantum Teleportation of a Squeezed State](#). In: *Physical Review A* 72.4 (Oct. 2005), p. 042304. ISSN: 1050-2947, 1094-1622 (cit. on p. 30).
- [54] Hidehiro Yonezawa, Samuel L. Braunstein, and Akira Furusawa. [Experimental Demonstration of Quantum Teleportation of Broadband Squeezing](#). In: *Physical Review Letters* 99.11 (Sept. 2007), p. 110503. ISSN: 0031-9007, 1079-7114 (cit. on p. 30).
- [55] Noriyuki Lee et al. [Teleportation of Nonclassical Wave Packets of Light](#). In: *Science* 332.6027 (Apr. 2011), pp. 330–333. ISSN: 0036-8075, 1095-9203 (cit. on p. 30).
- [56] Shengshuai Liu, Yanbo Lou, and Jietai Jing. [Orbital Angular Momentum Multiplexed Deterministic All-Optical Quantum Teleportation](#). In: *Nature Communications* 11.1 (Aug. 2020), p. 3875. ISSN: 2041-1723 (cit. on pp. 30, 249).
- [57] Hao Zhao et al. [Real Time Deterministic Quantum Teleportation over 10 Km of Single Optical Fiber Channel](#). In: *Optics Express* 30.3 (Jan. 2022), p. 3770. ISSN: 1094-4087 (cit. on p. 30).
- [58] Meiru Huo et al. [Deterministic Quantum Teleportation through Fiber Channels](#). In: *Science Advances* 4.10 (Oct. 2018), eaas9401. ISSN: 2375-2548 (cit. on p. 30).
- [59] Igor Konieczniak. [Teletransporte de informação quântica entre campos de cores distintas](#). PhD thesis. São Paulo: Universidade de São Paulo, Mar. 2019 (cit. on pp. 30, 103, 137, 151, 191, 211, 250).
- [60] Lucas Nunes Faria. [Análise bimodal de teletransporte de estados quânticos da luz no domínio da frequência](#). MA thesis. São Paulo: Universidade de São Paulo, Dec. 2020 (cit. on pp. 30, 103, 151, 211, 250).

- [61] Hiroki Takesue et al. [Quantum Teleportation over 100 Km of Fiber Using Highly Efficient Superconducting Nanowire Single-Photon Detectors](#). In: *Optica* 2.10 (Oct. 2015), p. 832. ISSN: 2334-2536 (cit. on p. 30).
- [62] Raju Valivarthi et al. [Quantum Teleportation across a Metropolitan Fibre Network](#). In: *Nature Photonics* 10.10 (Oct. 2016), pp. 676–680. ISSN: 1749-4885, 1749-4893 (cit. on p. 30).
- [63] Florian Kaiser et al. [Towards Continuous-Wave Regime Teleportation for Light Matter Quantum Relay Stations](#). In: *IEEE Journal of Selected Topics in Quantum Electronics* 21.3 (May 2015), pp. 69–77. ISSN: 1077-260X, 1558-4542. eprint: [1412.7648](#) (quant-ph) (cit. on p. 30).
- [64] Dario Lago-Rivera et al. [Long Distance Multiplexed Quantum Teleportation from a Telecom Photon to a Solid-State Qubit](#). In: *Nature Communications* 14.1 (Apr. 2023), p. 1889. ISSN: 2041-1723 (cit. on p. 31).
- [65] Mariagrazia Iuliano et al. [Qubit Teleportation between a Memory-Compatible Photonic Time-Bin Qubit and a Solid-State Quantum Network Node](#). In: *npj Quantum Information* 10.1 (Nov. 2024), p. 107. ISSN: 2056-6387 (cit. on p. 31).
- [66] F. A. S. Barbosa et al. [Assumption-Free Measurement of the Quantum State of Light: Exploring the Sidebands of Intense Fields](#). In: *Physical Review A* 102.6 (Dec. 2020), p. 063705. ISSN: 2469-9926, 2469-9934 (cit. on pp. 31, 86, 94, 95, 97, 217, 249).
- [67] Jonatan Bohr Brask. [Gaussian States and Operations – a Quick Reference](#). Mar. 2022. arXiv: [2102.05748](#) [quant-ph] (cit. on p. 35).
- [68] Alessio Serafini. [Quantum Continuous Variables: A Primer of Theoretical Methods](#). Boca Raton: CRC Press, Taylor & Francis Group, CRC Press is an imprint of the Taylor & Francis Group, an informa business, 2017. ISBN: 978-1-4822-4634-6 (cit. on pp. 35, 57, 283).
- [69] A. Ferraro, S. Olivares, and Matteo G. A. Paris. [Gaussian States in Quantum Information](#). Napoli Series on Physics and Astrophysics. Bibliopolis, 2005. ISBN: 978-88-7088-483-8 (cit. on pp. 35, 126, 130).
- [70] Gilbert Grynberg, Alain Aspect, and Claude Fabre. [Introduction to Quantum Optics: From the Semi-classical Approach to Quantized Light](#). Cambridge University Press, Sept. 2010. ISBN: 978-1-139-49084-9 (cit. on pp. 35, 37, 41, 47, 271, 272).
- [71] Marlan O. Scully and M. Suhail Zubairy. [Quantum Optics](#). Cambridge: Cambridge University Press, 1997. ISBN: 978-0-521-43595-6 (cit. on pp. 36, 39, 41, 53, 206, 271).
- [72] Christian Weedbrook et al. [Gaussian Quantum Information](#). In: *Reviews of Modern Physics* 84.2 (May 2012), pp. 621–669 (cit. on pp. 37, 38, 40, 44, 157).

- [73] Marco G. Genoni et al. **Detecting Quantum Non-Gaussianity via the Wigner Function**. In: *Physical Review A* 87.6 (June 2013), p. 062104. ISSN: 1050-2947, 1094-1622 (cit. on p. 38).
- [74] H. P. Robertson. **An Indeterminacy Relation for Several Observables and Its Classical Interpretation**. In: *Physical Review* 46.9 (Nov. 1934), pp. 794–801. ISSN: 0031-899X (cit. on p. 38).
- [75] Gerardo Adesso, Sammy Ragy, and Antony R. Lee. **Continuous Variable Quantum Information: Gaussian States and Beyond**. In: *Open Systems & Information Dynamics* 21.01n02 (June 2014), p. 1440001. ISSN: 1230-1612, 1793-7191 (cit. on p. 38).
- [76] Leonard Mandel and Emil Wolf. **Optical Coherence and Quantum Optics**. Cambridge: Cambridge University Press, 1995. ISBN: 978-0-521-41711-2 (cit. on pp. 41, 64, 271).
- [77] A. Einstein, B. Podolsky, and N. Rosen. **Can Quantum-Mechanical Description of Physical Reality Be Considered Complete?** In: *Physical Review* 47.10 (May 1935), pp. 777–780. ISSN: 0031-899X (cit. on pp. 42, 106).
- [78] Akira Furusawa and Nobuyuki Takei. **Quantum Teleportation for Continuous Variables and Related Quantum Information Processing**. In: *Physics Reports* 443.3 (May 2007), pp. 97–119. ISSN: 0370-1573 (cit. on pp. 43, 105).
- [79] Daniel F. Walls and Gerard J. Milburn. **Quantum Optics**. 2nd ed. 2008. Springer eBook Collection. Berlin, Heidelberg: Springer Berlin Heidelberg, 2008. ISBN: 978-3-540-28573-1 (cit. on pp. 44, 49, 51).
- [80] R. F. Werner and M. M. Wolf. **Bound Entangled Gaussian States**. In: *Physical Review Letters* 86.16 (Apr. 2001), pp. 3658–3661. ISSN: 0031-9007, 1079-7114 (cit. on pp. 45, 47).
- [81] Lu-Ming Duan et al. **Inseparability Criterion for Continuous Variable Systems**. In: *Physical Review Letters* 84.12 (Mar. 2000), pp. 2722–2725 (cit. on pp. 45, 106, 206).
- [82] Asher Peres. **Separability Criterion for Density Matrices**. In: *Physical Review Letters* 77.8 (Aug. 1996), pp. 1413–1415. ISSN: 0031-9007, 1079-7114 (cit. on p. 46).
- [83] R. Simon. **Peres-Horodecki Separability Criterion for Continuous Variable Systems**. In: *Physical Review Letters* 84.12 (Mar. 2000), pp. 2726–2729. ISSN: 0031-9007, 1079-7114 (cit. on pp. 46, 207).
- [84] Bárbara Abigail Ferreira Ribeiro et al. **Exploring Entanglement in Open Cavity Parametric Oscillators: From Triply to Doubly Resonant Cavities**. In: *Physical Review A* 102.2 (Aug. 2020), p. 023522. ISSN: 2469-9926, 2469-9934 (cit. on pp. 47, 201).

- [85] M. D. Reid and P. D. Drummond. [Quantum Correlations of Phase in Nondegenerate Parametric Oscillation](#). In: *Physical Review Letters* 60.26 (June 1988), pp. 2731–2733 (cit. on p. 48).
- [86] M. D. Reid and P. D. Drummond. [Correlations in Nondegenerate Parametric Oscillation: Squeezing in the Presence of Phase Diffusion](#). In: *Physical Review A* 40.8 (Oct. 1989), pp. 4493–4506. ISSN: 0556-2791 (cit. on p. 48).
- [87] M. Martinelli et al. [Classical and Quantum Properties of Optical Parametric Oscillators](#). In: *Brazilian Journal of Physics* 31.4 (Dec. 2001), pp. 597–615. ISSN: 0103-9733 (cit. on pp. 48, 50, 53, 104, 143, 190, 201).
- [88] Marcelo Martinelli. [Compressão de ruído quântico e efeitos transversos em osciladores paramétricos óticos](#). PhD thesis. São Paulo: Universidade de São Paulo, Feb. 2002 (cit. on pp. 48, 146).
- [89] M. Martinelli et al. [Experimental Study of the Spatial Distribution of Quantum Correlations in a Confocal Optical Parametric Oscillator](#). In: *Physical Review A* 67.2 (Feb. 2003), p. 023808. ISSN: 1050-2947, 1094-1622 (cit. on p. 48).
- [90] A. S. Villar et al. [Generation of Bright Two-Color Continuous Variable Entanglement](#). In: *Physical Review Letters* 95.24 (Dec. 2005), p. 243603. ISSN: 0031-9007, 1079-7114 (cit. on pp. 48, 143).
- [91] A. S. Villar et al. [Direct Production of Tripartite Pump-Signal-Idler Entanglement in the Above-Threshold Optical Parametric Oscillator](#). In: *Physical Review Letters* 97.14 (Oct. 2006), p. 140504. ISSN: 0031-9007, 1079-7114 (cit. on pp. 48, 104).
- [92] Alessandro S. Villar et al. [Entanglement in the Above-Threshold Optical Parametric Oscillator](#). In: *Journal of the Optical Society of America B* 24.2 (Feb. 2007), p. 249. ISSN: 0740-3224, 1520-8540 (cit. on pp. 48, 139, 148, 156).
- [93] A. S. Coelho et al. [Three-Color Entanglement](#). In: *Science* 326.5954 (Nov. 2009), pp. 823–826. ISSN: 0036-8075, 1095-9203 (cit. on p. 48).
- [94] F. A. S. Barbosa et al. [Hexapartite Entanglement in an Above-Threshold Optical Parametric Oscillator](#). In: *Physical Review Letters* 121.7 (Aug. 2018), p. 073601. ISSN: 0031-9007, 1079-7114 (cit. on pp. 48, 191, 249).
- [95] Rayssa Bruzaca De Andrade. [An Optical Parametric Oscillator for a Light-Atomic Media Interface](#). PhD thesis. São Paulo: Universidade de São Paulo, June 2018 (cit. on pp. 48, 53, 55, 151).
- [96] R. Graham and H. Haken. [The Quantum-Fluctuations of the Optical Parametric Oscillator. I.](#) In: *Zeitschrift für Physik A Hadrons and nuclei* 210.3 (June 1968), pp. 276–302. ISSN: 0939-7922 (cit. on p. 48).

- [97] R. Graham. [The Quantum-Fluctuations of the Optical Parametric Oscillator. II.](#) In: *Zeitschrift für Physik A Hadrons and nuclei* 210.4 (Aug. 1968), pp. 319–336. ISSN: 0939-7922 (cit. on p. 48).
- [98] Howard Carmichael. [An Open Systems Approach to Quantum Optics Lectures Presented at the Université Libre de Bruxelles, October 28 to November 4, 1991.](#) Aufl. 1993. Berlin: Springer Berlin, 2014. ISBN: 978-3-662-13926-4 (cit. on p. 49).
- [99] C. Fabre et al. [Noise Characteristics of a Non-Degenerate Optical Parametric Oscillator - Application to Quantum Noise Reduction.](#) In: *Journal de Physique* 50.10 (1989), pp. 1209–1225. ISSN: 0302-0738 (cit. on pp. 50, 51, 106).
- [100] Hans-A. Bachor and Timothy C. Ralph. [A Guide to Experiments in Quantum Optics.](#) John Wiley & Sons, Oct. 2019. ISBN: 978-3-527-41193-1 (cit. on pp. 53, 58, 76, 77, 116, 170, 186, 226, 229).
- [101] Paolo Tombesi and Daniel F. Walls. [Quantum Measurements in Optics.](#) NATO ASI Series, Series B: Physics 282. New York: Springer Science, 1992. ISBN: 978-1-4615-3386-3 (cit. on p. 53).
- [102] Samuel L. Braunstein and Peter Van Loock. [Quantum Information with Continuous Variables.](#) In: *Reviews of Modern Physics* 77.2 (June 2005), pp. 513–577. ISSN: 0034-6861, 1539-0756 (cit. on p. 53).
- [103] Alessandro S. Villar. [The Conversion of Phase to Amplitude Fluctuations of a Light Beam by an Optical Cavity.](#) In: *American Journal of Physics* 76.10 (Oct. 2008), pp. 922–929. ISSN: 0002-9505, 1943-2909 (cit. on pp. 53, 77, 83, 109, 162).
- [104] Bonny L. Schumaker. [Noise in Homodyne Detection.](#) In: *Optics Letters* 9.5 (May 1984), p. 189. ISSN: 0146-9592, 1539-4794 (cit. on p. 54).
- [105] Horace P. Yuen and Vincent W. S. Chan. [Noise in Homodyne and Heterodyne Detection.](#) In: *Optics Letters* 8.3 (Mar. 1983), p. 177. ISSN: 0146-9592, 1539-4794 (cit. on p. 54).
- [106] Bahaa E. A. Saleh and Malvin Carl Teich, eds. [Fundamentals of Photonics.](#) Wiley Series in Pure and Applied Optics. Hoboken, NJ: Wiley-Interscience, 2001. ISBN: 978-0-471-21374-1 (cit. on pp. 55, 64).
- [107] F. A. S. Barbosa et al. [Quantum State Reconstruction of Spectral Field Modes: Homodyne and Resonator Detection Schemes.](#) In: *Physical Review A* 88.5 (Nov. 2013), p. 052113. ISSN: 1050-2947, 1094-1622 (cit. on pp. 55, 63, 72, 76, 111, 113, 160, 162, 194, 204).
- [108] Roy J. Glauber. [The Quantum Theory of Optical Coherence.](#) In: *Physical Review* 130.6 (June 1963), pp. 2529–2539. ISSN: 0031-899X (cit. on p. 55).

- [109] Christopher C. Gerry and Peter Knight. *Introductory Quantum Optics*. Second edition. Cambridge, United Kingdom New York, NY: Cambridge University Press, 2024. ISBN: 978-1-139-15120-7 (cit. on p. 59).
- [110] Paul Horowitz. *The Art of Electronics*. Third edition. New York, NY: Cambridge University Press, 2015. ISBN: 978-0-521-80926-9 (cit. on p. 63).
- [111] A. S. Coelho et al. [Analyzing the Gaussian Character of the Spectral Quantum State of Light via Quantum Noise Measurements](#). In: *Physical Review A* 92.1 (July 2015), p. 012110. ISSN: 1050-2947, 1094-1622 (cit. on pp. 67, 68, 194, 196, 281).
- [112] F. A. S. Barbosa et al. [Beyond Spectral Homodyne Detection: Complete Quantum Measurement of Spectral Modes of Light](#). In: *Physical Review Letters* 111.20 (Nov. 2013), p. 200402. ISSN: 0031-9007, 1079-7114 (cit. on pp. 70, 77, 149, 160, 249).
- [113] Marcelo Martinelli. [From Spectral Matrix to Sideband Structure: Exploring Stereo Multimodes](#). In: *Journal of the Optical Society of America B* 40.5 (May 2023), p. 1277. ISSN: 0740-3224, 1520-8540 (cit. on p. 72).
- [114] P. Galatola et al. [System Control by Variation of the Squeezing Phase](#). In: *Optics Communications* 85.1 (Aug. 1991), pp. 95–103. ISSN: 0030-4018 (cit. on p. 77).
- [115] Raul Leonardo Rincon Celis. [Sideband Four-Mode Entanglement in a Four-wave Mixing Process](#). PhD thesis. São Paulo: Universidade de São Paulo, Oct. 2022 (cit. on p. 86).
- [116] Amnon Yariv, Pochi Yeh, and Amnon Yariv. *Photonics: Optical Electronics in Modern Communications*. 6th ed. The Oxford Series in Electrical and Computer Engineering. New York: Oxford University Press, 2007. ISBN: 978-0-19-517946-0 (cit. on pp. 94, 97).
- [117] George B. Arfken, Hans-Jurgen Weber, and Frank E. Harris. *Mathematical Methods for Physicists: A Comprehensive Guide*. 7th ed. Amsterdam ; Boston: Elsevier, 2013. ISBN: 978-0-12-384654-9 (cit. on p. 97).
- [118] Amar C Vutha et al. [Displacement Operators: The Classical Face of Their Quantum Phase](#). In: *European Journal of Physics* 39.2 (Mar. 2018), p. 025405. ISSN: 0143-0807, 1361-6404 (cit. on p. 98).
- [119] S. Pirandola and S. Mancini. [Quantum Teleportation with Continuous Variables: A Survey](#). In: *Laser Physics* 16.10 (Oct. 2006), pp. 1418–1438. ISSN: 1555-6611 (cit. on pp. 101, 103, 110, 250).
- [120] Akira Furusawa and Peter Van Loock. [Quantum Teleportation and Entanglement: A Hybrid Approach to Optical Quantum Information Processing](#). 1st ed. Wiley, Mar. 2011. ISBN: 978-3-527-40930-3 (cit. on pp. 102, 103, 112, 176).

- [121] Samuel L. Braunstein, Christopher A. Fuchs, and H. J. Kimble. [Criteria for Continuous-Variable Quantum Teleportation](#). In: *Journal of Modern Optics* 47.2-3 (Feb. 2000), pp. 267–278. ISSN: 0950-0340, 1362-3044 (cit. on pp. 103, 126, 127, 130, 250).
- [122] P. Van Loock, Samuel L. Braunstein, and H. J. Kimble. [Broadband Teleportation](#). In: *Physical Review A* 62.2 (July 2000), p. 022309. ISSN: 1050-2947, 1094-1622 (cit. on pp. 103, 221).
- [123] J. E. S. César et al. [Extra Phase Noise from Thermal Fluctuations in Nonlinear Optical Crystals](#). In: *Physical Review A* 79.6 (June 2009), p. 063816. ISSN: 1050-2947, 1094-1622 (cit. on pp. 104, 149, 150, 156, 204, 206).
- [124] K.C. Peng et al. [Generation of Two-Mode Quadrature-Phase Squeezing and Intensity-Difference Squeezing from a Cw-NOPO](#). In: *Applied Physics B: Lasers and Optics* 66.6 (June 1998), pp. 755–758. ISSN: 0946-2171, 1432-0649 (cit. on pp. 104, 143).
- [125] R. Rendell and A. Rajagopal. [Entanglement of Pure Two-Mode Gaussian States](#). In: *Physical Review A* 72.1 (July 2005), p. 012330. ISSN: 1050-2947, 1094-1622 (cit. on p. 105).
- [126] C Fabre et al. [Squeezing in Detuned Degenerate Optical Parametric Oscillators](#). In: *Quantum Optics: Journal of the European Optical Society Part B* 2.2 (Apr. 1990), pp. 159–187. ISSN: 0954-8998 (cit. on p. 106).
- [127] D. B. Horoshko, M. M. Eskandary, and S. Ya. Kilin. [Quantum Model for Traveling-Wave Electro-Optical Phase Modulator](#). In: *Journal of the Optical Society of America B* 35.11 (Nov. 2018), p. 2744. ISSN: 0740-3224, 1520-8540 (cit. on p. 107).
- [128] Bing Qi, Philip G. Evans, and Warren P. Grice. [Passive State Preparation in the Gaussian-modulated Coherent-States Quantum Key Distribution](#). In: *Physical Review A* 97.1 (Jan. 2018). ISSN: 2469-9926, 2469-9934 (cit. on p. 108).
- [129] Haley Weinstein et al. [High Fidelity Artificial Quantum Thermal State Generation Using Encoded Coherent States](#). Oct. 2024. arXiv: [2405.03881 \[quant-ph\]](https://arxiv.org/abs/2405.03881) (cit. on p. 108).
- [130] Wim Vassen et al. [A Frequency-Stabilized Titanium Sapphire Laser for High-Resolution Spectroscopy](#). In: *Optics Communications* 75.5 (Mar. 1990), pp. 435–440. ISSN: 0030-4018 (cit. on p. 109).
- [131] C. W. Gardiner and P. Zoller. [Quantum Noise: A Handbook of Markovian and Non-Markovian Quantum Stochastic Methods with Applications to Quantum Optics](#). Third edition. Berlin: Springer, 2010. ISBN: 978-3-642-06094-6 (cit. on p. 109).

-
- [132] Holger F. Hofmann et al. [Fidelity and Information in the Quantum Teleportation of Continuous Variables](#). In: *Physical Review A* 62.6 (Nov. 2000), p. 062304 (cit. on pp. 126, 221).
 - [133] Alexei Zubarev, Marina Cuzminschi, and Aurelian Isar. [Continuous Variable Quantum Teleportation of a Thermal State in a Thermal Environment](#). In: *Results in Physics* 39 (Aug. 2022), p. 105700. ISSN: 22113797 (cit. on p. 126).
 - [134] A. Uhlmann. [The “Transition Probability” in the State Space of a \$*\$ -Algebra](#). In: *Reports on Mathematical Physics* 9.2 (Apr. 1976), pp. 273–279. ISSN: 0034-4877 (cit. on p. 126).
 - [135] Richard Jozsa. [Fidelity for Mixed Quantum States](#). In: *Journal of Modern Optics* 41.12 (Dec. 1994), pp. 2315–2323. ISSN: 0950-0340, 1362-3044 (cit. on p. 126).
 - [136] Christopher A. Fuchs and Carlton M. Caves. [Mathematical Techniques for Quantum Communication Theory](#). In: *Open Systems & Information Dynamics* 3.3 (Oct. 1995), pp. 345–356. ISSN: 1230-1612, 1573-1324 (cit. on p. 127).
 - [137] Paulina Marian and Tudor A. Marian. [Optimal Purifications and Fidelity for Displaced Thermal States](#). In: *Physical Review A* 76.5 (Nov. 2007), p. 054307 (cit. on p. 130).
 - [138] H Scutaru. [Fidelity for Displaced Squeezed Thermal States and the Oscillator Semigroup](#). In: *Journal of Physics A: Mathematical and General* 31.15 (Apr. 1998), pp. 3659–3663. ISSN: 0305-4470, 1361-6447 (cit. on p. 130).
 - [139] Paulina Marian and Tudor A. Marian. [Uhlmann Fidelity between Two-Mode Gaussian States](#). In: *Physical Review A* 86.2 (Aug. 2012), p. 022340. ISSN: 1050-2947, 1094-1622 (cit. on p. 130).
 - [140] N. J. Cerf, A. Ipe, and X. Rottenberg. [Cloning of Continuous Quantum Variables](#). In: *Physical Review Letters* 85.8 (Aug. 2000), pp. 1754–1757 (cit. on p. 133).
 - [141] Frédéric Grosshans and Philippe Grangier. [Quantum Cloning and Teleportation Criteria for Continuous Quantum Variables](#). In: *Physical Review A* 64.1 (June 2001), p. 010301. ISSN: 1050-2947, 1094-1622 (cit. on pp. 133, 159).
 - [142] Alessandro De Sousa Villar. [Emaranhamento multicolor entre feixes intensos de luz](#). PhD thesis. São Paulo: Universidade de São Paulo, Apr. 2007 (cit. on pp. 137, 139, 142).
 - [143] Antonio Sales Oliveira Coelho. [Emaranhamento multicor para redes de informação quântica](#). PhD thesis. São Paulo: Universidade de São Paulo, Apr. 2013 (cit. on pp. 137, 142).
 - [144] Túlio Brito Brasil. [Emaranhamento Multicor Para Conexão de Sistemas Quânticos](#). PhD thesis. São Paulo: Universidade de São Paulo, Mar. 2021 (cit. on p. 137).

- [145] Paula Sampaio Meirelles. *Uma proposta experimental para o teletransporte bicolor de estados quânticos da luz*. PhD thesis. São Paulo: Universidade de São Paulo, Feb. 2016 (cit. on p. 137).
- [146] Felipe Alexandre Silva Barbosa. *Robustez do emaranhamento em variáveis contínuas e fotodetecção de feixes intensos no domínio espectral*. PhD thesis. São Paulo: Universidade de São Paulo, June 2013 (cit. on p. 137).
- [147] R. W. P. Drever et al. *Laser Phase and Frequency Stabilization Using an Optical Resonator*. In: *Applied Physics B: Lasers and Optics* 31.2 (June 1983), pp. 97–105. ISSN: 1432-0649 (cit. on pp. 139, 142, 155).
- [148] Katiuscia Nadyne Cassemiro. *Correlações quânticas multicolores no oscilador paramétrico ótico*. PhD thesis. São Paulo: Universidade de São Paulo, Apr. 2008 (cit. on p. 139).
- [149] J.L. Hall et al. *Stabilization and Frequency Measurement of the I₂-Stabilized Nd:YAG Laser*. In: *IEEE Transactions on Instrumentation and Measurement* 48.2 (Apr. 1999), pp. 583–586. ISSN: 0018-9456 (cit. on p. 139).
- [150] R. Paschotta. *Optical Fiber Communications - an Encyclopedia Article*. In: *RP Photonics Encyclopedia*. RP Photonics AG, 2005 (cit. on p. 140).
- [151] Mattia Cantono et al. *Opportunities and Challenges of C+L Transmission Systems*. In: *Journal of Lightwave Technology* 38.5 (Mar. 2020), pp. 1050–1060. ISSN: 0733-8724, 1558-2213 (cit. on p. 140).
- [152] Takeshi Hoshida et al. *Ultrawideband Systems and Networks: Beyond C+L-Band*. In: *Proceedings of the IEEE* 110.11 (Nov. 2022), pp. 1725–1741. ISSN: 0018-9219, 1558-2256 (cit. on p. 140).
- [153] Flávio Campopiano Dias De Moraes. *Construção e caracterização de um laser contínuo de titânio-safira*. MA thesis. São Paulo: Universidade de São Paulo, June 2013 (cit. on p. 140).
- [154] J. E. Debs et al. *Piezo-Locking a Diode Laser with Saturated Absorption Spectroscopy*. In: *Applied Optics* 47.28 (Oct. 2008), p. 5163. ISSN: 0003-6935, 1539-4522 (cit. on p. 140).
- [155] B. Willke et al. *Spatial and Temporal Filtering of a 10-W Nd:YAG Laser with a Fabry–Perot Ring-Cavity Premode Cleaner*. In: *Optics Letters* 23.21 (Nov. 1998), p. 1704. ISSN: 0146-9592, 1539-4794 (cit. on p. 141).
- [156] Anthony E. Siegman. *Lasers*. Mill Valley, California: University Science Books, 1986. ISBN: 978-0-935702-11-8 (cit. on pp. 141, 155).

- [157] T. Preuschoff, M. Schlosser, and G. Birkl. [Digital Laser Frequency and Intensity Stabilization Based on the STEMlab Platform \(Originally Red Pitaya\)](#). In: *Review of Scientific Instruments* 91.8 (Aug. 2020), p. 083001. ISSN: 0034-6748 (cit. on pp. 142, 155, 159).
- [158] L. Neuhaus et al. [PyRPL \(Python Red Pitaya Lockbox\) — An Open-Source Software Package for FPGA-controlled Quantum Optics Experiments](#). In: *2017 Conference on Lasers and Electro-Optics Europe & European Quantum Electronics Conference (CLEO/Europe-EQEC)*. June 2017, pp. 1–1 (cit. on pp. 142, 155, 159).
- [159] Rakesh P. Borase et al. [A Review of PID Control, Tuning Methods and Applications](#). In: *International Journal of Dynamics and Control* 9.2 (June 2021), pp. 818–827. ISSN: 2195-268X, 2195-2698 (cit. on p. 142).
- [160] Stefan Ast, Moritz Mehmet, and Roman Schnabel. [High-Bandwidth Squeezed Light at 1550 Nm from a Compact Monolithic PPKTP Cavity](#). In: *Optics Express* 21.11 (June 2013), p. 13572. ISSN: 1094-4087 (cit. on p. 144).
- [161] Felix Mann et al. [Low-Noise Quantum Frequency Conversion in a Monolithic Cavity with Bulk Periodically Poled Potassium Titanyl Phosphate](#). In: *Physical Review Applied* 20.5 (Nov. 2023), p. 054010. ISSN: 2331-7019 (cit. on pp. 144, 285).
- [162] Fabian Steinlechner et al. [Efficient Heralding of Polarization-Entangled Photons from Type-0 and Type-II Spontaneous Parametric Downconversion in Periodically Poled KTiOPO₄](#). In: *Journal of the Optical Society of America B* 31.9 (Sept. 2014), p. 2068. ISSN: 0740-3224, 1520-8540 (cit. on p. 144).
- [163] Herman Vanherzeele and John D. Bierlein. [Magnitude of the Nonlinear-Optical Coefficients of KTiOPO₄](#). In: *Optics Letters* 17.14 (July 1992), p. 982. ISSN: 0146-9592, 1539-4794 (cit. on p. 145).
- [164] Michael V. Pack, Darrell J. Armstrong, and Arlee V. Smith. [Measurement of the \$\chi^{\(2\)}\$ Tensors of KTiOPO₄, KTiOAsO₄, RbTiOPO₄, and RbTiOAsO₄ Crystals](#). In: *Applied Optics* 43.16 (June 2004), p. 3319. ISSN: 0003-6935, 1539-4522 (cit. on p. 145).
- [165] Robert W. Boyd. Nonlinear Optics. 4th ed. San Diego: Academic Press is an imprint of Elsevier, 2019. ISBN: 978-0-12-811002-7 (cit. on p. 145).
- [166] Kiyoshi Kato and Eiko Takaoka. [Sellmeier and Thermo-Optic Dispersion Formulas for KTP](#). In: *Applied Optics* 41.24 (Aug. 2002), p. 5040. ISSN: 0003-6935, 1539-4522 (cit. on pp. 146, 148).
- [167] Mikhail N. Polyanskiy. [Refractiveindex.info Database of Optical Constants](#). In: *Scientific Data* 11.1 (Jan. 2024), p. 94. ISSN: 2052-4463 (cit. on pp. 146, 148).

- [168] G. D. Boyd and D. A. Kleinman. **Parametric Interaction of Focused Gaussian Light Beams**. In: *Journal of Applied Physics* 39.8 (July 1968), pp. 3597–3639. ISSN: 0021-8979 (cit. on p. 146).
- [169] Ryan S. Bennink. **Optimal Collinear Gaussian Beams for Spontaneous Parametric Down-Conversion**. In: *Physical Review A* 81.5 (May 2010), p. 053805. ISSN: 1050-2947, 1094-1622 (cit. on p. 146).
- [170] Andrew Wade. **Quantum Limited Measurements in Gravitational Wave Detectors**. PhD thesis. Canberra: The Australian National University, 2016 (cit. on p. 146).
- [171] B. Boulanger et al. **Optical Studies of Laser-Induced Gray-Tracking in KTP**. In: *IEEE Journal of Quantum Electronics* 35.3 (Mar. 1999), pp. 281–286. ISSN: 00189197 (cit. on pp. 146, 149, 150).
- [172] Luis F. Muñoz-Martínez et al. **Exploring Six Modes of an Optical Parametric Oscillator**. In: *Physical Review A* 98.2 (Aug. 2018), p. 023823. ISSN: 2469-9926, 2469-9934 (cit. on pp. 148, 191, 249).
- [173] Túlio Brito Brasil et al. **Two-Colour High-Purity Einstein-Podolsky-Rosen Photonic State**. In: *Nature Communications* 13.1 (Aug. 2022), p. 4815. ISSN: 2041-1723 (cit. on p. 149).
- [174] S. Wang, V. Pasiskevicius, and F. Laurell. **Dynamics of Green Light-Induced Infrared Absorption in KTiOPO₄ and Periodically Poled KTiOPO₄**. In: *Journal of Applied Physics* 96.4 (Aug. 2004), pp. 2023–2028. ISSN: 0021-8979, 1089-7550 (cit. on pp. 149, 150).
- [175] A. Alexandrovski, M. Fejer, and G. Mitchell. **CW Gray-Track Formation in KTP**. In: *Conference on Lasers and Electro-Optics. Postconference Edition. CLEO '99*. Baltimore, MD, USA: Opt. Soc. America, 1999, pp. 531–532. ISBN: 978-1-55752-595-6 (cit. on p. 149).
- [176] A. J. Fallon et al. **Measurement of the ⁸⁷Rb D -Line Vector Tune-out Wavelength**. In: *Physical Review A* 105.3 (Mar. 2022), p. L030802. ISSN: 2469-9926, 2469-9934 (cit. on p. 151).
- [177] Hans Marin Florez. **Espectroscopia de correlação em condição de transparência eletromagneticamente induzida: regime dinâmico e ressonâncias das bandas laterais em átomos frios**. PhD thesis. São Paulo: Universidade de São Paulo, May 2016 (cit. on p. 154).
- [178] Wance Wang, Sarthak Subhankar, and Joseph W. Britton. **A Practical Guide to Feedback Control for Pound–Drever–Hall Laser Linewidth Narrowing**. In: *Applied Physics B* 131.7 (July 2025), p. 146. ISSN: 0946-2171, 1432-0649 (cit. on p. 155).

- [179] Jiangrui Gao et al. [Generation and Application of Twin Beams from an Optical Parametric Oscillator Including an \$\alpha\$ -Cut KTP Crystal](#). In: *Optics Letters* 23.11 (June 1998), p. 870. ISSN: 0146-9592, 1539-4794 (cit. on p. 156).
- [180] Haijun Kang et al. [Experimental Demonstration of Robustness of Gaussian Quantum Coherence](#). In: *Photonics Research* 9.7 (July 2021), p. 1330. ISSN: 2327-9125 (cit. on p. 157).
- [181] G. H. Dos Santos et al. [Decomposing Spatial Mode Superpositions with a Triangular Optical Cavity](#). In: *Physical Review Applied* 16.3 (Sept. 2021), p. 034008. ISSN: 2331-7019 (cit. on p. 161).
- [182] T.W. Hansch and B. Couillaud. [Laser Frequency Stabilization by Polarization Spectroscopy of a Reflecting Reference Cavity](#). In: *Optics Communications* 35.3 (Dec. 1980), pp. 441–444. ISSN: 00304018 (cit. on p. 169).
- [183] H. Nyquist. [Thermal Agitation of Electric Charge in Conductors](#). In: *Physical Review* 32.1 (July 1928), pp. 110–113 (cit. on p. 171).
- [184] Gerd Keiser. [Optical Fiber Communications](#). 4th ed. New York, NY: McGraw-Hill Companies, 2011. ISBN: 978-0-07-338071-1 (cit. on p. 171).
- [185] Shijie Sun et al. [Signal Demodulation Methods for Electrical Tomography: A Review](#). In: *IEEE Sensors Journal* 19.20 (Oct. 2019), pp. 9026–9035. ISSN: 1530-437X, 1558-1748, 2379-9153 (cit. on p. 174).
- [186] Pauli Virtanen et al. [SciPy 1.0: Fundamental Algorithms for Scientific Computing in Python](#). In: *Nature Methods* 17.3 (Mar. 2020), pp. 261–272. ISSN: 1548-7091, 1548-7105 (cit. on p. 181).
- [187] Ralf Gommers et al. [Scipy/Scipy: SciPy 1.12.0](#). Zenodo. Jan. 2024 (cit. on pp. 181, 183, 188).
- [188] Allen Downey. [Think DSP: Digital Signal Processing in Python](#). First edition. Sebastopol, CA: O'Reilly Media, Inc, 2016. ISBN: 978-1-4919-3845-4 (cit. on p. 183).
- [189] Robert V. Hogg, Joseph W. McKean, and Allen T. Craig. [Introduction to Mathematical Statistics](#). Eighth edition, global edition. Harlow, Essex, United Kingdom: Pearson, 2020. ISBN: 978-1-292-26476-9 (cit. on p. 185).
- [190] Eric Benhamou. [A Few Properties of Sample Variance](#). Sept. 2018. arXiv: [1809.03774 \[math\]](#) (cit. on p. 185).
- [191] Matt Newville et al. [Lmfit/Lmfit-Py: 1.3.2](#). Zenodo. July 2024 (cit. on p. 188).
- [192] Eric O. LEBIGOT (EOL) et al. [Lmfit/Uncertainties: 3.2.2](#). Zenodo. July 2024 (cit. on p. 188).
- [193] Michael Bass and Optical Society of America, eds. [Handbook of Optics](#). 2nd ed. New York: McGraw-Hill, 1995. ISBN: 978-0-07-047740-7 (cit. on p. 190).

- [194] Chunchun Liu et al. High-Efficiency Continuously Tunable Single-Frequency Doubly Resonant Optical Parametric Oscillator. In: *Applied Optics* 50.10 (Apr. 2011), p. 1477. ISSN: 0003-6935, 1539-4522 (cit. on p. 190).
- [195] Jianwei Xu. Quantifying Coherence of Gaussian States. In: *Physical Review A* 93.3 (Mar. 2016), p. 032111. ISSN: 2469-9926, 2469-9934 (cit. on p. 283).
- [196] Gerardo Adesso and Animesh Datta. Quantum versus Classical Correlations in Gaussian States. In: *Physical Review Letters* 105.3 (July 2010), p. 030501. ISSN: 0031-9007, 1079-7114 (cit. on p. 284).
- [197] Lars S. Madsen et al. Experimental Investigation of the Evolution of Gaussian Quantum Discord in an Open System. In: *Physical Review Letters* 109.3 (July 2012), p. 030402. ISSN: 0031-9007, 1079-7114 (cit. on p. 284).
- [198] Felix Mann et al. Noise Analysis of a Quasi-Phase-Matched Quantum Frequency Converter and Higher-Order Counter-Propagating SPDC. In: *Optics Express* 32.24 (Nov. 2024), p. 42225. ISSN: 1094-4087 (cit. on p. 285).
- [199] Felix Mann et al. Hong-Ou-Mandel Effect with Two Frequency-Entangled Photons of Vastly Different Color. Apr. 2025. arXiv: 2504.03304 [quant-ph] (cit. on p. 285).
- [200] Emma L. Pearce et al. Sensing Techniques with Undetected Photons in the Mid-Infrared. In: *Advanced Photon Counting Techniques XIX*. Ed. by Mark A. Itzler, K. Alex McIntosh, and Joshua C. Bienfang. Orlando, United States: SPIE, May 2025, p. 16. ISBN: 978-1-5106-8685-4 (cit. on p. 285).
- [201] Gunnar Blume et al. Long Wavelength, Small Quantum Interferometer Module: Shrinking MIR OCT Systems via Quantum Entanglement. In: *Quantum Sensing, Imaging, and Precision Metrology III*. Ed. by Selim M. Shahriar. San Francisco, United States: SPIE, Mar. 2025, p. 118. ISBN: 978-1-5106-8532-1 (cit. on p. 285).
- [202] Felipe Gewers et al. Multi-Color Continuous Variables Unconditional Quantum Teleportation: From Near-Infrared to Telecommunications' L-Band. In: *Quantum 2.0 Conference and Exhibition*. Rotterdam: Optica Publishing Group, 2024, QW2B.5. ISBN: 978-1-55752-518-5 (cit. on p. 286).
- [203] Felix Mann et al. Hong-Ou-Mandel Interference of Two Photons of Vastly Different Color. In: *Quantum 2.0 Conference and Exhibition*. Rotterdam: Optica Publishing Group, 2024, QM2B.6. ISBN: 978-1-55752-518-5 (cit. on p. 286).
- [204] Felix Mann et al. Higher-Order Counter-Propagating SPDC and a Complete Analysis of the Noise Spectrum of a Bulk ppKTP Quantum Frequency Converter. In: *Quantum 2.0 Conference and Exhibition*. Rotterdam: Optica Publishing Group, 2024, QW3A.48. ISBN: 978-1-55752-518-5 (cit. on p. 286).

- [205] Felix Mann et al. [A Monolithic Bulk ppKTP Cavity for Quantum Frequency Conversion from 637 Nm to Telecom Wavelength](#). In: *CLEO 2023*. San Jose, CA: Optica Publishing Group, 2023, FF2L.6. ISBN: 978-1-957171-25-8 (cit. on p. 286).

Appendix

A – CANONICAL QUANTIZATION OF THE FREE ELECTROMAGNETIC FIELD

The classical electromagnetic field gives a very good description of most optical phenomena. In some cases the classical theory is able to describe seemingly non-classical effects such as photoelectric bunching and the photoelectric counting statistics [70]. This is a result of the fact that for the most applications the non-classical features of light are not relevant, and therefore can be circumvented.

On the other hand, light is fundamentally quantum, and this must be taken into account for the correct description of more subtle phenomena. One remarkable example is the spontaneous emission of an atom that is a direct result of the quantum nature of the field. In this work, we explore the quantum nature of the light and its effects. The major objective is to provide the basis for quantum technologies that use these characteristics to achieve advantages over classical methods.

To describe the non-classical features of light it is necessarily to quantize the electromagnetic field, that is, to describe it in the formalism of quantum mechanics. The *canonical quantization* is the main approach used to quantize a classical theory. It consists of writing the Hamiltonian of the system in terms of the canonical variables and promoting these variables to the corresponding Hermitian quantum operators. Here I will follow the treatment in [70, 71, 76].

A.1 Free Field Plane Wave Decomposition

In this section, we demonstrate the decomposition of the free electromagnetic field in terms of monochromatic plane waves. We start with the Maxwell's equations for an electromagnetic field in free space (SI units):

$$\nabla \times \mathbf{E}(\mathbf{r}, t) = -\frac{\partial}{\partial t} \mathbf{B}(\mathbf{r}, t) \quad (\text{A.1a})$$

$$\nabla \times \mathbf{B}(\mathbf{r}, t) = \frac{1}{c^2} \frac{\partial}{\partial t} \mathbf{E}(\mathbf{r}, t) \quad (\text{A.1b})$$

$$\nabla \cdot \mathbf{E}(\mathbf{r}, t) = 0 \quad (\text{A.1c})$$

$$\nabla \cdot \mathbf{B}(\mathbf{r}, t) = 0, \quad (\text{A.1d})$$

where $c = \sqrt{\mu_0 \epsilon_0}$ is the light speed in vacuum, and $\mathbf{E}(\mathbf{r}, t)$ and $\mathbf{B}(\mathbf{r}, t)$ are the electric and magnetic field vectors, respectively, at the spatial coordinate \mathbf{r} and time t .

To express the free electromagnetic field more conveniently, we introduce the vector potential $\mathbf{A}(\mathbf{r}, t)$. Establishing the Coulomb gauge condition, the vector potential satisfies the following constraint:

$$\nabla \cdot \mathbf{A}(\mathbf{r}, t) = 0. \quad (\text{A.2})$$

The electric and magnetic fields are then expressed in terms of \mathbf{A} as follows:

$$\mathbf{E}(\mathbf{r}, t) = -\frac{\partial}{\partial t} \mathbf{A}(\mathbf{r}, t), \quad (\text{A.3a})$$

$$\mathbf{B}(\mathbf{r}, t) = \nabla \times \mathbf{A}(\mathbf{r}, t). \quad (\text{A.3b})$$

Consequently, the vector potential satisfies the homogeneous wave equation:

$$\nabla^2 \mathbf{A}(\mathbf{r}, t) - \frac{1}{c^2} \frac{\partial^2}{\partial t^2} \mathbf{A}(\mathbf{r}, t) = 0. \quad (\text{A.4})$$

The normal modes of the vector potential can be defined using any complete set of solutions that satisfy Equation (A.2). The appropriate choice of normal modes is determined by the boundary conditions imposed on the electromagnetic field. For simplicity, we assume periodic boundary conditions on the surface of a cubic volume with total volume V and edge length L . Under these conditions, plane wave modes provide a natural basis, allowing for a convenient treatment using Fourier expansions while also ensuring well-defined linear momentum.

The vector potential in terms of a complete set of plane waves that satisfy both the periodic boundary conditions and the wave Equation (A.4), is given by [70]:

$$\mathbf{A}(\mathbf{r}, t) = \sum_{\mathbf{k}} \mathbf{A}_{\mathbf{k}}(\mathbf{r}, t) = \sum_{\mathbf{k}} \epsilon_{\mathbf{k}} \frac{\mathcal{E}_{\mathbf{k}}^{(1)}}{\omega_k} [\alpha_{\mathbf{k}}(t) e^{i\mathbf{k}\cdot\mathbf{r}} + \alpha_{\mathbf{k}}^*(t) e^{-i\mathbf{k}\cdot\mathbf{r}}], \quad (\text{A.5})$$

where $\epsilon_{\mathbf{k}}$ is the unitary polarization vector, $\omega_k = ck$ is the angular frequency, and $\alpha_{\mathbf{k}}(t) = \alpha_{\mathbf{k}} e^{-i\omega_k t}$ is the complex normal variable of the mode. The quantity $\mathcal{E}_{\mathbf{k}}^{(1)}$ denotes the amplitude of an electric field whose total energy is equal to that of a single photon, $\hbar\omega_k$, within the quantization volume:

$$\mathcal{E}_{\mathbf{k}}^{(1)} = \sqrt{\frac{\hbar\omega_k}{2\epsilon_0 V}}. \quad (\text{A.6})$$

The wavevector \mathbf{k} is constrained by the periodic boundary conditions and satisfies the relation:

$$\mathbf{k} = \frac{2\pi}{L} \mathbf{n}, \quad \text{where,} \quad \mathbf{n} = (n_x, n_y, n_z), \quad (\text{A.7})$$

with n_x, n_y and n_z being positive or negative integers.

The Coulomb gauge, also known as the transverse gauge, ensures that $\mathbf{A}_k(\mathbf{r}, t)$ is transverse to \mathbf{k} . Therefore, it is possible to decompose the unitary polarization vector $\boldsymbol{\epsilon}_k$ into a pair of orthogonal basis vectors $(\boldsymbol{\epsilon}_{1k}, \boldsymbol{\epsilon}_{2k})$, which span the plane perpendicular to \mathbf{k} and satisfy the following conditions:

$$\alpha_k(t)\boldsymbol{\epsilon}_k = \alpha_{1k}(t)\boldsymbol{\epsilon}_{1k} + \alpha_{2k}(t)\boldsymbol{\epsilon}_{2k}, \quad (\text{A.8a})$$

$$\begin{cases} \mathbf{k} \cdot \boldsymbol{\epsilon}_{sk} = 0, & (s = 1, 2) \\ \boldsymbol{\epsilon}_{sk}^* \cdot \boldsymbol{\epsilon}_{s'k} = \delta_{ss'}, & (s, s' = 1, 2) \\ \boldsymbol{\epsilon}_{1k} \times \boldsymbol{\epsilon}_{2k} = \frac{\mathbf{k}}{k}. \end{cases} \quad (\text{A.8b})$$

With this definition, each mode ℓ is specified by the four parameters $\ell = (n_x, n_y, n_z; s)$, allowing the vector potential to be rewritten as:

$$\begin{aligned} \mathbf{A}(\mathbf{r}, t) &= \sum_{\mathbf{k}} \sum_s \mathbf{A}_{sk}(\mathbf{r}, t) = \sum_{\mathbf{k}} \sum_s \boldsymbol{\epsilon}_{sk} \frac{\mathcal{E}_k^{(1)}}{\omega_k} [\alpha_{sk}(t)e^{i\mathbf{k}\cdot\mathbf{r}} + \alpha_{sk}^*(t)e^{-i\mathbf{k}\cdot\mathbf{r}}] \\ &= \sum_{\ell} \mathbf{A}_{\ell}(\mathbf{r}, t) = \sum_{\ell} \boldsymbol{\epsilon}_{\ell} \frac{\mathcal{E}_{\ell}^{(1)}}{\omega_{\ell}} [\alpha_{\ell}(t)e^{i(\mathbf{k}_{\ell}\cdot\mathbf{r})} + \alpha_{\ell}^*(t)e^{-i(\mathbf{k}_{\ell}\cdot\mathbf{r})}]. \end{aligned} \quad (\text{A.9})$$

Substituting Equation (A.9) into (A.3a) and (A.3b), we obtain the normal mode decomposition of the electromagnetic fields in terms of polarized monochromatic travelling plane waves:

$$\mathbf{E}(\mathbf{r}, t) = \sum_{\ell} \mathbf{E}_{\ell}(\mathbf{r}, t) = \sum_{\ell} \boldsymbol{\epsilon}_{\ell} i \mathcal{E}_{\ell}^{(1)} [\alpha_{\ell}(t)e^{i(\mathbf{k}_{\ell}\cdot\mathbf{r})} - \alpha_{\ell}^*(t)e^{-i(\mathbf{k}_{\ell}\cdot\mathbf{r})}], \quad (\text{A.10a})$$

$$\mathbf{B}(\mathbf{r}, t) = \sum_{\ell} \mathbf{B}_{\ell}(\mathbf{r}, t) = \sum_{\ell} \boldsymbol{\epsilon}'_{\ell} i \frac{\mathcal{E}_{\ell}^{(1)}}{c} [\alpha_{\ell}(t)e^{i(\mathbf{k}_{\ell}\cdot\mathbf{r})} - \alpha_{\ell}^*(t)e^{-i(\mathbf{k}_{\ell}\cdot\mathbf{r})}], \quad (\text{A.10b})$$

where $\boldsymbol{\epsilon}'_{\ell} = \frac{\mathbf{k}_{\ell}}{k_{\ell}} \times \boldsymbol{\epsilon}_{\ell}$.

A.2 Energy of the Electromagnetic Field

The energy H_R of the free electromagnetic field is given by the integral of the energy density over the volume V :

$$H_R = \frac{\epsilon_0}{2} \int_V dr^3 [\mathbf{E}^2(\mathbf{r}, t) + c^2 \mathbf{B}^2(\mathbf{r}, t)]. \quad (\text{A.11})$$

Substituting the expansions for the electric and magnetic fields, given by Equation (A.10), into Equation (A.11), and using the orthogonality of the plane wave modes, we obtain:

$$H_R = 2\epsilon_0 V \sum_{\ell} [\mathcal{E}_{\ell}^{(1)}]^2 |\alpha_{\ell}(t)|^2 = \sum_{\ell} \hbar w_{\ell} |\alpha_{\ell}(t)|^2. \quad (\text{A.12})$$

This result shows that the total electromagnetic energy is simply the sum of the energies associated with each mode, with no cross terms appearing. Solving the homogeneous wave equation (Equation (A.4)) for the decomposed vector potential (A.9), we find that the system's dynamics are governed by the equation:

$$\left(\frac{d^2}{dt^2} + \omega_{\ell}^2 \right) \alpha_{\ell}(t) = 0, \quad (\text{A.13})$$

for each mode ℓ . Therefore, the system's Hamiltonian is equivalent to that of an infinite set of uncoupled harmonic oscillators, one for each possible wave vector \mathbf{k} and for each of the two polarization states ϵ_{sk} . With this equivalence established, we can quantize the free electromagnetic field by applying the same quantization procedure used for the classical harmonic oscillator.

For each mode ℓ , we define the pair of canonical variable as:

$$P_{\ell}(t) = \sqrt{\frac{\hbar}{2}} (\alpha_{\ell}(t) + \alpha_{\ell}^*(t)), \quad (\text{A.14a})$$

$$Q_{\ell}(t) = -\sqrt{\frac{\hbar}{2}} i (\alpha_{\ell}(t) - \alpha_{\ell}^*(t)). \quad (\text{A.14b})$$

With these definitions, the Hamiltonian H_R takes the form:

$$H_R = \sum_{\ell} \hbar w_{\ell} |\alpha_{\ell}(t)|^2 = \sum_{\ell} \frac{\omega_{\ell}}{2} (P_{\ell}^2(t) + Q_{\ell}^2(t)). \quad (\text{A.15})$$

By substituting Equations (A.14a), (A.14b), and (A.15) into the Hamiltonian formulation and explicitly expressing the time dependence as $\alpha_{\ell}(t) = \alpha_{\ell} e^{-i\omega_{\ell} t}$, it follows directly that Hamilton's equations are satisfied:

$$\frac{d}{dt} P_{\ell}(t) = \frac{\partial H_R}{\partial Q_{\ell}}, \quad \frac{d}{dt} Q_{\ell}(t) = -\frac{\partial H_R}{\partial P_{\ell}}. \quad (\text{A.16})$$

This confirms that $P_{\ell}(t)$ and $Q_{\ell}(t)$ are indeed the canonical variables associated with each harmonic oscillator mode ℓ .

A.3 Canonical Quantization

The method of canonical quantization then proceeds by associating the conjugate canonical variables $P_\ell(t)$ and $Q_\ell(t)$ (Equation (A.14)) of each mode with a time-independent hermitian operators \hat{P}_ℓ and \hat{Q}_ℓ , in the Schrödinger picture. These operators satisfy the canonical commutation relations:

$$\begin{aligned} [\hat{P}_\ell, \hat{Q}_{\ell'}] &= i\hbar\delta_{\ell\ell'}, \\ [\hat{P}_\ell, \hat{P}_{\ell'}] &= [\hat{Q}_\ell, \hat{Q}_{\ell'}] = 0. \end{aligned} \quad (\text{A.17a})$$

From these canonical operators, we define the normalized quadrature operators:

$$\hat{p}_\ell = \sqrt{\frac{2}{\hbar}} \hat{P}_\ell, \quad \hat{q}_\ell = \sqrt{\frac{2}{\hbar}} \hat{Q}_\ell. \quad (\text{A.18})$$

The normal-mode complex amplitude $\alpha_\ell(t)$ is then promoted to the operator \hat{a}_ℓ . From Equation (A.18) and the commutation relations, described in Equation (A.17a), we obtain:

$$\hat{p}_\ell = \hat{a}_\ell + \hat{a}_\ell^\dagger, \quad \hat{q}_\ell = -i(\hat{a}_\ell - \hat{a}_\ell^\dagger), \quad (\text{A.19a})$$

$$[\hat{p}_\ell, \hat{q}_{\ell'}] = 2i\delta_{\ell\ell'}, \quad [\hat{p}_\ell, \hat{p}_{\ell'}] = [\hat{q}_\ell, \hat{q}_{\ell'}] = 0 \quad (\text{A.19b})$$

$$\hat{a}_\ell = \frac{\hat{p}_\ell + i\hat{q}_\ell}{2}, \quad (\text{A.19c})$$

$$[\hat{a}_\ell, \hat{a}_{\ell'}^\dagger] = \delta_{\ell\ell'}, \quad [\hat{a}_\ell, \hat{a}_{\ell'}] = [\hat{a}_\ell^\dagger, \hat{a}_{\ell'}^\dagger] = 0. \quad (\text{A.19d})$$

In the context of quantum harmonic oscillator theory, we can identify the operators \hat{a}_ℓ and \hat{a}_ℓ^\dagger as being the annihilation and creation operators, respectively, associated with mode ℓ .

Substituting these definitions into the classical Hamiltonian (A.15), the quantized electromagnetic field Hamiltonian operator is given by:

$$\hat{H}_R = \sum_\ell \frac{\omega_\ell}{2} (\hat{P}_\ell^2 + \hat{Q}_\ell^2) = \sum_\ell \hbar\omega_\ell \left(\hat{a}_\ell^\dagger \hat{a}_\ell + \frac{1}{2} \right). \quad (\text{A.20})$$

This expression describes an ensemble of independent quantum harmonic oscillators, and together with the commutation relations (A.19d), fully determines the quantum structure of the radiation field.

The electromagnetic field operators are then obtained by replacing the classical mode complex amplitudes $\alpha_\ell(t)$ and $\alpha_\ell^*(t)$, with their corresponding annihilation and creation operators, \hat{a}_ℓ and \hat{a}_ℓ^\dagger , respectively. Therefore, the quantized vector potential, electric field, and magnetic field operators are given by the following Hermitian operators:

$$\hat{\mathbf{A}}(\mathbf{r}) = \sum_{\ell} \mathcal{E}_{\ell}^{(1)} \boldsymbol{\epsilon}_{\ell} \left(e^{i(\mathbf{k}_{\ell} \cdot \mathbf{r})} \hat{a}_{\ell} + e^{-i(\mathbf{k}_{\ell} \cdot \mathbf{r})} \hat{a}_{\ell}^{\dagger} \right) = \hat{\mathbf{A}}^{(+)}(\mathbf{r}) + \hat{\mathbf{A}}^{(-)}(\mathbf{r}), \quad (\text{A.21a})$$

$$\hat{\mathbf{E}}(\mathbf{r}) = \sum_{\ell} i \mathcal{E}_{\ell}^{(1)} \boldsymbol{\epsilon}_{\ell} \left(e^{i(\mathbf{k}_{\ell} \cdot \mathbf{r})} \hat{a}_{\ell} - e^{-i(\mathbf{k}_{\ell} \cdot \mathbf{r})} \hat{a}_{\ell}^{\dagger} \right) = \hat{\mathbf{E}}^{(+)}(\mathbf{r}) + \hat{\mathbf{E}}^{(-)}(\mathbf{r}), \quad (\text{A.21b})$$

$$\hat{\mathbf{B}}(\mathbf{r}) = \sum_{\ell} i \mathcal{E}_{\ell}^{(1)} \frac{\mathbf{k} \times \boldsymbol{\epsilon}_{\ell}}{\omega_{\ell}} \left(e^{i(\mathbf{k}_{\ell} \cdot \mathbf{r})} \hat{a}_{\ell} - e^{-i(\mathbf{k}_{\ell} \cdot \mathbf{r})} \hat{a}_{\ell}^{\dagger} \right) = \hat{\mathbf{B}}^{(+)}(\mathbf{r}) + \hat{\mathbf{B}}^{(-)}(\mathbf{r}). \quad (\text{A.21c})$$

Here, the non-Hermitian operator $\hat{\mathbf{E}}^{(+)}(\mathbf{r})$ and its Hermitian conjugate $\hat{\mathbf{E}}^{(-)}(\mathbf{r})$, correspond to the positive- and negative-frequency components of the electric field, analogous to the analytic signal in classical electromagnetism. Similar decompositions apply to $\hat{\mathbf{A}}(\mathbf{r})$ and $\hat{\mathbf{B}}(\mathbf{r})$.

B – SUPPLEMENTARY CHARACTERIZATIONS OF QUANTUM TOMOGRAPHY MEASUREMENTS

In this appendix, we present additional characterizations of the quantum tomography measurement discussed in Section 6.2. While these details were omitted from the main text as they are not essential to the primary conclusions, they are included here for completeness. As a recap, the measurements were performed at an analysis frequency of 15 MHz, with the OPO crystal maintained at 38.5°C. The pump power was 26.48(2) mW, with an oscillation threshold of 16.6(3) mW, resulting in a normalized pump power of $\sigma = 1.59(3)$. The total intensity, determined by summing the contributions from both detectors at each station, was 2.06(1) mW for the signal and 1.14(1) mW for the idler.

B.1 Signal-to-Noise Ratio and Stationary Conditions

The signal-to-noise ratio (SNR), defined as the ratio of the variance of the acquired voltage with light incident on the detectors ($\Delta^2 V_{light}$) to the variance without light (i.e., electronic noise $\Delta^2 V_{dark}$), is shown in Figure 71 for all three scanning conditions. As observed in the figure, one of Alice’s detectors exhibits higher electronic noise compared to the other. Nevertheless, the SNR remains adequate, and the electronic noise is properly addressed in our data analysis.

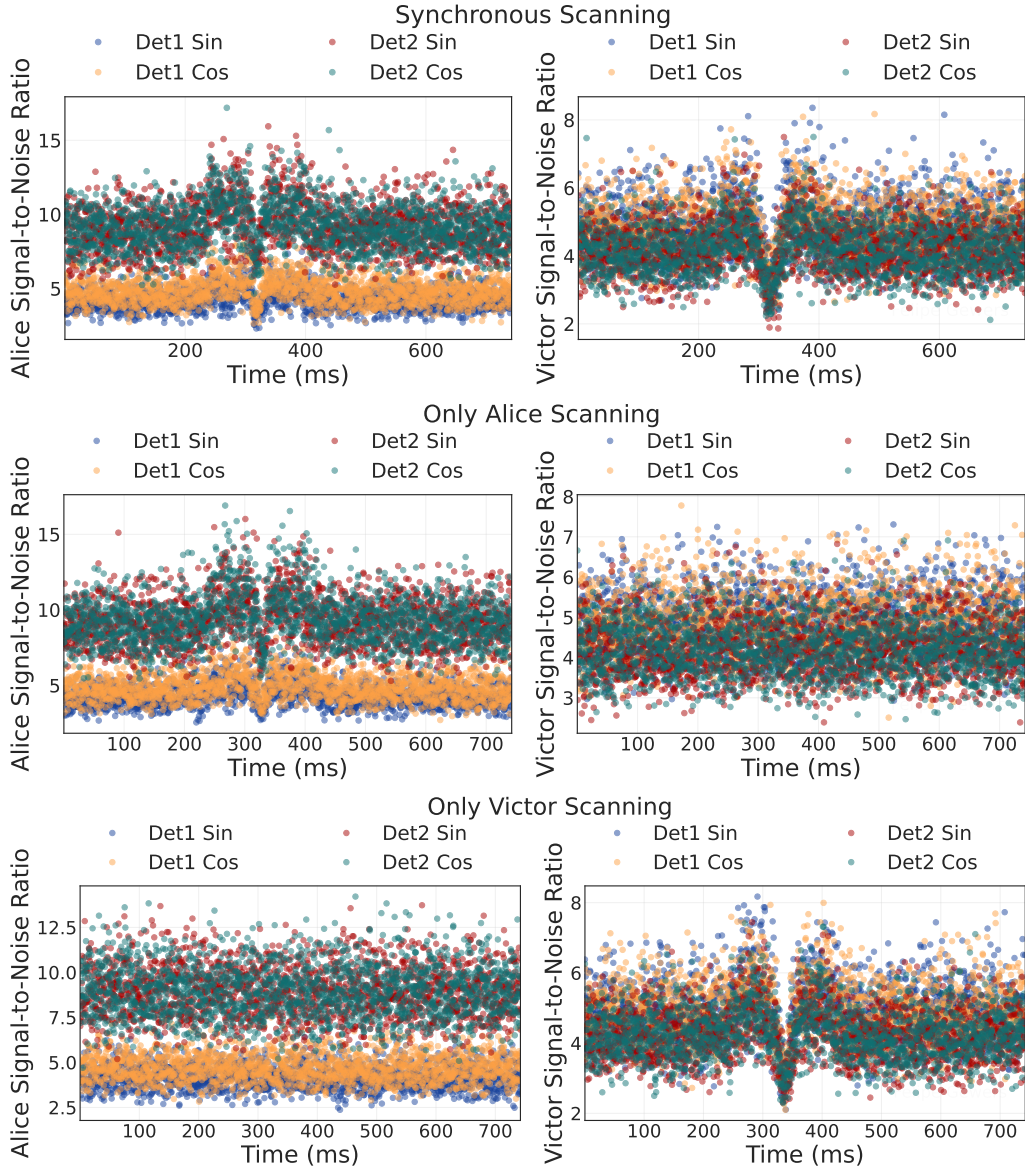


Figure 71 – Signal-to-noise ratio (SNR) in the quantum tomography measurement for the three scanning configurations.

The stationarity of the acquired data during the tomography measurement can also be verified. Figures 72 and 73 show the single-field and two-field stationarity conditions, respectively, for all three scanning configurations. The measured stationarity condition is confirmed as the obtained values remain close to zero, indicating that the electronic local oscillators (eLOs) used in the quadrature demodulation step were indeed orthogonal. Additionally, Figure 74 shows the kurtosis of the acquired signal for all scanning conditions, with values close to zero. This result, based on the measurement of both orthogonal quadratures, indicates that the generated fields are stationary and correspond to Gaussian states, as further detailed in Section 3.1.3.2.

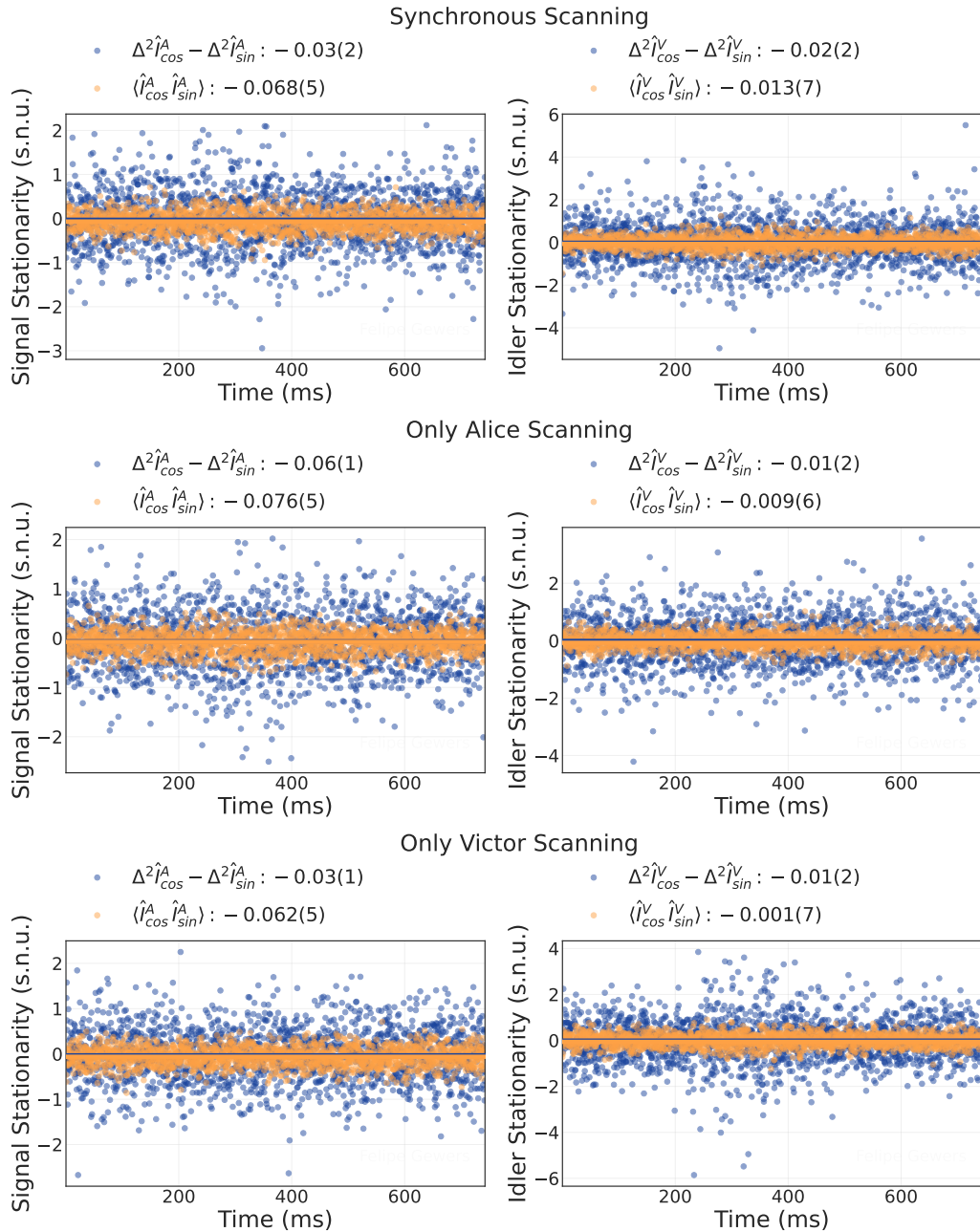


Figure 72 – Stationarity condition for a single field in the quantum tomography measurement, shown for all scanning configurations. The near-zero values confirm orthogonality of the electronic local oscillator (eLO) during quadrature demodulation.

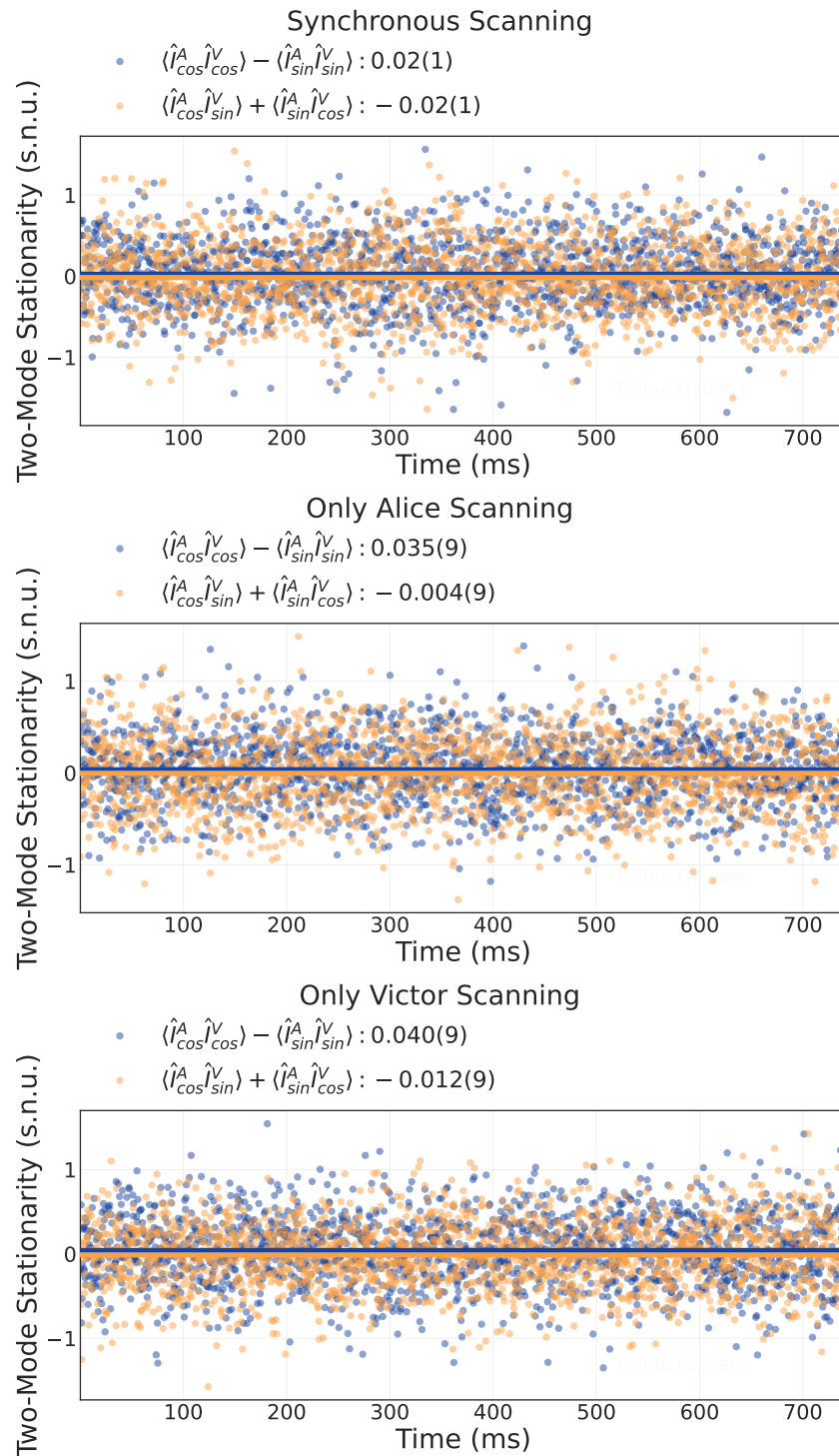


Figure 73 – Stationarity condition for two fields in the quantum tomography measurement, presented for all scanning configurations. Near-zero values confirm the orthogonality of the eLOs during quadrature demodulation.

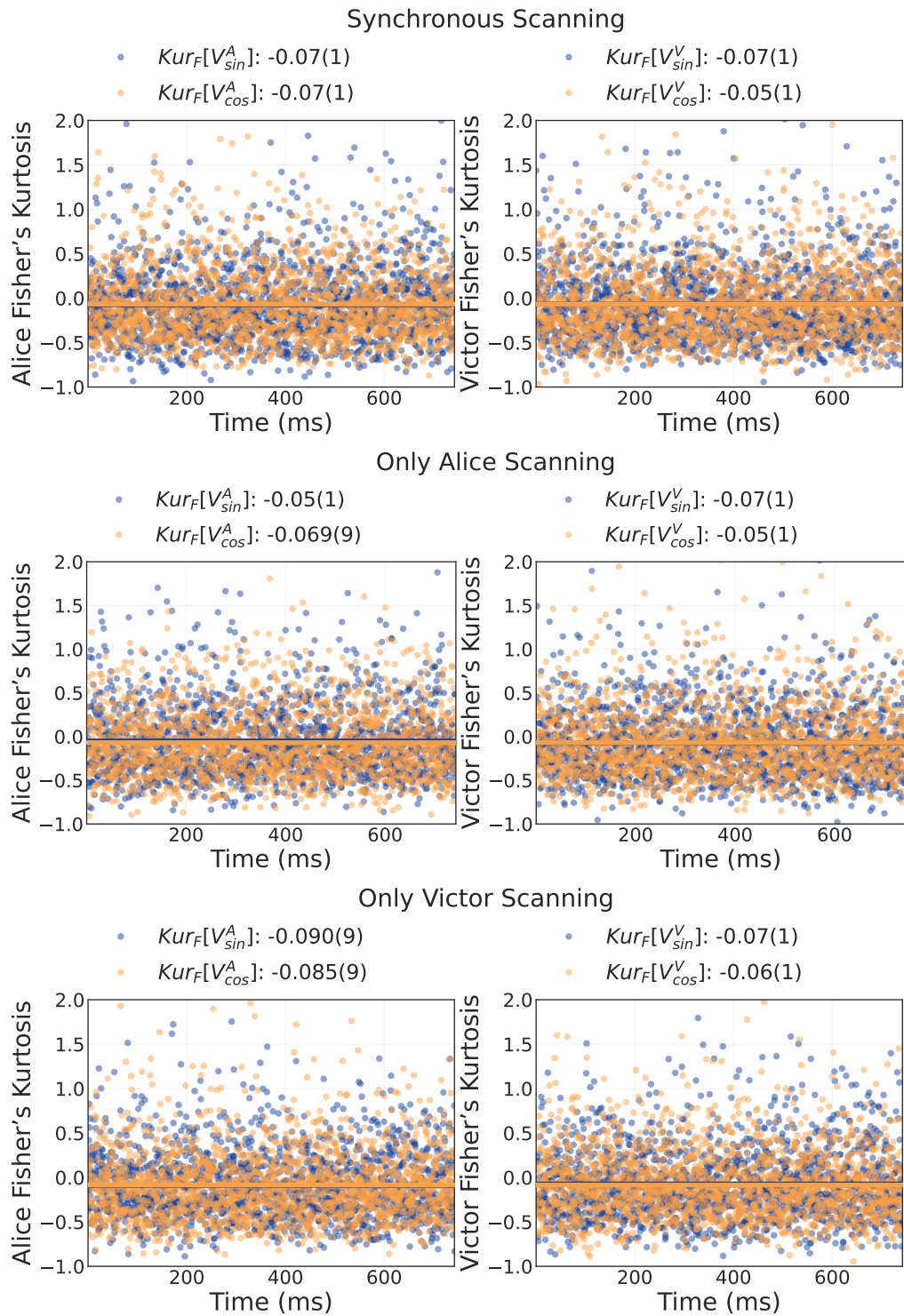


Figure 74 – Kurtosis of the acquired signal for all scanning conditions in the quantum tomography measurement. The near-zero kurtosis values for both orthogonal quadratures indicates that the generated fields are Gaussian and stationary [111].

The fitting procedure used in Figures 42 and 43 to obtain the full covariance matrix elements requires specific parameters from the analysis cavities. The cavity impedance matching factor is determined from its transmission and reflection profiles (Figure 40), while the bandwidth and mismatch factor of the cavities must be characterized prior to the measurement. These values are used as initial parameters in the fitting minimization process but are allowed to be optimized during the procedure. The final optimized values obtained from the tomography measurement are presented in Table 24, and they show good agreement with the expected values.

Table 24 – Parameters of the analysis cavities obtained from the fitting procedure used to extract the covariance matrix elements.

Analysis cavity parameter	Signal	Idler
Cavity bandwidth (MHz)	6.79(9)	6.85(9)
Normalized cavity bandwidth ($\Omega_{af}/\Delta\omega_{acav}$)	2.21(3)	2.19(3)
Impedance matching factor d	0.89(13)	0.66(7)
Spatial mismatch factor f^2	0.13(4)	0.07(2)

B.2 Additional Characterizations of the Measured State

Given the full covariance matrix of the four modes, including the two sideband modes associated with the signal and idler, it becomes possible to extract multiple quantifiers characterizing both local quantum states and, more significantly, the nature of the correlations between them. In this section, we present several of these quantifiers based on our characterized covariance matrix. Rather than detailing their individual interpretations and interconnections, we instead refer the reader to authoritative sources for a detailed discussion. These results will be of particular interest to readers already familiar with these quantifiers.

Table 25 displays the DGCZ criterion, as introduced in Section 2.1.4.1, applied to the upper and lower sideband modes ($\pm\Omega$). Because the system follows a stationary process, its symmetry ensures that several variance terms in the sum and difference spaces are equal, as reflected in the table. The presence of a normalized DGCZ parameter below one confirms entanglement between the signal's lower sideband (s_-) and the idler's upper sideband (i_+), as well as between the signal's upper sideband (s_+) and the idler's lower sideband (i_-).

Table 25 – DGCZ criterion applied to the upper and lower sideband modes ($\pm\Omega$).

Term	Value (s.n.u)	dB (s.n.u)
$\Delta^2 \hat{p}_-^{(s-,i_+)} = \Delta^2 \left(\frac{p_{-\Omega}^{(s)} - p_\Omega^{(i)}}{2} \right)$	0.9(1)	-0.6(5)
$\Delta^2 \hat{q}_+^{(s-,i_+)} = \Delta^2 \left(\frac{q_{-\Omega}^{(s)} + q_\Omega^{(i)}}{2} \right)$	0.9(1)	-0.6(5)
$\frac{\Delta^2 \hat{p}_-^{(s-,i_+)} + \Delta^2 \hat{q}_+^{(s-,i_+)}}{2}$	0.9(1)	-0.6(5)
$\Delta^2 \hat{p}_-^{(s+,i_-)} = \Delta^2 \left(\frac{p_\Omega^{(s)} - p_{-\Omega}^{(i)}}{2} \right)$	0.7(1)	-1.4(6)
$\Delta^2 \hat{q}_+^{(s+,i_-)} = \Delta^2 \left(\frac{q_\Omega^{(s)} + q_{-\Omega}^{(i)}}{2} \right)$	0.7(1)	-1.4(6)
$\frac{\Delta^2 \hat{p}_-^{(s+,i_-)} + \Delta^2 \hat{q}_+^{(s+,i_-)}}{2}$	0.7(1)	-1.4(6)

Table 26 presents additional properties of the covariance matrix in the symmetric/antisymmetric (\mathcal{S}/\mathcal{A}) basis. The first two columns list the purity and mean occupation number for various subsystems: the signal field (first row), the idler field (second row), the joint signal-idler system (third row), and the full covariance matrix, incorporating both bases (last row). These parameters are standard in continuous-variable quantum optics, with additional discussion available in [68]. The covariance matrix corresponding to each subsystem was obtained through the partial trace operation. The very small occupation number of the signal field justifies modeling the sideband modes of the deflected beam, which is directed to Victor, as a vacuum state. This deflected beam, which constitutes 0.5% to 1% of the total signal, is sent to Victor for input state creation. In the last column, we report a coherence quantifier specific to Gaussian states, as defined in [195], providing insight into the coherence properties of the system.

Table 26 – Purity, mean occupation number, and coherence quantifier for the covariance matrix in symmetric/antisymmetric basis. Values are provided for the signal, idler, joint system, and full covariance matrix.

	Purity (%)	Occupation Number	Coherence
$\mathbf{V}_s^{(s)}, \mathbf{V}_a^{(s)}$	49.0	0.55	0.47
$\mathbf{V}_s^{(i)}, \mathbf{V}_a^{(i)}$	39.6	0.81	0.59
$\mathbf{V}_s^{(s,i)}, \mathbf{V}_a^{(s,i)}$	34.5	1.36	1.70
$\mathbf{V}_{s/a}^{(s,i)}$	12.1	2.71	3.44

Table 27 reports the von Neumann entropy for the signal, idler, and the composite quantum state in the symmetric/antisymmetric (\mathcal{S}/\mathcal{A}) basis. From these entropy values, the von Neumann mutual information is calculated, which quantifies the total correlations

(both classical and quantum) between the signal and idler subsystems. This mutual information can be decomposed into two components: quantum discord and one-way classical information, both of which depend on the direction of information flow. The table presents results for both directions. Quantum discord quantifies the quantum correlations in a bipartite system, encompassing not only entanglement but also more general forms of quantum coherence. It is a versatile measure of non-classical correlations, with potential applications in quantum computing, communication, and cryptography [196, 197]. Although such correlations are expected, to the best of our knowledge, this work is the first to present experimentally measured quantum discord values for an optical parametric oscillator (OPO) operating in the above-threshold regime.

Table 27 – The von Neumann entropy, mutual information, quantum discord, and one-way classical information for the signal, idler, and composite quantum state in the symmetric/antisymmetric (\mathcal{S}/\mathcal{A}) basis. Results are presented for both directions of information flow.

	Von Neumann Entropy	Mutual Information	Gaussian Quantum Discord	One Way Classical Information
$\mathbf{V}_s^{(s)}, \mathbf{V}_a^{(s)}$	0.98	—	—	—
$\mathbf{V}_s^{(i)}, \mathbf{V}_a^{(i)}$	1.21	—	—	—
$\mathbf{V}_s^{(s,i)}, \mathbf{V}_a^{(s,i)}$	1.54	0.65	—	—
$\mathbf{V}_s^{(s)} \rightarrow \mathbf{V}_s^{(i)}$	—	—	0.20	0.45
$\mathbf{V}_s^{(i)} \rightarrow \mathbf{V}_s^{(s)}$	—	—	0.25	0.40

C – PUBLICATIONS

Articles published in peer-reviewed journals

The following articles were published in collaboration during the course of my PhD. While these works are not discussed in this thesis, they reflect significant contributions to the field and were part of collaborative efforts during my doctoral research period. Additional publications directly associated with the work presented in this thesis will be written and submitted following the thesis deposit.

- Mann, Felix, Helen M. Chrzanowski, **Felipe Gewers**, Marlon Placke, and Sven Ramelow. "Noise analysis of a quasi-phase-matched quantum frequency converter and higher-order counter-propagating SPDC." *Optics Express* 32, no. 24 (2024): 42225-42239 [[198](#)].
- Mann, Felix, Helen M. Chrzanowski, **Felipe Gewers**, Marlon Placke, and Sven Ramelow. "Low-noise quantum frequency conversion in a monolithic cavity with bulk periodically poled potassium titanyl phosphate." *Physical Review Applied* 20, no. 5 (2023): 054010 [[161](#)].

Articles currently in the preprint stage

- Mann, Felix, Helen M. Chrzanowski, **Felipe Gewers**, Marlon Placke, and Sven Ramelow. "Hong-Ou-Mandel Effect with Two Frequency-Entangled Photons of Vastly Different Color." *arXiv*, April 4, (2025): 2504.03304 [[199](#)].

Papers presented and published in conference proceedings

- Pearce, Emma L., Aron Vanselow, Ivan Zorin, Inna Kviatkovsky, Paul Kaufmann, **Felipe Gewers**, Atta Ur Rehman Sherwani, et al. "Sensing Techniques with Undetected Photons in the Mid-Infrared." In *Advanced Photon Counting Techniques XIX*, pp. 16. SPIE, 2025 [[200](#)].
- Blume, Gunnar, David Feise, Alexander Sahm, Philipp Hildenstein, Nils Werner, Johannes Zender, Fabian Wendt, **Felipe Gewers**, et al. "Long Wavelength, Small Quantum Interferometer Module: Shrinking MIR OCT Systems via Quantum Entanglement." In *Quantum Sensing, Imaging, and Precision Metrology III*, pp. 118. SPIE, 2025 [[201](#)].

- **Gewers, Felipe**, Gabriel Borba, Beatriz Moura, Túlio Brasil, Rayssa B. de Andrade, R. Medeiros de Araújo, Igor Konieczniak, Paulo Nussenzveig, and Marcelo Martinelli. "Multi-Color Continuous Variables Unconditional Quantum Teleportation: From Near-Infrared to Telecommunications' L-Band." In *Quantum 2.0*, pp. QW2B-5. Optica Publishing Group, 2024 [202].
- Mann, Felix, Helen M. Chrzanowski, **Felipe Gewers**, Marlon Placke, and Sven Ramelow. "Hong-Ou-Mandel interference of two photons of vastly different color." In *Quantum 2.0*, pp. QM2B-6. Optica Publishing Group, 2024 [203].
- Mann, Felix, Helen M. Chrzanowski, **Felipe Gewers**, Marlon Placke, and Sven Ramelow. "Higher-order counter-propagating SPDC and a complete analysis of the noise spectrum of a bulk ppKTP quantum frequency converter." In *Quantum 2.0*, pp. QW3A-48. Optica Publishing Group, 2024 [204].
- Mann, Felix, **Felipe Gewers**, Helen M. Chrzanowski, and Sven Ramelow. "A monolithic bulk ppKTP cavity for quantum frequency conversion from 637 nm to telecom wavelength." In *CLEO: Fundamental Science*, pp. FF2L-6. Optica Publishing Group, 2023 [205].